

# **Characterization and Optimization of an Extractor-type Catalytic Membrane Reactor for Meta-xylene Isomerization over Pt-HZSM-5 Catalyst**

by

**Michael Olawale Daramola**



Dissertation presented for the degree of Doctor of Philosophy (PhD) in  
Engineering (Chemical Engineering) in the Department of Process  
Engineering at the University of Stellenbosch, South Africa.

Promoters:

Prof. A. J. Burger  
Prof. L. Lorenzen  
Dr. A. Giroir-Fendler

December 2010

---

## Declaration

I, the undersigned, hereby declare that the work contained in this dissertation is my own original work and that I have not previously in its entirety or in part, submitted it at any university for a degree.

\_\_\_\_\_  
Signature

\_\_\_\_\_  
Name in full

\_\_\_\_\_/\_\_\_\_\_/\_\_\_\_\_  
Date

Copyright © 2010 Stellenbosch University

All rights reserved

---

## Summary

Future chemical production is faced with a challenge of limited material and energy resources. However, process intensification might play a significant role to alleviating this problem. Vision of process intensification through multifunctional reactors has stimulated research on membrane-based reactive separation processes, in which membrane separation and catalytic reaction occur simultaneously in one unit. These processes are rather attractive applications because they are potentially compact, less capital intensive, and have lower processing costs than traditional processes. Moreover, they often enhance the selectivity and yield of the target product.

For about three decades, there has been a great evolution in p-Xylene production technology, with many equipment improvements being instituted in the industry. Typically, these improvements bring economic as well as processing advantages to the producers. Such developments are vital, as the capital costs for process equipment to produce and separate p-Xylene from xylene isomers, especially into high purity p-Xylene, still remain very high. However, with numerous advantages of membrane-based reactive separation processes compared to the conventional processes, the research focus has been channelled toward application of MFI-type zeolite membranes for *in situ* separation and isomerization of xylene in extractor-type catalytic membrane reactors. To contribute to this research line, this study has focused on characterization and optimization of an extractor-type catalytic membrane reactor (e-CMR) equipped with a nanocomposite MFI-alumina membrane as separation unit for m-Xylene isomerization over Pt-HZSM-5 catalyst.

Nanocomposite MFI-alumina zeolite membranes (tubes and hollow fibres) used in this study were prepared via a so-called “hydrothermal pore-plugging synthesis technique” developed by Dalmon and his group more than a decade ago. In this concept, MFI material is grown by 'pore-plugging' direct hydrothermal synthesis in a porous matrix rather than forming thin films on top of the support. The advantages of this type of architecture over conventional film-like zeolite membranes include: (i) minimization of the effect of thermal expansion mismatch between the support and the zeolite, (ii) easy to scale-up, and (iii) easy module assembly, because the separative layer (zeolite crystals) are embedded within the pores of the ceramic support, reducing the effects of abrasion and thermal shocks. After membrane synthesis, the membrane quality and separation performance of these membranes were evaluated through single gas permeation ( $H_2$ ), binary gas separation (n-butane/ $H_2$ ) and ternary vapour mixture of xylene isomers using the vapour permeation (VP) method with p-Xylene as the target product. After evaluating the xylene isomer separation performance of the

---

membranes, the membranes were used in extractor-type catalytic membrane reactors to carry out m-Xylene isomerization over Pt-HZSM-5 catalyst with p-Xylene as the target product.

This dissertation has shown that nanocomposite MFI-alumina membrane tubes and hollow fibre membranes were selective to p-Xylene from xylene isomers. The dissertation also reports for the first time in open literature the excellent xylene separation performance of nanocomposite MFI-alumina membrane tubes at higher xylene loading (or vapour pressure). Unlike their film-like counterparts, the membranes still maintain increased selectivity to p-Xylene at higher xylene vapour pressures without showing a drastic decrease in selectivity. This outstanding property makes it a promising choice for pervaporation applications where concentration profile is usually a major problem at higher loading of xylene.

With the use of nanocomposite MFI-alumina hollow fibre membranes, this research has demonstrated that membrane configuration and effective membrane wall thickness play a prominent role in enhancing cross membrane flux. Results presented in the study show, for the first time in open literature, that nanocomposite MFI-alumina hollow fibre membrane could enhance p-Xylene fluxes during the separation of ternary vapour mixture of xylene due to the smaller effective wall thickness of the membrane (membrane thickness  $<1 \mu\text{m}$ ) when compared to conventional randomly oriented MFI zeolite films (membrane thickness  $>3 \mu\text{m}$ ). During xylene isomers separation with nanocomposite hollow fibre membrane, about 30% increase in p-Xylene flux was obtained compared to the membrane tubes, operated under the same conditions. Additionally, hollow fibres offer the added advantage of membrane surface-to-volume ratios as high as  $3000 \text{ m}^2/\text{m}^3$  compared to conventional membrane tubes. Using this type of system could be instrumental in reducing both the size and cost of permeating modules for future xylene separation processes. However, obtaining high quality nanocomposite MFI-alumina membrane fibres is subject to the availability of high quality fibre supports.

Regarding the application of nanocomposite MFI-alumina membrane tubes as extractor-type catalytic membrane reactors (referred to as extractor-type zeolite catalytic membrane reactor (e-ZCMR) in this study) for m-Xylene isomerization over Pt-HZSM-5, the results presented in this study further substantiate and confirm the potentials of e-ZCMRs over conventional fixed-bed reactors (FBRs). In the combined mode (products in the permeate plus products in the retentate), the e-ZCMR displayed 16-18% increase in p-Xylene yield compared to an equivalent fixed-bed reactor operated at the same operating conditions. On the basis of the high p-Xylene-to-o-Xylene (p/o) and p-Xylene-to-m-Xylene (p/m) separation factors offered by the membranes, p-Xylene compositions in the permeate-only mode (products in the permeate stream) in the range 95%-100% were obtained in the e-ZCMR. When a defect-free nanocomposite MFI-alumina membrane tube with p-Xylene-to-o-Xylene (p/o) separation factor  $>400$  was used, ultra pure p-Xylene with p-Xylene purity

---

approaching 100% in the permeate-only mode was obtained. Moreover, the e-ZCMR displayed 100% para-selectivity in the permeate-only mode throughout the temperatures tested. This is not possible with conventional film-like MFI-type zeolite membranes. Therefore, the application of nanocomposite MFI-alumina membranes in extractor-type catalytic membrane reactors could catalyse the development of energy-efficient membrane-based process for the production of high purity p-Xylene.

Furthermore, in this dissertation, a report on modelling and sensitivity analysis of an e-ZCMR equipped with a nanocomposite MFI-alumina membrane tube as separation unit for m-Xylene isomerization over Pt-HZSM-5 catalyst is presented. The model output is in fair agreement with the experimental results with percentage errors (absolute) of 17%, 29%, 0.05% and 19.5% for p-Xylene yield in combined mode, p-Xylene selectivity in combined mode, p-Xylene selectivity in permeate-only mode and m-Xylene conversion, respectively. Therefore, the model is adequate to explain the behaviour of e-ZCMR during m-Xylene isomerization over Pt-HZSM-5 catalyst. The model is also adaptable to e-ZCMRs of different configurations such as hollow fibre MFI-alumina membrane-based e-ZCMRs. To gain more insight into the behaviour of the model to small changes in certain design parameters, sensitivity analysis was performed on the model. As expected, the sensitivity analysis revealed that intrinsic property of membrane (porosity, tortuosity), membrane effective thickness and reactor size (indicated with reactor internal diameter) play a significant role on the performance of e-ZCMR during p-Xylene production from the mixed xylenes. MFI-alumina zeolite membranes with optimized parameters such as membrane porosity, membrane tortuosity, and membrane effective wall thickness might enhance transport of p-Xylene through the membrane and thus resulting in higher p-Xylene flux through the membrane. This eventually would translate into an increase in p-Xylene yield in permeate-only mode. As far as it could be ascertained, this is the first report in open literature on modelling study with sensitivity analysis of e-ZCMR equipped with nanocomposite MFI-alumina membrane tubes as separation unit for m-Xylene isomerization over Pt-HZSM-5 catalyst.

In addition, the results of this study have confirmed previous research efforts reported on the application of extractor-type catalytic membrane reactors, having MFI-type membranes as separation units, for p-Xylene production via m-Xylene isomerization over a suitable catalyst. Also, new ideas were developed, tested and proposed that now provide a solid basis for further scale-up and techno-economical studies. Such studies are necessary to evaluate the competitiveness of the technology with the traditional processes for the production of high purity p-Xylene from mixed xylene.

In summary, the encouraging results, as documented in this dissertation and also communicated to researchers in the area of membrane-based reactive separation (in the form

---

of four peer-reviewed international scientific publications and four conference proceedings), could provide a platform for developing a scaled-up membrane-based energy-efficient industrial process for producing high purity p-Xylene through isomerization.

---

## Opsomming

Die produksie van chemiese stowwe word belemmer deur die uitdaging van beperkte materiaal- en energiebronne. Prosesuitbreiding kan egter 'n noemenswaardige rol in die verligting van hierdie probleem speel. Die moontlike gebruik van multi-funksionele reaktore in prosesuitbreiding het navorsing in membraan-gebaseerde reaktiewe skeidingsprosesse (waar membraanskeiding en die katalitiese reaksie gelyktydig in 'n enkele eenheid plaasvind) aangemoedig. Hierdie prosesse is aantreklik omdat hulle potensieel kompak en minder kapitaal-intensief is en ook teen laer koste as tradisionele prosesse bedryf kan word. Dit is ook dikwels die geval dat die multi-funksionele reaktor die selektiwiteit en opbrengs van die gewenste produk verhoog.

In die afgelope drie dekades was daar 'n sterk verandering in die tegnologie wat gebruik word in die produksie van p-Xileen, met vele verbeterings aan nuwe toerusting wat in die nywerheid in bedryf gestel is. Hierdie verbeteringe hou gewoonlik ekonomiese-, sowel as bedryfsvoordele vir die produsente in. Ontwikkelings in hierdie veld is noodsaaklik aangesien die kapitale uitgawes vir die toerusting om p-Xileen, veral baie suiwer p-Xileen, van xileenpolimere te produseer en te skei, steeds baie hoog is. Met talle voordele gekoppel aan membraangebaseerde reaktiewe skeidingsprosesse in vergelyking met normale prosesse, is die navorsing egter gekanaliseer na die gebruik van MFI-tipe zeolietmembrane vir die in-situ skeiding en isomerisasie van xileen in ekstraksie-tipe katalitiese membraanreaktore. As bydrae tot hierdie navorsingsveld het hierdie studie op die karakterisering en optimering van 'n ekstraksie-tipe katalitiese membraanreaktor (e-KMR), toegerus met 'n nanosaamgestelde MFI-alumina membraan as skeidingseenheid vir m-Xileen isomerisasie in die teenwoordigheid van 'n Pt-HZSM-5 katalis, gefokus.

Nanosaamgestelde MFI-alumina zeolietmembrane (buisse en hol vesels) wat in hierdie studie gebruik is, is voorberei deur die sogenaamde "hidrotermiese porie-sperring sintese tegniek" wat meer as 'n dekade gelede ontwikkel is deur Dalmon en sy groep. In hierdie tegniek word MFI-materiaal gekweek deur direkte hidrotermiese sintese in 'n poreuse matriks, eerder as die vorming van dun films bo-op die ondersteuningsbasis. Die voordele van hierdie ontwerp bo dié van die konvensionele filmagtige zeolietmembrane sluit in: (i) minimering van die effek van termiese uitsetting op die gaping tussen die ondersteuningsbasis en die zeoliet, (ii) die gemak van opskalering, en (iii) die gemak waarmee die modules aanmekaar gesit kan word, omdat die skeidingslaag (zeolietkristalle) binne die porieë van die keramiek-ondersteuningsbasis geleë is, wat die effek van erodering en termiese skok verminder. Ná die membraansintese is die membraankwaliteit en skeidingsvermoë ge-evalueer deur enkel-gas-deurdringing ( $H_2$ ), binêre-gas-skeiding (n-butaan/ $H_2$ ), en ternêre

---

dampmengsel van xileen-isomere deur die gebruik van die damp-deurdringingsmetode met p-Xileen as die teikenproduk.

Hierdie tesis het gewys dat nanosaamgestelde MFI-alumina membraanbuise en hol vesel membrane selektief was ten opsigte van p-Xileen vanuit xileen-isomere. Die tesis doen ook, vir die eerste keer in die oop literatuur verslag, oor die uitstekende p-Xileen skeidingsvermoë van nanosaamgestelde MFI-alumina buise by hoër xileenladings (of dampdrukke). Anders as hulle filmagtige eweknieë het die membrane steeds hul verhoogde selektiwiteit vir p-Xileen by hoër dampdrukke behou, sonder 'n merkbare verlaging in die selektiwiteit. Hierdie merkwaardige eienskap maak dit 'n belowende keuse vir pervaporasie toepassings, waar die konsentrasieprofiel (as gevolg van hoër xileenladings) gewoonlik 'n noemenswaardige probleem is.

Met die gebruik van nanosaamgestelde MFI-alumina membrane het hierdie navorsing gewys dat membraankonfigurasië en -wanddikte 'n prominente rol speel in die verbetering van vloei oor die membraan. Resultate wat in die studie voorgelê word, wys, vir die eerste keer in oop literatuur, dat hol vesel nanosaamgestelde MFI-alumina membrane die deurvloei van p-Xileen kan verbeter gedurende die skeiding van ternêre dampmengsels van xileen, as gevolg van die kleiner effektiewe wanddikte van die membraan ( $<1 \mu\text{m}$ ) wanneer dit vergelyk word met konvensionele kansgewys-geïntegreerde MFI-zeoliet films met 'n membraandikte van  $>3 \mu\text{m}$ . Tydens die skeiding van xileen-isomere met nanosaamgestelde hol vesel membrane is 'n verbetering van ongeveer 30 % in die deurvloei van p-xileen verkry, vergeleke met membraanbuise, by identiese bedryfstoele. Hol vesels bied ook die verdere voordeel van oppervlak-tot-volume verhoudings van so hoog as  $3000 \text{ m}^2/\text{m}^3$  vergeleke met konvensionele membraanbuise. Die gebruik van hierdie tipe sisteem kan deurslaggewend wees in die vermindering van die grootte en koste van deurlatingseenhede in toekomstige xileen-skeidingsprosesse. Die vervaardiging van hoë-kwaliteit nanosaamgestelde MFI-alumina membraanvesels is egter onderworpe aan die beskikbaarheid van hoë-kwaliteit vesel-ondersteuningsbassisse.

Wat die gebruik van nanosaamgestelde MFI-alumina membraanbuise as ekstraksie-tipe katalitiese membraanreaktore betref (ekstraksie-tipe zeoliet katalitiese membraanreaktor, of e-ZKMR in hierdie studie) vir m-Xileen isomerisasië in die teenwoordigheid Pt-HZSM-5, bevestig die resultate die potensiaal van e-ZKM reaktore bo konvensionele vaste-bed reaktore (VBR). In die gekombineerde verstelling (met produkte in die permeaat sowel as die retentaat) toon die e-ZKMR 'n 16 – 18% verbetering in die opbrengs van p-Xileen vergeleke met 'n ekwivalente VBR by dieselfde bedryfskondisies. Gegronde op die hoë p-Xileen-tot-o-Xileen (p/o) en p-Xileen-tot-m-Xileen (p/m) skeidingsfaktore wat deur die membraan gebied word, is p-Xileen-samestellings in die slegs-permeaat verstelling (produkte in die permeaatstroom) van tussen 95 en 100% in die e-ZKMR verkry. Toe 'n defek-vrye

---

nanosaamgestelde MFI-alumina membraanbuis met 'n (p/o) skeidingsfaktor van >400 gebruik is, is p-Xileen met 'n suiwerheid na aan 100% in die slegs-permeaat verstelling verkry. Die e-ZKMR het ook 100% para-selektiwiteit in die slegs-permeaat verstelling getoon by alle toets-temperature, iets wat onmoontlik is met gewone filmagtige MFI-tipe zeolietmembrane. Om hierdie rede is dit moontlik dat die gebruik van MFI-alumina membrane in ekstraksie-tipe katalitiese membraanreaktore die ontwikkeling van energie-doeltreffende membraan-gebaseerde prosesse vir die produksie van suiwer p-Xileen kan bevorder.

Verder word daar in hierdie tesis verslag gedoen oor die modelering en sensitiwiteitsanalise van 'n e-ZKMR wat toegerus is met 'n nanosaamgestelde MFI-alumina membraanbuis as skeidingseenheid vir m-Xileen isomerisasie in die teenwoordigheid van 'n Pt-HZSM-5 katalis. Die model-uitsette is redelik in ooreenstemming met eksperimentele resultate met absolute fout-persentasies van 17, 27, 0.05 en 19.5 % vir die p-Xileen opbrengs in die gekombineerde verstelling, p-Xileen selektiwiteit in die gekombineerde verstelling, p-Xileen selektiwiteit in die slegs-permeaat verstelling en m-Xileen omsetting, onderskeidelik. Om hierdie rede kan die model die gedrag van 'n e-ZKMR verduidelik tydens die m-Xileen isomerisasie in die teenwoordigheid van 'n Pt-HZSM-5 katalis. Die model kan ook aangepas word na e-ZKM reaktore met verskillende konfigurasies, soos hol vesel MFI-alumina membraan-gebaseerde e-ZKMRe. Om meer insig te kry in die gedrag van die model op klein veranderinge in sekere ontwerpparameters, is 'n sensitiwiteitsanalise op die model uitgevoer. Soos verwag, het die sensitiwiteitsanalise gewys dat die intrinsieke eienskappe van die membraan (porositeit, tortuositeit), die effektiewe van membraandikte en die reaktorgrootte (gemeet as die interne deursnit van die reaktor) 'n noemenswaardige rol speel in die gedrag van die e-ZKMR gedurende p-Xileen produksie vanuit gemengde xilene.

MFI-alumina zeolietmembrane met geoptimeerde parameters soos membraan-porositeit, -tortuositeit, en -wanddikte mag dalk die oordrag van p-Xileen deur die membraan bevorder en sodoende 'n hoër vloeï van p-Xileen oor die membraan bewerkstellig. Dit sal uiteindelik lei tot 'n verhoging in die opbrengs van p-Xileen in die slegs-permeaat verstelling. So ver dit vasgestel kon word, is hierdie die eerste verslag in die oop literatuur wat die modelering en sensitiwiteitsanalise van 'n e-ZKMR, toegerus met nanosaamgestelde MFI-alumina membraanbuise as skeidingseenheid vir m-Xileen isomerisasie in die teenwoordigheid van 'n Pt-HZSM katalis, aanspreek.

Verder ondersteun die resultate van hierdie studie vorige navorsingspogings op die gebruik van e-KMRe, met MFI-tipe membrane as skeidingseenhede, vir die produksie van p-Xileen deur middel van m-Xileen isomerisasie in die teenwoordigheid van 'n geskikte katalis. Verder is nuwe idees ontwikkel, getoets en voorgestel wat dien as 'n stewige basis vir verdere opskalering- en tegno-ekonomiese studies. Sodanige studies is nodig om die vatbaarheid van die tegnologie relatief tot die tradisionele prosesse te bepaal.

---

Ter opsomming, die bemoedigende resultate, soos in die tesis gedokumenteer (en ook gepubliseer in vier ewe-knie beoordeelde internasionale wetenskaplike joernale en vier konferensiestukke), kan as 'n platform dien vir die ontwikkeling van 'n opgeskaleerde membraan-gebaseerde energie-doeltreffende nywerheidsproses vir die produksie van suiwer p-Xileen deur middel van isomerisasie.

---

## Dedication

This work is dedicated to the memory of the following people:

My late co-supervisor, Dr. Sylvain MIACHON (1967-2009)

My late grandmother, Mrs. Owa Comfort FADUMILA (1925-1987)

My late father-in-law, Elder Isaac Adeoti ADEDAYO (1940-1983)

---

## Acknowledgements

There are so many people who have shaped my life up to this point. This dissertation represents not only the last few years, but the culmination of maturing and developing for about 30 years. There have been so many wonderful and positive influences in my life that have motivated me in my life goals. First and foremost, I thank Almighty God who is the giver of life and wisdom. Secondly, I would like to thank my promoter, Prof. A.J. Burger and my co-promoter, Prof. L. Lorenzen of the Department of Process Engineering, Stellenbosch University, South Africa where part of this work was done, for their unmatched guidance and moral support during this study. My unparalleled appreciation further goes to the National Research Foundation of South Africa and the Department of Process Engineering, Stellenbosch University for financial assistance for this study. Appreciation also goes to the staff of the Department of Process Engineering, Stellenbosch University for technical, analytical and administrative assistance. A special thanks to the people in the workshop, for their assistance throughout the modification and testing of the experimental set-up.

In addition, my gratitude goes to Dr. Anne Giroir-Fendler and the late Dr. Sylvain Miachon both of who were my supervisors at the Institute for Research on Catalysis and Environment (IRCE), France, for their guidance and friendliness, and for enabling me to use the facilities at the laboratory at IRCE for a total of twelve months to complete some parts of this study. Further, I would like to thank the French National Centre for Scientific Research, i.e. the Centre National de la Recherche Scientifique (CNRS); the French Embassy in South Africa for their financial contributions during the periods of my research at the IRCE, France. Gratitude also goes to the GRE group at IRCE for welcoming me into their group and providing assistance during my stay. In particular, I would like to extend my gratitude to Dr. Jean-Alain Dalmon for his help as a mentor while in France; Emmanuel Landrison and Cecile for their technical assistance; and Dr. Marc Pera-Titus for his assistance. My unparalleled appreciation also goes to Koffi Fiagy for his guidance on the modelling aspect of this study.

I also would like to acknowledge my friends in South Africa (Callisto, Ali, Ebenezer, Demilade, Tope, Benjamin, Eunice, Marion, and Pastor Funlola Olojede, who also provided editorial assistance for this manuscript); and in France, Zhiyong, Awad, Vola, Juliet, Mr and Mrs Festus Uzoma, for their moral support and friendship in the course of this study. Special thanks to Dr. & Mrs Kole Amigun, Dr. & Mrs Owojori Gbenga, Engr. Funmi Aransiola, members of the Seventh-Day Adventist Students' Movement (SDAM) of Stellenbosch University, members of the Association of Nigerian Students in Stellenbosch University

---

(ANSSU), and a host of others for their support. I will be an ingrate if I fail to acknowledge the invaluable support of my dear wife, Omotayo. She went through thick and thin with me in the course of this programme. Omotayo, I will forever be grateful to you.

Furthermore, I am grateful to the authority of the Obafemi Awolowo University, Nigeria for granting me study leave to undergo this programme and many thanks to my family, my parents and in-laws (Elder and Mrs Ezekiel Daramola and Mrs Esther Adedayo); my siblings and in-laws (Engr and Mrs F.O. Daramola, Yemi, Babafemi, Abiodun, Sade Adedayo, Gbenga, Foluke, Taiwo Adedayo, Mr and Mrs Nike Ola, Mr and Mrs. T.K. Ola, Damilola and Samson) for their encouragement and prayers at all times.

Lastly, I wish to express my gratitude to the reviewers of the dissertation for their thorough job and for their constructive comments which have helped to improve the quality of the dissertation.

---

## Table of Contents

Declaration .....	ii
Summary .....	iii
Opsomming .....	vii
Dedication .....	xi
Acknowledgements .....	xii
Table of Contents .....	xiv
List of Figures .....	xvi
List of Tables .....	xxii
Chapter 1: Motivation for the study and research objective .....	1
1.1 Motivation .....	1
1.2 Dissertation overview .....	5
1.3 Research benefits and novel contributions .....	6
Chapter 2: Literature review and state of the art .....	8
2.1 Commercial technologies for production and purification of p-Xylene .....	8
2.2 Catalysts for xylene isomerization .....	12
2.3 Membrane-based technology for the production and purification of PX .....	14
2.4 Concluding remark and scope for research .....	39
Chapter 3: Membrane preparation, characterization and experimental procedures .....	41
3.1 Membrane preparation techniques .....	41
3.2 Preparation of MFI zeolite membrane by “pore-plugging” technique .....	42
3.3 Membrane characterization techniques .....	48
3.4 Experimental set-up for xylene isomers separation .....	54
3.5 Result analysis and evaluation of membrane performance .....	59
3.6 Concluding remark .....	61
Chapter 4: Tubular MFI-alumina membranes for xylene isomer separation .....	62
4.1 Introduction .....	62
4.2 Membrane preparation, characterization and separation test .....	63
4.3 Results and discussion .....	64
4.4 Role of MFI confinement on the xylene vapour permeation performance .....	72
4.5. Concluding remark .....	73
Chapter 5: Hollow fibre MFI-alumina membranes for xylene isomer separation .....	75
5.1 Introduction .....	75
5.2 Membrane preparation, characterization and separation test .....	76
5.3 Results and discussion .....	79
5.4 Influence of porous structure of hollow fibres on separation performance .....	87
5.5 Concluding remark .....	91
Chapter 6: Experimental study of m-Xylene isomerization in e-ZCMR .....	92
6.1 Introduction .....	92
6.2 Experimental .....	93
6.3 Results and discussion .....	98
6.4 Ultra-pure p-Xylene production via m-Xylene isomerization in e-ZCMR .....	108
6.5 Concluding remark .....	112
Chapter 7: Modelling of e-ZCMR during m-Xylene isomerization .....	114
7.1 Introduction .....	114

---

7.2 Model development and formulation.....	115
7.3 Results and discussion .....	124
7.4 Effect of design variables on e-ZCMR performance.....	127
7.4.1 Effect of membrane effective thickness.....	130
7.4.2 Effect of membrane porosity and tortuosity .....	132
7.4.3 Effect of reactor size .....	135
7.5 Concluding remark.....	139
Chapter 8: Conclusions, recommendations and future outlook.....	140
8.1. Conclusions.....	140
8.2. Recommendations and future outlook .....	143
References.....	145
Symbols.....	167
Appendix.....	170
Appendix A: Evaluation of saturation system .....	170
Appendix B: Calibration of mass flow controller and flow meters and GC.....	172
Appendix C: Diffusivity and rate of reaction constants for reactor modelling.....	175
Appendix D: CMR testing rigs and operational procedures .....	176
Appendix E: List of published and submitted papers related to this work .....	181

---

## List of Figures

Figure 1.1:	Molecular structures of the three xylene isomers .....	2
Figure 1.2:	World supply /demand for xylenes (especially PX) [5].....	2
Figure 2.1:	Chevron p-Xylene crystallization process [16].....	9
Figure 2.2:	UOP Parex simulated moving bed for adsorptive separation. Nomenclature: AC, adsorbent chamber; RV, rotary valve; EC, extract column; RC, raffinate column. Lines: 2-desorbent; 5-extract; 9-feed; 12-raffinate. All other ports are closed at this time [21].....	11
Figure 2.3:	Flowsheet of the ExxonMobil XyMax isomerization process [22].....	12
Figure 2.4:	Schematic representation of pervaporation (left hand side) and vapour permeation (right hand side) across a membrane .....	16
Figure 2.5:	Key features of MFI zeolite: (1) crystal morphology, (2) straight and sinusoidal channels with intersections, (3) crystal framework and (4) detailed atomic structure (with permission from [82]).....	17
Figure 2.6:	P-Xylene adsorption in the MFI zeolite framework .....	17
Figure 2.7:	Characteristic inflection in p-Xylene adsorption isotherms on silicalite in the temperature range 273-323 K. Adapted from [84].....	19
Figure 2.8:	Adsorption kinetics of benzene, toluene, ethylbenzene and p/o/m-Xylenes in HZSM-5 at low loadings (<1 molec/uc). Adapted from [144].....	24
Figure 2.9:	Intracrystalline diffusion time constant for p-Xylene at 283 K in a fresh sample. Adapted from [83].....	27
Figure 2.10:	Membrane response as a function of p-Xylene feed concentration during PV of an equimolar p/o xylene feed at 298 K. Adapted from [170].....	29
Figure 2.11:	Effect of cation exchange on the VP performance of ZSM-5 zeolite membranes in the separation of ternary xylene isomer mixtures at 673 K and for p/m/o partial pressures of 0.23/0.83/0.26 kPa. Adapted from [176].....	33
Figure 2.12:	Normal-butane fluxes through an unsupported (F), a single supported (FS), and a double-sided (FSF) zeolite membrane as a function of (a) the sweep gas flow rate (the shaded region represents common sweep gas flow rate reported in literature), and (b) the adsorption equilibrium constant. Graph reproduced from [192].....	33
Figure 2.13:	Classification of CMRs: (a) extractor, (b) distributor, (c) flow-through contactor and (d) interfacial contactor. A and B represent reactants while P, P1, P2 are the products .....	34

---

Figure 2.14:	Schematic representation of the <i>p</i> -Xylene selective extraction in a MFI membrane from an isomerization reactor. The isomerization mechanism considered here corresponds to a metal-doped HZSM-5 catalyst .....35
Figure 2.15:	Chemical equilibrium for the <i>o</i> / <i>m</i> / <i>p</i> -Xylene ternary system as a function of temperature in the range 250-1500 K. (b) evolution of equilibrium constants $K_x$ [ $x=1$ ( <i>m</i> -Xylene $\leftrightarrow$ <i>o</i> -Xylene), $x=2$ ( <i>p</i> -Xylene $\leftrightarrow$ <i>m</i> -Xylene) and $x=3$ ( <i>p</i> -Xylene $\leftrightarrow$ <i>o</i> -Xylene)]; (b) equilibrium product distribution (molar basis) at the standard state [199].....35
Figure 2.16:	ExxonMobil patented process for <i>p</i> -Xylene production [200].....37
Figure 2.17:	Different extractor-type zeolite CMRs (e-ZCMRs) for xylene isomerization: (a) Inert Zeolite CMR (IZCMR), (b) Active Zeolite CMR (AZCMR) and (c) Bi-functional Zeolite CMR (BZCMR) reactor. Adapted from [188].....37
Figure 2.18:	<i>P</i> -Xylene yield (top) and <i>p</i> -Xylene production increase (bottom) as a function of temperature for xylene isomerization in an inert ZCMR based on Ba-ZSM-5/SS membrane [198].....38
Figure 2.19:	<i>M</i> -Xylene isomerization in a e-ZCMR with varying module temperature (Feed flow rate: 20mL/min, sweep flow rate: 20mL/min; for FBR, feed flow rate: 20mL/min) [190].....38
Figure 3.1:	The cross-section of the tubular support supplied by Pall-Exekia .....43
Figure 3.2:	Picture of the typical supports (tube and fibre) (picture not to scale).....43
Figure 3.3:	Picture of a fibre support sealed with swagelok connector before porosimetry test) (picture not to scale) .....45
Figure 3.4:	Typical curves of $N_2$ flux versus transsupport differential pressure obtained from gas-liquid displacement and corresponding pore size distribution obtained after data processing according to the set of Eq.3.1 to Eq.3.3.....45
Figure 3.5:	Pictures of Teflon <sup>R</sup> -lined autoclave used for hydrothermal synthesis: for membrane tubes (left handside), for hollow fibre membranes (right handside) (pictures not to scale).....46
Figure 3.6:	Temperature programme for membrane synthesis .....47
Figure 3.7:	Temperature programme for membrane calcination .....48
Figure 3.8:	XRD image analysis of the membrane fibre showing the formation of the membrane .....51
Figure 3.9:	Process Flow Diagram (PFD) for BDQT.....52
Figure 3.10:	Schematic of the permeation test module, showing the nanocomposite MFI-ceramic membrane unit sealed inside the module with graphite seals .....52
Figure 3.11:	Pictures of the stainless steel module showing its components: A&C are O-rings and B is the stainless steel module (picture not to scale).....53

---

Figure 3.12:	Pictures of the controlled electrical oven (left handside) and the graphite seals (right handside) used in this study (picture not to scale) .....	53
Figure 3.13:	Temperature programme used for high temperature pre-treatment of membranes pre-treatment... ..	54
Figure 3.14:	Process Flow Diagram (PFD) of the modified set-up used for separation and isomerization tests at IRCELYON.....	55
Figure 3.15:	Process Flow Diagrams (PFD) of the modified set-up used for separation and isomerization tests at the Department of Proceess Engineering, Stellenbosch University.....	56
Figure 3.16:	Pictures of the <i>Shimadzu GC-14A</i> used in this study .....	57
Figure 3.17:	Picture of the <i>Varian 3400</i> used in this study .....	58
Figure 3.18:	Schematic of the saturation system for xylene vapour saturation in N <sub>2</sub> gas...59	
Figure 4.1:	Hydrogen permeance as a function of time in a <i>n</i> -butane room-temperature desorption experiment. Adapted from [242] .....	65
Figure 4.2:	SEM micrograph of the membrane showing cross-section of the membrane support with the three layers with formation of nanocomposite material on the support .....	66
Figure 4.3:	SEM micrograph of the membrane showing surface view of the 0.2 μm-layer pore-plugged with zeolite crystals .....	66
Figure 4.4:	Xylene ternary vapour mixture separation as a function of temperature within a nanocomposite MFI-alumina membrane. Experimental conditions: p-/m-/o-Xylene feed partial pressures, 0.63 kPa / 0.27 kPa / 0.32 kPa; sweep gas flow rate, 15 mL(STP)/min; feed flow rate, 10 mL(STP)/min. The straight line corresponds to the MS fittings for p-Xylene flux, while the dashed lines for separation factors are a guide to the eye. Adapted from [242].....	69
Figure 4.5:	Xylene ternary vapour mixture separation as a function of N <sub>2</sub> sweep gas flow rate within a nanocomposite MFI-alumina membrane. Experimental conditions: p-/m-/o-Xylene feed partial pressures, 0.59 kPa / 0.45 kPa / 0.40 kPa; temperature, 473 K; feed flow rate, 10 mL(STP)/min. The straight line corresponds to the p-Xylene flux predicted by Eq. 4.1, while the dashed lines for separation factors are a guide to the eye. Adapted from [242].....	70
Figure 4.6:	Xylene ternary vapour mixture separation as a function of total xylene vapour pressure within a nanocomposite MFI-alumina membrane. Experimental conditions: p-/m-/o-Xylene feed composition, 1 : 1 : 1 up to 15 kPa and 1: 1 : 3 beyond 30 kPa; temperature, 473 K; feed flow rate, 10 mL(STP)/min, sweep flow rate, 15 mL(STP)/min. The ratios 1:1:1 & 1:1:3 refer to the composition ratio of the xylene isomer in the feed (p-Xylene:m-Xylene: o-Xylene) The straight and dashed lines, respectively, for xylene fluxes and separation factors are a guide to the eye.....	71
Figure 4.7:	Xylene VP as a function of total xylene vapour pressure with a film-like membrane at 373 K. Adapted from [183].....	73

---

Figure 5.1:	Pictures of the support fibre used for membrane synthesis .....	77
Figure 5.2:	SEM image of the cross-section of the support used for membrane synthesis.....	77
Figure 5.3:	Fibres mounted into their mechanical support tubes .....	78
Figure 5.4:	Schematic showing the section of a fibre mounted inside its mechanical fibre supports .....	78
Figure 5.5:	SEM image of the cross-section of the innermost layer of the hollow fibre MFI-alumina membrane .....	81
Figure 5.6:	Single vapour permeation flux as a function of temperature. <u>Experimental conditions</u> : p-/o-Xylene feed partial pressures, 3.77 kPa / 3.38 kPa; feed gas flow rate, 10 mL(STP)/min; sweep gas flow, 15 mL(STP)/min. Adapted from [248]..	82
Figure 5.7:	Xylene ternary vapour mixture separation as a function of temperature with nanocomposite MFI-alumina hollow fibre showing the permeation fluxes;(b) p/o and p/m separation factors. <u>Experimental conditions</u> : p-/m-/o-Xylene feed partial pressures, 0.62 kPa / 0.27 kPa / 0.32 kPa; sweep gas and feed flow rates as in Fig. 5.6 The straight and dashed curves are a guide to the eye. Adapted from [248].....	82
Figure 5.8:	Xylene ternary vapour mixture separation as a function of temperature with nanocomposite MFI-alumina hollow fibre showing the p/o and p/m separation factors. <u>Experimental conditions</u> : p-/m-/o-Xylene feed partial pressures, 0.62 kPa / 0.27 kPa / 0.32 kPa; sweep gas and feed flow rates as in Fig.5.6. The straight and dashed curves are a guide to the eye.Adapted from [248].....	83
Figure 5.9:	Xylene ternary vapour mixture separation as a function of temperature with nanocomposite MFI-alumina membrane tube showing permeation fluxes. <u>Experimental conditions</u> : p-/m-/o-Xylene feed partial pressures, 0.62 kPa / 0.27 kPa / 0.32 kPa; sweep gas and feed flow rates as in Fig.5.6. The straight and dashed curves are a guide to the eye.....	85
Figure 5.10:	Xylene ternary vapour mixture separation as a function of temperature with nanocomposite MFI-alumina membrane tube showing p/o and p/m separation factors. <u>Experimental conditions</u> : p-/m-/o-Xylene feed partial pressures, 0.62 kPa / 0.27 kPa / 0.32 kPa; sweep gas and feed flow rates as in Fig.5.6. The straight and dashed curves are a guide to the eye.....	85
Figure 5.11:	Evolution of the N <sub>2</sub> flux with the transfibre pressure in gas-liquid displacement tests for four representative hollow fibre supports belonging to families A-D and corresponding pore size distributions obtained after data processing. Adapted from [253].....	88
Figure 5.12:	SEM image of the cross-section of the hollow fibre support.....	88
Figure 5.13:	SEM image of the cross-section of the nanocomposite MFI-alumina hollow fibre membrane after synthesis .....	89

---

Figure 6.1:	Schematic of an e-ZCMR based on MFI-alumina catalytic membrane reactor with the catalyst packed in the lumen of the membrane tube .....96
Figure 6.2:	Schematic of an e-ZCMR based on MFI-alumina catalytic membrane reactor with the catalyst packed between the outer side of membrane tube and the module shell.....96
Figure 6.3:	SEM micrograph of the membrane showing formation of a nanocomposite zeolite material embedded in the 0.2 $\mu\text{m}$ layer of the support .....99
Figure 6.4:	Separation performance of nanocomposite MFI-alumina membranes as a function of sweep gas flow rate .....100
Figure 6.5:	Separation performance of nanocomposite MFI-alumina membranes as a function of temperature. <u>Experimental conditions</u> : Feed flow rate, 10 mL(STP)/min; sweep gas flow rate for an e-ZCMR, 15 mL(STP)/min; feed composition (p/m/o), 0.51 / 0.34 / 0.59 kPa.....100
Figure 6.6:	m-Xylene isomerization over Pt-HZSM-5 in an e-ZCMR at 573 K with the catalyst packed in the tube lumen.The combined mode corresponds to the addition of the retentate and permeate streams. <u>Experimental conditions</u> : feed composition, 2.30 kPa m-Xylene in 10 mL(STP)/min $\text{N}_2$ ; sweep gas flow rate into e-ZCMR, 40 mL(STP)/min; reaction time, 30 min.....102
Figure 6.7:	m-Xylene isomerization over Pt-HZSM-5 in an e-ZCMR and a FBR as a function of temperature and catalyst packing (IN, catalyst packed in the tube lumen; OUT, catalyst packed in the shell) showing the p-Xylene yield. <u>Experimental conditions</u> : feed composition, 2.30 kPa m-Xylene in 10 mL(STP)/min $\text{N}_2$ ; sweep gas flow rate into e-ZCMR, 40 mL(STP)/min; reaction time, 30 min.....102
Figure 6.8:	m-Xylene isomerization over Pt-HZSM-5 in an e-ZCMR and a FBR as a function of temperature and catalyst packing (IN, catalyst packed in the tube lumen; OUT, catalyst packed in the shell) showing the p-Xylene selectivity. <u>Experimental conditions</u> : feed composition, 2.30 kPa m-Xylene in 10 mL(STP)/min $\text{N}_2$ ; sweep gas flow rate into e-ZCMR, 40 mL(STP)/min; reaction time, 30 min.....103
Figure 6.9:	m-Xylene isomerization over Pt-HZSM-5 in an e-ZCMR and a FBR as a function of temperature and catalyst packing (IN, catalyst packed in the tube lumen; OUT, catalyst packed in the shell) showing the m-Xylene conversion. <u>Experimental conditions</u> : feed composition, 2.30 kPa m-Xylene in 10 mL(STP)/min $\text{N}_2$ ; sweep gas flow rate into e-ZCMR, 40 mL(STP)/min; reaction time, 30 min.....103
Figure 6.10:	p-Xylene, m-Xylene and o-Xylene molar composition in permeate in ZCMR-IN and ZCMR-OUT configurations as a function of temperature. <u>Experimental conditions</u> : feed composition, 2.30 kPa m-Xylene in 10 mL(STP)/min $\text{N}_2$ ; sweep gas flow rate into e-ZCMR, 40 mL(STP)/min; reaction time, 30 min.....104
Figure 6.11:	m-Xylene isomerization over Pt-HZSM-5 in an e-ZCMR at 673 K as a function of the GHSV. <u>Experimental conditions</u> : sweep gas flow rate into e-ZCMR, 40 mL(STP)/min; reaction time, 30 min .....104

---

Figure 6.12:	m-Xylene isomerization over Pt-HZSM-5 in an e-ZCMR at 673 K and 2.84-kPa m-Xylene feed partial pressure as a function of the reaction time. <u>Experimental conditions</u> : sweep gas flow rate into e-ZCMR, 40 mL(STP)/min.....	105
Figure 6.13:	p-Xylene yield as a function of temperature <u>Experimental conditions</u> : feed composition, 2.30 kPa m-Xylene in 10 mL(STP)/min N <sub>2</sub> ; sweep gas flow rate into e-ZCMR, 5 mL(STP)/min; reaction time, 30 min .....	109
Figure 6.14:	Xylene distribution in the feed and the product streams (permeate and retentate) at combined mode in e-ZCMR. <u>Experimental conditions</u> : Feed composition: 0.37 mL/min-MX. Sweep gas flow rate: 5mL (STP)/min. Reaction temperature: 473 K.....	110
Figure 6.15:	p-Xylene selectivity and m-Xylene conversion as a function of temperature in e-ZCMR. <u>Experimental conditions</u> : feed composition, 2.30 kPa m-Xylene in 10 mL(STP)/min N <sub>2</sub> ; sweep gas flow rate into e-ZCMR, 5 mL(STP)/min; reaction time, 30 min.....	110
Figure 7.1:	Xylene isomerization pathways of 1,3-methyl shift pathway (adapted from [280]).....	116
Figure 7.2:	Xylene isomerization pathways of 1,2-methyl shift pathway(adapted from [280]).....	116
Figure 7.3:	Schematic of the e-ZCMR packed with catalyst .....	119
Figure 7.4:	Schematic showing the transport (flux) across a membrane in e-ZCMR...	119
Figure 7.5:	Molar flow rate profile of xylene in e-ZCMR at the tube side during isomerization at 673 K (Line=simulation; points=experimental).....	125
Figure 7.6:	Molar flow rate profile of xylene in e-ZCMR at the shell side during isomerization at 673 K. (Lines=simulation; points=experimental).....	125
Figure 7.7:	Effect of membrane effective thickness on p-Xylene yield in permeate-only mode .....	131
Figure 7.8:	Effect of membrane porosity on p-Xylene yield in permeate-only mode ...	133
Figure 7.9:	Effect of membrane tortuosity on p-Xylene yield in permeate-only mode..	133
Figure 7.10:	Effect of reactor size on p-Xylene yield in permeate-only mode.....	136
Figure 7.11:	Effect reactor size on p-Xylene yield in combined mode .....	137
Figure 7.12:	A <i>tornado</i> diagram showing sensitivity of p-Xylene yield in permeate-only mode to positive 20% (+20%) changes in design variables .....	138
Figure 7.13:	A <i>tornado</i> diagram showing sensitivity of p-Xylene yield in permeate-only mode to negative 20% (-20%) changes in design variables.....	138

---

## List of Tables

Table 1.1:	Physical properties of xylene isomers .....	3
Table 2.1:	Comparison between polymeric and ceramic membranes .....	15
Table 2.2:	Henry's constants (mmol.g <sup>-1</sup> .Pa <sup>-1</sup> ) for p-Xylene adsorption in silicalite.....	21
Table 2.3:	Transport diffusion coefficients of pure aromatics on silicalite-1 and ZSM-5 single crystals at low coverage (<1 molec/uc).....	23
Table 2.4:	Separation of xylene binary/ternary mixtures by PV at ambient pressure using zeolite membranes prepared on $\alpha$ -alumina support.....	29
Table 2.5:	Literature survey on xylene isomer separation by VP at low xylene partial pressures (<1 kPa) using MFI-type zeolite membranes.....	31
Table 2.6:	Literature survey on xylene isomerization using extractor -type zeolite CMR based on MFI membranes compared to fixed-bed reactors .....	36
Table 3.1:	Column characteristics .....	58
Table 3.2:	Operating condition for GC analysis .....	58
Table 4.1:	Constant values used for parameter estimation .....	68
Table 5.1:	Properties of the nanocomposite MFI-alumina hollow fibre and MFI-alumina tubular membranes used in this study.....	77
Table 5.2:	Previous studies on xylene separation from binary p/o-Xylene and ternary p/m/o-Xylene mixtures using MF-type zeolite membranes .....	86
Table 5.3:	Membrane quality of the four hollow-fibre membrane families identified in this study as evaluated from room-temperature n-butane/H <sub>2</sub> and separation and p/m and p/o separation factors at the maximum temperature (range 473-523 K).....	90
Table 6.1:	Near equilibrium product distribution in FBR obtained in this study .....	95
Table 6.2:	Equilibrium product distribution obtained from open literature .....	95
Table 6.3:	Productivities in FBR, e-ZCMR-IN and e-ZCMR-OUT configurations at permeate-only mode (top values) and combined mode (bottom values). <u>Experimental conditions</u> : temperature, 573 K; m-Xylene feed partial pressure, 2.84 kPa; feed flow rate, 10 mL(STP)/min; sweep gas flow rate, 40 mL(STP)/min.....	105
Table 6.4:	Comparison of the results obtained in this study with the literature .....	108
Table 6.5:	Representative performance of e-ZCMR at 473 K .....	111

---

Table 6.6:	Productivity in e-ZCMR in permeate only mode (top values) and combined mode (bottom values) in (nmol.s <sup>-1</sup> .g <sub>cat</sub> <sup>-1</sup> ) at 473 K Productivity (nmol.s <sup>-1</sup> .g <sub>cat</sub> <sup>-1</sup> ) at 473 K.....	112
Table 7.1:	Rate of reaction constants used for reaction modelling at 673 K [280].....	124
Table 7.2:	Constant parameters used for reactor modelling.....	124
Table 7.3:	Comparison of experimental results with simulation results.....	126
Table 7.4:	Design variables considered for sensitivity analysis.....	129
Table 7.5:	Model output at 673 K and at the reference values of the design variables.....	130
Table 7.6:	Effect of membrane effective thickness.....	130
Table 7.7:	Effect of membrane porosity on e-ZCMR performance.....	132
Table 7.8:	Effect of membrane tortuosity on e-ZCMR performance.....	132
Table 7.9:	Effect of reactor size on e-ZCMR performance .....	136

---

## Chapter 1: Motivation for the study and research objective

In this chapter, the motivation for this study and the research objectives are clearly defined. The benefits of the research effort to the scientific and industrial community are also highlighted.

### 1.1 Motivation

Energy efficiency and energy saving are becoming increasingly important components of government policies around the world in response to a range of challenges, which include perceptions of resource scarcity, high energy prices, security of energy supply and environmental protection. In 2006, the total world energy consumption was 495.6 quintillion Joule (J) and the industrial sector accounted for about one-half of the total world energy consumption [1]. Despite the current economic downturn, it is expected that the world energy consumption will increase up to 711.9 quintillion Joule (J) over the 2006 to 2030 period due to the expected growth of the world's real Gross Domestic Product (GDP) on the purchasing power parity averaged 3.5 percent annually [1]. Over the next 25 years, worldwide industrial energy consumption is expected to grow from 183.8 quintillion Joule (J) in 2006 to 257.9 quintillion Joule (J) in 2030 at an average annual rate of 1.4% [1]. In petrochemical industry, energy accounts for more than 60% of the industry's cost structure. In 2006, five industries accounted for about 68% of the total energy consumed in industrial sector while the chemical sector is the largest industrial consumer of energy with about 29% of the energy [1]. Therefore, more energy-efficient technologies in the chemical industry could contribute significantly to nationwide and worldwide energy savings and a reduction of CO<sub>2</sub> emissions.

One of the high energy-intensive industrial processes is the production of high purity p-Xylene via separation/isomerisation from mixed xylenes and in the last 30 years, there has been a great evolution in p-Xylene production technology, with many equipment improvements being instituted in the industry. Typically, these improvements bring economic as well as processing advantages to the producers. Such developments are vital, as the capital costs for process equipment to produce and separate p-Xylene from xylene isomers, especially into high-purity p-Xylene, still remain very high.

Mixed xylenes (from the Greek *xylon*=wood), first discovered in crude wood spirit in 1850 by Cahours, constitutes a family of C<sub>8</sub>-aromatics with molecular formula C<sub>8</sub>H<sub>10</sub> including three constitutional isomers: o-Xylene (OX), m-Xylene (MX) and p-Xylene (PX). These constitutional isomers are referred to as mixed xylenes. The xylene isomers differ from one another by the relative position of the two methyl groups in the benzene ring. The molecular structures of these isomers are depicted in Figure 1.1.

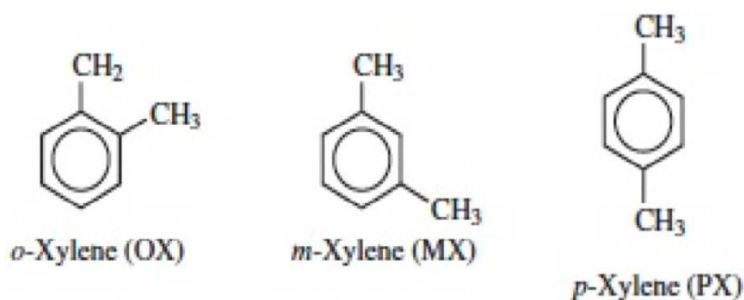


Figure 1.1: Molecular structures of the three xylene isomers.

Xylene isomers are important chemical intermediates. The world demand for xylene has been increasing steadily for more than a decade. For example, in 1999, the world demand for xylenes was about 22 Mt, *p*-Xylene holding about 80% of the market share [2]. The production value of mixed xylenes was estimated to approximately 5 billion US\$ in 1999, second only to benzene in aromatic production [3]. *P*-Xylene is almost exclusively used as raw material in the production of terephthalic acid (TPA) and dimethyl terephthalate (DMT), which are reacted with ethyleneglycol to form polyethylene terephthalate (PET), the raw material for polyester resin. Polyester resin is used to manufacture polyester fibres, films and fabricated items (e.g. beverage bottles). According to Tecnon OrbiChem [4], world *p*-Xylene demands are expected to rise at an average rate of 7% per year in the period 2008-2013, driven mainly by TPA and PET demand increase in China, other Asian countries and in the Middle East (Figure 1.2) - other countries not affected by this occurrence are excluded from Figure 1.2. Asian markets are foreseen as particularly tight, with demands exceeding the supply.

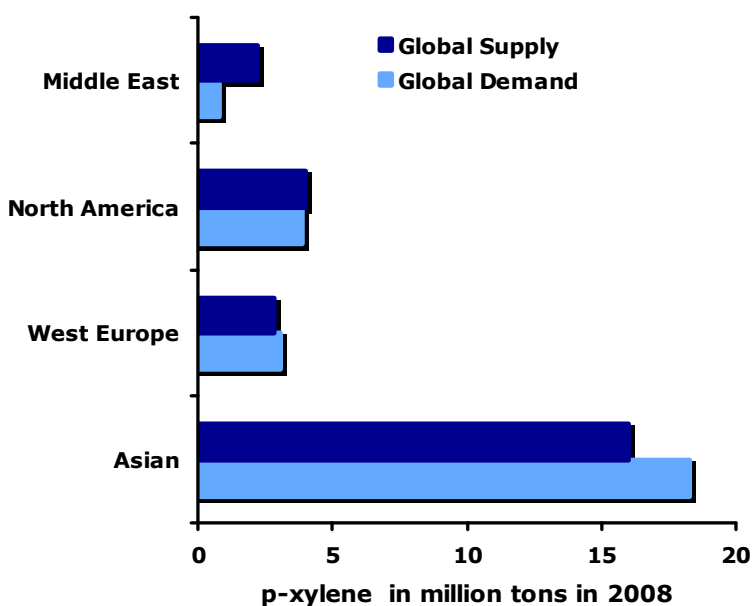


Figure 1.2: World supply /demand for xylenes (especially PX) [5].

---

The principal industrial sources of xylene isomer mixtures are high-severity catalytically reformed naphtha and pyrolysis distillates. The C<sub>8</sub> aromatic cut obtained from these sources contains a mixture of xylenes (50-60 wt.% m-Xylene and 20-25 wt.% o- and p-Xylenes) and ethylbenzene (EB) (15-30 wt.%) in the C<sub>8</sub> fractions obtained from naphtha reforming and steam cracking [6]. The surplus o-Xylene and m-Xylene can be converted into more valuable p-Xylene through catalytic isomerization with further purification by using convenient separation techniques.

The use of distillation is discouraged for p-Xylene separation and purification due to the close boiling points of xylene isomers (Table 1.1), translating into high energy demands. For example, petrochemical and chemical industries accounted for 13.7 quintillion Joule (J) in 1998 with about 35% of the energy consumption used in the manufacture and separation of organic chemicals (mainly for heating/cooling) [7]. Moreover, in 2004, the United States consumed nearly 105 quintillion Joule (J) on petrochemical and chemical industries' processes, corresponding to approximately one fourth of the world energy demand [8]. Therefore, it becomes imperative to move to more energy-efficient and environmentally-friendly processes for p-Xylene separation and purification involving the lowest number of heating/cooling steps.

Table 1.1: Physical properties of xylene isomers

Xylene isomers	M <sub>w</sub> (g.mol <sup>-1</sup> )	Normal Boiling point (K)	Normal Freezing point (K)	ΔH <sub>vap</sub> (kJ.mol <sup>-1</sup> )
PX	106.17	411.37	286.26	42.04
MX	106.17	412.12	225.13	42.04
OX	106.17	417.41	247.82	43.41

For the production of high purity p-Xylene via separation from xylene isomers and/or isomerization of less used isomers, membrane technology might be a promising option to achieve this goal. The technology behind membrane applications is potentially an energy-saving one, because the separation process takes place without phase transition. Besides, it is better for the environment, since the membrane approach requires the use of relatively simple and non-harmful materials and the recovery of minor but valuable components from a main stream using membranes can be done without substantial additional energy costs. Therefore, compared with conventional techniques (such as adsorption or crystallization), membranes can offer a simple, easy-to-operate, low-maintenance process

---

option [9-12]. In addition, extractor-type catalytic membrane reactors (e-CMRs) for simultaneous xylene isomerization and p-Xylene separation are receiving increasing attention by researchers. A special benefit of these intensified reactors is that the removal of one of the products provides a shift in equilibrium and also an integrated product purification thus decreasing the number of process units. Moreover, activity improvements are possible through selective removal of reaction rate inhibitors.

Against this background, therefore, this study contributes significantly in the research area through the further characterization and optimization of extractor-type catalytic membrane reactors, having nanocomposite MFI-type zeolite membranes as separation unit, for the production and purification of p-Xylene from xylene isomers.

Production of p-Xylene via isomerization is a chemical-equilibrium restricted reaction process. To obtain total conversion during xylene isomerization process in conventional catalytic reactors (fixed-bed reactors) is impossible. Therefore, existing industrial technology could only produce equilibrium or near equilibrium xylene mixtures. Recycling the xylene streams back into the process lines might ensure higher p-Xylene productivity, but at the expense of higher operational costs due to higher energy consumption. However, the use of e-CMRs could eliminate equilibrium restriction associated with production of p-Xylene in fixed-bed reactors with a drastic reduction in operational costs resulting from a reduction in energy consumption. The enormous potential of large-scale applications of xylene isomerization in oil and petrochemical industries promises major advances and development of such systems in a near future. However the development of such systems for high purity p-Xylene from xylene isomerization is retarded due partly to inadequate understanding of the system and to the absence of high-flux MFI-type zeolite membranes that have high selectivity for p-Xylene, especially at high loadings/partial pressures of xylene. To overcome this obstacle, in-depth understanding of the fundamental behaviour of the system and availability of high-flux membranes, having high selectivity for p-Xylene, is essential.

Regarding the use of nanocomposite MFI-ceramic membranes in e-CMRs for isomerization of m-Xylene to p-Xylene, the first preliminary study was reported by van Dyk *et al.* [13]. However, the study was limited to selectivity improvement in e-ZCMR, having a nanocomposite MFI-alumina membrane tube as separation unit, but with little detail on the influence of the operating variables on the performance of the system during the isomerization. Additionally, influence of operating variables (sweep gas, xylene loadings/partial pressures and sweep gas flow rate) on the separation performance of nanocomposite MFI-alumina membranes during xylene isomer separation has not been evaluated and reported. Furthermore, modelling and simulation study of an extractor-type catalytic membrane reactor, having a nanocomposite MFI-alumina membrane as separation

---

unit, has not been done and reported in open literature. Having in-depth understanding of all the aforementioned suggestions could be instrumental to optimization of the system and thus pave the way for speedy development of membrane-based reactive separation system for the production of high purity p-Xylene from mixed xylene.

As a result of this, the objective of this research was to characterize and optimize extractor-type zeolite catalytic membrane reactor (e-ZCMR), having nanocomposite MFI-alumina membranes as separation unit, for p-Xylene production and purification via separation and meta-xylene isomerization over Pt-HZSM-5 catalyst. Therefore, to realize the aforementioned objective, the study was divided into three parts:

- Characterization, performance evaluation and optimization of nanocomposite MFI-alumina membranes (tube and hollow fibres) during xylene isomers separation,
- Characterization, performance evaluation and optimization of e-ZCMR, having nanocomposite MFI-alumina membranes as separation unit, during m-Xylene isomerization over a Pt-HZSM-5 catalyst via experimental study and ;
- Modelling and sensitivity analysis of e-ZCMR, having nanocomposite MFI-alumina membranes as separation unit, during m-Xylene isomerization over a Pt-HZSM-5 catalyst to understand better the fundamental behaviour of e-ZCMR during xylene isomerization.

## 1.2 Dissertation overview

The dissertation is subsequently organized thus: Chapter 2 discusses the state of the art of the technology and reviews the literature on membrane technology and its application to the production and purification of p-Xylene from xylene isomers. The emphasis was on the application of MFI-type zeolite membranes for production and purification of p-Xylene from xylene isomers.

Chapter 3 outlines the preparation and characterization of MFI-type zeolite membranes with more emphasis on MFI-type zeolite membranes with nanocomposite architectures. The chapter also describes instrumentation and calibration as well as the experimental procedures used to produce the results described in subsequent chapters. Chapter 4 reports a study of the influence of operating variables on the separation performance of tubular nanocomposite MFI-ceramic membrane during the separation of ternary vapour mixture of xylene isomers. This chapter also showcases for the first time the relative goodness of MFI-Zeolite membrane with nanocomposite architecture over “film-like” type, particularly at higher loading of xylene. Chapter 5 reports for the first time in open literature, the performance of tubular nanocomposite MFI-ceramic at higher partial pressure of xylene isomers during ternary vapour mixture separation of xylene isomers.

Chapter 5 reports the evaluation of the separation performance of nanocomposite

---

MFI-ceramic hollow fibre during the separation of ternary vapour mixture of xylene. In this chapter, advantages of hollow fibre configuration over the tubular are demonstrated via experimental study. The study also reports, for the first time, the application of nanocomposite MFI-ceramic hollow fibre membranes for the separation of xylene vapour isomers

In Chapter 6, report of studies of the performance of extractor-type zeolite catalytic membrane reactors (e-ZCMR), which have nanocomposite MFI-ceramic membrane tube as a separation unit, during the production of p-Xylene from m-Xylene isomerization over Pt-HZSM-5 catalyst is presented. The chapter further provides information on the influence of operating variables on the performance of e-ZCMR during m-Xylene isomerization with a view to understanding the fundamental behaviour of e-ZCMR for m-Xylene isomerization and to optimizing the process. From this study, the best catalyst packing in e-ZCMR was obtained while the membrane displayed 100% p-Xylene selectivity with p-Xylene purity reaching 100% at the permeate side.

For in-depth understanding of the fundamental behaviour of e-ZCMR during m-Xylene isomerization over Pt-HZSM-5 catalyst, modelling and simulation study of the e-ZCMR for m-Xylene isomerization over Pt-HZSM-5 catalyst is presented in Chapter 7. Sensitivity analysis was also conducted on the model to understand the behaviour of the model to changes in certain parameters. The model output was compared with the experimental results for model validation and to understand the e-CMR during m-Xylene isomerization over Pt-HSZM-5 catalyst.

Chapter 8 summarizes the novel contributions of this research and suggests some useful recommendations for future research work.

### **1.3 Research benefits and novel contributions**

This study is an extension of a previous study which looked at the application of catalytic membrane reactors based on MFI-type zeolite membranes for the production of p-Xylene [13]. Preliminary work done in the previous study has provided solid evidence and platform for further extension of the study and optimization of the system. In this dissertation, new ideas were proposed. The ideas were developed and tested. The novel contributions from this research, as highlighted below, could be a platform upon which further researches in this area can be built:

- Separation performance of nanocomposite MFI-alumina membrane tube, at higher loadings/higher partial pressures of xylenes, during xylene isomers separation has been demonstrated and reported for the first time in open literature. Unlike their “film-like” counterparts, the membranes still maintain increased selectivity to

---

p-Xylene at higher xylene vapour pressures without showing a drastic decrease in selectivity.

- For the first time in open literature, the study has demonstrated and reported the performance evaluation of nanocomposite MFI-alumina hollow fibre membranes during xylene isomer separation. Furthermore, nanocomposite hollow fibre membrane prepared and evaluated displayed high selectivity to p-Xylene and showed about 30% increase in p-Xylene flux compared to a nanocomposite membrane tube prepared in a similar way as hollow fibre and operated at the same conditions.
- The study reports, in details, the influence of operating variables on the performance of an e-ZCMR, having a nanocomposite MFI-alumina membrane tube as separation unit, during m-Xylene isomerization over Pt-HZSM-5 catalyst. Furthermore, the study has shown a significant improvement on p-Xylene yield compared to the work of van Dyk *et al.*[13] and also for the first time in open literature, possibility of producing ultra-pure p-Xylene (~100%) in e-ZCMR during m-Xylene isomerization over Pt-HZSM-5 has been demonstrated and reported.
- The study reports, for the first time, modelling, simulation and sensitivity analysis of e-ZCMR, having a nanocomposite MFI-alumina membrane tube as separation unit, during m-Xylene isomerization to p-Xylene. The sensitivity analysis revealed that intrinsic property of the membrane (porosity, tortuosity), membrane effective thickness and reactor size play a significant role on the performance of e-ZCMR during p-Xylene production from the mixed xylenes.

In summary, the outcome of this research open up a research line to scale-up and optimize catalytic membrane reactors based on MFI-type zeolite membranes for p-Xylene production. The encouraging results, as documented in this dissertation, can provide a platform for developing scaled-up energy-efficient industrial process for producing p-Xylene through isomerization based on membrane technology. Furthermore, for quick and easy access to the novel contributions from this study, the novel contributions have been communicated to researchers working in the same research area and other related areas through articles published in international scientific journals (four published, two under review) and in conference proceedings (four conference proceedings). The published journal articles can be found in Appendix E.

---

## Chapter 2: Literature review and state of the art

In this chapter, relevant literature highlighting the current trends in the development and applications of MFI-type zeolite membranes to xylene isomer separation and isomerization are critically discussed.

### 2.1 Commercial technologies for production and purification of p-Xylene

The existing commercial technologies for separation and production of high purity p-Xylene from its isomers can be divided into three main groups: (1) fractional crystallization, (2) adsorption and (3) hybrid crystallization/adsorption [14]. Fractional crystallization and adsorption are currently commercially available, accounting, respectively, for about 40 and 60% of the p-Xylene world production. Although, the hybrid crystallization/adsorption process is yet to be commercialized, it has been successfully field-demonstrated and the first commercial unit is expected to be put in service in the near future. In addition to separation of p-Xylene from the C<sub>8</sub> cut, p-Xylene can be industrially produced via toluene disproportionation or o-Xylene and m-Xylene isomerization. This latter process is especially interesting for valorisation of leftover streams coming from adsorption and/or crystallization processes, highly enriched in o- and m-Xylenes. Currently, the industrial process for producing this involves either isomerization of the m-Xylenes or o-Xylene or disproportionation of toluene. Approximately, 40% of the currently used p-Xylene production processes, relying on either isomerization or toluene disproportionation, are based on ExxonMobil technology [15].

#### 2.1.1 Fractional crystallization

Low temperature fractional crystallization was the first and for many years the only commercial technique for separating p-Xylene from mixed xylenes. A number of crystallization processes have been commercialized over the years (e.g., Chevron, Krupp, Amoco, ARCO [Lyondell] and Phillips). A typical commercial crystallization process is shown in Figure 2.1.

This technology relies on the freezing point of p-Xylene which is much higher than that of the other xylene isomers (see Table 1.1). Thus, upon cooling, a pure solid phase of p-Xylene crystallizes first. Upon further cooling, a temperature is eventually reached where solid crystals of other isomers also form (eutectic point). P-Xylene usually begins crystallization at about 269 K and the p-Xylene/m-Xylene eutectic point is reached at about 205 K. In commercial practice, p-Xylene crystallization is carried out at a temperature just above the eutectic point. At that condition, p-Xylene is still soluble in the remaining C<sub>8</sub>

---

aromatics mother liquor solution. This limits the efficiency of crystallization processes to a per-pass p-Xylene recovery of about 60–65%.

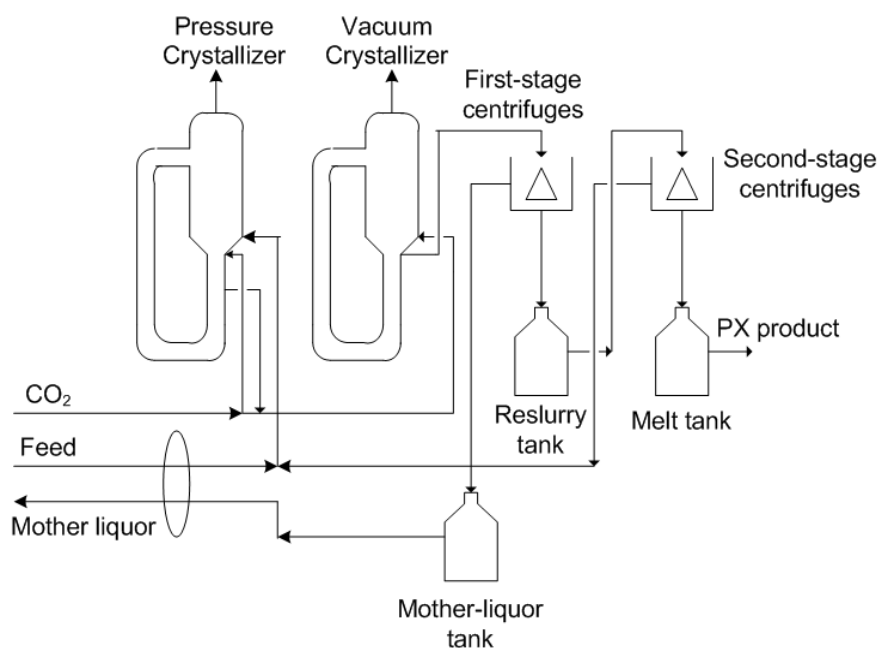


Figure 2.1: Chevron p-Xylene crystallization process [16].

The solid p-Xylene crystals are typically separated from the mother liquor by filtration or centrifugation. With regards to this step, achieving good separation depends on the p-Xylene crystal size distribution, thus, improving larger crystals. The p-Xylene crystal size is affected by the degree of supersaturation (and therefore by nucleation mechanism) upon crystallization, which is affected in turn by a number of parameters including temperature, agitation and the presence of crystal nuclei. To obtain good separation, p-Xylene is typically crystallized in one or two consecutive steps and further separated by centrifugation.

Commercial crystallisers use either direct contact or indirect refrigeration to promote crystallization. The latter has the disadvantage that the walls of the cooled surface tend to foul, which reduces heat transfer. The first crystallization step is usually carried out at the lowest temperature, the p-Xylene cake from this step reaching a purity of about 80–90%. The impurities in the p-Xylene cake arise from the mother liquor, wetting the crystal surface or being occluded in the cake. The efficiency of the solid–liquid separation depends on the temperature and the loading of the centrifuges. As the temperature falls, the viscosity and

---

density of the mother liquor rise sharply, making it more difficult to achieve effective separation.

In the second crystallization step, p-Xylene crystals are usually re-slurried from the former cake with a higher purity p-Xylene stream coming from the latter purification step. This second centrifugation step is enough in most cases to reach a p-Xylene purity >99%.

### **2.1.2 Adsorption process**

Adsorption constitutes the second and the most recent method for separating and producing high-purity p-Xylene. In this process, adsorbents such as molecular sieves are used to produce high-purity p-Xylene by preferential adsorption of p-Xylene from a mixed xylene stream. Separation is accomplished by exploiting the differences in affinity of the adsorbent for p-Xylene relative to the other C<sub>8</sub> isomers. The adsorbed p-Xylene is subsequently desorbed by displacement with a desorbent liquid stream. Typical p-Xylene recovery per-pass is >95% in a single step. Recycle rates to separation and isomerization units are much smaller in adsorption units than in crystallization systems.

At present, three processes based on adsorption are commercially available for p-Xylene separation and purification: UOP's Parex, IFP's Eluxyl and Toray's Aromax (this latter should not be confused with the Chevron's Aromax process for reforming of naphtha into aromatics). A comprehensive description of these processes is given by Minceva and Rodriguez [17]. In all of them, the feed and desorbent inlet and the product outlet ports are moved around the bed, simulating a moving bed (SMB). For example, Figure 2.2 shows the flowsheet diagram of the UOP's Parex adsorption process. Several adsorbent/desorbent combinations have been proposed in the literature to promote p-Xylene recovery from different mixtures. Typically, Ba- and K-exchanged zeolite molecular sieves are used as adsorbent and toluene (or tetraline) as desorbent [18]. Other examples of processes relying on selective adsorption for xylene separation and purification from the C<sub>8</sub> cut have been reported in the patent literature [19,20].

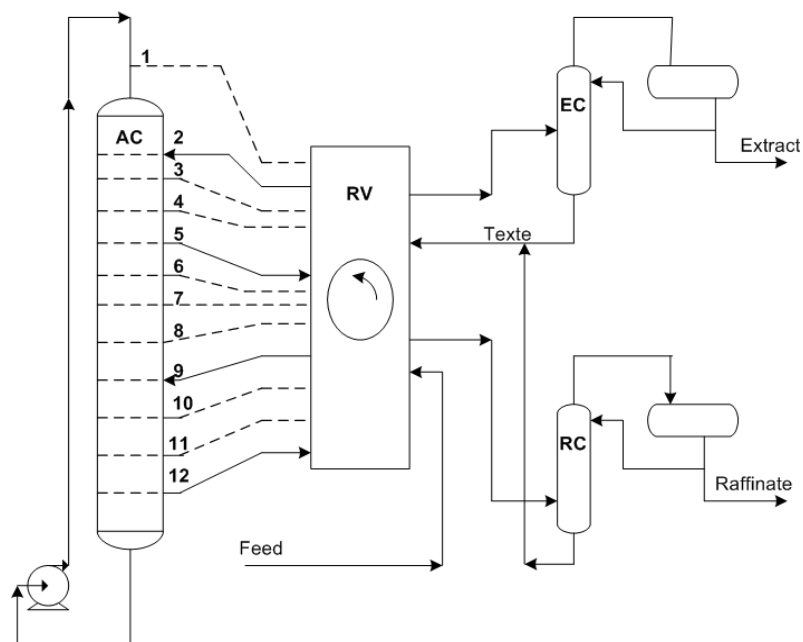


Figure 2.2: UOP Parex simulated moving bed for adsorptive separation. Nomenclature: AC, adsorbent chamber; RV, rotary valve; EC, extract column; RC, raffinate column. Lines: 2-desorbent; 5-extract; 9-feed; 12-raffinate. All other ports are closed at this time [21].

### 2.1.3 Hybrid crystallization / adsorption process

In 1994, the Institut Français du Pétrole (IFP) and Chevron announced the development of the Eluxyl hybrid process that reportedly combines the best features of adsorption and crystallization. In this process, a high concentrated p-Xylene stream (90-95%) is first produced from an adsorption unit and further purified in a small single-stage crystallizer with the filtrate recycled back to the adsorption unit [22]. Ultra-pure (>99.9%) p-Xylene can be easily and economically produced with this scheme for both retrofits of existing crystallization units as well as grass-roots units. This process has been successfully field-demonstrated but is yet to be commercialized.

### 2.1.4 P-Xylene from xylene isomerization

In 1975, ExxonMobil introduced into the market its first generation of xylene isomerization processes called *Mobil Vapour Phase Isomerization* (MVPI<sup>SM</sup>), relying on the use of a high-activity xylene isomerization catalyst (acid zeolite). The process was further improved in 1978 by introducing the Mobil Low Pressure Isomerization process (MLPI<sup>SM</sup>) with lower xylene losses and longer catalyst lifetime. In 1981, aromatics production was revolutionized by the introduction of the Mobil High Temperature Isomerization process (MHTI<sup>SM</sup>), capable of operating at higher ethylbenzene (EB) conversions and with lower

xylene losses than in MLPI<sup>SM</sup>, providing increased p-Xylene yields. To further reduce xylene losses, the Mobil High Activity Isomerization Process (MHAI<sup>SM</sup>) and the Advanced Mobil High Activity Isomerization Process (AMHAI<sup>SM</sup>) were introduced to the market in 1990 and 1999, respectively. In 2002, ExxonMobil introduced the most recent technology to date called XyMax (see flowsheet in Figure 2.3). This process includes the conversion of EB to benzene and ethylene, cracking of non-aromatics and isomerization of the p-Xylene-depleted feedstock to an equilibrium xylene mixture.

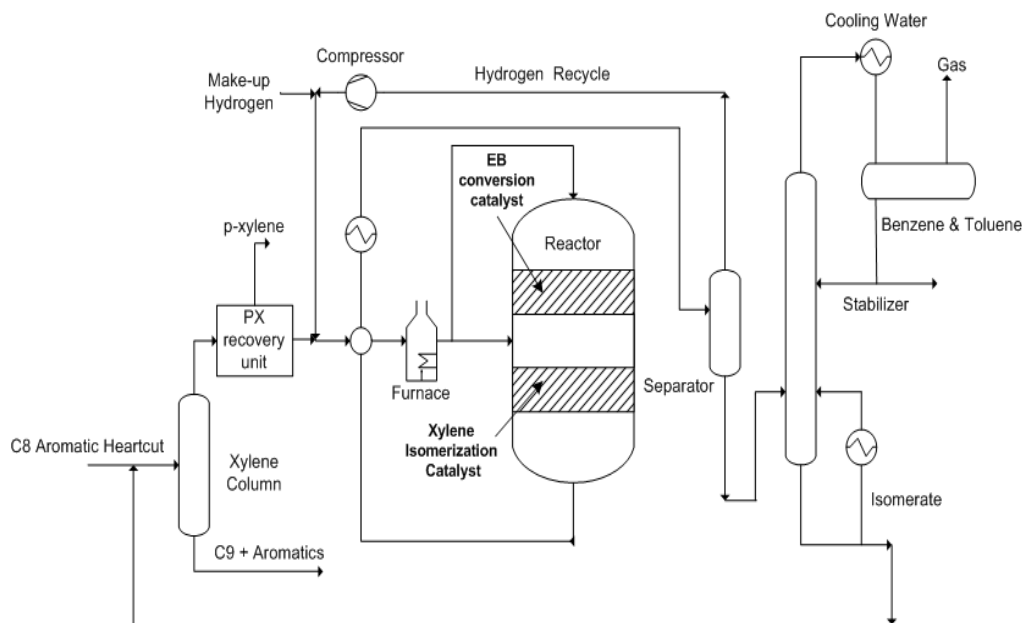


Figure 2.3: Flowsheet of the ExxonMobil XyMax isomerization process [22].

## 2.2 Catalysts for xylene isomerization

The choice of a catalysts for a particular reaction depends largely on some factors such as activity, selectivity, stability and even cost. A high activity is reflected either in the high productivity from relatively small reactors and catalysts volume or mild operating conditions, particularly temperatures, which enhance selectivity and stability if the thermodynamics is more favourable [23]. Moreover, high selectivity produces high yields of a desired product while suppressing undesirable competitive and consecutive reactions. Therefore, to make a catalyst highly selective for a target product, its pore volume and pore size distribution should be improved toward reducing limitations by internal diffusion. In addition, a catalyst with good stability changes only slowly over the course of time under conditions of use and regeneration. At the same time the catalysts must withstand comparison with competitive catalysts or processes with equivalent functions from the point of view of cost [23].

---

The most currently used catalysts in xylene isomerization plants are based to date on acid zeolites HMOR [24-26] and HZSM-5 [27, 28]. Other catalysts that have been studied for this reaction include zirconia modified with tungsten oxide [29], amorphous silica [30], and zeolites HY [31-34], beta [31], ITQ-13 [34], UZM-5 and UZM-6 [35], and HFER [36]. The reaction takes place at operating temperatures in the range 543-653 K. Acid-catalyzed xylene isomerization can occur either through an intramolecular mechanism involving benzenium-ion intermediates or through an intermolecular mechanism involving successive xylene disproportionation reactions and fast transalkylation between trimethylbenzene (TMB) and xylene molecules. The former mechanism is favoured when steric constraints in the vicinity of the acid sites inhibit the formation of bulky diphenylmethane intermediates of transalkylation (e.g., zeolite beta) or in the case of catalysts possessing very strong acid sites (e.g., zeolite HY). As a general rule, irrespective of their Si/Al ratios, larger pore size opening zeolites provide lower selectivities for p-Xylene compared to ZSM-5 zeolites, promoting TMB production by disproportionation. However, Henriques *et al.* [24] reported that H-MOR with Si/Al ratio of 75 provides higher resistance to deactivation (coking) due to its large pore size. Suppression of disproportionation reaction and promotion of secondary isomerization reaction for p-Xylene is enhanced by inactivation of non-selective acid sites on the external surface, leading to an increase in internal acid sites [37]. Dealuminated Y zeolites (DAY) with high Na content catalyze primarily the isomerization of m-Xylene and improve the conversion, but as the cation is exchanged by  $\text{NH}_4^+$ , disproportionation becomes more pronounced [38,39], promoting formation of toluene and TMB. Laforge *et al.* [40] have used zeolite MCM-22 (Si/Al=10) dealuminated with ammonium hexafluorosilicate for m-Xylene isomerization. Their results reflect that cups + sinus form of the catalyst give higher p-Xylene yields due to pore mouth poisoning of the sinusoidal active sites or poisoning of the hemicages by adsorbed 2,4-DMQ which hinders the activity of the neighbouring inner sites and that isomerization of m-Xylene occurs preferentially in sinusoidal channels.

Para-selectivity in xylene isomerization by zeolites has been improved by doping the zeolites with metals such as Pt, Ga and Zr through surface modification [37, 41]. At these conditions, in the presence of metals, m-Xylene isomerization proceeds via an intermolecular 1,2-methyl group shift model [37]. Hsu *et al.* [42] have reported a gradual activity in the order Pt/MOR << Pt/USY < Pt/ZSM-5 < Pd/ZSM-5 for m-Xylene and EB isomerization, increasing with temperature. The higher activity of Pt/ZSM-5 compared to USY is attributed to the higher acidity of the former, while the modest activity of Pt/modernite is attributed to a fast catalytic deactivation by coking. P-Xylene selectivity of Pt/ZSM-5 and Pd/ZSM-5 can reach values >90% at 573 K, but decreasing with temperature. Incorporation of oxides, P [43-45], Mg [46, 47] or B [47, 48] in the zeolite framework allows tuning of the diffusivity of xylenes into the zeolite pores [27].

---

### 2.3 Membrane-based technology for the production and purification of PX

The crystallization and adsorption techniques for p-Xylene separation and purification, discussed in section 2.1 of this chapter, are highly energy intensive (although to a lesser extent than in fractional distillation) and make use of batch processes. In an attempt to design less energy-intensive and more environmentally-friendly processes for p-Xylene production and purification, membrane-based technology has been proposed recently, as a promising alternative.

A membrane is defined essentially as a barrier, which separates two phases and restricts transport of various chemicals in a selective manner. A membrane can be homogenous or heterogeneous, symmetric or asymmetric in structure, solid or liquid; it can either carry a positive or negative charge or it can be neutral or bipolar. Transport through a membrane can be affected by convection or by diffusion of individual molecules, induced by an electric field or concentration, pressure or temperature gradient. The membrane thickness may vary from as small as 10 microns to few hundred micrometers.

In gas-separation membranes, classification has included porous and dense membranes [49-52]. Materials such as ceramic and metals have been used as supports. In some cases, the driving force in a gas-separation membrane is the pressure difference between the feed/retentate and the permeate; the heating/cooling costs can be dramatically reduced compared to crystallization or adsorption techniques. Furthermore, due to their modular nature and compact size, membranes can be integrated easily in already existing plants, offering the possibility of continuous operation without requiring sorbent regeneration.

Despite these general advantages compared to crystallization and adsorption techniques for p-Xylene separation and purification, the technico-economical feasibility of a membrane-based process will depend on the development of membrane materials with good affinity for p-Xylene for selective separation from its isomers. A first possibility deals with the use of polymers. Although specific xylene isomer separation has been studied with polyurethane [53], polyvinyl alcohol (PVA) [54] and polyamides [55-57], so far, none of these materials has provided substantial p/o and p/m xylene selectivities at reasonable permeabilities. Furthermore, whereas some researchers have proposed the introduction of side groups displaying strong interaction with xylenes to the polymer matrix [58-63], no remarkable improvement has been reported. This lack of selectivity, in addition to the inherent limitations of polymers in terms of thermal, chemical and mechanical stability, has triggered off the development of porous ceramic membranes for p-Xylene separation and purification. A general comparison of the characteristics of polymeric and ceramic membranes is provided in Table 2.1.

---

In particular, zeolites have been the major materials employed in the preparation of ceramic membranes for the separation of aromatics and several reviews on their synthesis and applications have been published [64-66], including a small overview by Fong *et al.* [67] focusing on catalytic membrane reactors (CMRs) applications for xylene isomerization. Although, the use of zeolite membranes for gas separation is still in an early technological stage (only one application of solvent dehydration by pervaporation has been commercialized to date [68]), they are expected to encounter applications at large scale and compete with other existing technologies in the coming years. The future gas separation applications will rely on their selectivity, permeability and stability characteristics. Moreover, the development of such materials will depend on the availability of high quality, defect-free membranes, preferentially synthesized through simple protocols leading to cost-effective processes [69].

Table 2.1: Comparison between polymeric and ceramic membranes

Ceramic membranes	Polymeric membranes
Do not swell	Do swell
Possibility of uniform, molecular sized pores allowing for molecular sieving	Do not have uniform molecular sized pores
Chemically resistant to solvents and low pH	Not chemically stable. Denatured at low pH
Thermally stable	Not thermally stable, denatured at high temperature
High cost of production	Lower cost of production
More brittle	Less brittle

Among the different available membrane technologies, xylene isomer separation using MFI membranes has been carried out either by pervaporation (PV) or vapour permeation (VP). These techniques rely both on the higher affinity of one or more species in a mixture to the membrane material and only differ from the phase of the feed (liquid in PV and vapour in VP, see Figure 2.4) and the permeate pressure (use of primary vacuum in PV). In addition, in VP, a sweep gas is applied to the permeate's side to reduce the surface coverage and thus it enhances the cross membrane flux of the permeating molecules due to an increase in the driving force. A detailed description of the fundamentals and applications of both processes can be found in some reference books and reviews [66, 70-73].

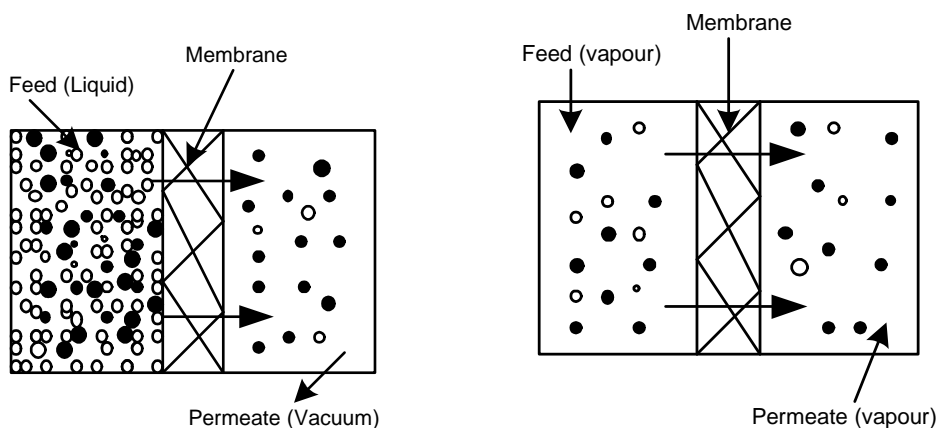


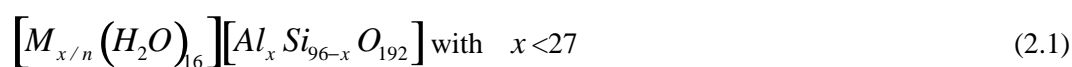
Figure 2.4: Schematic representation of pervaporation (left handside) and vapour permeation (right handside) across a membrane.

### 2.3.1 MFI-type zeolite membranes for xylene isomer separation

Zeolites are tridimensional crystalline aluminosilicates constituted by Si and Al tetrahedra linked through bridging oxygen atoms giving rise to the so-called *secondary building units* (SBUs), constituted by rings and prisms of various sizes. These units combine to generate frameworks with a regular distribution of molecular-sized pores and cavities. The general formula of zeolites is  $M_{x/n}[(AlO_2)_x(SiO_2)_y] \cdot zH_2O$ , with M defining the compensating cation (usually from groups I or II) with valence  $n$ . The Si/Al ratio of the zeolite structure and amount of cations control the surface properties of zeolites (e.g., hydrophobicity and acidity), and determine their adsorbent, catalytic and ion-exchange properties.

Among the different natural and artificial zeolite frameworks, the MFI structure consists of two main types namely ZSM-5 (Zeolite Socony Mobil-Five), discovered by Mobil in 1972 [74,75], with a natural analog (mutinaite) [76], and silicalite-1, developed by Union Carbide a few years later [77,78]. Both structures differ in their Si/Al ratio, showing a value in the range 10-10000 for ZSM-5 and >10000 for silicalite-1. The higher Si content of silicalite-1 provides a higher thermal stability and higher hydrophobic character than in the case of zeolite ZSM-5.

The elementary mesh in MFI zeolites contains 96  $TO_4$  tetrahedric units ( $T = Si$  or  $Al$ ), as can be deduced from the chemical formula [79]:



MFI-type zeolites possess a channel network based on near-circular straight ( $0.54 \times 0.56 \text{ nm}^2$ ) and elliptical sinusoidal ( $0.51 \times 0.55 \text{ nm}^2$ ) channels both defined by 10-membered rings (medium-pore zeolite) [80,81]. Straight and elliptical channels run parallel, respectively, to crystallographic directions  $a(1\ 0\ 0)$  and  $b(0\ 1\ 0)$ , generating perpendicular intersections with diameter of 0.89 nm. The key morphological features of MFI zeolite are schematically depicted in Figure 2.5. The pores provide three potential adsorption sites: (1) at the intersections, (2) along the cross (zig-zag) channels and (3) in the straight channels between the intersections (see Figure 2.6). Given the available pore sizes of its channel network, MFI is expected to promote diffusion of p-Xylene (kinetic diameter=5.8 Å) over bulkier o- and m-Xylene isomers (kinetic diameter=6.8 Å). This offers unique shape selectivity properties in adsorption and catalysis compared to larger pore zeolites.

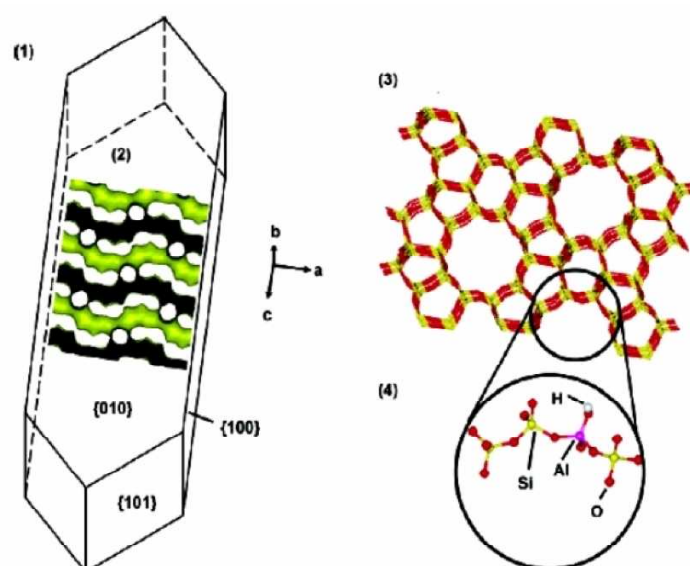


Figure 2.5: Key features of MFI zeolite: (1) crystal morphology, (2) straight and sinusoidal channels with intersections, (3) crystal framework and (4) detailed atomic structure (with permission from [82]).

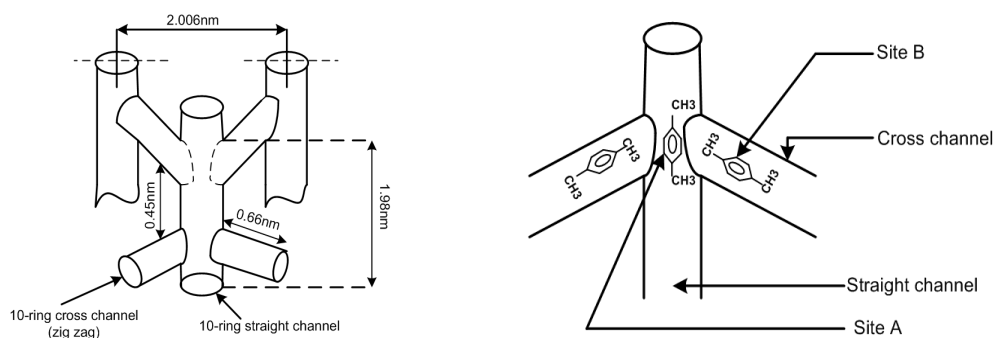


Figure 2.6: P-Xylene adsorption in the MFI zeolite framework.

---

All MFI-type zeolites show a polymorphic, monoclinic to orthorhombic, phase transition. Phase transitions are induced by temperature changes and the presence of adsorbed molecules (for instance aromatics or branched alkanes) within the framework. The transition temperature and mechanism are closely linked to the composition (Al content and other substituted elements) and defect density of the tetrahedral framework, besides the size and nature of the molecules adsorbed in the zeolite cavities. For instance, at room temperature, the as-synthesized ZSM-5 is orthorhombic (space group  $Pnma$ ), although H-containing ZSM-5 has monoclinic structure (space group  $P2_1/n.1.1$ ) [83]. Silicalite-1 is monoclinic at temperatures below 225-275 K (space group  $Pn2_1a$ ) and reversibly transforms into orthorhombic (space group  $Pnma$ ) at higher temperatures [82, 84]. Moreover, upon heating, it has been shown through molecular dynamics (MD) that the thermal expansion coefficient of silicalite-1 becomes negative above 450 K, indicating the existence of a higher temperature orthorhombic phase [82].

### 2.3.1.1 Adsorption of xylenes in MFI-type zeolites

As stated in section 2.3.1, the framework symmetry of MFI zeolites is strongly related to the nature and amount of guest molecules adsorbed in the channel network. It has been reported in the literature that at higher temperatures (>323-353 K), aromatic species (e.g., benzene, toluene, xylenes) adsorb in MFI zeolites following a *Langmuirian* adsorption pattern with a maximum adsorption capacity of 4 molecules/unit cell (silicalite-1 and HZSM-5). This adsorption pattern is similar to what is observed for most zeolites irrespective of their nature (i.e. cage-like or channel-like) and pore size [85-93]. At lower temperatures, however, the isotherms of benzene, toluene and p-Xylene on MFI display increased capacities with a step or inflection point at about 4 molecules/unit cell [94-96] (see Figure 2.7), giving an overall characteristic step-isotherm sometimes referred to as Type VI according to the classification of the IUPAC [85]. These abnormal adsorption properties of MFI at lower temperatures can be ascribed to a subtle interplay of increased sorbate-sorbate interactions and to the role of highly energetically heterogeneous surfaces.

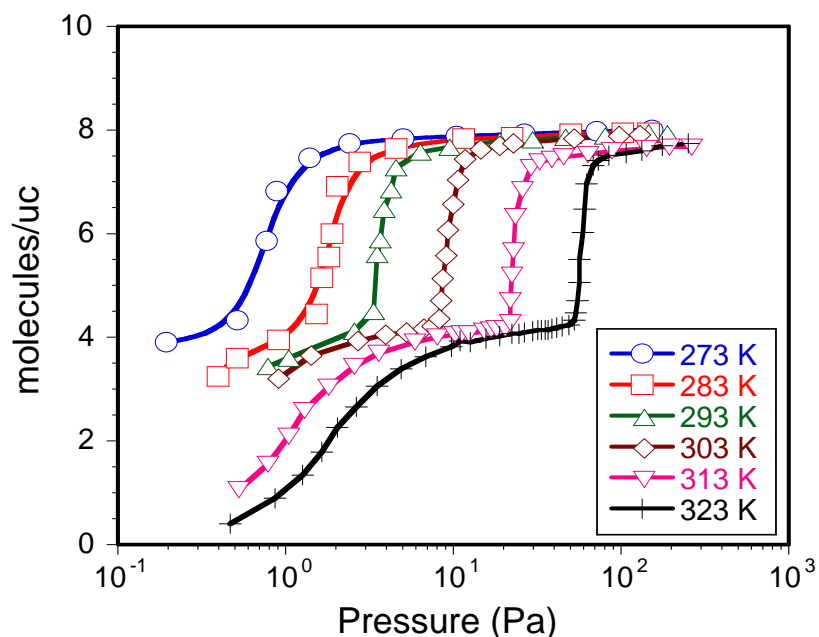


Figure 2.7: Characteristic inflection in p-Xylene adsorption isotherms on silicalite in the temperature range 273-323 K. Adapted from [84].

A number of XRD/neutron diffraction and calorimetric studies has revealed that orthorhombic MFI undergoes a phase transition from the so-called ORTHO phase (orthorhombic  $Pnma$ ,  $2 < \text{molecules/uc} < 4$ ) to the PARA phase at higher p-Xylene loadings (orthorhombic  $P2_12_12_1$ ,  $4 < \text{molecules/uc} < 8$ ) [97-106]. Besides the fact that the cross channels in PARA MFI are rather skewed, there is little structural difference between the ORTHO and PARA phases. In both cases, the differential heat and entropy of p-Xylene adsorption show similar values, about  $-80 \text{ kJ.mol}^{-1}$  and  $-32 \text{ J.mol}^{-1}.\text{K}^{-1}$ , respectively, for HZSM-5 [107,108]. Moreover, the adsorption strength and transition temperature of the zeolite framework induced by p-Xylene adsorption can be strongly affected by the Al content and nature of the exchangeable cation present in the ZSM-5 framework [107].

A series of FTIR, Raman and NMR experimental studies [109-111], supported by theoretical calculations (Molecular Dynamics and Monte Carlo) [112-117] supports the effect of size entropy effects (i.e. the ability of a molecule to fit in a confined space) on the observed inflection of the p-Xylene adsorption isotherm on MFI, the sorbate-sorbate interaction driving the phase change in the zeolite structure. In the case of silicalite-1 and HZSM-5, below 4 molecules/unit cell, the sorbate p-Xylene molecules are mainly located in the channel intersections, while above 4 molecules/unit cell, sorbate molecules tend to occupy sites along the cross channels. The sites along the straight channels between intersections are left largely unoccupied owing to steric hindrance by the sorbate molecules at the intersections.

The preference of certain aromatic molecules to adsorb in different MFI sites giving rise to an inflection in their corresponding adsorption isotherm can be modelled using a

---

dual-site Langmuir adsorption isotherm [118]:

$$q = q_{M,A} \frac{K_A P}{1 + K_A P} + q_{M,B} \frac{K_B P}{1 + K_B P} \quad (2.2)$$

where subscripts  $A$  and  $B$  indicate independent adsorption sites, corresponding to the channels and intersections in the MFI framework (see Figure 2.6 for details). This isotherm has also been used to model the adsorption of long-chain and branch alkanes in MFI [119-121].

Discrimination of the active sites can be done by performing adsorption experiments at low loadings. In this situation, Eq. 2.2 can be linearized to a Henry's adsorption isotherm with a characteristic slope or Henry's coefficient:

$$H_A = \lim_{P \rightarrow 0} \frac{q}{P} = \lim_{P \rightarrow 0} \frac{dq}{dP} \rightarrow q_{M,A} K_A \quad (2.3)$$

where, according to the nomenclature of Eq. 2.2, the subscript  $A$  refers to channels. Table 2.2 collects some values of Henry's constants reported in the literature for p-Xylene adsorption at several temperatures.

In the case of co-adsorption of aromatic mixtures including p-Xylene or mixtures of xylene isomers, p-Xylene adsorbs preferentially at higher enough p-Xylene partial pressures by locating specifically in the MFI channel intersections [122-126]. The adsorption behaviour of aromatic mixtures is highly competitive and non ideal due to structural (and energetic) heterogeneity of MFI zeolite channels ascribed to the tight fit of the aromatic molecules in the MFI channels. This particular behaviour can be modelled using the classical Ideal Adsorbed Solution Theory (IAST) developed by Myers and Prausnitz [127]. Unlike the extended Langmuir isotherm, the approach provides a thermodynamically consistent framework for modelling mixture adsorption in zeolites without the need of detailed physical models for the sorbate. This model has been applied with success by Chempath *et al.* [116] and Li and Talu [122] for modelling, respectively, p/m-Xylene/toluene and p-Xylene/benzene binary adsorption in silicalite-1 at 300 K.

Table 2.2: Henry's constants (mmol.g<sup>-1</sup>.Pa<sup>-1</sup>) for p-Xylene adsorption in silicalite

T (K)	Talu <i>et al.</i> [95] <sup>*</sup>	Richard and Rees [108] <sup>*</sup>	Li and Talu [128] <sup>*</sup>	Grahn <i>et al.</i> [129] <sup>†</sup>
323	0.022	1.06	0.53	0.18
343	0.0054	0.18	0.11	0.029
368	0.0010	0.022	0.016	5.7x10 <sup>-3</sup>
393	2.2x10 <sup>-4</sup>	0.0037	0.0032	9.4x10 <sup>-4</sup>
423	2.6x10 <sup>-5</sup>	3.0x10 <sup>-4</sup>	3.2x10 <sup>-4</sup>	5.5x10 <sup>-5</sup>

<sup>\*</sup> Extrapolated from the complete isotherm data. <sup>†</sup> Ultrathin silicalite layer

Following the guidelines of solution thermodynamics, the IAST approach relies on an analogy with the Raoult's Law for vapor-liquid equilibria through the expression:

$$P y_i = P_i^o(T, \Phi) x_i \quad (2.4)$$

where  $y_i$  and  $x_i$  are the molar fractions of the  $i^{th}$  species in the gas and 'fluid' phases, respectively,  $T$  is the absolute temperature,  $\Phi$  is the surface potential, and  $P$  is the total pressure of the gas phase. This equation allows the representation of a  $y$ - $x$  equilibrium diagram using the following definition of surface potential (formally equivalent to the classical spreading pressure):

$$\Phi = \int_0^{P_i} \frac{q}{P_i} dP_i \text{ with } \Phi_i = \Phi \text{ for } \forall i \quad (2.5)$$

It is noteworthy that, taking into account the ideal character of aromatic mixtures, no further correction of Eq. 2.4 including 'surface' activity coefficients is necessary. Moreover, compared to the Raoult's Law, there is a subtle difference in the meaning of  $P_i^o$ . In the case of vapour-liquid equilibria,  $P_i^o(T)$  is the saturation vapour pressure of species  $i$  at the temperature of the solution, while  $P_i^o(T, \Phi)$  is the adsorptive saturation pressure (actual saturation vapour pressure) at the solution temperature and surface potential  $\Phi$ . Beyond the  $y$ - $x$  equilibrium diagram, a loading diagram is also necessary, which connects the total adsorbed amount,  $q_i$ , with the gas phase mole fraction of species  $i$ . The following expressions are proposed:

---


$$\frac{1}{q^T} = \sum_{i=1}^N \frac{x_i}{q_i^o(\Phi)} ; \quad q_i = x_i q^T \quad (2.6)$$

where  $q^T$  is the total loading,  $q_i^o(\Phi)$  is the loading of pure species  $i$  at surface potential  $\Phi$ , and  $q_i$  is the loading of species  $i$  for the given mixture.

### 2.3.1.2 Diffusion of xylenes in MFI-type zeolites

Two types of diffusivities can be measured in zeolites [130]: Fick or transport diffusivities,  $D_T$ , and self-diffusivities,  $D^*$ . The fundamental difference between both relies on the presence of finite gradients. Transport diffusivities are measured under *non-equilibrium* conditions in which finite gradients of loading exist ( $\nabla q_T \neq 0$ ), while self-diffusivities are measured under *equilibrium* conditions ( $\nabla q_T = 0$ ) where finite gradients of loading do not exist and involve mass transfer of identical but labelled molecules.

The channels (straight and sinusoidal) in MFI zeolites are sufficiently wide to allow diffusion of single aromatic molecules with a kinetic diameter approaching the pore size. Transport diffusivities of aromatics in zeolites can be measured using conventional macroscopic techniques (e.g., zero-length column, gravimetry, FTIR) [131-137], while self-diffusivities have been measured using microscopic techniques (e.g., pulsed-field gradient NMR, quasi-elastic neutron scattering, neutron spin echo, frequency response) [138-142]. Figure 2.8 shows an example of uptake curves measured by gravimetry for the diffusion of several aromatics in HZSM-5 at low vapour pressures. In contrast to this diffusion pattern, at sufficiently high xylene loadings distortion of the MFI framework leads to faster diffusion of bulkier xylene isomers (i.e. o- and m-Xylene) [143]. Table 2.3 summarizes some of the values reported in the literature for transport diffusivities of aromatics in MFI zeolites at low loadings (<1 molec/unit cell). The diffusivity values listed in Table 2.3 should be considered as only indicative for comparison purposes between different sorbates, since the measured values depend strongly on the analytical technique and on the pre-treatment of the zeolite samples prior to the adsorption measurements.

Table 2.3: Transport diffusion coefficients of pure aromatics on silicalite-1 and ZSM-5 single crystals at low coverage (<1 molec/uc)

Aromatic species	Zeolite (Si/Al)	D at 400 K (m <sup>2</sup> /s)	E <sub>a</sub> (kJ/mol)	Technique	Refs.
Benzene	Silicalite-1	5.0x10 <sup>-13</sup>	7.4	ZLC	[131]
Benzene	Silicalite-1	5.0x10 <sup>-13</sup>	4.3	TGA	[132]
Benzene	HZSM-5 (135)	~10 <sup>-13</sup>	6.2	TGA	[132]
Benzene	Silicalite-1	6.0x10 <sup>-14</sup>	6.7	TGA	[133]
Benzene	Silicalite-1	2.0x10 <sup>-13</sup>	6.5	ZLC	[134]
Benzene	HZSM-5 (335)	1.5x10 <sup>-15</sup>	5.5	FTIR	[135]
Benzene	Silicalite-1	2.5x10 <sup>-14</sup>	5.8	CS	[151]
Benzene	Silicalite-1	2.7x10 <sup>-15</sup>	19.4	TGA	[153] <sup>*</sup>
Benzene	Silicalite-1	9.0x10 <sup>-15</sup>	16.0	CVM	[154]
Benzene	Silicalite-1	8.0x10 <sup>-15</sup>	-	CVM	[155]
Benzene	HZSM-5 (40)	1.8x10 <sup>-15</sup>	48.0	CVM	[155]
Benzene	HZSM-5 (1000)	4.5x10 <sup>-15</sup>	44.0	CVM	[155]
Benzene	HZSM-5 (39.7)	4.5x10 <sup>-11</sup>	5.3	VOL	[144] <sup>*</sup>
Benzene	Silicalite-1	5.6x10 <sup>-11</sup>	21.0	TGA	[156]
Toluene	Silicalite-1	1.2x10 <sup>-14</sup>	-	CVM	[155] <sup>*</sup>
Toluene	HZSM-5 (40)	2.1x10 <sup>-15</sup>	51.0	CVM	[155] <sup>*</sup>
Toluene	HZSM-5 (39.7)	9.0x10 <sup>-12</sup>	5.5	VOL	[144] <sup>*</sup>
p-Xylene	Silicalite-1	8.0x10 <sup>-12</sup>	6.4	ZLC	[131]
p-Xylene	Silicalite-1	1.8x10 <sup>-15</sup>	7.2	FTIR	[151]
p-Xylene	Silicalite-1	~10 <sup>-12</sup>	7.2	ZLC	[152]
p-Xylene	Silicalite-1	1.0x10 <sup>-14</sup>	19.0	TGA	[153] <sup>*</sup>
p-Xylene	Silicalite-1	3.2x10 <sup>-15</sup>	18.0	DRP	[154]
p-Xylene	Silicalite-1	9.0x10 <sup>-15</sup>	-	CVM	[155] <sup>*</sup>
p-Xylene	HZSM-5 (40)	7.0x10 <sup>-16</sup>	58.0	CVM	[155] <sup>*</sup>
p-Xylene	HZSM-5 (39.7)	9.0x10 <sup>-12</sup>	18.1	VOL	[144] <sup>*</sup>
p-Xylene	Silicalite-1	3.1x10 <sup>-11</sup>	15.0	TGA	[156]
o-Xylene	Silicalite-1	1.1x10 <sup>-15</sup>	24.0	DRP	[154]
o-Xylene	HZSM-5 (39.7)	3.0x10 <sup>-13</sup>	35.5	VOL	[144] <sup>*</sup>
m-Xylene	HZSM-5 (39.7)	8.0x10 <sup>-15</sup>	37.7	VOL	[144] <sup>*</sup>
EB	HZSM-5 (39.7)	1.2x10 <sup>-12</sup>	21.9	VOL	[144] <sup>*</sup>
EB	Silicalite-1	5.0x10 <sup>-11</sup>	22.0	TGA	[156]

<sup>\*</sup> 323 K, ZLC, zero-length column; TGA, thermogravimetric analysis; VOL, Microvolumetry; CS, circulating system; CVM, constant volume method; DRP, constant-pressure desorption.

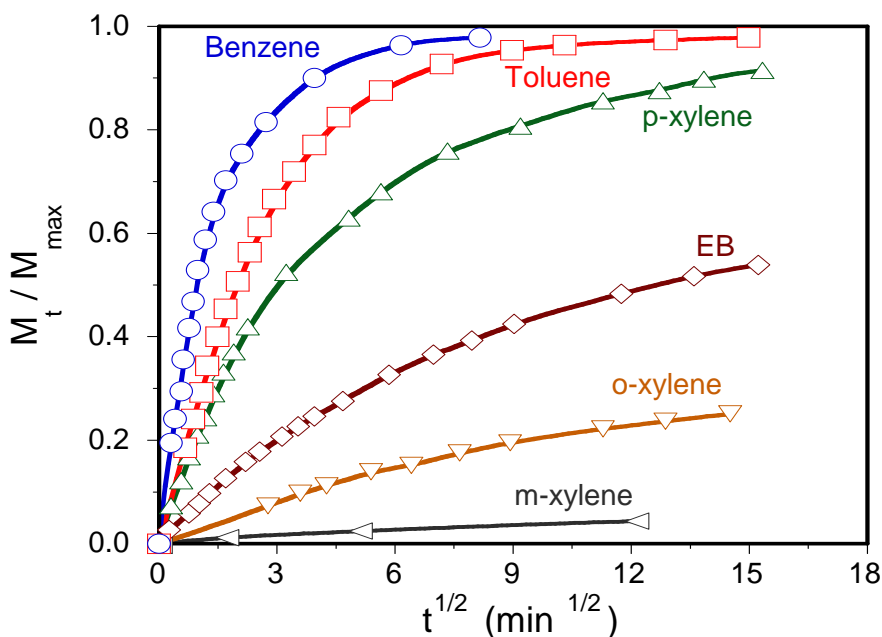


Figure 2.8: Adsorption kinetics of benzene, toluene, ethylbenzene and p/o/m-Xylenes in HZSM-5 at low loadings (<1 molec/uc). Adapted from [144].

Self- and transport diffusivities have also been calculated by molecular simulations (Monte Carlo and Molecular Dynamics). In general terms, self-diffusivities tend to agree fairly well with the values measured by microscopic methods [145,146]. The diffusivities measured by macroscopic methods are often found between one and three orders of magnitude lower than the values measured by microscopic methods, especially for p-Xylene. Ruthven [147] has interpreted this discrepancy in terms of anisotropic diffusion behaviour.

The diffusivity of aromatics in MFI depends strongly on the degree of polycrystallinity of the sample and on the particle shape. For instance, Muller *et al.* [148], using time-resolved FTIR spectroscopy, have shown that the p-Xylene diffusivity on silicalite-1 single crystals is about three orders of magnitude higher than the value measured on polycrystalline samples. Furthermore, using a frequency response method (FR), Song *et al.* [149] have reported self-diffusivities between 1-3 orders of magnitude higher in spheric (twinned) than in cube-shaped silicalite-1 particles at the same loading and temperature conditions. In addition, the acidity of the MFI framework, as well as the history of the samples (number of calcination steps between consecutive xylene uptake experiments), might also affect the diffusion behaviour of aromatic species [137].

The generalized Maxwell-Stefan theory (GMS) earlier developed by Krishna [145,150] from mixture diffusion on bulk fluids provides an adequate basis for the description of multi-component mass transfer of adsorbed species in zeolites when surface diffusion along the surface within the zeolite pores is the rate limiting step. Since the size of the

---

permeating molecules is of the same order as that of the micropores, the GMS theory conventionally assumes that movement of a species is caused by a driving force, which is balanced by the friction experienced from the other species and the pore walls. Taking the isothermal gradient of chemical potential of the  $i^{\text{th}}$  species,  $-\nabla_T \mu_i$ , as the driving force, and treating vacancy sites as active species. The general form of the GMS equations applied to surface diffusion is described as follows:

$$-\rho_p \frac{q_i}{RT} \nabla_T \mu_i = \sum_{\substack{j=1 \\ j \neq i}}^c \frac{(q_j N_i^S - q_i N_j^S)}{q_{M,j} \mathcal{D}_{ij}^S} + \frac{N_i^S}{\mathcal{D}_{iV}^S} \quad i,j=1,\dots,C \quad (2.7)$$

where  $q_i$  and  $N_i^S$  are the molar loading and the surface flux of the  $i^{\text{th}}$  species, respectively. Note that in this equation, the MS formalism involves the use of MS diffusivities rather than Fickian or transport diffusivities, because surface fluxes are related to chemical potential gradients instead of loading gradients.

The first term on the right-hand side in Eq. 2.7 reflects the friction exerted between two sorbate molecules, while the second term represents the friction between a sorbate molecule and the pore wall. Both interactions can be modelled, respectively, by means of *MS counterexchange diffusivities*,  $\mathcal{D}_{ij}^S$ , and *MS surface or 'jump' diffusivities*,  $\mathcal{D}_i^S$ . Note that, in the particular case that  $\mathcal{D}_{ij}^S \rightarrow \infty$  the first term in the right-hand side of Eq. 2.7 vanishes. This implies that the surface motion of the sorbate species  $i$  does not affect the motion of sorbate species  $j$ .

Mechanistically, the MS surface diffusivity,  $\mathcal{D}_i^S$ , can be related to the displacement of the sorbate molecules,  $\lambda$ , and the jump frequency,  $\nu(q^T)$ , which, for strongly confined aromatic molecules, is expected to depend on the number of occupied sites,  $q^T$  as follows [157]:

$$\mathcal{D}_i^S(q^T) = \frac{1}{z} \lambda^2 \nu_i(q^T) = \frac{1}{z} \lambda^2 \nu_i(0) f(q^T) \quad (2.8)$$

The expression of function  $f(q^T)$  depends on the degree of confinement of the diffusing molecules within the zeolite host and on the sorbate-sorbate interactions [158]. In the case of multicomponent diffusion, the *MS counterexchange diffusivities* can be modelled using the *Vignes* relationship [157]:

---


$$D_{ij}^S(q_T) = [D_i^S(0)]^{\theta_i/(\theta_i+\theta_j)} [D_j^S(0)]^{\theta_j/(\theta_i+\theta_j)} \quad (2.9)$$

The temperature-dependence of the MS surface diffusivities at zero coverage,  $D_i^S(0)$  can be modelled according to an Arrhenius-type equation [159,160]:

$$D_i^S(0) = D_{i,T \rightarrow \infty}^S(0) \exp\left(-\frac{E_i^S}{RT}\right) \quad (2.10)$$

where  $D_{i,T \rightarrow \infty}^S(0) = A_i^S$ , the pre-exponential factor and  $E_i^S$  is the activation energy.

The surface chemical potential gradients may be expressed in terms of the molar loadings gradients by introduction of the matrix of thermodynamic factors,  $\Gamma_{ij}$  [157]:

$$\frac{q_i}{RT} \nabla \mu_i = \sum_{j=1}^N \Gamma_{ij} \frac{q_{i,M}}{q_{j,M}} \nabla q_j \quad (2.11)$$

$$\Gamma_{ij} \equiv \left( \frac{q_{j,M}}{q_{i,M}} \right) \frac{q_i}{P_i} \frac{\partial P_i}{\partial q_j} \quad i, j = 1, \dots, C \quad (2.12)$$

The form of the thermodynamic factors is determined by the form of the mixture adsorption isotherm. In the case of pure p-Xylene diffusion, Krishna *et al.* [161] have developed an expression to account for the inflection of the adsorption isotherm on the thermodynamic factors by using the dual-site Langmuir isotherm (Eq. 2.2). This expression turns into the classical Darken equation at sufficiently low loadings (<4 molec/uc) relating Fickian and MS surface diffusivities ( $D_i^S$  vs.  $D_i^S$ ) as follows [162,163]:

$$D_i^S = \frac{D_i^S}{1 - \sum_{j=1}^C \theta_j} \quad (2.13)$$

For example, Figure 2.9 illustrates the evolution of the p-Xylene 'Fickian' surface diffusivity as a function of loading. In the particular situation of infinite dilution ( $\ll 1$  molec/uc), both diffusivities converge and are expected to be equal (i.e.  $D_1^S \rightarrow D_1^S$ ).

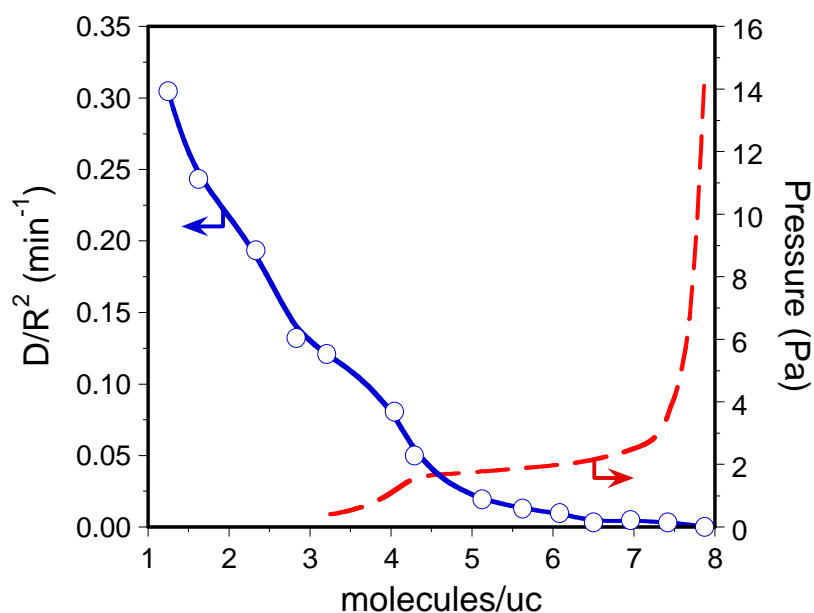


Figure 2.9: Intracrystalline diffusion time constant for p-Xylene at 283 K in a fresh sample. Adapted from [83].

### 2.3.1.3 Xylene pervaporation (PV) within MFI-type zeolite membranes

Only few useful studies which deal with the PV separation of xylene isomers using zeolite membranes have been published in the literature. Table 2.4 collects the most representative separation data obtained at ambient pressure and near-room temperature. In a series of papers, Nishiyama and co-workers [164-166] have studied the PV performance of aromatics within ferrierite (FER) and mordenite (MOR) membranes synthesized by dry gel conversion. The highest selectivities have been reported on FER membranes, achieving values as high as 600 for benzene/PX separation (benzene feed concentration=0.5 mol%) at 303 K and higher than 16 for p/m-Xylene separation. However, in all cases, the pervaporated fluxes are very low, showing values lower than  $0.01 \mu\text{mol}\cdot\text{m}^{-2}\cdot\text{s}^{-1}$  in the case of p/m-Xylene separation. Moreover, PV fluxes can be drastically reduced as a result of fouling probably due to the role of nanosized defects and grain boundaries, as has been pointed out by Wegner *et al.* [167].

In the case of MFI-type zeolite membranes, the main limitation of PV for p-Xylene separation is ascribed to the high xylene loadings that are achieved in the MFI structure,

---

especially at near-room temperature. As stated in sub-section 2.3.1.2 high xylene loadings might cause a distortion of the MFI unit cell (transition from ORTHO to PARA phase) involving channel 'swelling', leading to single-file diffusion, xylene isomers not being able to diffuse one another in the zeolite channels. Single-file diffusion of xylene isomers can also be promoted in nanosized grain boundaries between adjacent zeolite grains. In this diffusional regime, xylene isomers with the slowest permeation rate (i.e. o-Xylene and m-Xylene) might limit diffusion, blocking p-Xylene separation and reducing (or even inverting) p-Xylene selectivity. Unlike the separation of lighter gases, energetic and entropic effects play a major role in xylene isomer separation and ultimately determine the membrane performance

The best p-Xylene separation performance by PV from xylene isomer mixtures has been reported to date by Yuan *et al.* [168] on template-free hydrothermally synthesized silicalite-1 membranes, showing p-Xylene fluxes and p/o-selectivities up to  $13.7 \mu\text{mol}\cdot\text{m}^{-2}\cdot\text{s}^{-1}$  and 40, respectively. Xiang and Ma [169] have also reported MFI membranes displaying partial selectivity to p-Xylene, but with much higher p-Xylene fluxes (about  $75 \mu\text{mol}\cdot\text{m}^{-2}\cdot\text{s}^{-1}$ ). Yuan *et al.* [168] have reported that the room-temperature p-Xylene selectivity of MFI membranes depends strongly on the p-Xylene concentration in the liquid feed (see Figure 2.10). At higher p-Xylene loadings, single-file diffusion is promoted due to an increased distortion of the MFI unit cell, the membrane losing its ability to discriminate p-Xylene among the other xylene isomers. The same authors have also reported extremely long stabilisation periods (>24 h) to achieve steady-state p-Xylene selectivities on the grounds of a slow and progressive distortion of the MFI unit cell upon p-Xylene adsorption and diffusion.

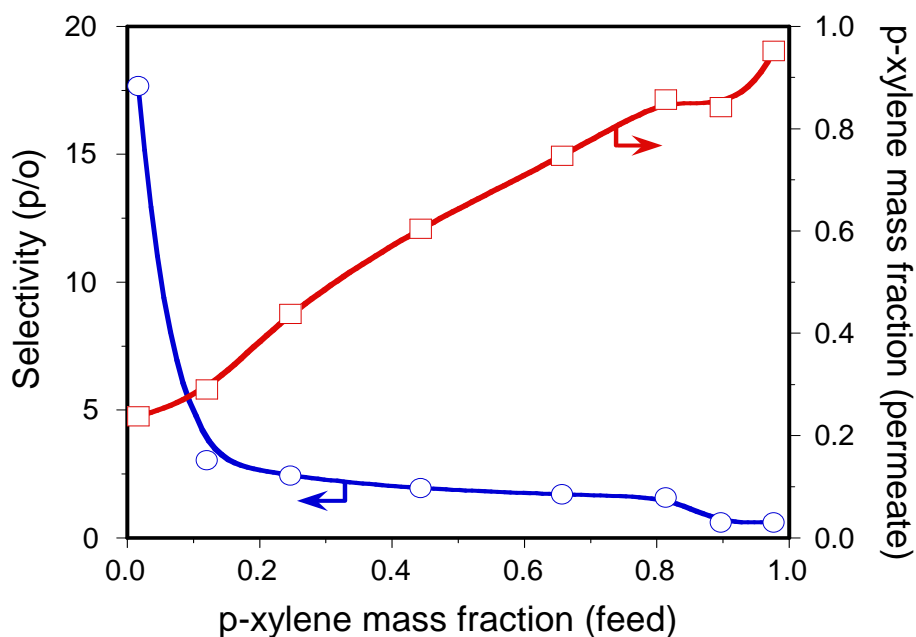


Figure 2.10: Membrane response as a function of p-Xylene feed concentration during PV of an equimolar p/o xylene feed at 298 K. Adapted from [170].

Table 2.4: Separation of xylene binary/ternary mixtures by PV at ambient pressure using zeolite membranes prepared on  $\alpha$ -alumina support

Membrane type	Thickness ( $\mu\text{m}$ )	Mixture (%)	T (K)	Flux ( $\mu\text{mol.m}^{-2}.\text{s}^{-1}$ )	Selectivity (-)	Ref.
MFI	1.5	p-Xylene (50) o-Xylene (50)	299	200 200	~1	[167]
MFI*	-	p-Xylene m-Xylene	299	75 4.9	15	[169]
MFI	3-5	p-Xylene (50) o-Xylene (50)	323	13.7 0.3	40	[168]
MFI	20	p-Xylene (24) m-Xylene (51) o-Xylene (25)	303	2.3 1.0 0.2	p/m: 2.3 p/o: 11.5	[171]
MFI	15	p-Xylene (50) o-Xylene (50)	303	1.3 0.8	~2	[170]
MOR	10	benzene p-Xylene	295	130 2.6	164	[164]
FER	10	benzene (50) p-Xylene (50)	303	37 2	100	[165]
FER	-	p-Xylene o-Xylene	303	0.0021 <0.0004	>16	[166]

\* Experiments performed at 17 atm.

---

### 2.3.1.4 Xylene vapour permeation (VP) in MFI membranes

A relatively higher number of studies compared to PV have been published in the past years reporting on the xylene isomer separation performance of MFI membranes by VP. Table 2.5 collects the most representative results. Unlike PV, at sufficiently low xylene partial pressures (<2 kPa) and in the temperature range 295-673 K, MFI membranes can show optimal selectivity for p-Xylene separation by VP. The permeation performance of these membranes is more dependent on molecular sieving than on preferential adsorption. In particular, Lai *et al.* [172] and Xomeritakis *et al.* [106,173] have shown that b-oriented MFI membranes show much better p-/o-Xylene separation factors (up to 480) than in the case of c-oriented or random MFI membranes, the p-Xylene permeance achieving a value of 200 nmol.m<sup>-2</sup>.s<sup>-1</sup>.Pa<sup>-1</sup> at 473 K for a feed mixture of 0.45 and 0.35 kPa p- and o-Xylene partial pressures, respectively.

The evolution of pure p-, m- and o-Xylene fluxes with temperature shows a characteristic maximum in the range 523-673 K (denoted as T<sub>max</sub>) for all the membranes considered in Table 2.5. In the case of xylene isomer separation from ternary mixtures, p-Xylene still shows a maximum with temperature; m-Xylene and o-Xylene fluxes now displaying minimum values (for example, see Fig. 4.4). The value of the maximum temperature for p-Xylene flux depends not only on the competition between adsorption and surface diffusion phenomena in the zeolite channels, but also on the amount and characteristics of nanosized defects and grain boundaries in the zeolite matrix. A detailed parametric study on the effect of temperature and feed partial pressure on the xylene permeation and separation performance of MFI membranes has been recently published by Yeong *et al.* [174].

In the case of randomly oriented MFI membranes, the highest p/o and p/m-Xylene separation factors and fluxes at low xylene partial pressures have been reported by Gump *et al.* [175] on self-supported isomorphous BZSM-5 films. If we consider supported MFI membranes, the best trade-off between p-Xylene selectivity and flux has been reported on nanocomposite materials either in tubular or hollow-fibre configurations (see Table 2.5 and Table 5.2).

Unlike membrane films, the improved separation performance of these materials should be ascribed to a reduction of intercrystalline defects in the zeolite material due to its intimate confinement in the porous network of the support. The p-Xylene separation capacity of ZSM-5 zeolite membranes can be tuned to a certain extent by exchanging the cation in the zeolite framework. Tarditi *et al.* [176] have reported that Ba-exchanged ZSM-5 membranes show much higher p/o and p/m-Xylene separation factors compared to Na and Sr-exchanged

counterparts (up to the double, see Fig. 2.11), despite a strong reduction of p-Xylene fluxes probably due to the decrease in the pore size of the channels.

Table 2.5: Literature survey on xylene isomer separation by VP at low xylene partial pressures (<1 kPa) using MFI-type zeolite membranes

Membrane	Support material / geometry	Thickness ( $\mu\text{m}$ )	$T_{\text{max}}$ (K)	$\Pi_{\text{max}}$ p-Xylene ( $\text{nmol.m}^{-2}.\text{s}^{-1}.\text{Pa}^{-1}$ )	SF (p/o) (-)	Refs.
b-oriented MFI films <sup>a</sup>	$\alpha$ -alumina / disk	1	423	200	480	[172] [179]
c-oriented MFI films <sup>a</sup>	$\alpha$ -alumina / disk	30	423	30	3	[172] [179]
h0h-oriented MFI films <sup>a</sup>	$\alpha$ -alumina / disk	2	403	40	60	[172] [179]
B-ZSM-5 film <sup>b</sup>	SS / tubular (inner surface)	30	425	2.6	60	[175]
MFI film (self-supported) <sup>b</sup>	Temporary Teflon <sup>R</sup> support	90	473	82	250	[178]
Ultra thin MFI films <sup>a</sup>	$\alpha$ -alumina / disk	0.5	663	300 (663 K) 600 (373 K)	3 16	[180]
Silicalite-1 film <sup>b</sup>	$\alpha$ -alumina / disk	3	400	12	60	[177]
Silicalite-1 film <sup>a</sup>	$\gamma$ -alumina / tubular (outer surface)	2-10	480	4	1	[181]
Silicalite-1 film <sup>b</sup>	SS/disk	4	373	1220	2.4	[182]
HZSM-5 <sup>b</sup>	SS/disk	7	373	711	2.3	[182]
MFI film <sup>b</sup>	$\alpha$ -alumina / tubular		573	9.5 (523 K)	17.8	[183]
MFI film <sup>a</sup>	$\alpha$ -alumina / disk	1-40	548	20 (398 K)	60-300	[106]
ZSM-5 film <sup>a</sup>	SS / tubular (outer surface)	15-20	673	51	4	[184]
Silicalite-1 film <sup>c</sup>	SS / tubular (outer surface)	25	673	11.9	8	[185]
HZSM-5-alumina nanocomposite <sup>d</sup>	$\alpha$ -alumina / tubular	2-3	673	10 (450 K)	7.0	[186]
ZSM-5 (b-oriented)	$\alpha$ -alumina / disk	-	493	200	483	[187]
Al-ZSM-5/Silicalite-1 (bi-layered) <sup>e</sup>	Sintered porous SS/disk	12	373	0.4	~5	[188]
BaZSM-5 (100% Ba <sup>2+</sup> ) <sup>f</sup>	SS / tubular	15-20	543	65	19	[176] [189]
Silicalite-1 film <sup>g</sup>	$\alpha$ -alumina / disk	2-3	573	23	~20	[190]

<sup>a</sup>Prepared via seeded hydrothermal synthesis

<sup>b</sup>Prepared via *in situ* seeded hydrothermal synthesis

<sup>c</sup>Prepared via hydrothermal synthesis

<sup>d</sup>Prepared via pore-plugging *in situ* hydrothermal synthesis

<sup>e</sup>Prepared via *in situ* seeded hydrothermal synthesis (3 cycles)

<sup>f</sup>Prepared via secondary growth

<sup>g</sup>Prepared via *in situ* hydrothermal crystallization

---

The xylene permeation and separation performance of zeolite membranes can be modelled on the basis of the Maxwell-Stefan (MS) equation as in the case of xylene diffusion modelling within zeolite crystals. Combining Eq. 2.11 and Eq. 2.12 and using the single-site Langmuir isotherm to derive the thermodynamic factors,  $\Gamma_{ij}$ , the following classical expression is obtained for pure xylene permeation under 'weak confinement' [189,191]:

$$J = \frac{\varepsilon \rho_{MFI} \mathcal{D}^S(0) q_M}{\tau \ell} \ln \left[ \frac{1 + K P_R}{1 + K P_P} \right] \quad (2.14)$$

where  $P_R$  and  $P_P$  are the retentate and permeate pressures, respectively and  $K$  and  $\mathcal{D}_i^S$  are the adsorption constant and the MS surface diffusivity at zero loading:

$$K = \exp \left[ \frac{\Delta S^\circ}{R} - \frac{\Delta H^\circ}{RT} \right] \quad (2.15)$$

$$\mathcal{D}_i^S(0) = \mathcal{D}_{i,T \rightarrow \infty}^S(0) \exp \left( -\frac{E_i^S}{RT} \right) \quad (2.16)$$

The set of Eq. 2.14 to Eq. 2.16 has also been used for modelling p-Xylene permeation in ternary xylene mixtures at low xylene partial pressures, at the conditions where the membranes show higher selectivity. This approach is, however, restricted to systems with moderate distortion of the MFI framework. Otherwise, important discrepancies are observed when using the set of Eq. 2.14 to Eq. 2.16 for modelling xylene mixture permeation, as has been reported by Tarditi *et al.* [189] from their study on BaZSM-5/SS membranes.

Gardner *et al.* [192] have shown through modelling of *n*-butane permeation that xylene permeation within MFI membranes can be significantly enhanced compared to single supported films when zeolite films are on both sides of the porous support (see Figure 2.12). It is well known that partial pressure drop across the support makes the loadings higher on the downstream side of the zeolite in the presence of a support, the lower driving forces resulting in lower fluxes. Depositing films on both sides of the support might reduce the effect of the support at high loadings, far from Henry's regime.

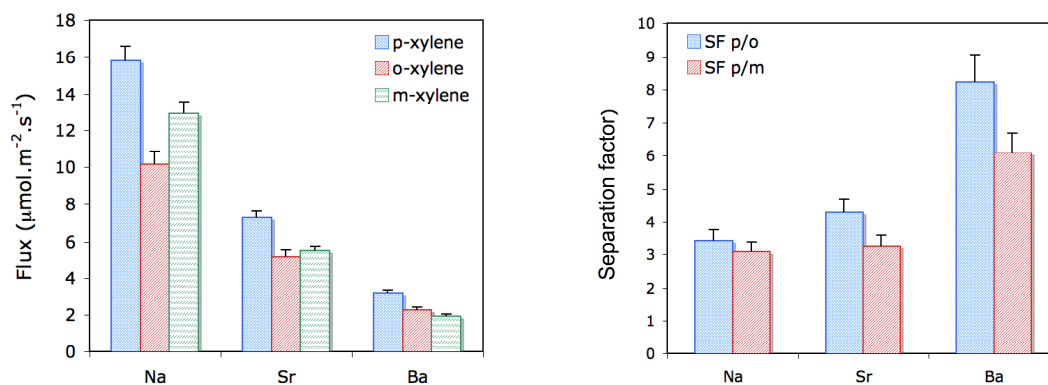


Figure 2.11: Effect of cation exchange on the VP performance of ZSM-5 zeolite membranes in the separation of ternary xylene isomer mixtures at 673 K and for p/m/o partial pressures of 0.23/0.83/0.26 kPa. Adapted from [176].

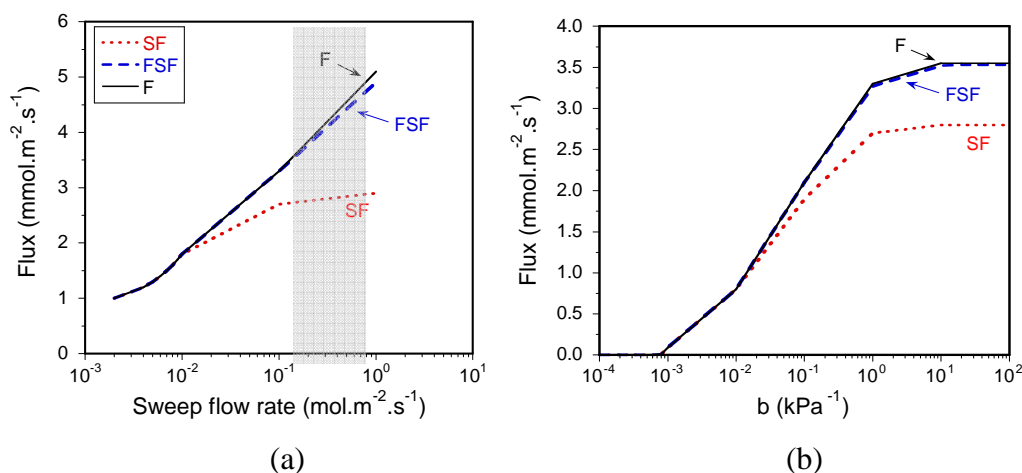


Figure 2.12: Normal-butane fluxes through an unsupported (F), a single supported (FS), and a double-sided (FSF) zeolite membrane as a function of (a) the sweep gas flow rate (the shaded region represents common sweep gas flow rate reported in literature), and (b) the adsorption equilibrium constant. Graph reproduced from [192].

### 2.3.2 CMRs for xylene isomerization

Limited material and energy resources have increasingly become a challenge for future chemical production. Process intensification can contribute to the solution of this problem. From an engineering point of view, the vision of process intensification through multifunctional reactors has activated research on catalytic membrane reactors. According to the IUPAC definition, a membrane reactor is a device combining a membrane-based separation and a chemical reaction in one unit [193]. So far this engineering vision of a chemical membrane reactor could not be realized due to a lack in temperature resistant and chemically stable highly selective membranes. During the last few years, inorganic

membranes based on ceramics, zeolites, metals, carbon or as a hybrid material have been developed so that the realization of a chemical membrane reactor is increasingly possible.

Catalytic membrane reactors (CMRs), where membrane separation is coupled with a catalytic reaction in the same unit, are attractive applications because they are potentially compact, less capital intensive and have lower operating costs than more conventional processes. On the basis of the way the membrane and the catalyst are combined, CMRs have been broadly classified [194] as: (1) extractor-type (e-CMR), (2) distributor-type (d-CMR), and (3) contactor-type (c-CMR which also include flow-through or interfacial), these latter being operated in either flow-through or interfacial configurations. Figure 2.13 compares schematically these three CMR configurations. In all cases, the membrane can show inherent catalytic character or only act as a separation/contactor unit between the phases and the catalyst. More specific details about these configurations and application domains can be found in reference books and reviews [195-197].

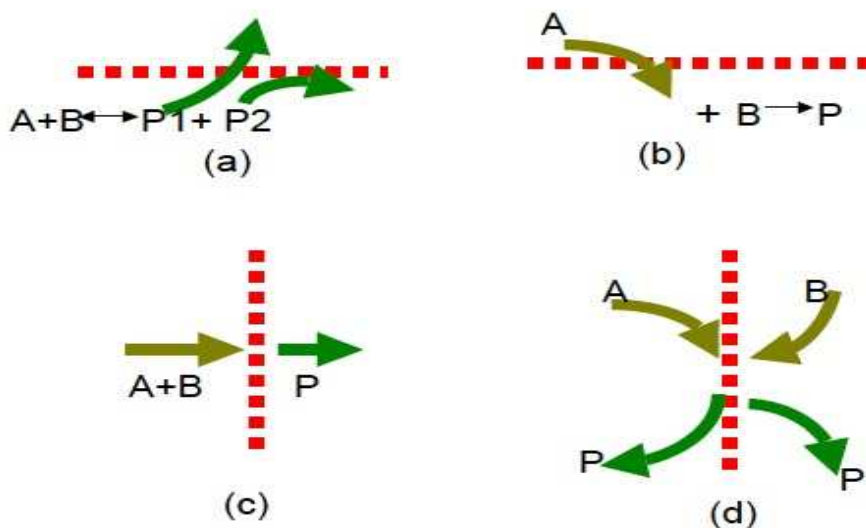


Figure 2.13: Classification of CMRs: (a) extractor, (b) distributor, (c) flow-through contactor and (d) interfacial contactor. A and B represent reactants while P, P1, P2 are the products.

Extractor-type CMRs are by far the most widespread application of CMRs. Classical applications of this configuration range from dehydrogenation, isomerization and esterification/etherification reactions to hormone synthesis and wastewater biological treatment. In this configuration, selective removal of one/more products from the reaction zone enhances the conversion of the reaction by shifting the equilibrium position or by promoting the catalytic activity.

The combination of a MFI membrane with an isomerization catalyst in an e-CMR has been proposed by several authors to promote *p*-Xylene recovery. Table 2.6 compiles the available data published in the literature. In this concept, selective *p*-Xylene by the membrane promotes the *p*-Xylene yield and productivity when compared to a convectional fixed-bed reactor. The scheme of this concept is represented in Fig. 2.14. Figure 2.15 shows the evolution of the equilibrium reaction constants as well as the equilibrium product distribution for the three xylene isomers. Note that from this figure the influence of temperature on *o*-Xylene and *m*-Xylene equilibrium conversions is higher than in the case of *p*-Xylene.

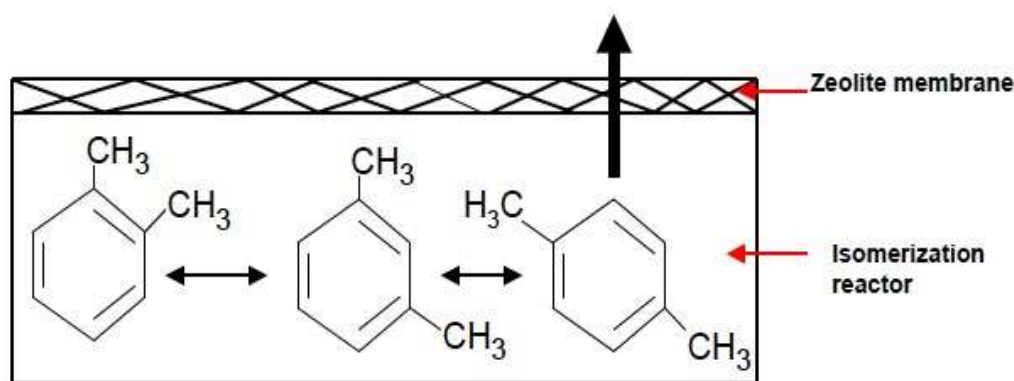


Figure 2.14: Schematic representation of the *p*-Xylene selective extraction in a MFI membrane from an isomerization reactor. The isomerization mechanism considered here corresponds to a metal-doped HZSM-5 catalyst.

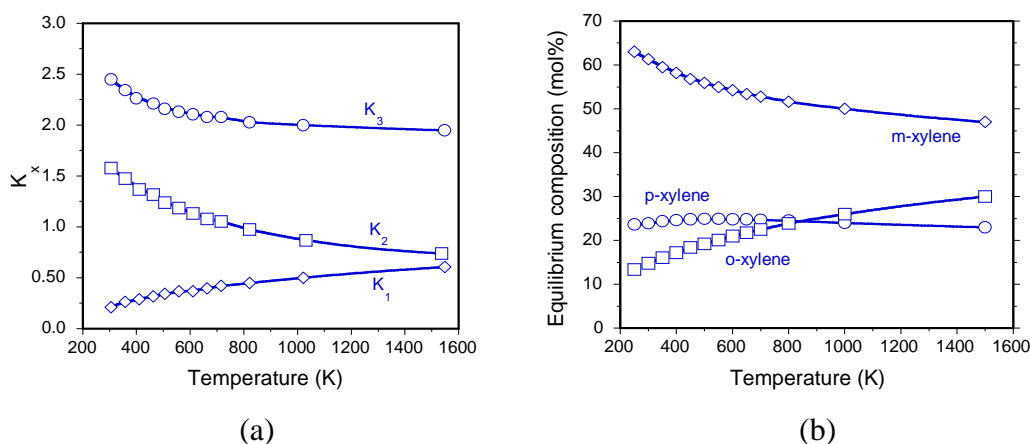


Figure 2.15: Chemical equilibrium for the *o*/*m*/*p*-Xylene ternary system as a function of temperature in the range 250-1500 K. (a) evolution of equilibrium constants  $K_x$  [ $x=1$  (*m*-Xylene  $\rightleftharpoons$  *o*-Xylene),  $x=2$  (*p*-Xylene  $\rightleftharpoons$  *m*-Xylene) and  $x=3$  (*p*-Xylene  $\rightleftharpoons$  *o*-Xylene)]; (b) equilibrium product distribution (molar basis) at the standard state [199].

Table 2.6: Literature survey on xylene isomerization using extractor -type zeolite CMR based on MFI membranes compared to fixed-bed reactors.

Membrane type	T (K)	p-Xylene yield (%)		p-Xylene selectivity (%)		Ref.
		e-CMR	FBR	e-CMR	FBR	
Inert silicalite / $\alpha$ -alumina tube <sup>a</sup>	577	11.2	10.2	65	58	[186]
Inert Ba-ZSM-5/SS <sup>b</sup>	643	25	21	69	52	[198]
Inert silicalite / $\alpha$ -alumina disk <sup>a</sup>	603	21.3	18.5	44.6	35	[190]
Catalytic H-ZSM-5/SS disk <sup>c</sup>	673	11.8	9.45	-	-	[182]
Catalytic H-ZSM-5/SS disk <sup>a</sup>	673	6.9	5.87	66.7	55.6	[182]
Catalytic H-ZSM-5/SS disk <sup>d</sup>	673	7.3	6.98	30.1	30.1	[182]

Feed composition: <sup>a</sup>m-Xylene feed; <sup>b</sup>ternary mixture of xylene feed; <sup>c</sup>p-Xylene feed; <sup>d</sup>o-Xylene feed

An application relying on this combined membrane-catalyst concept for xylene isomerization has been recently patented by MobilExxon [200]. A general scheme of this process is depicted in Fig. 2.16. In this process, the fresh feed containing a mixture of xylene isomers is fed into a xylene splitter where the isomers are separated. The exit stream from the splitter (which contains xylenes and EB) enters a xylene recovery unit relying on fractional crystallization and/or molecular sieving to separate p-Xylene from other components. The p-Xylene depleted stream is sent to an e-CMR to be converted into benzene and/or xylenes, p-Xylene being selectively extracted from the reaction zone using a zeolite membrane.

In all the above stated applications, the MFI membrane acts as a non-catalytic p-Xylene extractor. Nevertheless, the MFI membrane can also display catalytic activity. Figure 2.17 illustrates the different membrane-to-catalyst combinations in e-CMRs for xylene isomerization [188]: (a) combination of a catalyst with an inert MFI membrane used as separation unit, (b) an e-CMR provided with a catalytically active membrane (the membrane acts both as a catalyst and a separation unit), and (c) bi-functional zeolite membrane where a catalyst thin film (e.g., HZSM-5) is placed on top of an inert silicalite-1 membrane.

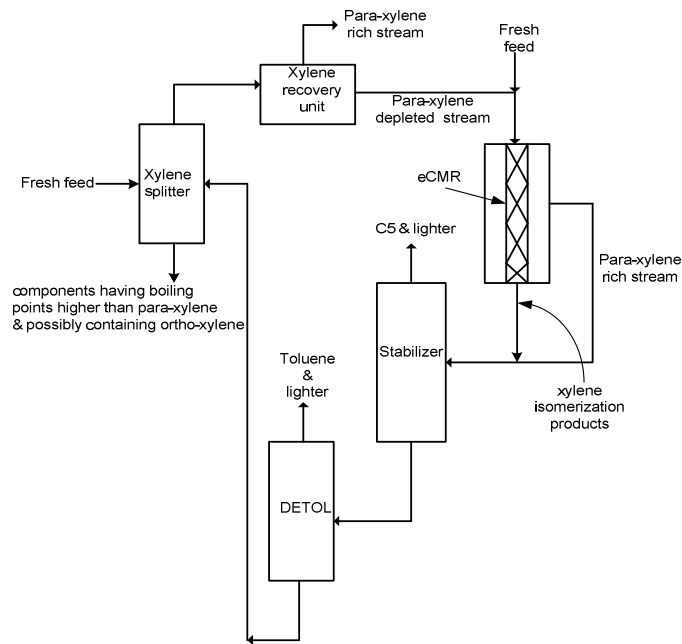


Figure 2.16: ExxonMobil patented process for p-Xylene production [200].

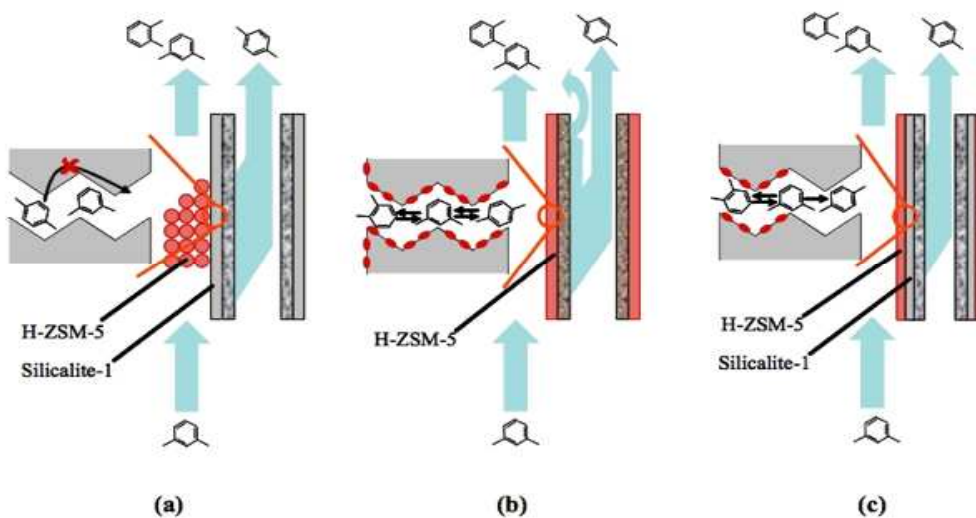


Figure 2.17: Different extractor-type zeolite CMRs (e-ZCMRs) for xylene isomerization: (a) Inert Zeolite CMR (IZCMR), (b) Active Zeolite CMR (AZCMR) and (c) Bi-functional Zeolite CMR (BZCMR) reactor. Adapted from [188].

Tarditi *et al.* [198] have reported isomerization of m-Xylene and ternary xylene vapour in a ZCMR using a Ba-exchanged HZSM-5 membrane and a commercial Pt/ silica-alumina catalyst. In the case of ternary xylene mixtures, the feed p/m/o xylene partial pressures were kept at the values 0.23 kPa / 0.83 kPa / 0.26 kPa. These authors have reported an enhancement of about 26% of p-Xylene yield during m-Xylene isomerization at

643 K compared to a fixed-bed reactor operated at comparable experimental conditions (see Fig. 2.18). Comparable results have been reported by Zhang *et al.*[190] in a recent paper (see Fig. 2.19).

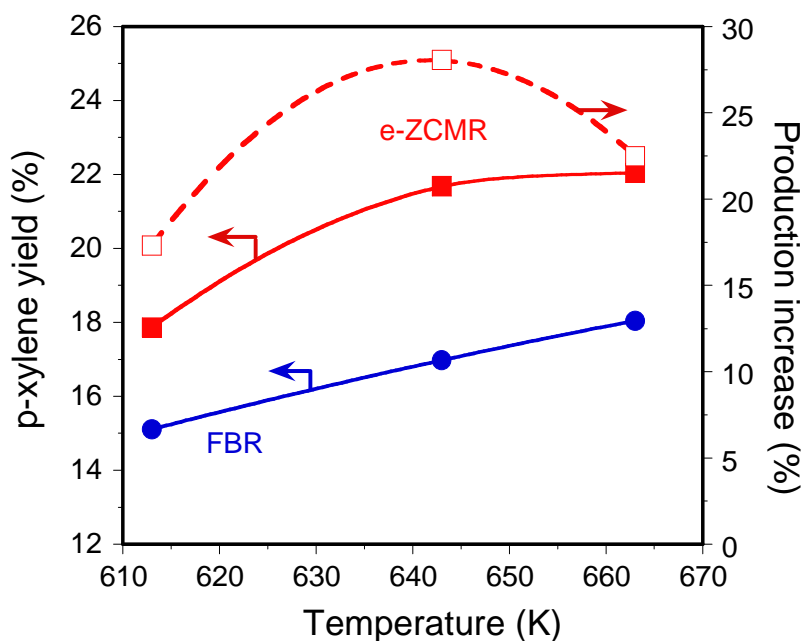


Figure 2.18: P-Xylene yield (top) and p-Xylene production increase (bottom) as a function of temperature for xylene isomerization in an inert ZCMR based on Ba-ZSM-5/SS membrane [198].

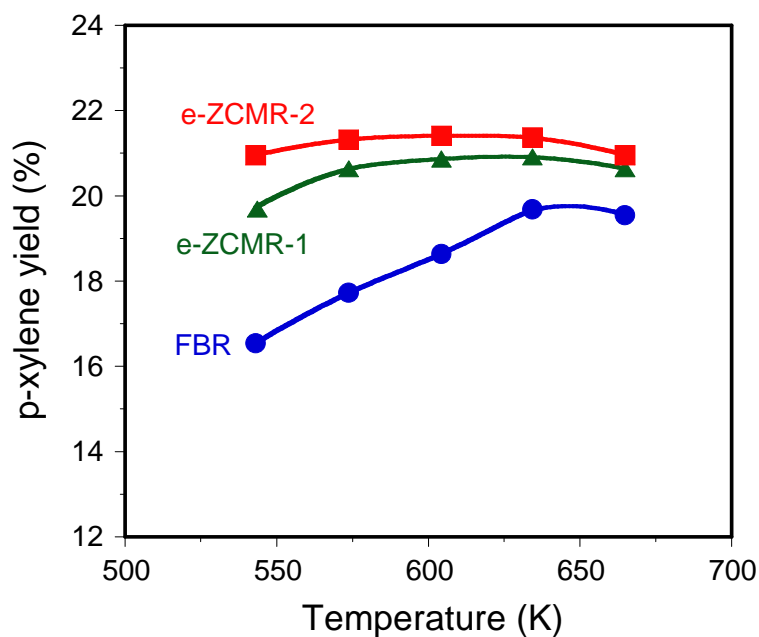


Figure 2.19: M-Xylene isomerization in a e-ZCMR with varying module temperature (Feed flow rate: 20mL/min, sweep flow rate: 20mL/min; for FBR, feed flow rate: 20mL/min) [190].

---

In the case of xylene isomerization using MFI membranes with nanocomposite architecture, van Dyk *et al.* [186] have reported an increase of about 10% of p-Xylene yield (when retentate and permeate amounts are combined) over a conventional FBR. In this study, xylene isomerization was carried out at 577 K with m-Xylene saturated in dry N<sub>2</sub> up to a total feed gas flow rate of 7 mL(STP)/min and with a sweep gas flow rate of 10 mL(STP)/min. Additionally, 100% p-Xylene selectivity at the permeate side was reported when the reactor was operated at permeate-only mode. Again, when the temperature was increased to 633 K and sweep gas flow rate decreased to 7 mL(STP)/min, a decrease in p-Xylene yield was observed while the p-Xylene selectivity remained unchanged.

Deshayes *et al.* [201] have reported a simulation and modelling study of xylene isomerization reaction in an industrial FBR and the effect of the incorporation of multi-tubes containing Na-ZSM-5/SS membranes upon the catalytic performance of the reactor. In the latter case, an increase of about 12% in p-Xylene production over a conventional FBR has been computed.

In the case of catalytically active MFI membranes, the only example of application in the open literature has been reported by Haag and co-workers [182]. In this study, the membrane consisted of a HZSM-5 layer grown on top of a porous stainless steel (SS) disk. The authors have reported an increase by 15% of m-Xylene conversion at 673 K compared to a FBR, while p-Xylene selectivity is enhanced by 10%. At higher temperatures, however, no further improvement of either conversion or p-Xylene selectivity was achieved, probably due to the poor separation quality of the membrane ascribed to a high number of intercrystalline defects.

## **2.4 Concluding remark and scope for research**

In this chapter, a short overview of the state of the art of the application of MFI-type zeolite membranes for gas/vapour separation, especially xylene isomer separation and purification has been presented. Various challenges have been highlighted. Above all, it has been shown that the use of MFI-type zeolite membranes for p-Xylene separation/production is promising. However, availability of high-flux selective membranes for the production of high purity p-Xylene from mixed xylenes is still a major problem. Furthermore, in-depth understanding of the fundamental behaviour of e-CMRs, having nanocomposite MFI-type zeolite membranes as separation units, during the production of high purity p-Xylene via isomerization of m-Xylene is essential.

Based on the aforementioned problems, the remaining chapters of this dissertation will demonstrate the promising potentials of nanocomposite MFI-type zeolite membranes for the production and purification of p-Xylene from mixed xylenes through:

- 
- The study of the influence of operating variables (temperature, sweep gas flow rate and xylene loading/partial pressures) on the separation performance of nanocomposite MFI-alumina membranes during xylene isomer separation. Results from this study might provide useful information on the behaviour of these membranes, especially, at higher xylene loadings. The information might be instrumental in optimizing preparation protocol of the membranes for high selectivity.
  - Preparation and evaluation of the separation performance of nanocomposite MFI-alumina hollow fibre membranes during xylene isomers separation. The results of the investigation will provide information about the behaviour of nanocomposite MFI-alumina hollow fibre membranes during xylene isomers separation. Furthermore, the results might give insight into the possibility of enhancing p-Xylene flux in e-CMR having nanocomposite MFI-alumina hollow fibre membrane as separation unit.
  - Investigation of the influence of operating variables and reactor configuration on the performance of an e-CMR, having nanocomposite MFI-alumina membrane as separation unit, during m-Xylene isomerization to p-Xylene over Pt-HZSM-5 catalyst. The investigation will provide detailed information on the fundamental behaviour of the e-ZCMR during m-Xylene isomerization to p-Xylene. Understanding the role played by the aforementioned variables on the performance of the e-CMR might be helpful in the optimization of the operating conditions and as well as the reactor configuration.
  - Modelling and sensitivity analysis of e-CMR, having nanocomposite MFI-alumina membrane as separation unit, during m-Xylene isomerization to p-Xylene over Pt-HZSM-5 catalyst. Results from the investigation will explain and solidify the observations from the experimental studies. Furthermore, results from the sensitivity analysis might give insight into the scaling-up of the system.

---

## Chapter 3: Membrane preparation, characterization and experimental procedures

In this chapter, a short overview of techniques for preparing MFI-type zeolite membranes is presented with a focus on the preparation of nanocomposite MFI-alumina membranes (hollow fibres and tubes). Also, experimental procedures and methods of result analysis employed in this study are presented.

### 3.1 Membrane preparation techniques

Several strategies have been proposed for the synthesis of MFI zeolite membranes on porous supports (most usually  $\alpha$ -alumina). Among them, dry-gel conversion and liquid-phase hydrothermal synthesis are commonly used for the synthesis of zeolite films onto a porous support in one or several batch cycles. The former method consists of the deposition of a layer containing the Si and Al precursors as a dry amorphous aluminosilicate gel onto the support using sol-gel techniques, followed by zeolitization under the presence of vapours [202,203]. This has the advantage of promoting nucleation on the support, avoiding crystal nucleation in the homogeneous phase and reducing the waste reactants. The advantage of this technique is that it allows strict control of the zeolite amount deposited but formation of cracks in the amorphous layer could be a major setback.

Most often, MFI zeolite membranes have been prepared by direct or *in situ* hydrothermal synthesis in an autoclave at 443-473 K under autogeneous pressure using an organic template as structure-directing agent (SDA), usually tetrapropylammoniumhydroxide (TPAOH) and/or tetrapropylammoniumbromide (TPABr) [204]. In this one-step process, nucleation and growth processes take place in the presence of a support. However, this simple strategy presents some drawbacks. As a matter of fact, the zeolite layer should be formed from nuclei that appear during the hydrothermal treatment. Their number and distribution homogeneity on the support depend on a number of parameters, such as the surface properties, that are difficult to control. Moreover, the formation of nuclei competes with crystal growth processes, which might limit the nuclei density due to mass-transfer limitations. This implies in practice the need to grow thick zeolite films to obtain continuous and well-intergrown layers.

The quality and reproducibility of zeolite membranes can be improved by seeding the support prior to hydrothermal synthesis, decoupling the nucleation and growth steps [205,206]. This method is referred to in the literature as 'seed hydrothermal synthesis' or 'secondary growth method' [205,206]. Since the nutrient concentration needed for secondary growth is lower than that required for *in situ* hydrothermal synthesis, further nucleation is

---

strongly reduced and almost all crystal growth takes place over the existing crystal seeds. Furthermore, by carefully controlling the seed layer coating the support using a convenient technique, crystallization of undesired zeolite phases can be discouraged, and the rate and direction of crystal growth can be controlled to a certain extent.

### **3.2 Preparation of MFI zeolite membrane by “pore-plugging” technique**

For more than a decade, the engineering group at the Institute of Research on Catalysis and Environment, Lyon (IRCELYON) situated in France, has been actively involved in the development of nanocomposite MFI-type zeolite membranes for separation and catalytic reaction processes [191,207-210]. In this concept, the MFI material is grown by 'pore-plugging' direct hydrothermal synthesis in a porous matrix rather than forming thin films on top. The advantages of this type of architecture over conventional film-like zeolite membranes include: (i) reduced effect of thermal expansion mismatch between the support and the zeolite, (ii) easier to scale-up, and (iii) easier module assembly because the separative layer (zeolite crystals) are embedded within the pores of the ceramic support, reducing the effects of abrasion and thermal shocks. Moreover, unlike film-like zeolite membranes [211,212], the confinement of the zeolite material at the nanoscale avoids pore opening at high temperatures (>400 K).

#### **3.2.1 Preparation of tubular and hollow fibre nanocomposite MFI-alumina membranes**

At IRCELYON, standard procedure for preparation of nanocomposite MFI-alumina zeolite membranes involves 5 stages:

##### **3.2.1.1 Support characterization**

The membrane supports are usually asymmetrical Pall-Exekia  $\alpha$ -alumina tube (o.d. 10 mm, i.d. 7 mm, length 15 cm) for membrane tubes and alumina supports of dimensions (o.d. 1.65 mm, i.d. 1.44 mm) with porosity 43% for nanocomposite MFI-alumina hollow fibres. The quality of the supports could be determined using porosimetry technique.

In this study, the membrane supports used were asymmetrical  $\alpha$ -alumina supports supplied by Pall-Exekia for the tubes and asymmetrical  $\alpha$ -alumina fibres supplied by Dr. Thomas Schiestel of Interfacial Engineering and Matreial Science Group in Fraunhofer Institute for Interfacial Engineering and Biotechnology in Germany. The cross-section of the supports and a picture of the typical supports (tubes and fibres) are depicted in Fig. 3.1 and Fig. 3.2.

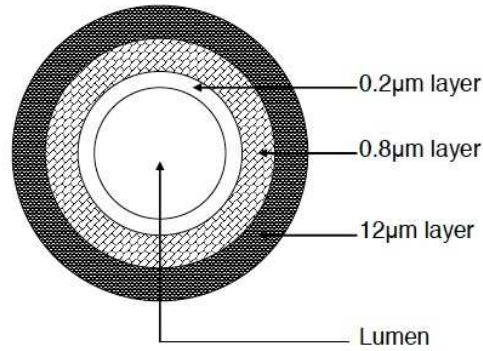


Figure 3.1: The cross-section of the tubular support supplied by Pall-Exekia.



Figure 3.2: Picture of the typical supports (tube and fibre) (picture not to scale).

At IRCELYON, the technique used to evaluate the quality of support is gas-liquid displacement test. During the test as performed in this study, one end of the support was sealed and the other end was connected to an automatic porometer (WSI, USA). In the case of hollow fibres' supports, one end was sealed with glue, while the other was connected to the porometer via a Swagelok connector (see Fig. 3.3). The mounted supports were then soaked in ethanol for at least 24 hours to ensure proper pore filling by capillarity in a similar way as that proposed by the ASTM standard procedure F316-86 [213]. Subsequently, the wetted supports were subjected to an increasing differential pressure across the support and the  $N_2$  flux through the support was monitored. Figure 3.4 shows the typical curves of  $N_2$  flux versus differential pressure across the support obtained in these tests. The 'wet' curve represents the  $N_2$  flux for the wetted sample starting at the first bubble point (FBP) and showing a rapid increase with the pressure across the support as the solvent is expelled from the support pores.

---

After complete removal of the solvent, the pressure was automatically reduced to the starting value and then increased again, thereby obtaining the 'dry' curve. At sufficiently high pressures across the support, the 'wet' and 'dry' curves should converge, the trend becoming linear as expected from the Hagen-Poiseuille equation for a system accomplishing the heuristic condition  $P_m \cdot d > 0.1 \text{ Pa}\cdot\text{m}$  (omission of Knudsen contribution) [214], where  $P_m$  is the mean pressure between the retentate and permeate sides of the fibre, being computed as:

$$P_m = P_{ret} + \frac{\Delta P}{2} \quad (3.1)$$

The pore size distribution was obtained from the experimental trend of the  $N_2$  flux with the pressure across the support by solving the Fredholm equation of the 1<sup>st</sup> kind defined by Eq. 3.2:

$$J_{N_2} = \int_0^{\infty} K(d, P_m, \Delta P) f(d) \delta d \quad (3.2)$$

where  $J_{N_2}$  is the  $N_2$  flux,  $K$  is the Kernel,  $f(d)$  is the number pore size distribution and  $d$  is the pore size, the latter being related to the differential pressure across the support by Laplace Law:

$$d = \frac{4\gamma \cos \theta}{\Delta P} \quad (3.3)$$

where  $d$  is the pore size,  $\gamma$  is the surface tension of ethanol (taken as  $23.0 \text{ mN}\cdot\text{m}^{-1}$ ),  $\theta$  is the contact angle (taken as 0) and  $\Delta P$  is the transsupport differential pressure.



Figure 3.3: Picture of a fibre support sealed with swagelok connector before porosimetry test (picture not to scale).

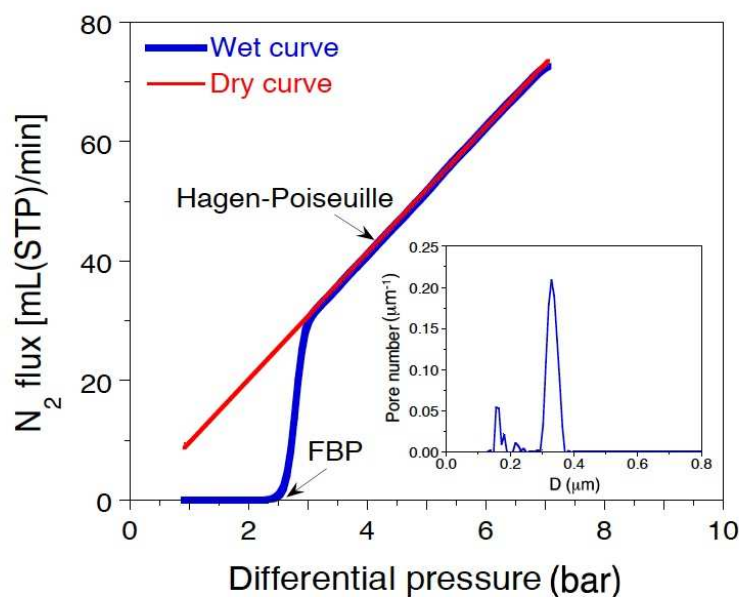


Figure 3.4: Typical curves of  $N_2$  flux versus transsupport differential pressure obtained from gas-liquid displacement and corresponding pore size distribution obtained after data processing according to the set of Eq.3.1 to Eq.3.3.

### 3.2.1.2 Precursor preparation and maturation

In this study, the precursor solution consisted of structure directing agent (SDA, 1 M tetrapropylammonium hydroxide, TPAOH, supplied by Sigma-Aldrich), and the silica source (Aerosil 380 from Degussa). For the synthesis of zeolite, 45 ml of the SDA (TPAOH) 1M (Aldrich) and 6.0 g of the source of silica, Aerosil 380 (Degussa) were mixed and slightly diluted with 5 ml of demineralized/distilled water to form a clear solution of the molar composition 1.0  $SiO_2$ : 0.45 TPAOH: 27.8  $H_2O$  (pH ~ 14). The solution was then stirred on a magnetic stirrer at 500 rpm for 72 hours at room temperature for maturation. To prepare hollow fibre membranes, the quantity of precursor required was calculated on the basis of a previous experiment on membrane tubes, considering the ratios of volume of precursor/porous volume/surface of the membrane (for examples of the calculation, see [215]).

---

### 3.2.1.3 Hydrothermal synthesis of nanocomposite MFI membranes

At the expiration of the 72 hours, the resulting clear solution was centrifuged at 4000 rpm for 30 minutes using a Universal-32 centrifuge (Hettich Zentrifugen). After centrifuging, the support was inserted in a Teflon<sup>R</sup>-lined autoclave (see Fig 3.5) and the clear precursor solution carefully poured on it until the Teflon<sup>TM</sup> was filled up. The Teflon<sup>TM</sup> tube was left for about 10 minutes and then covered with the lid. The unit was placed in a stainless steel autoclave. Some water drops were added into the space between the Teflon<sup>TM</sup> tube and the stainless steel autoclave to avoid a reduction in the solution during the synthesis by condensation. Then the stainless steel autoclave was carefully sealed with 6 nuts and bolts and put into a pre-programmed oven for synthesis according to the temperature programme depicted in Fig. 3.6. During this stage, there was crystallization of zeolite MFI inside the pores of the alumina matrix. Subsequently, the synthesis was subjected to an interruption for 9 hours at ambient temperature, and then increased to 443 K for 72 hours after which the temperature was reduced to ambient temperature. For the preparation of hollow fibre MFI-alumina membrane, nine fibres of 23 cm length each were inserted entirely in a Teflon autoclave containing approximately 25 ml of the solution of precursor in order to maintain the conditions as close as possible to the preparation of the membrane tubes.

At the end of the hydrothermal synthesis, the tube or fibres containing zeolite were recovered. The membrane tubes or fibres then underwent three successive washings with demineralized/distilled water to get rid of the zeolite which crystallized outside the support, until the pH of water is neutral. The sample was then dried at 373 K in a furnace under nitrogen flow for 12 hours to remove water condensed in the mesopores, before measuring their weights. The fibres/ membrane tubes were weighed before and after the synthesis to obtain the mass of zeolite deposited.



Figure 3.5: Pictures of Teflon<sup>R</sup>-lined autoclave used for hydrothermal synthesis: for membrane tubes (left handside), for hollow fibre membranes (right handside) (pictures not to scale).

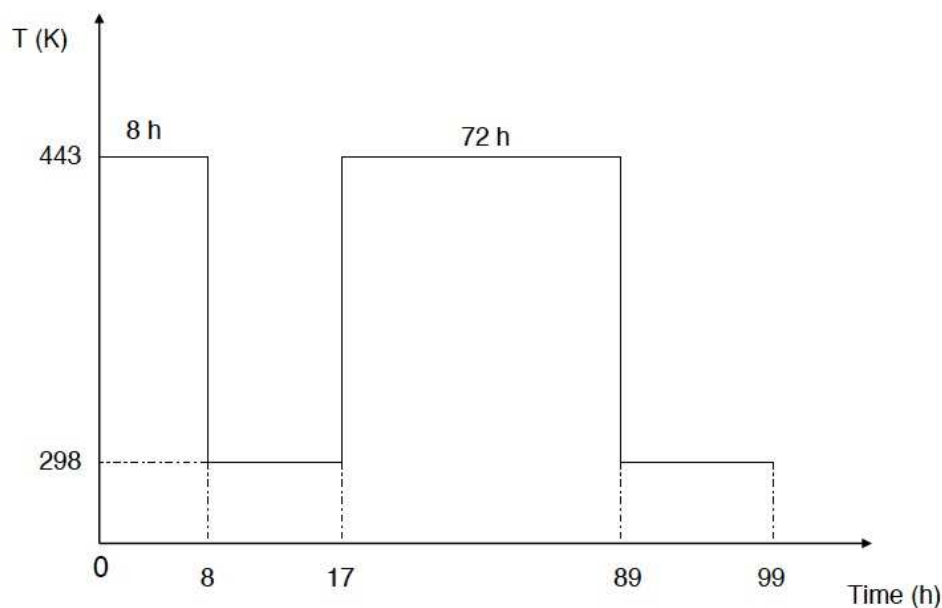


Figure 3.6: Temperature programme for membrane synthesis.

#### 3.2.1.4 Single gas permeation before calcination

After the hydrothermal synthesis, in order to ensure that the precursor penetrated well in all the pores, the single gas permeation with nitrogen gas was conducted and measured. At this juncture, it is expected that the membrane material should not show  $N_2$  gas permeation in as much as the porosity of the support is occupied by the zeolite whose pores themselves are occupied by the molecules of the structuring agent (TPAOH). This test of nitrogen permeation conducted at ambient temperature is an indicator that there are no defects in the membrane. During the test, the pressure difference was fixed at 400 mbar. To indicate that the precursor penetrates well in the pores, the nitrogen flow must be zero or very low  $\leq 0.02$  mL(STP)/min (lower than the limit of detection of the apparatus).

#### 3.2.1.5 Membrane calcination

In order to release/void the porosity of the crystals of zeolite, it is necessary to eliminate the molecules of TPAOH imprisoned in the micropores. This is done by calcination of the membrane. To calcinate the membranes (both hollow fibres and tubes), the membrane was placed in a quartz cell and subjected to calcination under air flow at 773 K for 4 hours based on the procedure of previous studies [191,207-210]. This condition was adopted to

---

avoid any damage to the structure of the support and the zeolitic matter. The temperature profile adopted for the calcination is depicted in Fig. 3.7.

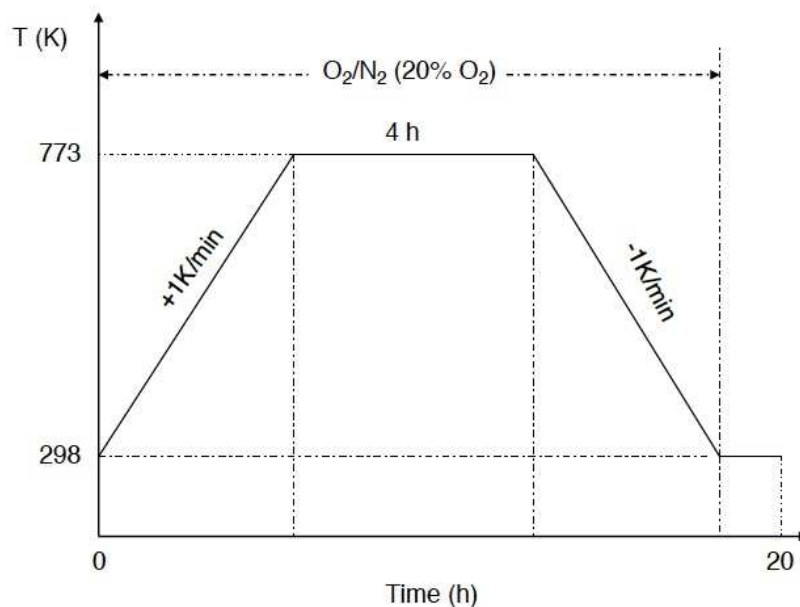


Figure 3.7: Temperature programme for membrane calcination.

### 3.3 Membrane characterization techniques

Several techniques have been used for defect characterization in polycrystalline zeolite membranes. Such techniques include microscopy (e.g. SEM, HRTEM, AFM) [216,217], Mercury porosimetry [218] and permoporometry [219,220]. Concerning permoporometry, it has been shown that dynamic desorption of a gas adsorbed beforehand (e.g., water or n-butane) under pressure difference of a non-adsorbing gas (e.g., hydrogen) provides valuable information of the defective structure of a membrane. Separation properties of a zeolite membrane are determined by the presence of defects, their adsorption characteristics and the gas properties in the mixture [221]. In zeolite membranes, permeating molecules are able to pass through both the intra-crystalline pores (zeolite pores) and inter-crystalline pore (gaps between the zeolite crystals). Some techniques for characterization of porous media have surfaced in literature. Permoporometry technique [222], bubble point technique [223], Coulter porosimetry [224], adsorption-desorption technique [221,225-228], mercury penetration [229,230] have been successfully applied [219,221,223,231]. However,

---

some of these methods are complicated and yield unsatisfactory results for asymmetric ceramics [223].

Meanwhile on adsorption/desorption technique, Pachtova and his co-workers [221] described a simpler technique for characterization of zeolite membrane. This method involves dynamic desorption of a gas adsorbed beforehand on zeolite membrane, under pressure difference of a non-adsorbed gas.

During the adsorption process, zeolite membrane, after high temperature pretreatment to remove moisture, is submitted to a certain partial pressure of an adsorbing gas. At this stage, different types of pores are filled up and thus plugged for all sizes up to a certain diameter called “critical diameter”[221]. With the assumption that zeolite pores are totally plugged by the adsorbing gas (such as n-butane) during adsorption (because the kinetic diameter of n-butane is within the range of intra-crystalline pores of MFI zeolite: 0.51-0.56 nm), the remaining opened pores after the adsorption will be inter-crystalline pores or defects. Therefore, during the desorption process, any defects larger than the critical diameter, which are not plugged easily during adsorption process, allow non-adsorbed gas (such as N<sub>2</sub> or H<sub>2</sub>) to permeate. The permeation significantly increases with time and it could be attributed to desorption of the adsorbed gas from the inter-crystalline pores or channels smaller than the critical diameters into the passageways resulting from the defects. Thus, it is expected that the relative and absolute permeance must be very low with slight increase with time for a higher quality membrane while a poor quality membrane should show a higher relative and absolute permeance with time.

At the same time, single-gas permeance measurements provides rapid and rough assessment of the quality of zeolite membranes towards the determination of the presence of defects [232-234] but this method does not allow direct discrimination of intercrystalline domains. Therefore, the most reliable and straightforward way to do this is by mixture gas separation such as n-butane/hydrogen mixture separation [235]. The low-temperature n-butane/H<sub>2</sub> separation is so sensitive that different laboratories have reported different separation factors on the very same material. This suggests a role of adsorbed species in grain boundaries, either by blocking [236] or promoting permeation [221] of the non-adsorbing species (H<sub>2</sub> in this case).

### **3.3.1 Physico-chemical techniques for characterizing MFI membranes**

Various techniques are used for physicochemical characterization of MFI membranes, such as (i) the adsorption of nitrogen, (ii) diffractometry with X-rays, and (iii) Scanning Electron Microscopy (SEM) coupled with the microanalysis by x-emission.

---

### 3.3.1.1 Adsorption of Nitrogen gas

The complete isotherms of N<sub>2</sub> adsorption-desorption allows the characterization of the porous texture of a material: the specific surface, porous volume and the shape of the pores. The properties of the texture of fibres/membrane tubes crushed before and after the synthesis of zeolite are obtained through complete isotherms of adsorption-desorption of N<sub>2</sub> at 77 K on an entirely automatic equipment, ASAP 2020-Micromeritics. A computer makes it possible to exploit the isotherms to extract the various characteristics texturally from the studied materials (specific surface, total porous volume, microporous volume, distribution of the diameter of pores). This technique makes it possible to study the microporosity and the mesoporosity of the membranes.

### 3.3.1.2 X-ray Diffraction (XRD)

This technique allows the determination of the nature of the crystallized phases by measuring the angles of diffraction of X-rays by the crystalline plane of the solid. These angles of diffraction are related to the characteristics of the crystal lattice ( $d_{hkl}$ = inter-reticular distance from the families of the plane HKL) and to the incidental radiation (*wavelength*  $L$ ) by the law of Bragg:

$$2d_{hkl}\sin \theta = k \lambda \quad (3.4)$$

where “ $d_{hkl}$ ” is the distance between 2 planes of index of Miller HKL in Å;  $\theta$  is the Bragg angle;  $\lambda$  is the wavelength of radiation in Å. In this study, the zeolitic structure of synthesized material was analyzed by using a diffractometer Philips PW 1050/81 (Cu K $\alpha$ .1+2 radiation). The analyses were carried out on the powder obtained before and after the hydrothermal synthesis.

### 3.3.1.3 Scanning Electron Microscopy (SEM) and EDX

Scanning Electron Microscopy makes it possible to observe the morphology of the membranes (thickness, infiltration in the support, defects, homogeneity) and also to have first-hand information about the size and shape of the grains of supported samples (ZSM-5). To examine the morphology of the zeolite crystals in the synthesized zeolitic fibres/ membrane, a small part of the membrane is cut and examined with HITACHI S800 functioning at 10 KV.

### 3.3.1.4 Characterization of the synthesized membranes in this study

In this study, the physical characterization of the synthesised membranes was done using Scanned Electron Microscopy (SEM) and X-ray Diffraction (XRD). For these tests,

---

some crushed membrane supports (tube or fibre), synthesized membranes (tube or fibre) and zeolite powder collected from the bottom of the autoclave were X-ray diffracted with a Philips PW1050/81 diffractometer (Cu  $K\alpha_{1+2}$  radiation) to qualify the structure of the synthesized zeolite material. The morphology of the raw membrane supports (tube or fibre) and membranes was inspected by SEM using a HITACHI S800 microscope operated at 15 kV. A typical result from X-ray diffraction analysis showing the XRD pattern for hollow fibre membranes is presented in Fig. 3.8.

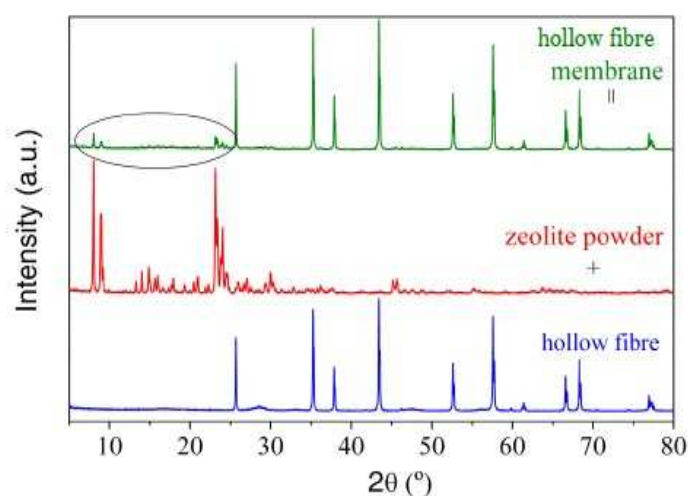


Figure 3.8: XRD image analysis of the membrane fibre showing the formation of the membrane.

To evaluate the transport or dynamic property of the membranes, single gas permeation measurement ( $H_2$  gas permeation), Basic Desorption Quality Test (BDQT) and binary gas mixture separation test (n-butane/ $H_2$ ) were used. Figure 3.9 depicts the process flow diagram of the set-up used for BDQT and n-butane/ $H_2$  mixture separation.

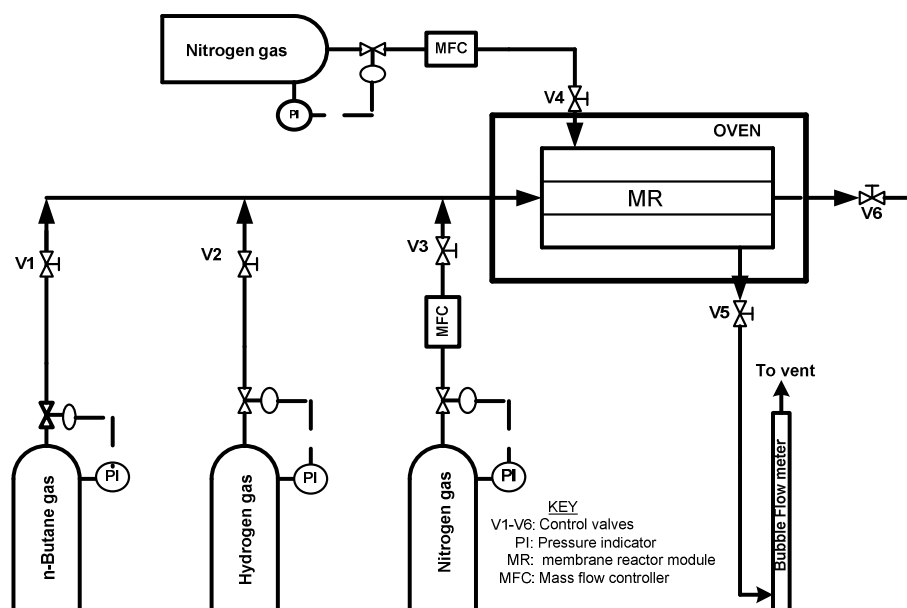


Figure 3.9: Process Flow Diagram (PFD) for BDQT.

Before any gas permeation or separation, firstly, the membrane was mounted into a stainless steel module depicted in Fig. 3.10 and subjected to high temperature pre-treatment (HTP) under the flow of 20 mL(STP)/min- $N_2$  gas, at both the tube side and the shell side as proposed by Ashebani *et al.*[232]. High temperature pre-treatment, carried out according to the temperature programme depicted in Fig.3.13 is necessary to desorb any moisture or contaminants from the membrane as this might affect the transport performance of the membrane. Figure 3.11 and Figure 3.12 also show the diagrams of a typical stainless steel module, the PID controlled electrical oven and the graphite seal used in this study.

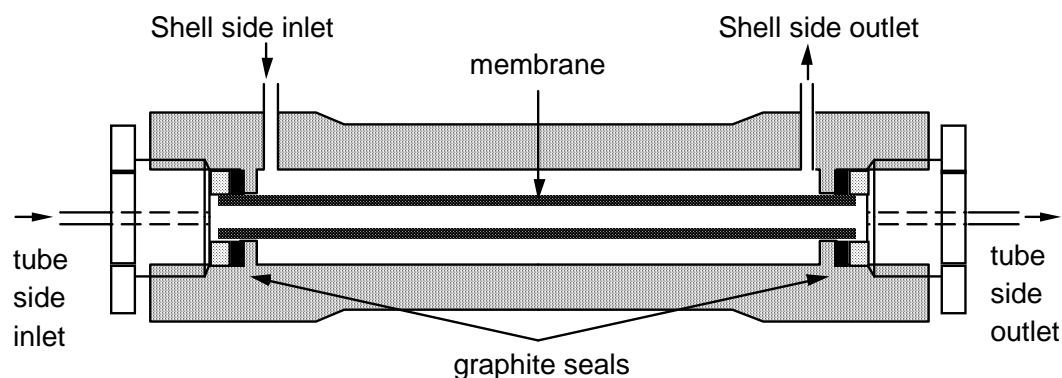


Figure 3.10: Schematic of the permeation test module, showing the nanocomposite MFI-ceramic membrane unit sealed inside the module with graphite seals.



Figure 3.11: Pictures of the stainless steel module showing its components: A&C are O-rings and B is the stainless steel module (picture not to scale).



Figure 3.12: Pictures of the controlled electrical oven (left hand side) and the graphite seals (right hand side) used in this study (picture not to scale).

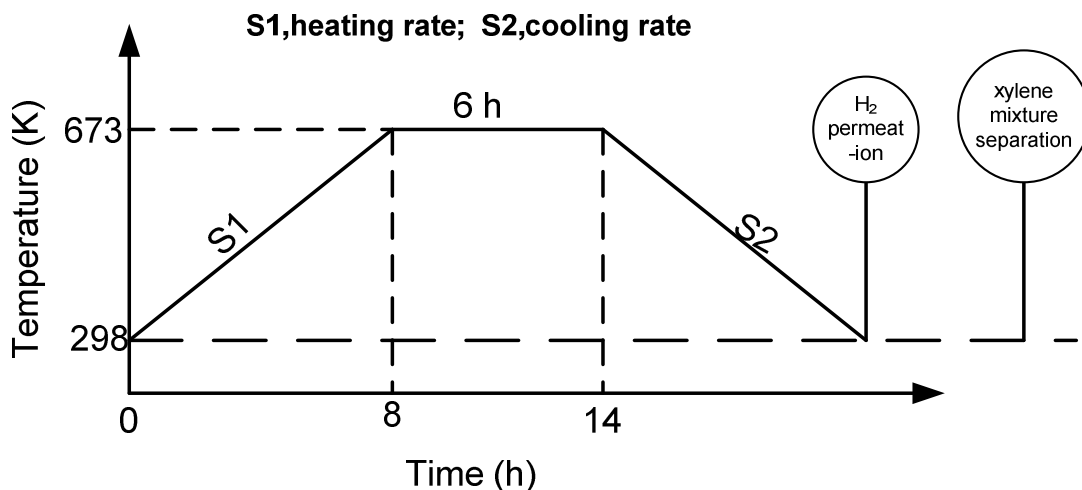


Figure 3.13: Temperature programme used for high temperature pre-treatment of membranes pre-treatment.

### 3.4 Experimental set-up for xylene isomers separation

This research was conducted at two different locations namely the Department of Process Engineering situated at Stellenbosch University, Stellenbosch, South Africa and the Institute of Research on Catalysis and Environment, Lyon (IRCELYON), France. At these locations, two different experimental set-ups were used. Both set-ups consist of a saturation system, PID controlled oven, mass flow controllers (Brooks (5840 series) or Hastings (HFM/HFC 200 series))/flow meters, and a GC equipped with FID. All these major units are linked with 0.25 inch stainless piping. Process Flow Diagrams (PFDs) for these set-ups are shown in Fig. 3.14 and Fig. 3.15 and their pictures and operational procedures are presented in Appendix D. The lines were heated with heating tapes to a desired temperature and maintained at this temperature (393 K in this study) to avoid vapour condensation and thus ensure proper xylene vapour during experimentation/test. The GC coupled with the set-up made online analysis of the feed, retentate and permeate streams possible because samples can be sent directly to the GC online without any interruption.

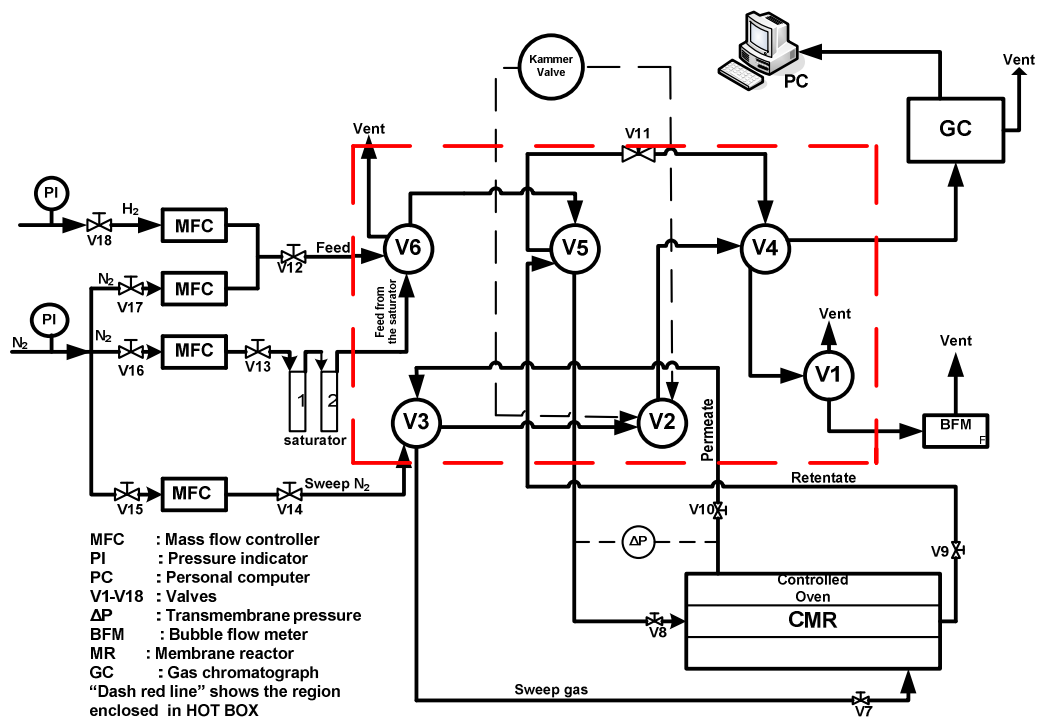


Figure 3.14: Process Flow Diagram (PFD) of the modified set-up used for separation and isomerization tests at IRCELYON.

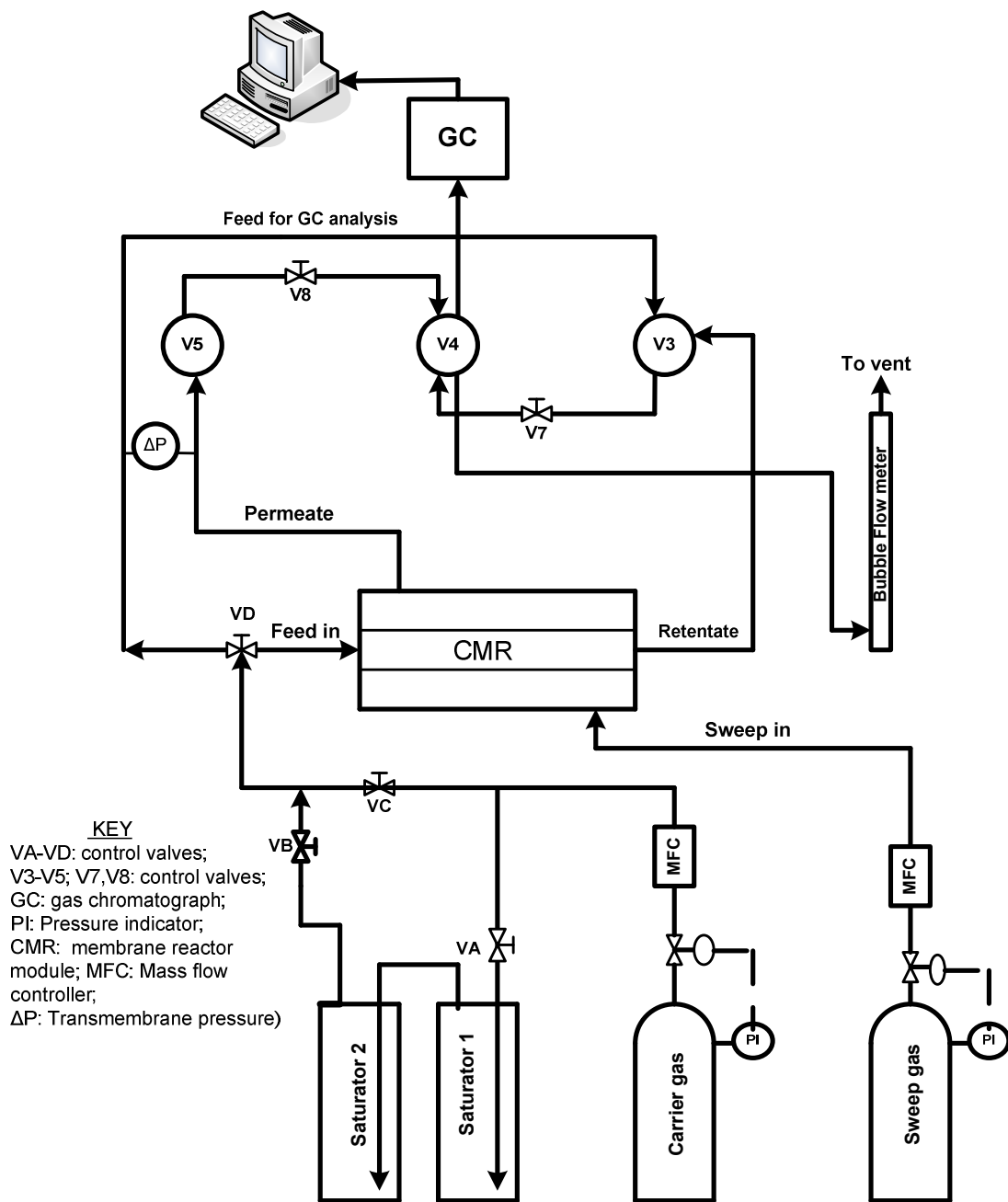


Figure 3.15: Process Flow Diagrams (PFD) of the modified set-up used for separation and isomerization tests at the Department of Process Engineering, Stellenbosch University.

---

The mass flow controllers/flow meters used in this study were pre-calibrated Brooks meters and Hastings meters. For accuracy of flow measurements, the mass flow controllers were re-calibrated for N<sub>2</sub> gas (used as carrier and sweep gas), and H<sub>2</sub> gas (used as feed gas and during activation of the catalyst). The calibration was carried out with the use of gas flow meters (ADM1000 and soap bubble flow meter). A description of the calibration technique is presented in Appendix B.

Two types of Gas Chromatograph (GC) were used in this research. The first was *Shimadzu GC-14A* (Fig. 3.16) and the second, a *Varian 3400* (Fig. 3.17). Both GCs were equipped with *Solgel Wax* capillary column and Flame Ionization Detection (FID) that ensure organic vapour detection and separation (see Table 3.1. for the characteristics of the column and Table 3.2. for the GC operating conditions). Before any analysis with the GCs, the GCs were calibrated using a multiple point external standard method. Detailed information on GC calibration can be found in Appendix B.



Figure 3.16: Pictures of the *Shimadzu GC-14A* used in this study.



Figure 3.17: Picture of the *Varian 3400* used in this study.

Table 3.1: Column characteristics

Column feature	Value
Code	SOLGEL WAX 054785
Film thickness ( $\mu\text{m}$ )	1
Internal diameter (ID) (mm)	0.53
Cross-sectional area ( $\text{cm}^2$ )	$2.21 \times 10^{-3}$
Length (m)	30

Table 3.2: Operating condition for GC analysis

Operating condition	FID
Carrier gas	Helium
Carrier gas pressure ( kPa )	24
Oven temperature (K)	343
Analytes	o-,m- and p-Xylene liquid
Temperature of the FID (K)	553
Carrier gas flow rate into the column ( ml/min)	3
Flow into the splitter ( ml/min)	60
Split ratio	1:20
Injector Temperature (K)	523

The saturation system consists of two saturation units combined in series (see Fig. 3.18). The saturation system was equipped with a controlled heating system (at SU, a waterbath was used) to raise the temperature of the liquid in the saturation system to the desired temperature. After coupling the system to the separation/isomerization testing bench, the saturation efficiency of the system was evaluated. The detailed procedure employed in the evaluation of the saturation efficiency is described in Appendix A. After evaluating the saturation system, the GCs were calibrated. Detailed procedure employed in the GC calibration is described in Appendix B.

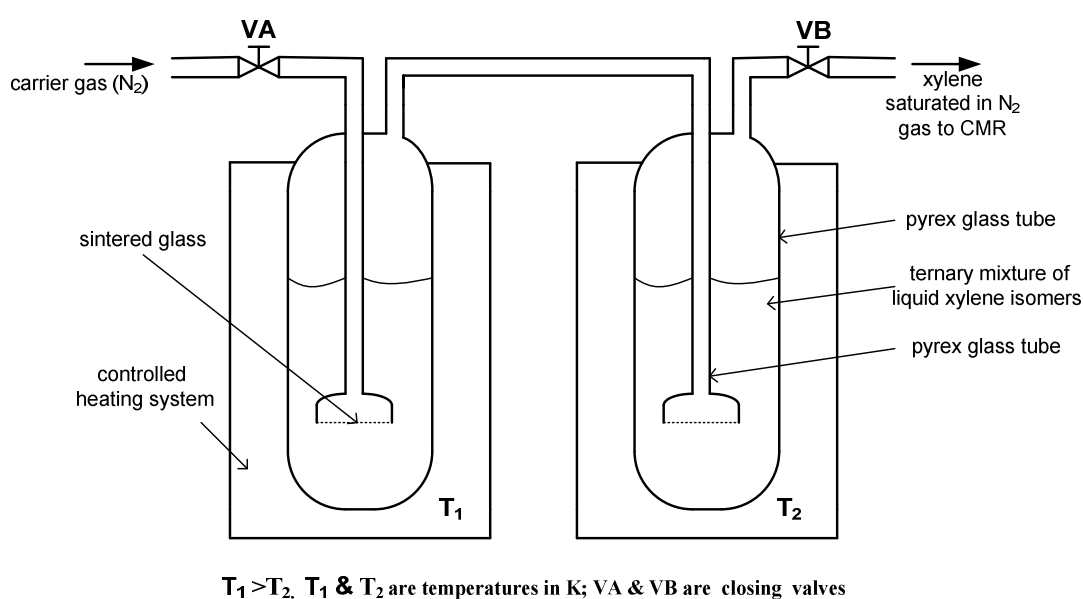


Figure 3.18: Schematic of the saturation system for xylene vapour saturation in  $N_2$  gas.

### 3.5 Result analysis and evaluation of membrane performance

Evaluation of membrane separation performance is usually based on (i) the flux or the permeance of the species through the membrane; (ii) membrane separation factor and (iii) membrane ideal selectivity.

---

### 3.5.1 Membrane flux and permeance

In this study, the permeance was obtained using the following equations:

$$\Pi_i = \frac{N_i}{A \cdot \Delta P_i} \quad [\text{mol} \cdot \text{m}^{-2} \cdot \text{s}^{-1} \cdot \text{Pa}^{-1}] \quad (3.5)$$

where

$$N_i = \frac{y_i \cdot Q_{STP}}{22400} \quad [\text{mol} \cdot \text{s}^{-1}] \quad (3.6)$$

$$Q_{STP} = Q_{measured} \left( \frac{273}{T_{bubbleflowmeter}} \right) \quad [\text{ml} \cdot \text{s}^{-1}] \quad (3.7)$$

$$y_i = \frac{P_i}{P_T} \quad [-] \quad (3.8)$$

$$P_T = \sum P_i + P_{N_2} \quad [\text{Pa}] \quad (3.9)$$

The change in partial pressure was estimated using the log mean partial pressure difference (analogous to the estimation of temperature difference (the driving force) in shell and tube heat exchanger) as shown by Eq. 3.10:

$$\Delta P_i = LMPD_i = \frac{\Delta P_i^1 - \Delta P_i^2}{\ln \left( \frac{\Delta P_i^1}{\Delta P_i^2} \right)} \quad [\text{Pa}] \quad (3.10)$$

Where;

$$\Delta P_i^1 = P_{i,in}^{feed} - P_{i,out}^{permeate} \quad (3.11)$$

$$\Delta P_i^2 = P_{i,out}^{retentate} - P_{i,in}^{sweep} \quad (3.12)$$

Since the sweep contains no xylene,  $P_{i,in}^{sweep} = 0$ . Therefore:

---


$$\Delta P_i^2 = P_{i,out}^{retentate} \quad (3.13)$$

### 3.5.2 Membrane separation factor (SF)

In this study, membrane separation factor (SF) is defined as the enrichment factor of one component to another in the permeate, as compared to the feed composition ratio:

$$Sf_{i/j} = \frac{\left( \frac{y_i}{y_j} \right)_{permeate}}{\left( \frac{y_i}{y_j} \right)_{feed}} \quad [-] \quad (3.14)$$

where  $y$  is the mole fraction and in this case,  $i$  = p-Xylene;  $j$  = m-Xylene or o-Xylene

### 3.5.3 Membrane ideal selectivity

Membrane ideal selectivity was defined as the ratio of the permeance of one component to another. Thus, the selectivity is:

$$\Pi_{i/j} = \frac{\Pi_i}{\Pi_j} \quad [-] \quad (3.15)$$

In this study,  $i$  is p-Xylene and  $j$  refers to m-Xylene and o-Xylene as the case may be.

### 3.6 Concluding remark

In this chapter, a short overview of the techniques employed in the synthesis and characterization of MFI-type zeolite membranes is presented. Also, procedures for the series of experiments conducted in this study are described. However; some of the experimental procedures that are not described in detailed here are discussed in subsequent chapters, where necessary. In subsequent chapters, results obtained from the experimental protocols described in this chapter are displayed and discussed.

---

## Chapter 4: Tubular MFI-alumina membranes for xylene isomer separation

In this chapter, results of the study of the influence of operating variables on the separation performance of a nanocomposite MFI-alumina membrane tube during the separation of ternary vapour mixture of xylene isomers are presented. Specifically, we shall focus on the evaluation of the behaviour of the membrane at higher loadings of xylene/higher partial pressures of xylene.

### 4.1 Introduction

The relevance of p-Xylene as intermediate in the synthesis of polymers necessitates the development of processes for its separation and purification. Because of their similar physical properties, xylene isomers can hardly be separated by distillation [3,237,238]. Currently, industry relies on fractional crystallization and preferential adsorption to separate xylene isomer mixtures. Both techniques are batch processes and energy-intensive, therefore inflating the production costs and their environmental impact. For example, the United States consumed nearly  $105 \times 10^{18}$  J in 2004, corresponding approximately to one fourth of the world's energy [8]. Petrochemical and chemical industries accounted for  $13.7 \times 10^{18}$  J in 1998 with about 35% of the energy consumption being used in manufacturing and separating organic chemicals (mainly for heating/cooling) [7]. It seems therefore imperative to move to more energy-efficient and environmentally-friendly processes involving less heating/cooling steps (and operating in continuous mode) for p-Xylene separation.

Membrane technology constitutes a promising option to achieve this goal. As the driving force in a gas-separation membrane is the pressure difference between the feed/retentate and permeate, the heating/cooling costs can be dramatically reduced compared to more conventional separation processes (e.g., distillation, crystallization or adsorption). Furthermore, the combination of membrane separation with (reactive) distillation in hybrid separation processes (for instance for distillate/residue separation) can also help to reduce cooling/heating costs and promote process intensification (see references [239,240]).

For the fact that polymeric membranes (e.g., PVA) have not proven to be successful for xylene isomer separation, researchers have moved to zeolites and other molecular sieve membranes. Several recent studies have pointed out the potential of MFI zeolite membranes for xylene separation and purification, either by pervaporation (PV) [168] or by vapour permeation (VP) [171,175,177,178,180,181,183,184,241]. As the kinetic diameter of p-Xylene ( $5.8 \text{ \AA}$ ) is smaller than that of o- and m-Xylene ( $6.8 \text{ \AA}$  each) and close to the pore size of the MFI channels ( $5.4 \times 5.6 \text{ \AA}$  and  $5.1 \times 5.6 \text{ \AA}$ ) [78], p-Xylene is expected to diffuse faster within the MFI framework therefore allowing its separation from a mixture of isomers.

---

Moreover, the lower size and ordered packing of p-Xylene promotes its adsorption in MFI channels, mainly driven by configurational entropy effects [144].

It has been established that the MFI framework can experience distortions induced by p-Xylene adsorption [81,104,106,115]. These distortions translate into phase changes, especially pronounced at near-ambient temperature and high p-Xylene loadings, leading to channel 'swelling' that renders the material unable to distinguish between the different xylene isomers. As a result, single-file diffusion may occur in the zeolite channels. This implies that xylene isomers with the slowest permeation rate (i.e. o- and m-Xylenes) might limit diffusion, blocking p-Xylene separation and reducing therefore membrane selectivity. This strong limitation of MFI materials hinders the application of MFI membranes for xylene separation at high loadings, for instance in PV separations.

Nevertheless, at sufficiently low xylene partial pressures (<2 kPa) and in the temperature range 295-673 K, MFI membranes can show optimal selectivity for p-Xylene separation by VP. By now, the best separation and permeation results have been obtained by Lai *et al.* [172] using 'microstructurally optimized' b-oriented MFI films prepared by secondary growth hydrothermal synthesis using a b-oriented seed layer and trimer-TPA as a template in the secondary growth step. The membranes offer p-Xylene permeances of about 200 nmol.m<sup>-2</sup>.s<sup>-1</sup>.Pa<sup>-1</sup> at 473 K for a feed mixture of 0.45 and 0.35 kPa p- and o-Xylene, respectively, with p/o-Xylene separation factors between 200-500.

Meanwhile first preliminary results reported on application of MFI-alumina zeolite membranes with nanocomposite architecture for xylene isomer separation via PV [186] showed very encouraging xylene isomer vapour separation properties. P-Xylene permeances of about 10 nmol.m<sup>-2</sup>.s<sup>-1</sup>.Pa<sup>-1</sup> with p/o and p/m of 7 and 21, respectively, have been reported at 473 K [186]. Compared to most commonly used film-like MFI membranes (either with preferential or random channel orientation), the membranes prepared here consist of randomly oriented MFI crystal nanocomposite grown inside an alumina porous matrix via a pore-plugging hydrothermal synthesis technique.

Therefore, this section reports additional mixture permeation data on xylene isomer separation using nanocomposite MFI-alumina tubular membranes, focusing specifically on the effect of the main operational variables (temperature, xylene vapour pressure and sweep gas flow rate). The goal was to show that, by confining the zeolite material, a nanocomposite MFI-alumina membrane can show high selectivity to p-Xylene at high xylene loadings compared to more conventional film-like MFI membranes.

## 4.2 Membrane preparation, characterization and separation test

The nanocomposite MFI-alumina membrane used in this study was prepared by pore-plugging hydrothermal synthesis technique using an asymmetrical Pall-Exekia

---

$\alpha$ -alumina tube (o.d. 10 mm, i.d. 7 mm, length 15 cm, active permeation area 26 cm<sup>2</sup>) as support. Details of this technique have been described in Chapter 3. The cross-sectional layers of the support have pore dimensions: outer layer, 12  $\mu$ m; intermediate layer, 0.8  $\mu$ m and innermost layer, 0.2  $\mu$ m. Characterization as well as the quality test of the membranes was by scanning electron microscopy with SEM (JSM-5800LV, 20 kV) coupled with EDX analysis (Edax Phoenix, 1- $\mu$ m microprobe); single gas hydrogen permeation, binary mixture separation with *n*-butane/H<sub>2</sub> and BDQT. These techniques have been described in detail in Chapter 3 of this dissertation.

Before the membrane quality test, the membrane was mounted on the membrane module and subjected to HTP at 673 K under a 20 mL(STP)/min N<sub>2</sub> flow on the retentate and permeate sides as described in Chapter 3 to remove adsorbed moisture and other contaminants. This pre-treatment was also carried out before each series of xylene VP tests.

The set-up used for membrane separation has been described in Chapter 3. Ternary mixture of xylene (p-Xylene, 99% purity; m-Xylene, 99% purity; o-Xylene, 97% purity) purchased from Sigma-Aldrich were saturated in dry N<sub>2</sub> at a 10-mL(STP)/min carrier flow at atmospheric pressure using two saturators combined in series. The first bubbler was kept at 323 K-363 K (depending on the desired xylene partial pressure) while the second bubbler was maintained at a temperature of about 6 K lower than the first to ensure saturation.

The permeate side of the membrane was swept using N<sub>2</sub> at several flow rates in the range 5-30 mL(STP)/min to investigate the influence of sweep gas flow rate. After attaining steady-state in about 5 hours, the compositions of the feed, retentate and permeate streams were analyzed online GC (*Shimadzu GC-14A*) equipped with a solgel-WAX capillary column and a flame ionization detector (FID). To avoid any condensation and ensure proper xylene partial pressure throughout the system, all the lines were heated and maintained at 393 K using heating tapes. Xylene vapour separation and permeation experiments were performed in Wicke-Kallenbach mode to prevent occurrence of viscous flow. In all the experiments, mass balances of each xylene isomer were closed with an experimental error <15%.

The membrane performance was evaluated in terms of permeation flux (or xylene permeance), p/o and p/m xylene permselectivity (or ideal selectivity), and p/o and p/m mixture separation factor following Eq. 3.5 to Eq. 3.15 presented in Chapter 3.

### **4.3 Results and discussion**

The results obtained in this section are presented, discussed and compared with existing literature in subsections 4.3.1 and 4.3.2.

---

### 4.3.1 Membrane quality

The membrane prepared in this study showed a room-temperature pure hydrogen permeance of  $0.49 \mu\text{mol}\cdot\text{m}^{-2}\cdot\text{s}^{-1}\cdot\text{Pa}^{-1}$  and a *n*-butane/ $\text{H}_2$  separation factor as high as 100 after pre-treatment. This latter value reflects good membrane quality in terms of low amount of intercrystalline defects. The good quality of the membrane prepared in this study can also be inferred from the extremely slow *n*-butane desorption dynamics under the presence of a transmembrane pressure of pure hydrogen at room temperature (see Fig. 4.1). The desorption dynamics is especially slow in the first 4 hours, the membrane taking about 29 hours to recover at least 90% of its original pure hydrogen permeance. As a matter of fact, in a standard desorption test, *n*-butane is expected to desorb faster from intercrystalline domains than from zeolite pores (intracrystalline), where adsorption forces are expected to be stronger. A slow desorption dynamics, especially at short times, is therefore an indicator of a low number of intercrystalline domains.

Furthermore, the SEM micrographs (see Fig. 4.2 and Fig. 4.3) confirm the formation of a nanocomposite material on the substrate, that is, no continuous MFI film is formed on top of the support. In addition, Fig. 4.2 shows the cross-section of the membrane support with the three layers while Fig. 4.3 shows good pore-plugging of the  $0.2\text{-}\mu\text{m}$  layer with zeolite crystals. The EDX analysis shows an average Si/Al ratio about 10-20 (semi-quantitative analysis) on the inner active layer. The material in the active layer corresponds accordingly to an Al-enriched H-ZSM-5 zeolite.

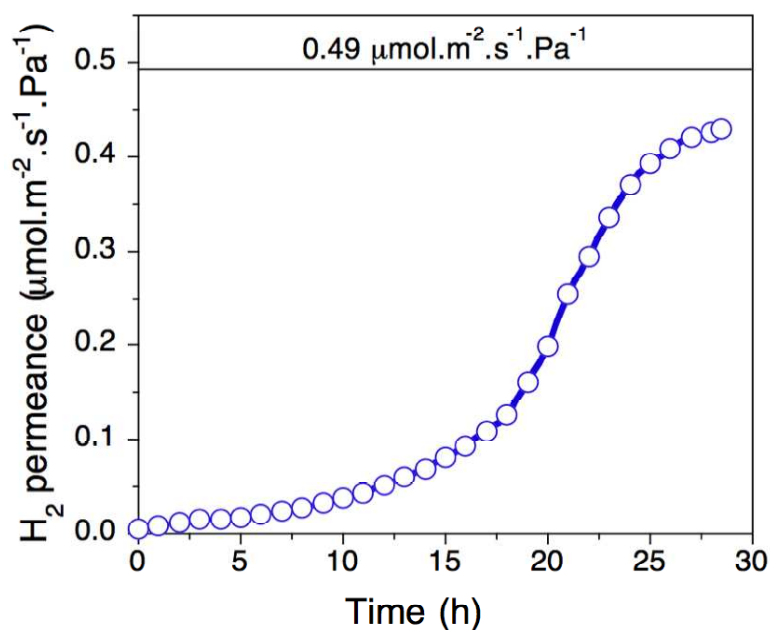


Figure 4.1: Hydrogen permeance as a function of time in a *n*-butane room-temperature desorption experiment. Adapted from [242].

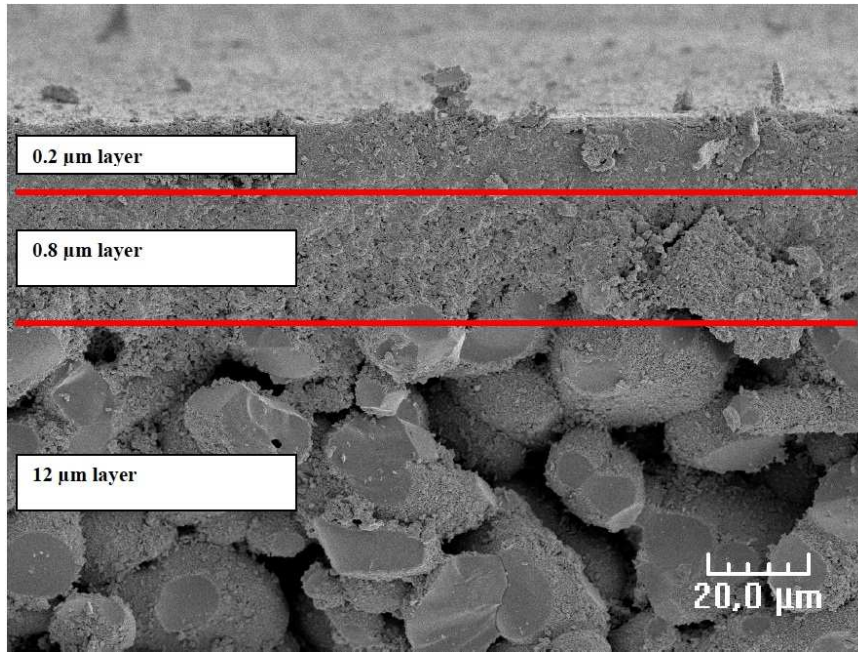


Figure 4.2: SEM micrograph of the membrane showing cross-section of the membrane support with the three layers with formation of nanocomposite material on the support.

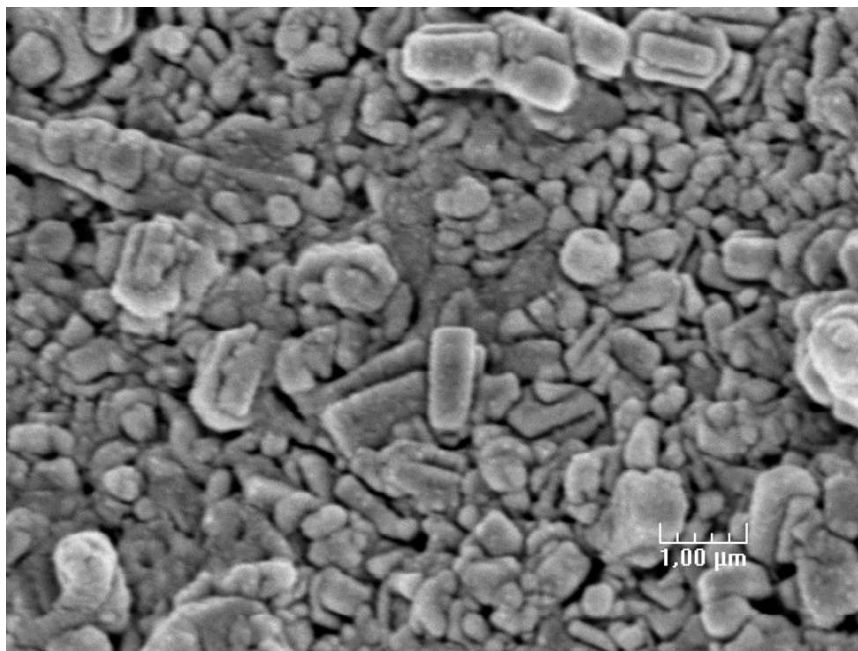


Figure 4.3: SEM micrograph of the membrane showing surface view of the 0.2 μm-layer pore-plugged with zeolite crystals.

---

### 4.3.2 Xylene vapour permeation

The results obtained are presented in the subsequent sub-sections 4.3.2.1 through 4.3.2.3. Parameter fitting was also attempted based on the Maxwell-Stefan (MS) adsorption-diffusion model. The temperature-dependence of the transmembrane p-Xylene flux has been well represented by a pure gas Maxwell-Stefan (MS) adsorption-diffusion model under weak confinement (the MS surface diffusivity does not depend on the xylene loading) neglecting the influence of the other xylene isomers as shown in Eq. 4.1:

$$N = \frac{c_{sat} \rho_{MFI} \varepsilon D_o(T)}{\tau \ell} \ln \left[ \frac{1 + K(T) \frac{P_R}{P^O}}{1 + K(T) \frac{P_P}{P^O}} \right] \quad (4.1)$$

where  $P_R$  and  $P_P$ , are the p-Xylene partial pressure in the retentate and permeate, respectively;  $\rho_{MFI}$ , the MFI density ( $\text{kg.m}^{-3}$ );  $\varepsilon$ , the porosity of the nanocomposite MFI / alumina structure [-];  $c_{sat}$ , the p-Xylene loading at saturation ( $\text{mol.kg}^{-1}$ );  $\tau$ , the membrane tortuosity;  $P^O$ , the reference atmospheric pressure (Pa);  $N$  is the flux in  $\text{mol.m}^{-2}.\text{s}^{-1}$  and  $\ell$ , the membrane effective thickness (m).

In the fitting process, zero-loading MS surface diffusivity at  $T_{ref}$   $\{D_o(T_{ref})\}$  and the diffusion activation energy ( $E_D$ ) were expressed by an Arrhenius-type equation using, respectively, Eq. 4.2 and Eq. 4.3:

$$K(T) = K(T_{ref}) \left[ -\frac{\Delta H_{ads}^O}{R} \left( \frac{1}{T} - \frac{1}{T_{ref}} \right) \right] \quad (4.2)$$

$$D_o(T) = D_o(T_{ref}) \left[ -\frac{E_D}{R} \left( \frac{1}{T} - \frac{1}{T_{ref}} \right) \right] \quad (4.3)$$

where  $K(T)$ ,  $K(T_{ref})$ , the adsorption constant of p-Xylene on MFI at  $T$  and  $T_{ref}$ , respectively ( $\text{Pa}^{-1}$ );  $\Delta H_{ads}^O$ , the standard adsorption enthalpy ( $\text{J.mol}^{-1}$ );  $E_D$ , the diffusion

activation energy;  $\{D_O(T_{ref})\}$ , the zero-loading MS surface diffusivity at  $T_{ref}$ ;  $R$ , the ideal gas constant ( $\text{J}\cdot\text{mol}^{-1}\cdot\text{K}^{-1}$ ) and  $T$  and  $T_{ref}$ , the main temperature and the mean temperature of the series, respectively, in this case,  $T_{ref} = 473 \text{ K}$ .

A Least-square non-linear optimization method, based on the Levenberg-Marquardt algorithm, was used to fit the zero-loading MS surface diffusivity at  $T_{ref}$  ( $D_O(T_{ref})$ ) and the diffusion activation energy ( $E_D$ ) by comparing the predicted and experimental p-Xylene fluxes. The parameters used in the fitting are presented in Table 4.1.

Table 4.1: Constant values used for parameter estimation

Property	value	Refs.
Ideal gas constant ( $\text{J}\cdot\text{mol}^{-1}\cdot\text{K}^{-1}$ )	8.314	-
MFI density ( $\text{kg}\cdot\text{m}^{-3}$ )	1700	-
Porosity of the nanocomposite MFI / alumina structure [-]	0.13	-
P-Xylene loading at saturation ( $\text{mol}\cdot\text{kg}^{-1}$ )	0.25	[95]
MS surface diffusivity at zero coverage at $T_{ref}$ ( $\text{m}^2\cdot\text{s}^{-1}$ ) at 473 K	$3.4 \times 10^{-13}$	[207]
Tortuosity	1.2	-
Reference to atmospheric pressure(Pa)	101325	-
Adsorption constant of p-Xylene on MFI at $T_{ref}$ ( $\text{Pa}^{-1}$ ) at 473 K	$4.1 \times 10^{-4}$	[235]
Standard adsorption enthalpy ( $\text{J}\cdot\text{mol}^{-1}$ )	-72000	[95,128]

\*value obtained with loading correction;  $\ell$ : effective MFI thickness (m, fitted parameter);  $E_D$ : diffusion activation energy ( $\text{J}\cdot\text{mol}^{-1}$ , fitted parameter).

### 5.3.2.1 Effect of Temperature

Figure 4.4 plots the evolution of the p-Xylene, m-Xylene and o-Xylene fluxes and p-Xylene to o-Xylene (p/o) and p-Xylene to m-Xylene (p/m) separation factors as a function of temperature in the range 373 K-700 K for the membrane prepared in this study. Since m-Xylene and o-Xylene signals in the permeate stream were below the detection limit of our GC, the p/o and p/m separation factors were computed from the minimum detectable o- and m-Xylene partial pressures in the permeate ( $10^{-3}$  kPa for m-Xylene and  $10^{-4}$  kPa for o-Xylene).

The p-Xylene transmembrane flux shows a maximum value of about  $3.5 \mu\text{mol}\cdot\text{m}^{-2}\cdot\text{s}^{-1}$  at 473 K, corresponding to a permeance of about  $11 \text{ nmol}\cdot\text{m}^{-2}\cdot\text{s}^{-1}\cdot\text{Pa}^{-1}$ . As expected for a nanocomposite material [208], the p-Xylene flux decreases monotonically after the maximum with no further increase at temperatures higher than 700 K.

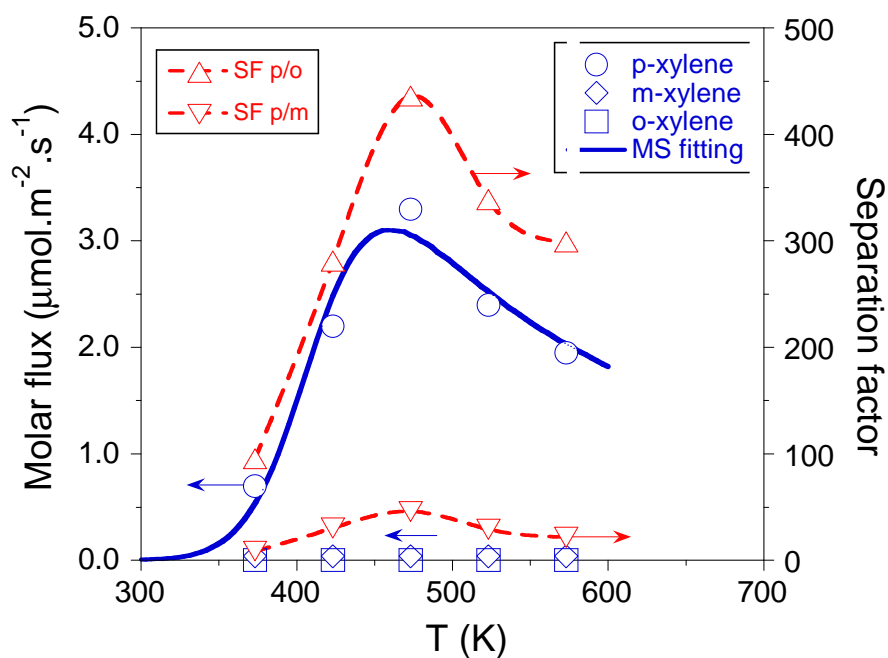


Figure 4.4: Xylene ternary vapour mixture separation as a function of temperature within a nanocomposite MFI-alumina membrane. Experimental conditions: p-/m-/o-Xylene feed partial pressures, 0.63 kPa / 0.27 kPa / 0.32 kPa; sweep gas flow rate, 15 mL(STP)/min; feed flow rate, 10 mL(STP)/min. The straight line corresponds to the MS fittings for p-Xylene flux, while the dashed lines for separation factors are a guide to the eye. Adapted from [242].

Regarding the MS fitting, the values obtained for the fitted MFI effective thickness and activation energy for p-Xylene diffusion are, respectively,  $\ell = 0.83 \pm 0.04 \mu\text{m}$  and  $E_D = 60 \pm 2 \text{ kJ}\cdot\text{mol}^{-1}$ . The latter value compares well with the value of about  $55 \text{ kJ}\cdot\text{mol}^{-1}$  measured by Masuda *et al.* [155] on H-ZSM-5 powders using the constant volume method, but is significantly higher than the value of about  $30 \text{ kJ}\cdot\text{mol}^{-1}$  measured by Ruthven *et al.* [152] and Niessen *et al.* [135] on large silicalite-1 single crystals.

The good prediction level of the MS model for the range of xylene total pressures considered here suggests that, as put forward by several authors [95,106], no relevant structural change of the MFI framework occurs upon p-Xylene adsorption at temperatures higher than 373 K (the 'critical' temperature). Moreover, as suggested by Grahn *et al.*[129] in a recent paper, the typical p-Xylene adsorption pattern can be altered due to size effects when tuning from microsized to nanosized particles, the isotherm not showing the typical 2 steps (S-form) at low temperatures. The presence of MFI crystals of size  $<200 \text{ nm}$  in a nanocomposite MFI-alumina membrane (the size of the support top layer), together with their strong confinement in the porous alumina network, might compensate the distortion of the MFI framework upon p-Xylene adsorption, avoiding the phase change traditionally observed for MFI powder at temperatures  $<400 \text{ K}$ .

### 4.3.2.2 Effect of sweep gas flow rate

Figure 4.5 plots the effect of the sweep gas flow rate on the membrane permeation and separation performance in the separation of ternary p/m/o-Xylene mixtures. As expected, the p-Xylene flux increases with the  $N_2$  flow rate up to a plateau value beyond 20 mL(STP)/min. The trend should be ascribed to a reduction of the p-Xylene permeate partial pressure as the sweep gas flow rate increases. This might contribute to a decrease of the p-Xylene surface coverage at the membrane/permeate surface and in its turn to an increase of the p-Xylene driving force across the membrane. This trend is qualitatively predicted by the MS model (Eq. 4.1) using the parameters obtained from the fittings of p-Xylene flux with the temperature (Fig.4.4). The p/m and p/o separation factors show an increase with the sweep gas flow rate, reaching a value as high as 1000 (practically infinite) at 473 K for sweep gas flow rates higher than 30 mL(STP)/min.

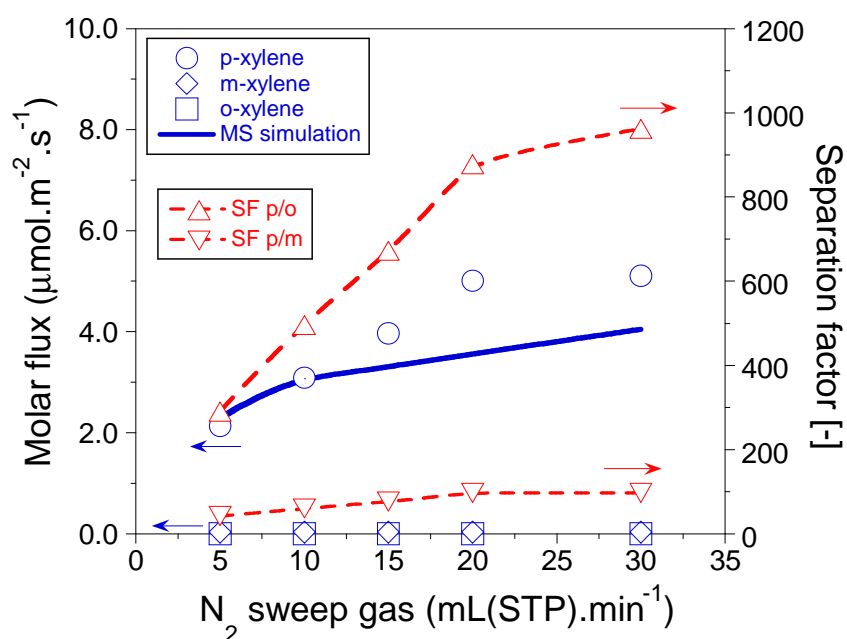


Figure 4.5: Xylene ternary vapour mixture separation as a function of  $N_2$  sweep gas flow rate within a nanocomposite MFI-alumina membrane. Experimental conditions: p-/m-/o-Xylene feed partial pressures, 0.59 kPa / 0.45 kPa / 0.40 kPa; temperature, 473 K; feed flow rate, 10 mL(STP)/min. The straight line corresponds to the p-Xylene flux predicted by Eq. 4.1, while the dashed lines for separation factors are a guide to the eye. Adapted from [242].

### 4.3.2.3 Effect of xylene feed partial pressure

Figure 4.6 shows the effect of the total xylene vapour pressure on the p/m/o xylene molar fluxes and the p/o and p/m separation factors at 473 K (the temperature corresponding to the maximum flux). As can be seen for an increase in total xylene pressure up to 150 kPa, the p-Xylene flux increases steadily with the total xylene vapour pressure for p/m/o-Xylene ternary mixtures up to 15 kPa and p-Xylene-to-m-Xylene-to-o-Xylene (p/m/o) ratios of 1 : 1 : 3 beyond 30 kPa. However, the permeance decreases steadily from 11 to  $1 \mu\text{mol}\cdot\text{m}^{-2}\cdot\text{s}^{-1}\cdot\text{Pa}^{-1}$ . The p/m separation factor remains practically invariable at a value of 200 with the xylene vapour pressure up to 150 kPa. In the case of the p-Xylene/o-Xylene (p/o) separation factor, after showing a maximum value of about 5000 at 30-kPa xylene vapour pressure, it drops drastically to a value lower than 100 at 130 kPa.

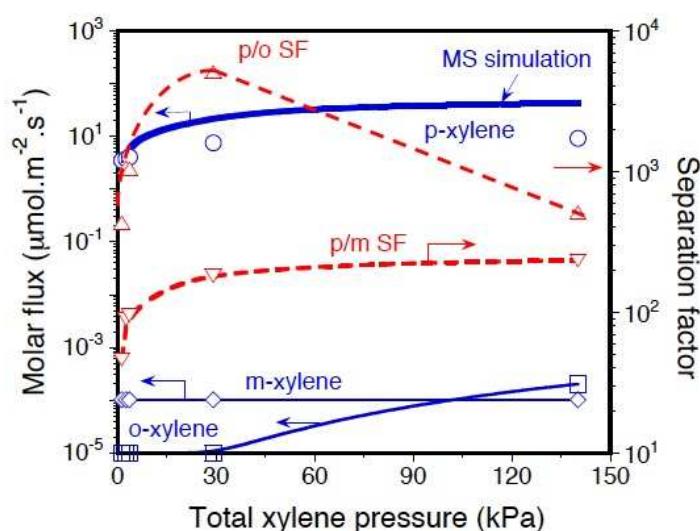


Figure 4.6: Xylene ternary vapour mixture separation as a function of total xylene vapour pressure within a nanocomposite MFI-alumina membrane. Experimental conditions: p-/m-/o-Xylene feed composition, 1 : 1 : 1 up to 15 kPa and 1 : 1 : 3 beyond 30 kPa; temperature, 473 K; feed flow rate, 10 mL(STP)/min, sweep flow rate, 15 mL(STP)/min. The ratios 1:1:1 & 1:1:3 refer to the composition ratio of the xylene isomer in the feed (p-Xylene:m-Xylene:o-Xylene) The straight and dashed lines, respectively, for xylene fluxes and separation factors are a guide to the eye.

The trend observed for the p-Xylene flux should be attributed to the higher surface coverage of p-Xylene and the retentate/membrane surface, enhancing therefore the p-Xylene driving force across the membrane as predicted by the MS model (Eq. 4.1). At lower xylene partial pressures, keeping the xylene isomers at equimolar composition, selective adsorption of p-Xylene on MFI blocks adsorption of other xylene isomers, thereby paving the way for

---

them to permeate. At higher xylene vapour pressure, however, o-Xylene adsorption becomes promoted, showing a slight permeation and contributing therefore to the observed decrease of the p/o xylene separation factor.

This result seems to indicate that, at high xylene coverage, distortion of the MFI framework occurs, higher xylene isomers being transported through the MFI layer. At this juncture, taking into account the similar adsorption properties of the three xylene isomers on MFI zeolites, single-file diffusion can become promoted, the three isomers competing then for passage through the zeolite pores. As a result, the slower permeating isomers (i.e. m-Xylene and o-Xylene) can reduce the permeance of the fastest one (p-Xylene), the membrane selectivity being therefore drastically reduced. Moreover, as put forward by O'Brien-Abraham *et al.* [170], sorbate-sorbate competition for passage within the MFI pores in xylene mixture vapour permeation might also reduce the accessibility of p-Xylene to MFI channels, hindering therefore its permeation.

#### **4.4 Role of MFI confinement on the xylene vapour permeation performance**

Unlike film-like membranes, where the membrane selectivity is strongly affected by the xylene vapour pressure, the membranes prepared in this study still exhibit high p/o and p/m separation factors for xylene pressures as high as 150 kPa and for a p/m/o ratio of 1 : 1 : 3. The improved selective character of the membranes prepared in this work should be attributed to their nanocomposite architecture, minimizing long term stresses and in its turn the distortion of the MFI framework at high xylene loadings. Note that the same property of nanocomposite materials enable them to avoid crystal opening at high temperature due to thermal expansion mismatch between MFI crystals and the alumina support.

In keeping with the results reported using PV, higher xylene concentrations might promote single-file diffusion within the MFI layer due to distortion of the MFI unit cell, thus making the material not being able to distinguish between the different xylene isomers xylene in the zeolite channels [168,172]. This fact might explain why, compared to pure xylene VP, o-Xylene flux is greatly enhanced over its pure value at comparable partial pressure in the presence of p-Xylene, as well as the long xylene flux transients (even longer than 24 hours). This general behaviour can be compensated to a certain extent when using nanocomposite materials. For example, Fig. 4.7 shows the p-Xylene permeation and separation performance from a mixture of isomers for film-like MFI membrane. This can be compared with the results for nanocomposite MFI-alumina membranes presented in Fig. 4.6. In general terms, due to confinement of the MFI material at the nanoscale, nanocomposite MFI-alumina membranes appear to minimize the intrinsic distortion of the unit cell upon p-Xylene adsorption. This fact, accompanied by a reduction of the number of nanosized grain boundaries, might limit single-file diffusion in such architectures, allowing higher separation factors at xylene vapour

pressures as high as 30 kPa and a drastic reduction of stabilization time to attain steady state. Experimental evidence of this hypothesis has been provided recently by Grahn *et al.* [129]. These authors have reported the disparities of the characteristic critical point of the p-Xylene/MFI system as long as the MFI particle size is reduced down to a few nanometers.

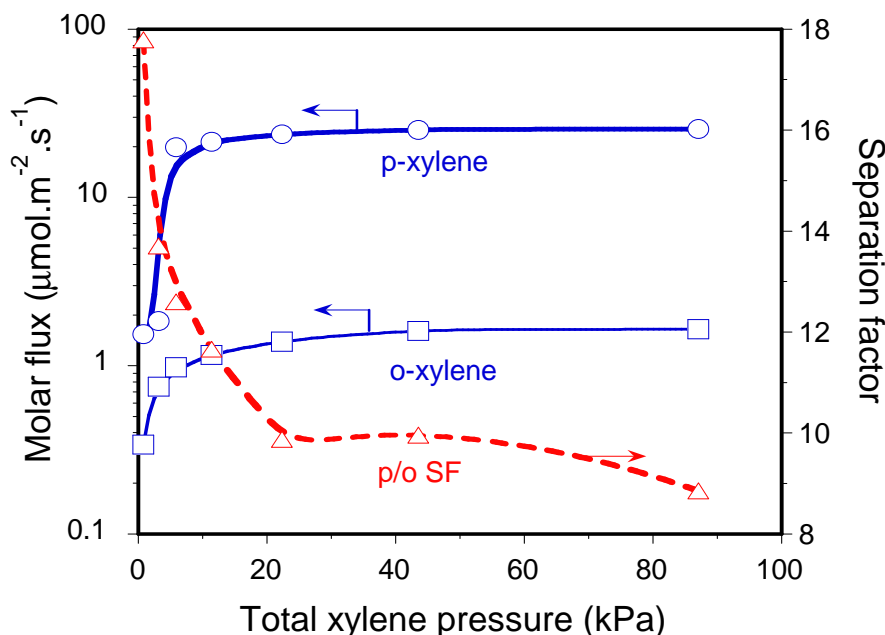


Figure 4.7: Xylene VP as a function of total xylene vapour pressure with a film-like membrane at 373 K. Adapted from [183].

Indeed, the high p-Xylene separation performance of the membranes prepared and tested in this study opens up a possible application of these materials to carry out xylene separation by PV, involving high xylene loadings. As far as we know, only Yuan *et al.* [168] have reported in the open literature, a p/o selectivity of 60 at 323 K during the separation of an equimolar p/o xylene binary mixture via PV. These authors used MFI membranes prepared via templateless seeded hydrothermal synthesis.

#### 4.5. Concluding remark

The results presented in this chapter report, for the first time in open literature, the excellent xylene separation performance of nanocomposite MFI-alumina membranes at high xylene loadings and high m- and o-Xylene compositions. The intimate contact of alumina and the MFI nanoparticles at the nanoscale allows compensation of long-term stresses, attenuating the distortion of the MFI framework upon xylene adsorption. This property of nanocomposite MFI-alumina membranes is outstanding, since, unlike their film-like counterparts, the

---

membranes can be operated at higher xylene vapour pressures without showing a dramatic decrease of their selectivity.

Furthermore, the hydrodynamics at the permeate side of the membranes plays a prominent role in their permeation and separation performance. As a matter of fact, the increase of turbulence in the permeate allows a drastic reduction of xylene partial pressures, promoting therefore permeation fluxes and selectivity to p-Xylene. It is also expected, although it was not investigated, that the use of vacuum pressure in the permeate side might further improve the permeation and separation performance. Regarding the modelling part of this study using Maxwell-Stefan's (MS) model, the aim was to support the absence of crystal swelling of the membranes at high p-Xylene partial pressures compared to more conventional film-like MFI membranes and, therefore, to enable reasonable conclusions about their potential use in industrial applications for p-Xylene purification and even in pervaporation. Actually, xylene/MFI system modelling is quite complex and therefore might not be described adequately with a simple model like the MS. This could explain the deviation observed between the model results and the experimental results. Furthermore, in this study, the effect of possible interactions among the operating variables is neglected. Therefore, it is recommended that this is considered by subsequent studies. It can be explored with the use of response surface methodology approach, and understanding it may pave the way for the optimization of the process.

Finally, the novel contribution described in this chapter has been published in Separation Science & Technology journal (*Sep. Sci. Tech.*). A sample of the publication is included in Appendix E.

---

## **Chapter 5: Hollow fibre MFI-alumina membranes for xylene isomer separation**

Evaluation of separation performance of a nanocomposite MFI-alumina hollow fibre membrane, prepared via pore-plugging technique during xylene isomer separation, is reported in this chapter. Separation performance of the hollow fibre membrane was compared to the performance of an equivalent membrane tube operated under the same operating conditions.

### **5.1 Introduction**

Two common materials used for membrane supports are stainless steel (SS) and alumina [184]. As difference in thermal expansion of the zeolite and the support layer could cause stress at the interface and thus cracks in the zeolite layer at high temperature, alumina of much lower thermal expansion than the stainless steel is preferred. Although SS is more ductile and compatible to most commonly used plant equipment parts, its higher thermal expansion is a great disadvantage. Moreover, to increase transmembrane flux of p-Xylene during xylene isomer separation, both the geometry of the support and the membrane thickness play a vital role [184].

Previous researchers in this area have reported the use of composite disks [106,175,179,180,181,241,243] for xylene isomer separation. All the above-stated studies dealing with MFI-type membranes have focused on the synthesis of continuous and well-intergrown thin films on top of a porous support that ensures mechanical resistance. In a series of previous studies by Dalmon and his group [191,207,208,209], reports on a different concept have emanated: the synthesis of 'nanocomposite' MFI-alumina membranes. In this architecture, which is compared to a film, the active phase is embedded into the host ceramic alumina porous network via pore-plugging hydrothermal synthesis. This does not only avoid individual membrane defects to exceed the size of the support pores, but it also provides a better mechanical resistance as well as a higher resistance to thermal shocks. Another consequence is that mass transfer within these membranes at high temperature is still governed by zeolite pores instead of intercrystalline openings that may appear in film-like configurations. Nanocomposite MFI-alumina membranes have already shown high potential for xylene isomer separation and for xylene isomerization when combined with a catalyst in extractor-type membrane reactors [186,242].

Recently, this concept was extended to the development and preparation of nanocomposite MFI-ceramic hollow fibre membranes for gas separation. Nanocomposite MFI-ceramic hollow fibre membranes have been reported to give pure gas permeance of about three times higher than those that are obtained with MFI tubular zeolite membranes. At the same time, these fibers offer higher module surface area/volume ratios [210]. As far as

---

could be ascertained, application of nanocomposite MFI-ceramic hollow fibre membranes for xylene isomer separation has not appeared in any open literature before. Therefore, this chapter reports the performance evaluation of nanocomposite MFI-alumina hollow fibre membranes during xylene isomer separation with p-Xylene being the target product. Compared to more conventional single tubes and planar geometries, hollow fibres present lower costs and larger surface-to-volume ratios ( $>1000 \text{ m}^2.\text{m}^{-3}$ ). Furthermore, this configuration also allows higher gas permeances due to their much lower effective membrane wall thickness.

## 5.2 Membrane preparation, characterization and separation test

The nanocomposite MFI-alumina hollow fibre membranes used in this study (o.d. 1.65 mm, i.d. 1.44 mm, porosity 43%) were prepared via a pore-plugging synthesis technique following the experimental protocol developed in previous studies [191,207,209] and described in Chapter 3. Figure 5.1 indicates the relevant dimensions of the fibres and Fig. 5.2 shows the micrograph of the cross-section of the membrane support. The MFI zeolite was synthesized by mixing together the structure directing agent (SDA, 1 M tetrapropylammonium hydroxide, TPAOH, supplied by Sigma-Aldrich), and the silica source (Aerosil 380 from Degussa). This mixture was slightly diluted with deionised water to form a clear solution with the molar composition 1.0  $\text{SiO}_2$ : 0.45 TPAOH: 27.8  $\text{H}_2\text{O}$  (pH close to 14) and matured for 3 days at room temperature under mild stirring. To ensure that the experimental conditions were kept as close as possible to the conditions used for preparation of conventional tubes, nine 23-cm long ceramic hollow fibres were inserted into a Teflon<sup>R</sup>-lined autoclave containing about 25 ml of precursor solution, and submitted to an interrupted hydrothermal synthesis at 423 K for 4 days. After the synthesis, the fibres were washed with deionised water, dried at 373 K for 12 hours, and calcined at 773 K for 4 hours under air flow.

The structure and purity of the synthesized zeolite material was confirmed by X-ray diffraction (XRD). Scanning Electron Microscopy (SEM) confirmed the formation of a nanocomposite material, that is, no continuous MFI film is formed on top of the support (see Li *et al.* [209] for further information). Table 5.1 lists the main properties of a representative MFI-alumina hollow fibre membrane after synthesis, further evaluated for xylene isomers separation.

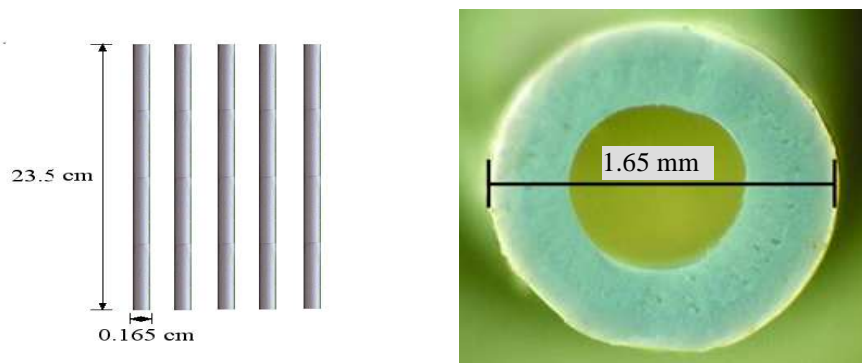


Figure 5.1: Pictures of the support fibre used for membrane synthesis.

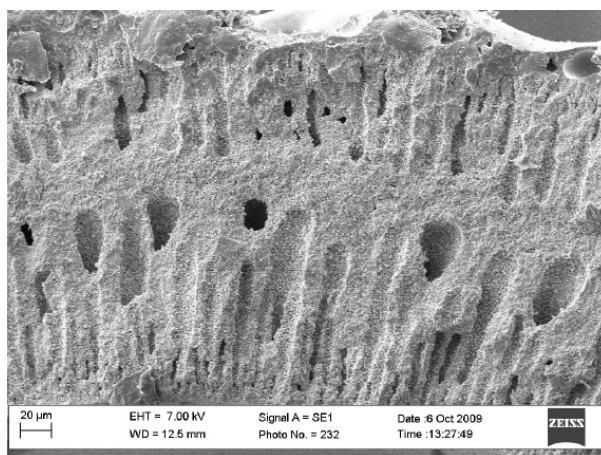


Figure 5.2: SEM image of the cross-section of the support used for membrane synthesis.

Table 5.1: Properties of the nanocomposite MFI-alumina hollow fibre and MFI-alumina tubular membranes used in this study

Property	Hollow fibre membrane	Membrane tube
Separation factor (H <sub>2</sub> /n-butane)(-)	101	>100
H <sub>2</sub> permeance (µmol.m <sup>-2</sup> .s <sup>-1</sup> .Pa <sup>-1</sup> )	1.33	0.49
Permeation length (cm)	13	13
Internal diameter (mm)	1.2	7
Effective thickness (µm)	<1	2-3
Permeation area (cm <sup>2</sup> )	9.94	26

After the synthesis, the *as*-calcined hollow fibres were immobilized on a supporting dense alumina perforated tube using a homemade low-temperature glaze, as shown in Fig. 5.3. The final ensemble was then mounted inside a graphite-sealed stainless steel module (see Fig. 5.4) and subjected to a high temperature pre-treatment at 673 K for 6 hours under 20 mL(STP)/min N<sub>2</sub> flow on both sides of the membrane to remove any adsorbed species (see Alshebani *et al.* [235] for further detail). The quality of the fibres was evaluated in terms of pure H<sub>2</sub> permeation and room-temperature *n*-butane/H<sub>2</sub> separation.

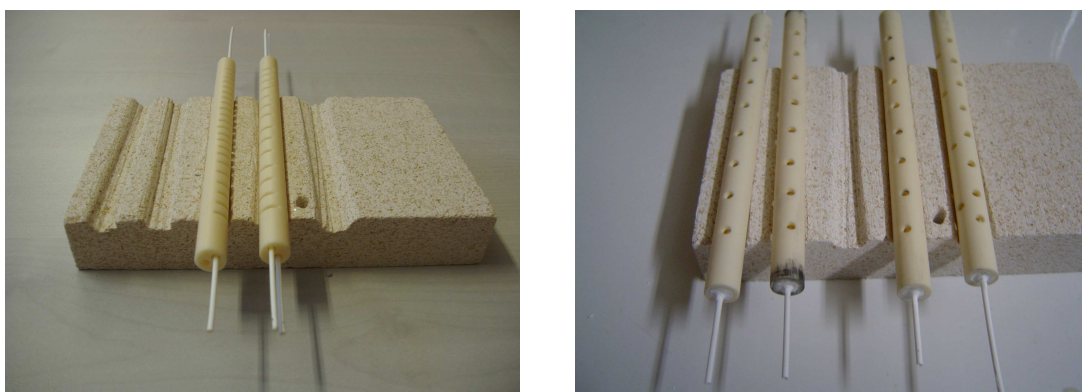


Figure 5.3: Fibres mounted into their mechanical support tubes.

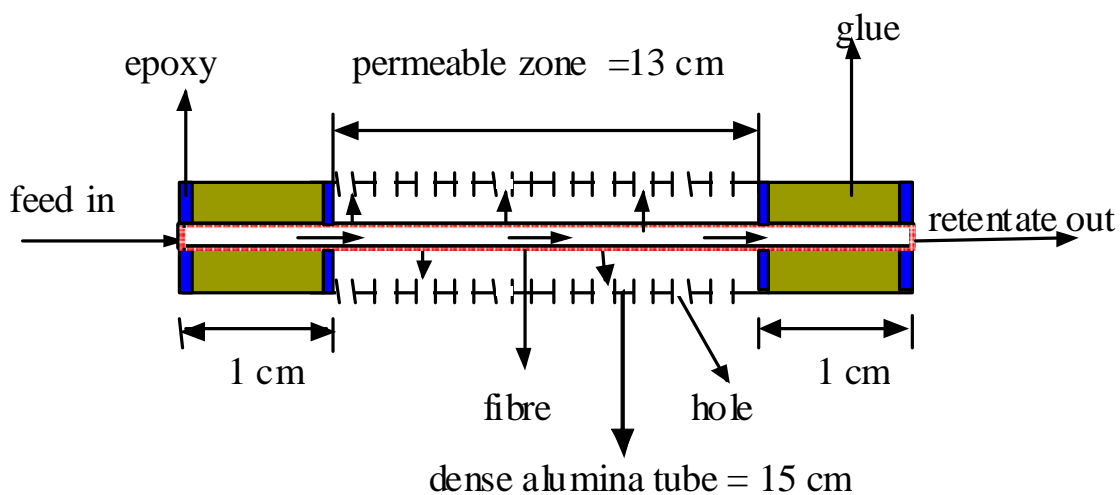


Figure 5.4: Schematic showing the section of a fibre mounted inside its mechanical fibre supports.

---

For the sake of comparison, the results obtained with the fibre were compared with the separation performance of a nanocomposite MFI-alumina membrane prepared on a Pall-Exekia tube operated under the same standard protocol as in the case of hollow fibres. The main characteristics of this membrane compared to those of the hollow fibres are listed in Table 5.1.

Separation testing was conducted with the rig described in Chapter 3. Pure o-Xylene and p-Xylene, as well as a mixture of xylene isomers (m-Xylene and p-Xylene, 99% purity; o-Xylene, 97% purity), all supplied by Sigma-Aldrich, were saturated in a 10-mL(STP)/min N<sub>2</sub> carrier flow at atmospheric pressure using the saturation system described in Chapter 3. The second saturator was maintained at a temperature of about 6 K lower than the former to ensure saturation. The permeate side of the membrane was swept with a counter-current 15-mL(STP)/min N<sub>2</sub> flow. The o- and p-Xylene partial pressures were, respectively, 3.38 kPa and 3.77 kPa in the pure xylene vapour permeation (VP) tests.

In the case of the ternary xylene mixture separation, the feed p-Xylene, m-Xylene and o-Xylene partial pressures were, respectively, 0.62, 0.27 and 0.32 kPa. In all cases, the temperature of the membrane system was varied from 423 to 673 K by increments of 50 K. In the experiments dealing with membrane tubes, the temperature was directly measured in the tube lumen while in the experiments using hollow fibres; the temperature was measured on the outer surface of the alumina supporting tube.

After attaining steady state in about 5 hours, the permeate and retentate streams were diverted to a gas chromatograph (*Shimadzu GC-14A*), equipped with a solgel-wax capillary column and a FID detector, for analysis. To avoid any condensation and ensure proper xylene partial pressure throughout the setup, all the lines were heated and maintained at 393 K with heating tape. Further, to prevent the occurrence of viscous flow within the fibres during the separation, the transfibre/transmembrane pressure was kept as low as possible ( $\Delta P \approx 0$ , Wicke-Kallenbach method). The effect of the temperature was evaluated in these experiments by decreasing the module temperature by increments of 50 K from 673 K to 423 K. The vapour permeance, flux of a given xylene (either pure or in a xylene isomer mixture) and separation factors (a xylene isomer mixture) were computed following Eq. 3.5 to Eq. 3.15 stated in Chapter 3. In all the experiments, mass balances of each xylene isomer were closed with an experimental error <3%.

### **5.3 Results and discussion**

Separation performance of the hollow fibre membrane compared to that of a membrane tube under the influence of changes in temperatures is presented in subsections 5.3.1 through 5.3.3.

---

### 5.3.1 Formation of nanocomposite MFI membrane and quality test

In keeping with the results previously reported on MFI-alumina membrane tubes [208,242], the nanocomposite MFI-alumina hollow fibres presented in this section do not show an increase of either pure hydrogen or p-Xylene and o-Xylene fluxes at temperatures higher than 673 K. This trend differs from what is usually found in film-like MFI membranes (silicalite-1 and ZSM-5) grown on alumina and stainless steel supports, where a sharp increase of flux is observed above 400 K [244-246]. For the two temperature points tested, the results showed a decrease in hydrogen permeance from  $1.33 \mu\text{mol.m}^{-2}.\text{s}^{-1}.\text{Pa}^{-1}$  obtained at room temperature (298 K) to about  $0.8 \mu\text{mol.m}^{-2}.\text{s}^{-1}.\text{Pa}^{-1}$  at 490 K. In addition, at room temperature, the *n*-butane/H<sub>2</sub> separation factor obtained for the hollow fibre is as high as 101 (see Table 5.1). Note that *n*-butane/H<sub>2</sub> separation factor higher than 25 is usually considered an indicator of good membrane quality at IRCE.

As reported by Gualtieri *et al.* [247] using high resolution X-ray diffraction, unlike film-like MFI membranes, a sample prepared by embedding MFI crystals in the pores of a support shows no contraction upon heating, namely the MFI cell keeps unchanged. This is an interesting feature of nanocomposite membranes, since, as proposed by Miachon *et al.* [208], contraction of MFI crystals could translate into inter-crystalline pore opening, contributing to a drastic reduction of membrane selectivity. In nanocomposite architecture, the zeolite crystals are constrained by the surrounding alumina grains, the support ruling the thermal behaviour of the zeolite material. Thus, the nanocomposite MFI-alumina hollow fibre membranes prepared and used in this study are thermally stable. For more information about the membrane, a sample of the XRD image analysis showing the formation of the membrane is depicted in Fig. 3.8 and a SEM image of the cross-section of the innermost layer of the hollow fibre membrane showing total pore-plugging of the layer with zeolite crystals is depicted in Fig. 5.5.

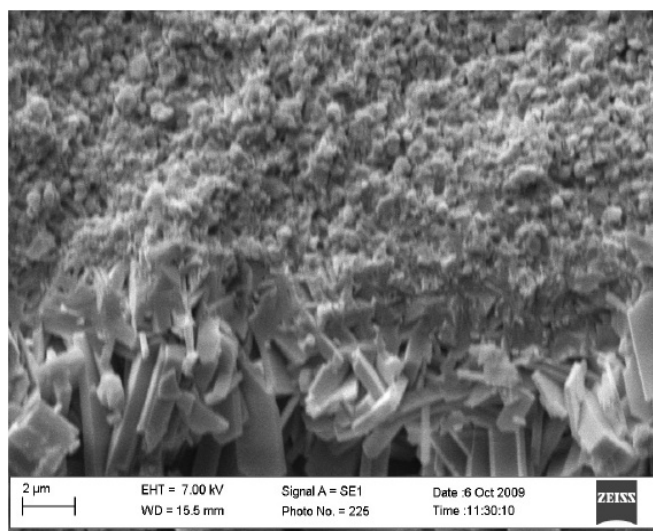


Figure 5.5: SEM image of the cross-section of the innermost layer of the hollow fibre MFI-alumina membrane.

### 5.3.2 Xylene vapour permeation and separation test

The evolution of p-Xylene and o-Xylene permeation fluxes with temperature is presented in Fig. 5.6. As can be seen, the p-Xylene flux shows a maximum flux with temperature of  $13.2 \mu\text{mol.m}^{-2}.\text{s}^{-1}$  at 573 K without further increase at temperatures higher than 700 K. The o-Xylene flux decreases monotonically with temperature in the range 523-673 K, showing a maximum value of  $109 \text{ nmol.m}^{-2}.\text{s}^{-1}$  at 523 K. The maximum computed p/o permselectivity obtained with these fibres is 210 at 623 K.

Figure 5.7 and Figure 5.8 show the evolution of the p-Xylene, m-Xylene and o-Xylene fluxes as a function of temperature (Fig. 5.7), as well as the p/o and p/m xylene separation factors (Fig. 5.8) in the separation of ternary xylene isomer mixtures using the hollow fibre prepared in this study. As can be seen, the p-Xylene flux shows a maximum with temperature of about  $5 \mu\text{mol.m}^{-2}.\text{s}^{-1}$  at 573 K, the m-Xylene flux showing in this temperature a minimum of  $37 \text{ nmol.m}^{-2}.\text{s}^{-1}$ . The o-Xylene permeances are extremely low,  $< 0.37 \text{ nmol.m}^{-2}.\text{s}^{-1}$ , showing a slightly increasing trend with temperature.

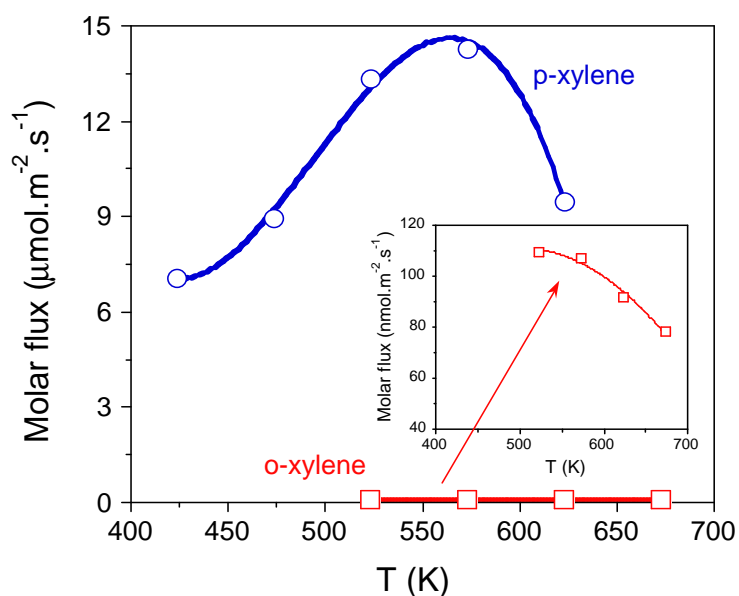


Figure 5.6: Single vapour permeation flux as a function of temperature. Experimental conditions: p-/o-Xylene feed partial pressures, 3.77 kPa / 3.38 kPa; feed gas flow rate, 10 mL(STP)/min; sweep gas flow, 15 mL(STP)/min. Adapted from [248].

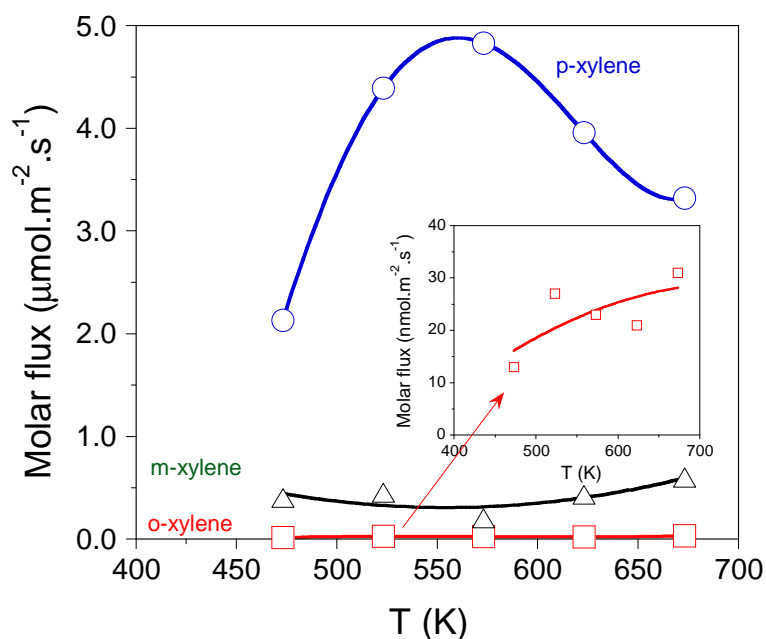


Figure 5.7: Xylene ternary vapour mixture separation as a function of temperature with nanocomposite MFI-alumina hollow fibre showing the permeation fluxes;(b) p/o and p/m separation factors. Experimental conditions: p-/m-/o-Xylene feed partial pressures, 0.62 kPa / 0.27 kPa / 0.32 kPa; sweep gas and feed flow rates as in Fig. 5.6. The straight and dashed curves are a guide to the eye. Adapted from [248].

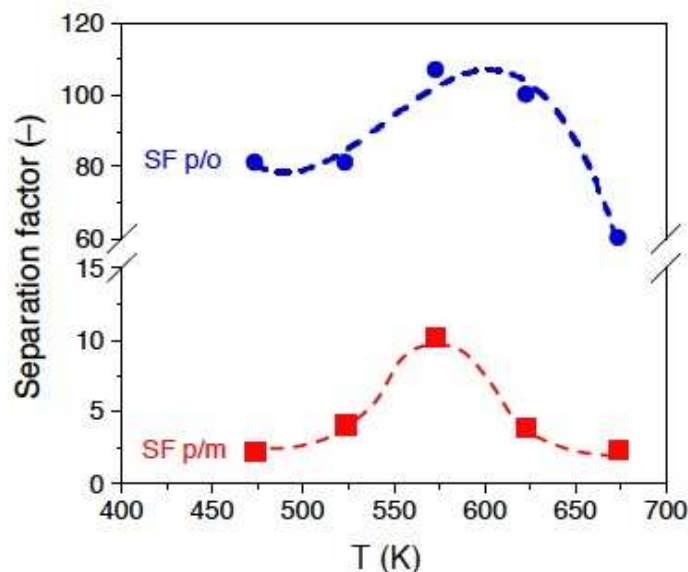


Figure 5.8: Xylene ternary vapour mixture separation as a function of temperature with nanocomposite MFI-alumina hollow fibre showing the p/o and p/m separation factors. Experimental conditions: p-/m-/o-Xylene feed partial pressures, 0.62 kPa / 0.27 kPa / 0.32 kPa; sweep gas and feed flow rates as in Fig.5.6. The straight and dashed curves are a guide to the eye. Adapted from [248].

The temperature dependence of pure p-Xylene flux within the synthesized hollow fibres prepared in this study (see Fig. 5.6) is qualitatively consistent with the trend reported by Gu *et al.* [183] for film-like MFI membranes at temperatures < 400 K. The flux pattern of pure p-Xylene is characterized by the presence of a maximum, which should be attributed to a competition between xylene adsorption and surface diffusion within the zeolite pores (adsorption-diffusion mechanism). This permeation behaviour is consistent with that commonly found for permeation of light hydrocarbons within film-like MFI membranes at temperatures lower than 400 K [246,249-251]. Although no maximum is observed in Fig. 5.6 for o-Xylene flux in the range of the temperature tested, it is expected that a maximum is observed at temperatures lower than 473 K. The pure p-Xylene fluxes obtained in this study are up to 160 times higher than those obtained for o-Xylene at 573 K. The permeation observed for o-Xylene should be ascribed, at least partially, to the presence of small intercrystalline defects and grain boundaries in the zeolite material.

Regarding the ternary mixture separation test, the results plotted in Fig. 5.7 confirm that, under lower enough xylene loadings, p-Xylene permeates selectively from mixtures of the three isomers within the MFI-alumina hollow fibres prepared in this study on the basis of the much higher diffusivity of p-Xylene compared to that of m-Xylene and o-Xylene. Under an adsorption-diffusion mechanism, raising the temperature reduces the surface coverage of xylene molecules, lowering therefore the driving force for mass transfer, but increasing the

---

surface diffusivity of the adsorbed xylenes. The presence of a minimum of m-Xylene flux at 573 K in Fig. 5.8, where the maximum of p-Xylene flux is located, should be attributed to competitive adsorption and diffusion between both isomers. Note that this result is qualitatively consistent with the observation reported by Xomeritakis *et al.* [106] for film-like alumina-supported MFI membranes. Moreover, as put forward by O'Brien-Abraham *et al.* [170], sorbate-sorbate competition for passage within the MFI pores in xylene mixture vapour permeation might hinder, to some extent, p-Xylene permeation, reducing thereby p-Xylene fluxes compared to pure p-Xylene vapour permeation. In the case of the MFI-alumina hollow fibres prepared in this study, the maximum p-Xylene flux at 573 K is reduced from 13.2 to 4.5  $\mu\text{mol.m}^{-2}.\text{s}^{-1}$  (see Fig. 5.6 and Fig. 5.7).

### 5.3.3 Hollow fibres MFI vs. MFI membrane tubes

To compare the separation performance of the nanocomposite MFI-alumina hollow fibres over conventional MFI-alumina tubular membranes, ternary vapour mixture separation was carried out using a tubular MFI-alumina membrane described in Chapter 4.

Figure 5.9 and Figure 5.10 show the xylene permeation and separation performance of the MFI-alumina membrane tube. The p-Xylene flux shows a similar qualitative trend with temperature to that obtained for MFI-alumina hollow fibres, with a maximum value of about 3.5  $\mu\text{mol.m}^{-2}.\text{s}^{-1}$  at 473 K.

The results plotted in Fig. 5.7 and Fig. 5.9 show that both nanocomposite MFI-alumina hollow fibres and membrane tubes prepared via pore-plugging hydrothermal synthesis show similar trends of p-Xylene mixture fluxes as a function of temperature. The displacement of the maximum p-Xylene flux from 573 K in MFI-alumina hollow fibres to 473 K in MFI-alumina tubes could be ascribed to a lack of accuracy in the temperature measurement in the former case (the temperature could not be directly measured in the lumen of the hollow fibres). The membrane tubes show better p/o xylene separation factors than the hollow fibres, probably due to a better sealing of the permeation module in the former case during the xylene vapour permeation tests.

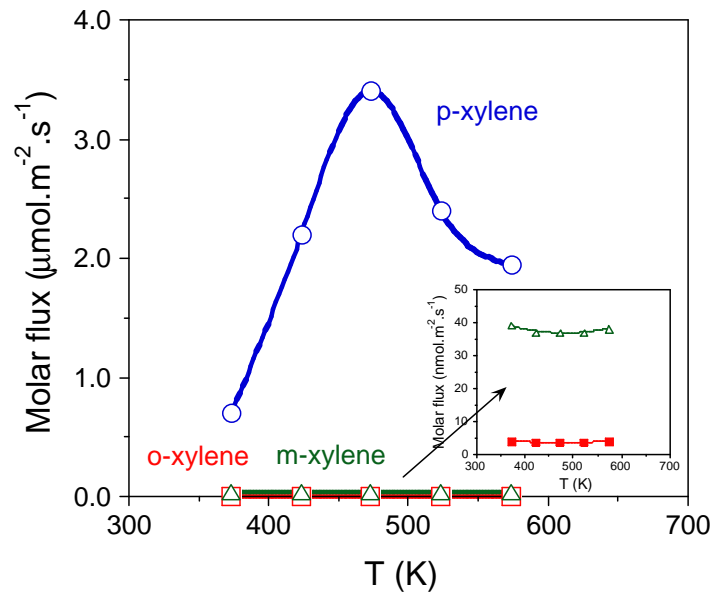


Figure 5.9: Xylene ternary vapour mixture separation as a function of temperature with nanocomposite MFI-alumina membrane tube showing permeation fluxes. Experimental conditions: p-/m-/o-Xylene feed partial pressures, 0.62 kPa / 0.27 kPa / 0.32 kPa; sweep gas and feed flow rates as in Fig.5.6. The straight and dashed curves are a guide to the eye.

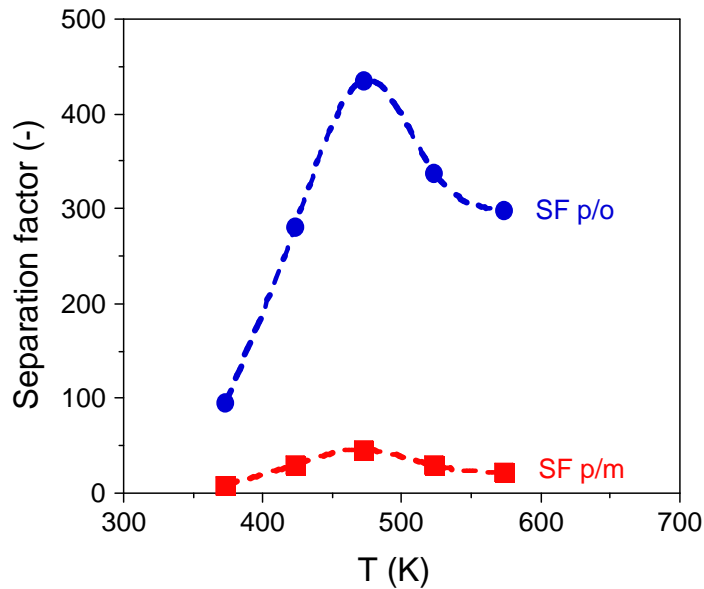


Figure 5.10: Xylene ternary vapour mixture separation as a function of temperature with nanocomposite MFI-alumina membrane tube showing p/o and p/m separation factors. Experimental conditions: p-/m-/o-Xylene feed partial pressures, 0.62 kPa / 0.27 kPa / 0.32 kPa; sweep gas and feed flow rates as in Fig.5.6. The straight and dashed curves are a guide to the eye.

Furthermore, although the MFI-alumina hollow fibres show that mixture p-Xylene fluxes are about 30% higher than those of MFI-alumina membrane tubes, the p-Xylene vapour permeances show the same order of magnitude, about  $10 \text{ nmol.m}^{-2}.\text{s}^{-1}.\text{Pa}^{-1}$ . Table 5.2 compares the mixture permeation and separation results obtained in this study on hollow fibre and membrane tube with some of the comparable results reported in Table 2.5 on xylene separation using MFI-type zeolite membranes. Excluding b-and c-oriented well-intergrown supported MFI films, among the results reported in the literature on randomly-oriented MFI membranes prepared on tubular geometries, the hollow fibres prepared in this study offer an excellent trade-off between p/o-Xylene separation factors and mixture p-Xylene permeances. The p-Xylene permeances obtained in this study on hollow fibres are about 4 times higher than the values obtained by Gump *et al.* [175] on MFI membranes tubes. Furthermore, the nanocomposite nature of the fibres renders the synthesis extremely reproducible.

Table 5.2: Previous studies on xylene separation from binary p/o-Xylene and ternary p/m/o-Xylene mixtures using MF-type zeolite membranes

Membrane	Zeolite thickness ( $\mu\text{m}$ )	$T_{\text{max}}$ (K)	$\Pi_{\text{max}}$ ( $\text{nmol.m}^{-2}.\text{s}^{-1}.\text{Pa}^{-1}$ )	SF (p/o)	Refs.
Silicalite-1 film <sup>b</sup>	3	400	12	60	[177]
BZSM-5 film <sup>b</sup>	30	425	2.6	60	[175]
MFI film (self-supported) <sup>b</sup>	90	473	82	250	[178]
Ultra thin MFI films <sup>a</sup>	0.5	663	300 (663 K) 600 (373 K)	3 16	[180]
MFI film <sup>a</sup>	1-40	548	20 (398 K)	60-300	[106]
b-oriented MFI films <sup>a</sup>	1	423	200	480	[172] [179]
c-oriented MFI films <sup>a</sup>	30	423	30	3	[172] [179]
h0h-oriented MFI films <sup>a</sup>	2	403	40	60	[172] [179]
Silicalite-1 film <sup>a</sup>	2-10	480	4	1	[181]
ZSM-5 film <sup>a</sup>	15-20	673	51	4	[184]
HZSM-5 alumina nanocomposite <sup>c</sup>	2-3	673	10 (450 K)	7.0	[186]
HZSM-5 alumina nanocomposites <sup>c</sup>	1.5-4	473	11	>400	This study
HZSM-5 alumina nanocomposites <sup>c</sup>	0.5-1.5	573	9	107	This study

<sup>a</sup>Prepared via seeded hydrothermal synthesis ;<sup>b</sup>Prepared via *in situ* hydrothermal synthesis <sup>c</sup>Prepared via pore-plugging *in situ* hydrothermal synthesis.  $\Pi_{\text{max}}$  : maximum p-Xylene permeance; SF: separation factor.

---

#### 5.4 Influence of porous structure of hollow fibres on separation performance

As presented in the preceding sections of this chapter, the extension of nanocomposite MFI-alumina concept to hollow-fibre geometries could enhance separation performance of xylene isomers in terms of the p-Xylene flux compared to the membrane tubes. Besides, the higher surface-to-volume ratio can be exploited to develop a compact separation unit for xylene isomer separation. Notwithstanding the optimal reproducibility of the synthesis protocols for MFI membrane synthesis, the synthesis of MFI-alumina hollow fibres usually suffers from lower reproducibility than in the case of membrane tubes. This shortcoming could be mainly ascribed to the intrinsic complexity of the porous structure of hollow fibres (presence of different pore families differing in size and shape), whose nature depends strongly on the manufacturing conditions. As a matter of fact, the strong sensitivity of the pore plugging efficiency in the preparation of MFI-alumina membrane tubes on the support pore size has been reported with the maximum admissible value being about 0.5  $\mu\text{m}$  [207]. Extending this conclusion to hollow fibres, the maximum 'effective' pore size of these supports should not exceed, in principle, this critical value. Based on this hypothesis, a preliminary assessment was carried out of the role of the porous structure of hollow fibres on the separation performance of nanocomposite MFI-alumina hollow fibres during xylene isomer separation. The goal was to draw correlations between the maximum pore size and/or the form of the pore size distribution of raw hollow fibres on the further separation performance of the MFI-alumina materials that help for a rapid process intensification.

Alumina hollow fibres with dimensions described in section 5.2., prepared by a wet spinning process following the methodology described by Goldbach *et al.* [252], were used to prepare membranes used for this preliminary study and the membranes were synthesized following the protocol described in Chapter 3. The quality of the synthesized membranes was assessed by using n-butane/H<sub>2</sub> binary mixture separation test, SEM analysis and XRD analysis. First and foremost, before membrane synthesis, the quality of the hollow fibre supports was evaluated by gas-liquid displacement using an automated porometer (WSI, USA) operated in dead-end mode as described in Chapter 3. Based on the results of these tests, the fibre supports were grouped into 4 families according to their pore size distributions. Figure 5.11 depicts the results obtained from the support quality test while Fig. 5.12 and Fig. 5.13 show the morphology of the fibre supports and the MFI-alumina hollow fibre membranes as obtained from SEM analysis. After membrane quality test, the membranes were subjected to xylene isomers separation following the procedure described in section 5.2 of this chapter. The results of the separation tests are shown in Table 5.3.

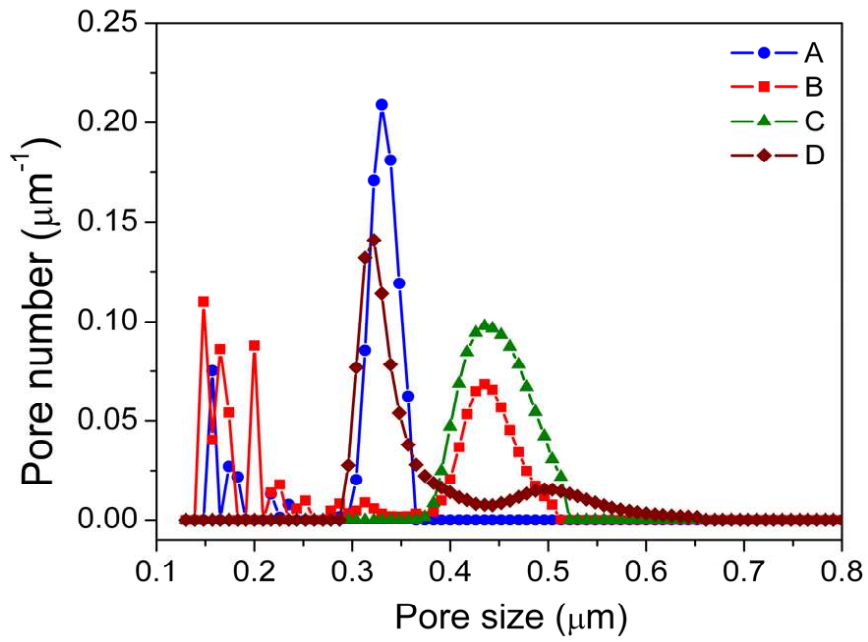


Figure 5.11: Evolution of the  $\text{N}_2$  flux with the transfibre pressure in gas-liquid displacement tests for four representative hollow fibre supports belonging to families A-D and corresponding pore size distributions obtained after data processing. Adapted from [253].

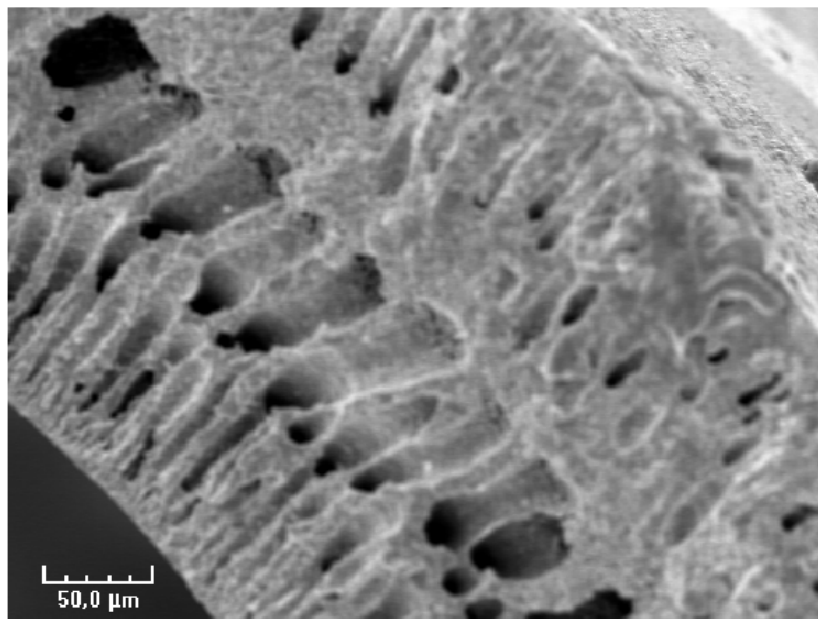


Figure 5.12: SEM image of the cross-section of the hollow fibre support.

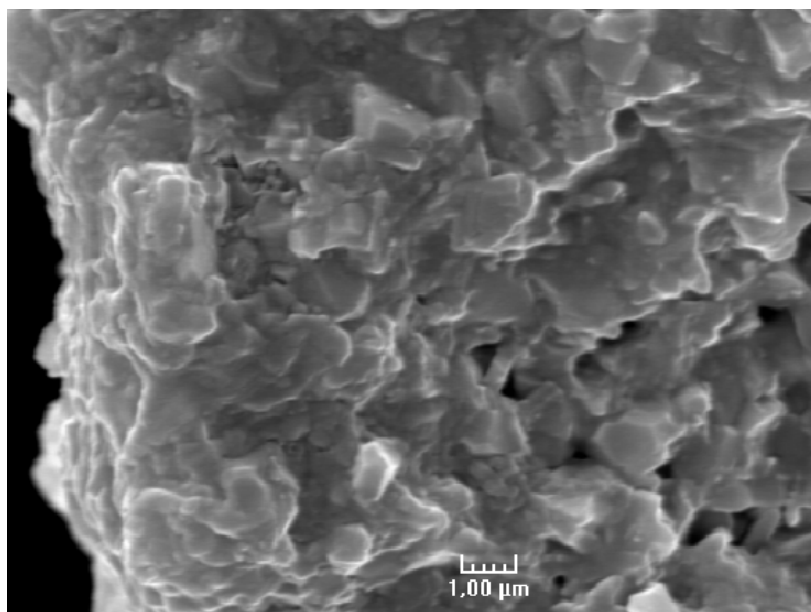


Figure 5.13: SEM image of the cross-section of the nanocomposite MFI-alumina hollow fibre membrane after synthesis.

#### 5.4.1 Discussion of results

The XRD analysis (see Fig. 3.8 for a sample) indicates that a highly pure MFI zeolite phase was synthesized. Furthermore, from the SEM micrographs corresponding to the raw hollow fibres (Fig. 5.12), the support exhibits large finger-like pores in the central part of the wall thickness and smaller pores near the inner and outer surfaces. Taking into account the principle of measurement in the gas-liquid displacement tests, relying on Laplace Law (Eq. 3.3), only these latter pores are expected to be duly characterized by this technique, but not the largest central ones. At the same time, the SEM micrographs obtained on the hollow fibres after synthesis reflect the formation of large MFI crystals in the finger-like pores, while the smallest pores near the inner and outer surfaces appear to be completely plugged (see Fig. 5.13). However, incomplete pore plugging in larger surface pores, which is difficult to visualize by SEM microscopy, cannot be ruled out, providing potential non-selective shortcuts during gas separation.

Table 5.3: Membrane quality of the four hollow-fibre membrane families identified in this study as evaluated from room-temperature *n*-butane/H<sub>2</sub> and separation and p/m and p/o separation factors at the maximum temperature (range 473-523 K).

Hollow fibre family	Largest pore size (μm)	SF <i>n</i> -C <sub>4</sub> H <sub>10</sub> /H <sub>2</sub>	SF p/m	SF p/o
A	0.3-0.5	>300	70 ± 25	9 ± 1
B	0.5-0.6	50-300	19 ± 5	7 ± 1
C	0.5-0.6	20-50	12 ± 5	7 ± 1
D	>0.6	<20	<7	<3

The results of the preliminary investigation collected in Table 5.3 suggest an important role of the porous structure of the *raw* hollow fibres (surface pores) on the final membrane quality after synthesis. In principle, hollow fibres displaying maximum pore sizes larger than 0.6 μm, corresponding to First Bubble Point (FBPs) in ethanol lower than 130 kPa, appear to be detrimental to achieving complete pore plugging. This observation can be linked to the *n*-butane/H<sub>2</sub> separation factors of the MFI-alumina hollow fibres. As can be inferred from Table 5.3, the *n*-butane/H<sub>2</sub> separation factor shows a decreasing trend in the order A→D, being <20 for D-type supports. Note that, as a reference, a *n*-butane/H<sub>2</sub> separation factor higher than 25 is usually considered as an indicator of good membrane quality in terms of an absence of a large amount of intercrystalline defects [208]. The results obtained from xylene isomers separation test also corroborated the results obtained from butane/H<sub>2</sub> test (see Table 5.3). For this separation, the use of A-type supports gave p-Xylene to m-Xylene (p/m) separation factors of at least 50. In all cases, the p/o separation factors remain lower than 15, being slightly promoted for the MFI-alumina samples prepared on A-type supports. The fact that the hollow fibre membranes prepared here show preferential permeation of o-Xylene rather than m-Xylene in the separation of ternary xylene isomer mixtures might be attributed to higher steric constraints of o-Xylene than m-Xylene in the passage within grain boundaries and/or small-sized mesopores, thereby promoting single-file diffusion of the former one.

From this preliminary study, the mean pore size of the support top layer was found to play a crucial role on the final membrane quality. The membranes showing the best quality correspond to those prepared with 0.1 and 0.2-μm toplayer supports, being gas-tight before template removal and showing *n*-butane/H<sub>2</sub> separation factor of about 60 after calcinations. In contrast, the membranes synthesized with 0.5 and 0.8-μm support toplayers were not statistically gas-tight before template removal, reflecting an absence of complete pore plugging. These latter materials show, accordingly, extremely low *n*-butane/H<sub>2</sub> separation factors (<20). To derive a logical conclusion as regards the influence of porous structure of

---

hollow fibre on separation performance of nanocomposite MFI-alumina hollow fibre membranes, a detailed investigation by another student was going on at the time this dissertation was compiled. However, this study serves as an impetus to the on-going investigation.

### 5.5 Concluding remark

As it has been demonstrated in this chapter, nanocomposite MFI-alumina hollow fibres are promising candidates for selective p-Xylene separation from a ternary vapour mixture of xylene isomers. The MFI-alumina fibres show a maximum p-Xylene flux of  $4.5 \mu\text{mol}\cdot\text{m}^{-2}\cdot\text{s}^{-1}$  at 573 K, with no indication of possible further increase in flux beyond this temperature. As far as could be ascertained, a report on the evaluation of separation performance of nanocomposite MFI-alumina hollow fibre membranes for xylene vapour mixture separation has not surfaced in any open literature until now. The advantage of nanocomposite MFI-ceramic hollow fibre is not only limited to the possibility of performing selective separations at high temperatures, but its higher fluxes over conventional randomly oriented MFI zeolite films due to their thin effective thickness ( $<1 \mu\text{m}$ ) is an addition. Hollow fibres also offer the added advantage of membrane surface-to-volume ratios as high as  $3000 \text{ m}^2/\text{m}^3$  compared to more conventional membrane tubes. For instance, a 5-fibre bundle occupying the volume meant for a single alumina tube could double the p-Xylene productivity operating at the temperature where the maximum flux is obtained, taking into account the higher separation surface of the bundle ( $5 \times 9.94 \sim 50 \text{ cm}^2$  vs.  $26 \text{ cm}^2$  for alumina tubes). Using this type of system might be instrumental in reducing both the size and cost of permeating modules for future xylene separation processes.

On the influence of porous structure of hollow fibres on the gas/vapour separation performance, the results of the preliminary study, as reported in this chapter, have shown that good fibre supports are necessary to obtain defect-free and high separation-performance nanocomposite MFI-alumina hollow fibre membranes for xylene vapour mixture separation. However, the results presented in this work open up a research line to scale-up the fibre preparation process aimed at obtaining fibre bundles for xylene isomers separation.

For quick dissemination of the novel contributions described in this chapter to the scientific community, two articles have evolved. One is already published in the Journal of Membrane Science (*J. Membr. Sci.*) and the second has been accepted for publication in the same journal.

---

## Chapter 6: Experimental study of m-Xylene isomerization in e-ZCMR

This chapter reports the study of the influence of operating variables and reactor configuration on the performance of an extractor-type zeolite catalytic membrane reactor, having a nanocomposite MFI-alumina membrane tube as separation unit, during m-Xylene isomerization over Pt-HZSM-5 catalyst. Results obtained were compared with existing literature to arrive at logical conclusions.

### 6.1 Introduction

Limited material and energy resources have increasingly become a challenge for future chemical production but process intensification can contribute to the solution of this problem. From an engineering standpoint the vision of process intensification through multifunctional reactors has activated research on catalytic membrane reactors. According to the IUPAC definition, a membrane reactor is a device combining a membrane-based separation and a chemical reaction in one unit [193]. So far this engineering vision of a chemical membrane reactor could not be realized due to a lack in temperature resistant and chemically stable and highly selective membranes. During the last few years, inorganic membranes based on ceramics, zeolites, metals, carbon or as a hybrid material have been developed so that the realization of a chemical membrane reactor is increasingly possible.

Regarding p-Xylene production via xylene isomerization in extractor-type zeolite catalytic membrane reactor (e-ZCMR), limited study has appeared in the literature. The combination of a supported MFI membrane (film-like) with an isomerization catalyst in an e-CMR (hereinafter referred to as 'e-ZCMR') to promote p-Xylene production has been proposed in a few number of previous studies [190,198,201]. In the case of catalytically active MFI membranes, the only example of application in the literature has been reported by Haag *et al.* [182]. Film-like MFI membranes have some shortcomings such as a mismatch between the thermal expansion coefficients of the support and the zeolite material at higher operation temperatures. This enhances permeation of undesirable isomers through inter-crystalline defects, contributing to a reduction of the membrane selectivity. The occurrence becomes more pronounced if the membrane support is stainless steel because of the higher disparity between its thermal expansion coefficients and that of the MFI phase. Taking into account that xylene separation and isomerization is industrially carried out at temperatures about 673 K, this limitation acts, in practice, as a hindrance for the industrialization of MFI membranes.

Nevertheless, as pointed out in a series of previous studies [191,207-209], the shortcoming ascribed to film-like membranes can be overcome by using nanocomposite

---

MFI-alumina membranes, where the zeolite crystals are embedded within the support pores instead of forming a film. The advantages of nanocomposite architectures compared to zeolite films include defect control and higher mechanical and thermal stability. These membranes have shown promising xylene isomer separation performance [186,242,248].

Regarding the xylene isomerization using MFI-alumina membranes with nanocomposite architecture, a report of a preliminary study has shown an increase of about 10% p-Xylene yield (when retentate and permeate amounts are combined) over a conventional FBR [13,186]. Therefore, this chapter reports further research efforts on m-Xylene isomerization over Pt-HZSM-5 catalysts in e-ZCMRs with nanocomposite MFI-alumina membrane tubes as separation and catalyst packing units. The influence of operating variables such as the gas hourly space velocity (GHSV = feed volumetric flow per catalyst volume), the reaction time and the catalyst location (i.e. packed in the membrane lumen or in the module shell) were also investigated. The results reported in this study open up an avenue for promoting the performance of e-ZCMRs when applied to m-Xylene isomerization.

## **6.2 Experimental**

### **6.2.1 Membrane preparation, characterization and separation test**

The membrane used in this study was prepared via a pore-plugging synthesis technique on an asymmetrical Pall-Exekia  $\alpha$ -alumina tube (o.d. 10 mm, i.d. 7 mm, length 15 cm, active permeation area 26 cm<sup>2</sup>) as described in Chapter 3 of this dissertation. Detailed description can be obtained from Refs. [191,207]. The cross-sectional layers of the support have the following mean pore diameters: outer layer, 12  $\mu$ m; intermediate layer, 0.8  $\mu$ m; inner layer, 0.2  $\mu$ m. The nanocomposite nature of the fibres was inspected by SEM (JSM-5800LV, 20 kV) coupled with EDX analysis (Edax Phoenix, 1- $\mu$ m microprobe). The resulting nanocomposite membrane from this support has equivalent membrane thickness <3 $\mu$ m. The estimation of the membrane effective thickness was done indirectly through Maxwell-Stefan modelling of the pure N<sub>2</sub> and CO<sub>2</sub> permeance on the guidance of a previous study [209].

The quality of the membrane was evaluated by single gas hydrogen permeation and room-temperature n-butane/H<sub>2</sub> binary mixture separation. The quality of the membrane was further confirmed with xylene ternary vapour mixture separation tests. The tests were conducted as described in the previous chapters. The p/m/o-Xylene vapour pressures feeding the membrane were, respectively, 0.51, 0.34 and 0.59 kPa. Nitrogen gas was swept over the permeate side of the membrane. Before isomerization, the influence of the sweep gas flow rate was investigated within the range 5-40 mL (STP)/min to obtain sweep gas flow rates

---

beyond which improvement on p-Xylene production (as a function of sweep gas flow rate on the permeate side) is not practically possible in e-ZCMR; that is, the sweep gas flow rate on the permeate side at which the xylene partial pressure became considerably low or null. More details on the set-up and experimental protocol used for performing the xylene separation tests can be found in Daramola *et al.* [248].

Prior to the separation tests, the membrane was mounted into the membrane module and subjected to a high temperature pre-treatment for 6 hours at 673 K to remove adsorbed species on the guidance of a previous study [235], and in all the xylene VP experiments, mass balances of each xylene isomer were closed with an experimental error <3%. Moreover, to prevent occurrence of viscous flow within the fibres during the separation, the transmembrane pressure (total) was kept as low as possible ( $\Delta P \approx 0$ , Wicke-Kallenbach method).

### 6.2.2 Meta-xylene isomerization

To evaluate the performance of extractor-type catalytic membrane reactors for xylene isomerization effectively, it is essential to avoid side reactions. Therefore, to avoid or minimise side reactions during m-Xylene isomerization in extractor-type catalytic membrane reactors, xylene isomerization is always carried out below equilibrium position [198]. Operating below the equilibrium position depends on: (i) the amount of catalysts; and (ii) the flow rate or gas hourly space velocity (GHSV) of the feed.

In the preliminary study with e-CMR having a nanocomposite MFI-alumina membrane tube as separation unit, 2.18 g of Pt-HZSM-5 catalyst was used and the reactor was fed with feed at very high feed flow rate [13,186]. However, there was no indication as to whether the amount of the catalyst ensured conversion below equilibrium. To clarify this, an experimental investigation was conducted in this study to ensure that suitable amount of catalyst ensuring conversion below equilibrium, was used in the e-ZCMR.

In most of the previous kinetic studies of xylene isomerization over a catalyst, laboratory-scale integral reactor of stainless steel (id 2 cm) [42]; pulse microreactor [254,255]; gradientless reactor [256]; a riser simulator [39]; and continuous flow microreactor [257] have been used. However, in this study, a fixed-bed reactor (FBR) made of stainless steel tube having equivalent dimensions as the e-ZCMR was used to isomerize m-Xylene to p-Xylene. The lumen of the FBR was packed with 2.18 g of commercial Pt-HZSM-5 catalyst supplied by Süd-Chemie (specific surface > 500 m<sup>2</sup>.g<sup>-1</sup>; density, 0.53 g.cm<sup>-3</sup>). The catalyst was mixed with inert glass beads, increasing the total weight of the bed to 4.86 g. The catalytic bed was activated by passing H<sub>2</sub> over the catalytic bed for 3 hours at 673 K [13,186]. The feed containing 2.30 kPa m-Xylene saturated in N<sub>2</sub> gas was sent into the reactor at a flow rate of 10 mL(STP)/min, and the isomerization was carried out at a temperature range

573 K-673 K at a step increase of 50 K. The results obtained were compared with literature to ensure that the conversion was, indeed, below equilibrium position.

Table 6.1 shows the results obtained from this investigation and Table 6.2 depicts the m-Xylene isomerization equilibrium product distribution as reported in open literature. When the results in the tables are compared, it is clear that the amount of catalyst, 2.18 g, will enable m-Xylene conversion below equilibrium at the feed flow rate of 10 mL (STP)/min. As a result of this, subsequent isomerization experiments reported in this study were carried out at the established condition (mass of catalyst: 2.18 g; total weight of the bed: 4.86 g; and feed flow rate: 10 mL (STP)/min).

Table 6.1: Near equilibrium product distribution in FBR obtained in this study

Near equilibrium product distribution for m-Xylene isomerization (%)			
T (K)	MX	OX	PX
573	52.8	27.4	19.8
623	51.9	28.5	19.6
673	50.7	29.6	19.7

Table 6.2: Equilibrium product distribution obtained from open literature

Equilibrium product distribution for m-Xylene isomerization (%)				
T (K)	MX	OX	PX	Refs.
573	53.6	22.5	23.9	[258,259]
623	52.9	23.4	23.7	[260]
673	52.3	24.1	23.5	[258,259]

The set-up used for carrying out the m-Xylene isomerization experiments with e-ZCMR is the same as one used above and for the VP tests. Specifically, in the catalytic tests, the lumen of the tubular MFI-alumina membrane was packed with 2.18 g of commercial Pt-HZSM-5 catalyst to the configuration schematically depicted in Fig. 6.1 and Fig. 6.2. The catalyst was mixed with glass beads, increasing the total weight of the bed to 4.86 g and the catalytic bed was activated as described in section 6.2.2. Meta-xylene saturated in N<sub>2</sub> was fed into the reactor at a partial pressure in the range 2.45-2.84 kPa and at a flow rate of 10 mL(STP)/min, while the permeate side (for e-ZCMR) was swept with N<sub>2</sub> at a flow rate of 40 mL(STP)/min. The temperature was kept in the range 523-673 K. For comparison with a conventional FBR, a stainless steel tube with the same dimensions as the e-ZCMR was used and packed with the same amount of fresh Pt-HZSM-5 catalyst, while the isomerization reaction was carried out at the same operating conditions. Again, for comparison, some

experiments were carried out packing the catalyst between the outer side of the membrane tube, close to the outermost layer and the module shell. After attaining stability in 4 hours, the streams were sent to GC for analysis.

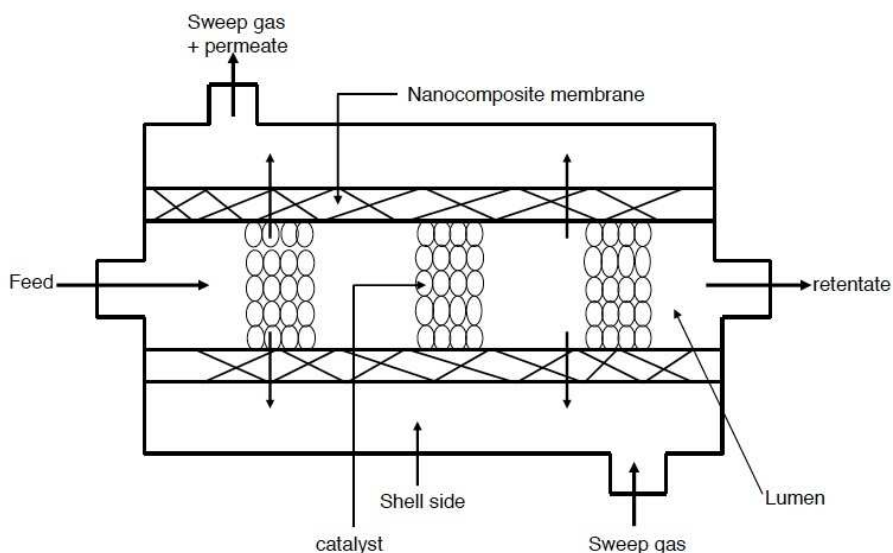


Figure 6.1: Schematic of an e-ZCMR based on MFI-alumina catalytic membrane reactor with the catalyst packed in the lumen of the membrane tube.

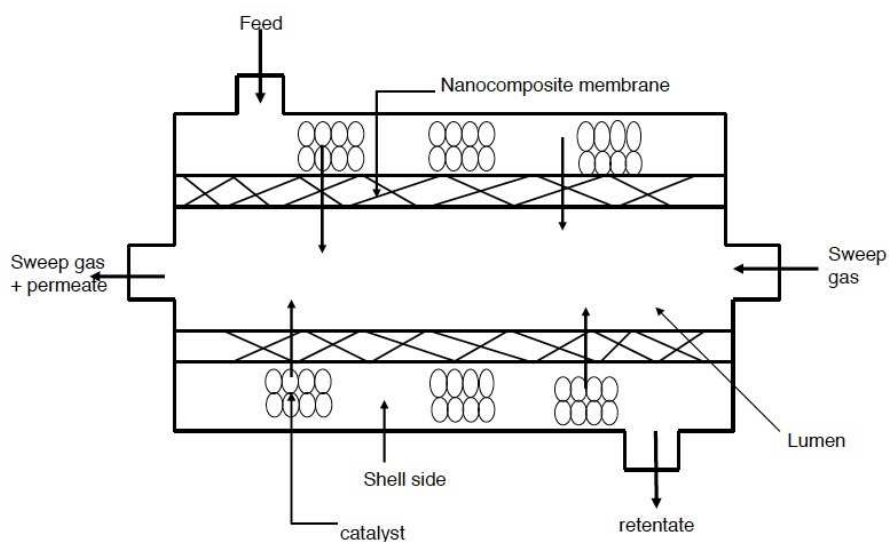


Figure 6.2: Schematic of an e-ZCMR based on MFI-alumina catalytic membrane reactor with the catalyst packed between the outer side membrane tube and the module shell.

---

For each experiment, m-Xylene conversion ( $X_{MX}$ ), p-Xylene yield ( $Y_{PX}$ ) and p-Xylene selectivity ( $S_{PX}$ ) were calculated using the set of Eq. 6.1 to Eq. 6.7:

$$X_{MX} = \frac{(x_{MX} \cdot Q)^{feed} - (x_{MX} \cdot Q)^{perm+ret}}{(x_{MX} \cdot Q)^{feed}} \quad (6.1)$$

$$Y_{PX}^{ret} = \frac{(x_{PX} \cdot Q)^{ret}}{(x_{MX} \cdot Q)^{feed} - [(x_{MX} \cdot Q)^{ret} + (x_{MX} \cdot Q)^{perm}]} \cdot 100\% \quad (6.2)$$

$$Y_{PX}^{perm} = \frac{(x_{PX} \cdot Q)^{perm}}{(x_{MX} \cdot Q)^{feed} - [(x_{MX} \cdot Q)^{ret} + (x_{MX} \cdot Q)^{perm}]} \cdot 100\% \quad (6.3)$$

$$S_{PX}^{ret} = \frac{(x_{PX} \cdot Q)^{ret}}{(x_{PX} \cdot Q)^{ret} + (x_{OX} \cdot Q)^{ret}} \cdot 100\% \quad (6.4)$$

$$S_{PX}^{perm} = \frac{(x_{PX} \cdot Q)^{perm}}{(x_{PX} \cdot Q)^{perm} + (x_{OX} \cdot Q)^{perm}} \cdot 100\% \quad (6.5)$$

$$S_{PX}^{comb} = \frac{(x_{PX} \cdot Q)^{perm} + (x_{PX} \cdot Q)^{ret}}{[(x_{PX} + x_{OX}) \cdot Q]^{perm} + [(x_{PX} + x_{OX}) \cdot Q]^{ret}} \cdot 100\% \quad (6.6)$$

$$Y_{PX}^{comb} = Y_{PX}^{perm} + Y_{PX}^{ret} \quad (6.7)$$

where  $Q$ ,  $x$ ,  $Y$ , and  $S$  represent the volumetric flow rate in mL(STP)/min, mole fraction, yield and selectivity, respectively, of either, PX, MX or OX. The analysis of results was based on permeate-only mode and combined mode operations. Permeate-only mode considers products in the permeate stream and the combined mode considers both the permeate stream and the retentate. Some replicated experiments showed that m-Xylene conversion, p-Xylene yield and selectivity were accurate to within  $\pm 10\%$ .

---

## 6.3 Results and discussion

### 6.3.1 Membrane preparation, characterization and separation test

After pre-treatment, the membrane prepared in this study showed a room-temperature pure hydrogen permeance of  $0.31 \mu\text{mol.m}^{-2}.\text{s}^{-1}.\text{Pa}^{-1}$  and a separation factor of 66 for *n*-butane/H<sub>2</sub> separation. This latter value reflects a good membrane quality in terms of low amount of inter-crystalline defects. Furthermore, the SEM micrograph (Fig.6.3) confirm the formation of a nanocomposite material on the substrate, that is, no continuous MFI film formation on the top of the support and good pore plugging of the  $0.2 \mu\text{m}$  layer with zeolite crystals. The EDX analyses show an average Si/Al ratio of about 10-20 (semi-quantitative analysis) on the inner active layer. The material in the active layer corresponds accordingly to an Al-enriched HZSM-5 zeolite.

Figure 6.4 shows the xylene coverage (in terms of xylene partial pressures) in the permeate side of the membrane as a function of sweep gas flow rate. From Fig.6.4, it can be observed that the xylene coverage (indicated by the *p*-Xylene partial pressures) decreased to a value of about 0.02 kPa from the value of about 0.18 kPa as sweep gas flow rate increased to 40 mL(STP)/min (where the partial pressure of *p*-Xylene is small or ideally null) from 5 mL(STP)/min. Beyond 40 mL(STP)/min, no further decrease in partial pressure of *p*-Xylene or xylene coverage is practically possible. Thus, 40 mL(STP)/min was used throughout for isomerization in this study. Figure 6.5 confirms the *p*-Xylene preferential separation of the membrane, achieving a maximum *p*-Xylene flux of about  $3.5 \mu\text{mol.m}^{-2}.\text{s}^{-1}$  with a maximum *p*-Xylene permeance of about  $10 \text{ nmol.m}^{-2}.\text{s}^{-1}.\text{Pa}^{-1}$  at about 450 K, with *p*/*o* and *p*/*m* mixture separation factors up to 50 and 55, respectively. In most permeation experiments, no *m*-Xylene was found in the permeate streams. Accordingly, the corresponding partial pressures have been estimated from the detection limit of the GC (0.001 kPa). Furthermore, during the separation test, no isomerization products were detected in the permeate and the retentate streams indicated that the membrane was inert to xylene isomerization during this period. It should be emphasized also that the membrane maintained a repeatable separation performance despite several thermal cycles it went through to conduct the separation test. This testifies to the high thermal stability of the membrane.

The permeation behaviour of *p*-Xylene as a function of temperature depicted in Fig. 6.4 is qualitatively consistent with the trends already found in previous studies on either nanocomposite MFI-alumina membranes or hollow fibres [186,242,248]. The *p*-Xylene flux shows a maximum value of  $3.5 \mu\text{mol.m}^{-2}.\text{s}^{-1}$ , at about 450 K, corresponding to a permeance of about  $9.5 \text{ nmol.m}^{-2}.\text{s}^{-1}.\text{Pa}^{-1}$ . The highest attainable *p*/*o* and *p*/*m* xylene separation factors are about 50 and 55, respectively. It is noteworthy that, compared to the previous studies [186,242,248], the membrane shows comparable *p*/*o* and *p*/*m* separation factors at the

---

maximum temperature, while usually the former separation factors are about one order of magnitude higher. The lower capacity of this membrane, to discriminate *o*-Xylene, should be attributed to a higher amount of intercrystalline defects in the membrane, as can be deduced from the lower *n*-butane/H<sub>2</sub> separation factors at room temperature (66 vs. >100). Additionally, this observation might be attributed to the higher concentration of *o*-Xylene in the feed in this study compared to the previous study [242]. At higher concentration of *o*-Xylene, *o*-Xylene flux through the membrane is enhanced due to its higher coverage at the feed side.

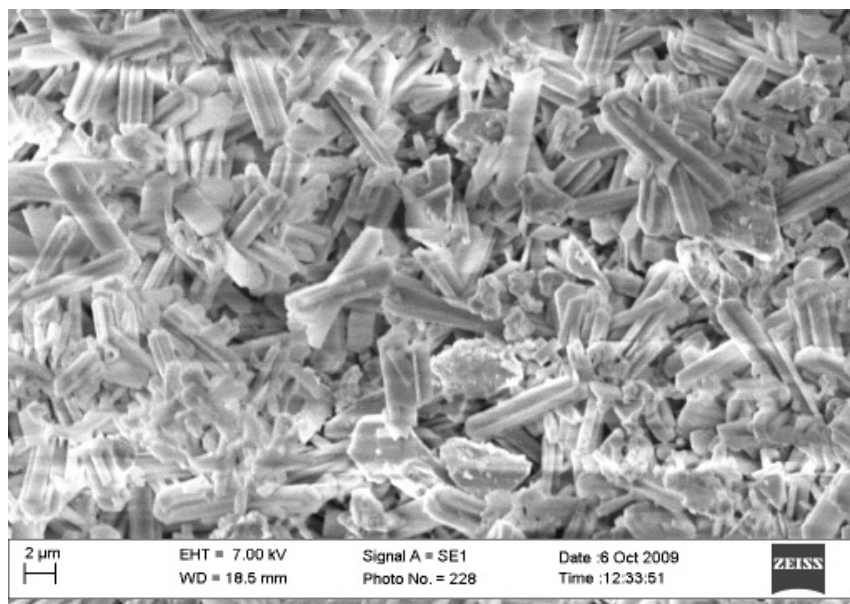


Figure 6.3: SEM micrograph of the membrane showing formation of a nanocomposite zeolite material embedded in the 0.2 μm layer of the support.

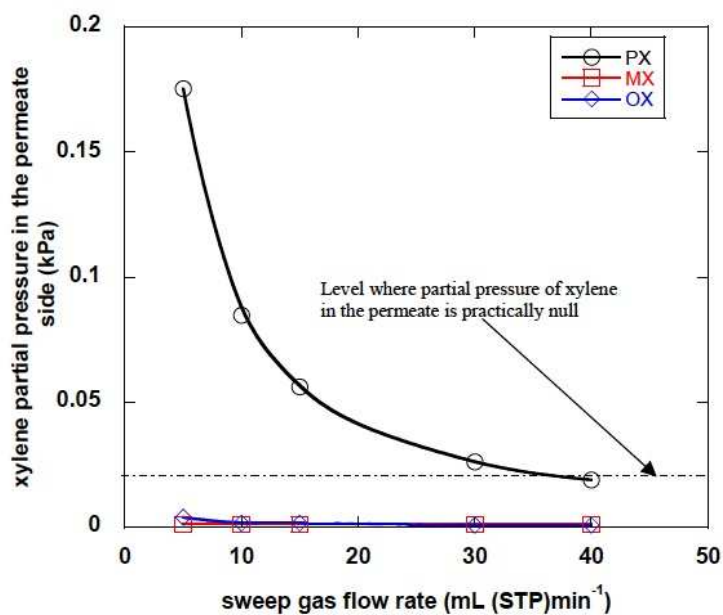


Figure 6.4: Separation performance of nanocomposite MFI-alumina membranes as a function of sweep gas flow rate.

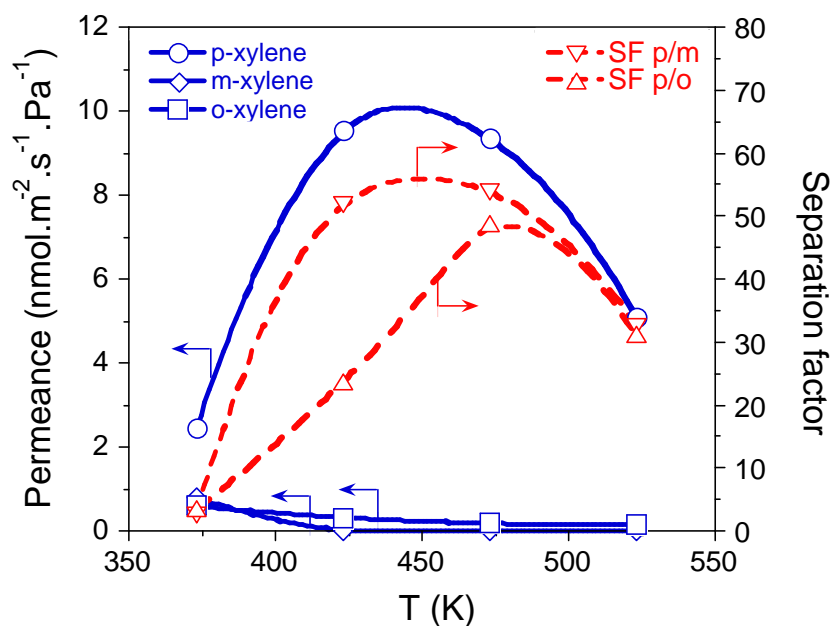


Figure 6.5: Separation performance of nanocomposite MFI-alumina membranes as a function of temperature. Experimental conditions: Feed flow rate, 10 mL(STP)/min; sweep gas flow rate for an e-ZCMR, 15 mL(STP)/min; feed composition (p/m/o), 0.51 / 0.34 / 0.59 kPa.

---

### 6.3.2 Meta-xylene isomerization

Figure 6.6 plots the results for a representative m-Xylene isomerization experiment performed on an e-ZCMR at 573 K. A significant transformation of m-Xylene into p-Xylene is obtained, with a p-Xylene yield and selectivity, about 25 and 45%, respectively, for combined mode operation.

Figure 6.7 to Figure 6.9 plot the influence of temperature (range 523-673 K), GHSV, reaction time and catalyst position in the reactor (i.e. in the tube lumen or in the module shell) on the m-Xylene isomerization performance of a FBR and an e-ZCMR packed with Pt-HZSM-5 catalyst in terms of p-Xylene yield, selectivity and m-Xylene conversion. As can be seen in Fig. 6.7 to Fig 6.9, higher m-Xylene conversions and p-Xylene yields can be obtained in the e-ZCMR compared to the FBR with the catalyst packed in the tube lumen due to selective p-Xylene extraction from the reaction zone by the membrane. The m-Xylene conversion reaches a value of about 62% at 523 K in the ZCMR, the p-Xylene yield and selectivity attaining values, up to 28% and 46%, respectively, in combined mode.

Table 6.5 lists the p-Xylene and o-Xylene productivities at 573 K at permeate-only mode and combined mode for the three reactor configurations considered in this study, namely FBR, e-ZCMR-IN and e-ZCMR-OUT. As can be seen, the higher p-Xylene productivity corresponds to the e-ZCMR-IN configuration, approaching a value of about  $12.1 \text{ nmol.s}^{-1}.\text{g}_{\text{cat}}^{-1}$  at combined mode operation.

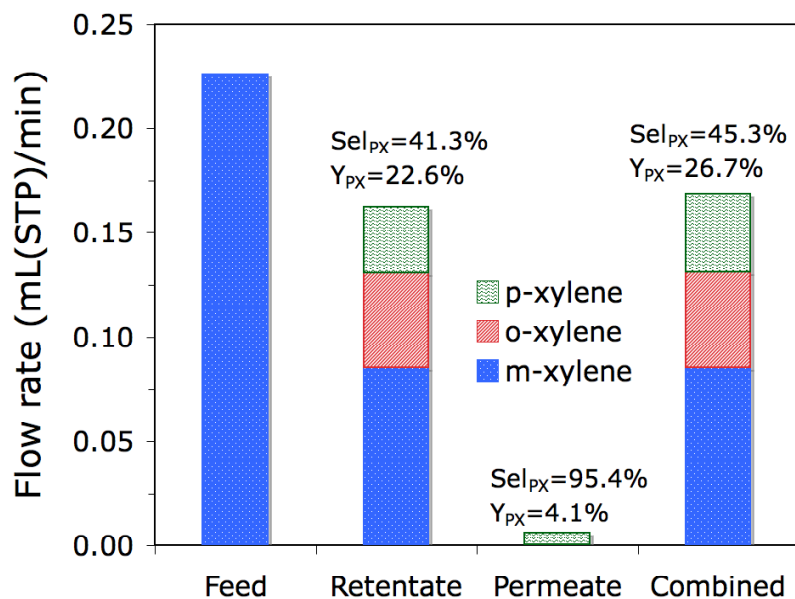


Figure 6.6: m-Xylene isomerization over Pt-HZSM-5 in an e-ZCMR at 573 K with the catalyst packed in the tube lumen. The combined mode corresponds to the addition of the retentate and permeate streams. Experimental conditions: feed composition, 2.30 kPa m-Xylene in 10 mL(STP)/min N<sub>2</sub>; sweep gas flow rate into e-ZCMR, 40 mL(STP)/min; reaction time, 30 min.

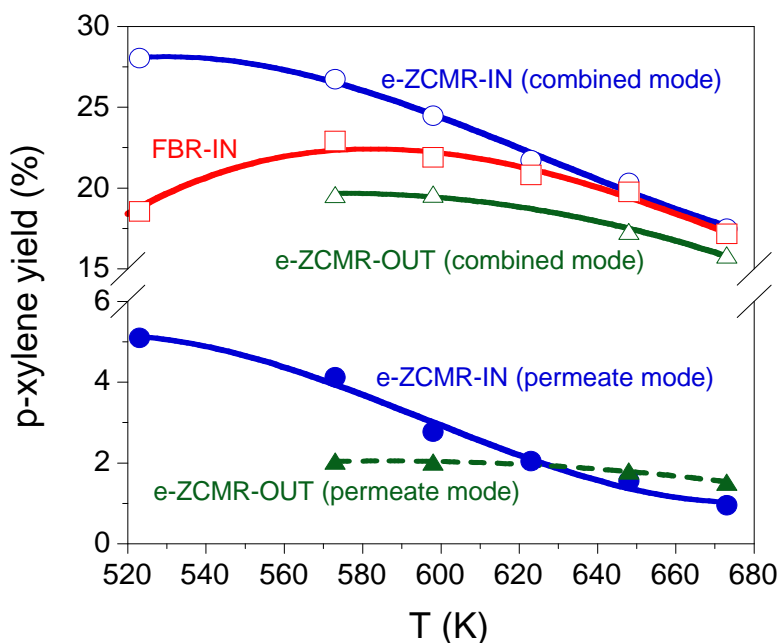


Figure 6.7: m-Xylene isomerization over Pt-HZSM-5 in an e-ZCMR and a FBR as a function of temperature and catalyst packing (IN, catalyst packed in the tube lumen; OUT, catalyst packed in the shell) showing the p-Xylene yield. Experimental conditions: feed composition, 2.30 kPa m-Xylene in 10 mL(STP)/min N<sub>2</sub>; sweep gas flow rate into e-ZCMR, 40 mL(STP)/min; reaction time, 30 min.

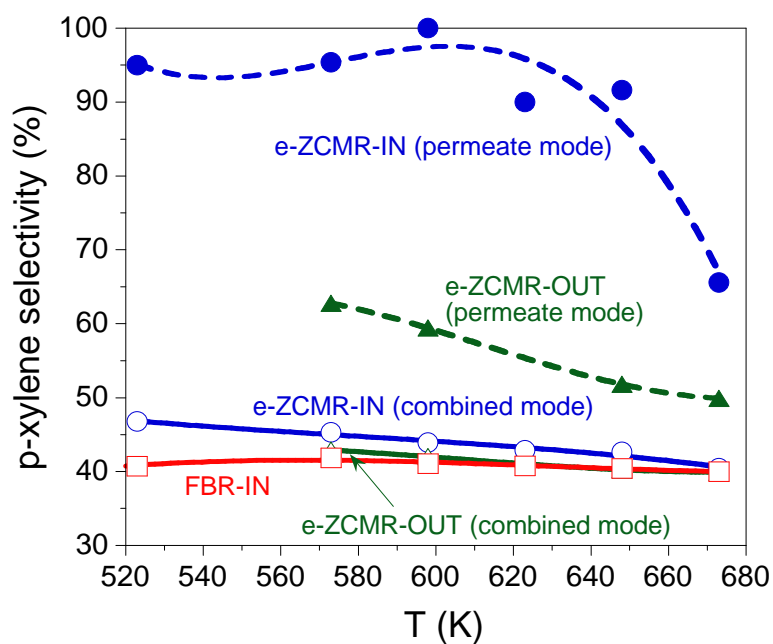


Figure 6.8: m-Xylene isomerization over Pt-HZSM-5 in an e-ZCMR and a FBR as a function of temperature and catalyst packing (IN, catalyst packed in the tube lumen; OUT, catalyst packed in the shell) showing the p-Xylene selectivity. Experimental conditions: feed composition, 2.30 kPa m-Xylene in 10 mL(STP)/min N<sub>2</sub>; sweep gas flow rate into e-ZCMR, 40 mL(STP)/min; reaction time, 30 min.

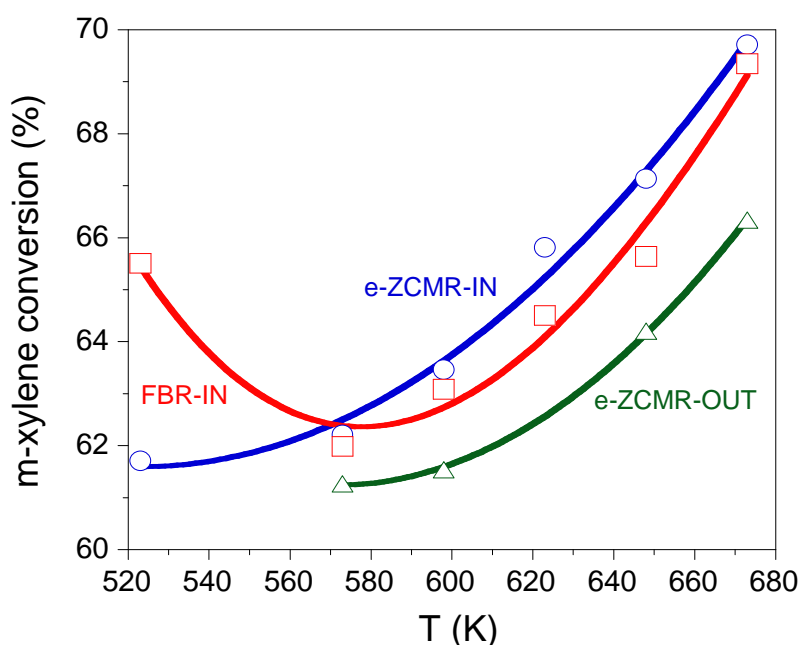


Figure 6.9: m-Xylene isomerization over Pt-HZSM-5 in an e-ZCMR and a FBR as a function of temperature and catalyst packing (IN, catalyst packed in the tube lumen; OUT, catalyst packed in the shell) showing the m-Xylene conversion. Experimental conditions: feed composition, 2.30 kPa m-Xylene in 10 mL(STP)/min N<sub>2</sub>; sweep gas flow rate into e-ZCMR, 40 mL(STP)/min; reaction time, 30 min.

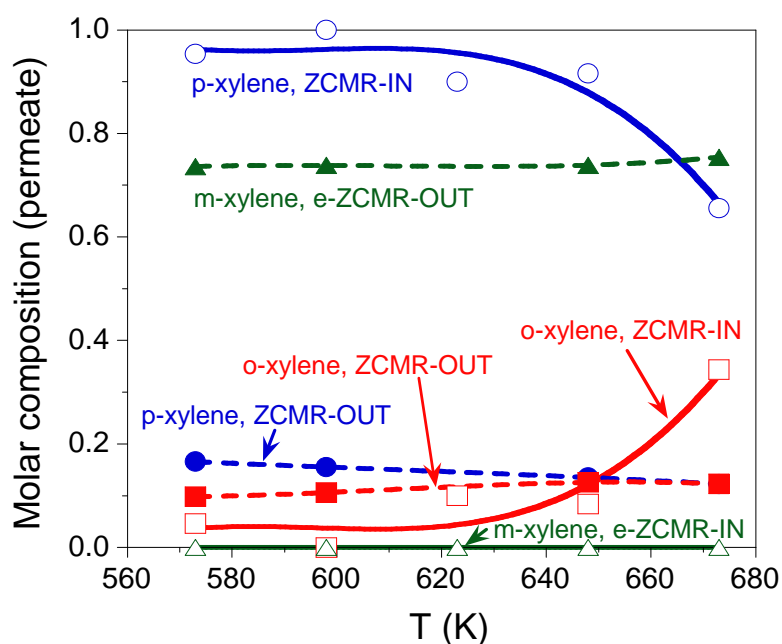


Figure 6.10: p-Xylene, m-Xylene and o-Xylene molar composition in permeate in ZCMR-IN and ZCMR-OUT configurations as a function of temperature. Experimental conditions: feed composition, 2.30 kPa m-Xylene in 10 mL(STP)/min  $N_2$ ; sweep gas flow rate into e-ZCMR, 40 mL(STP)/min; reaction time, 30 min.

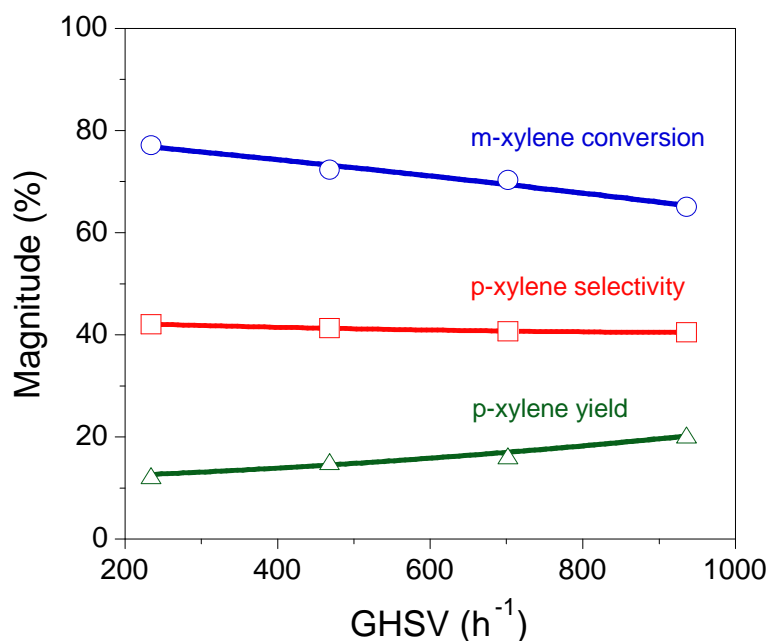


Figure 6.11: m-Xylene isomerization over Pt-HZSM-5 in an e-ZCMR at 673 K as a function of the GHSV. Experimental conditions: sweep gas flow rate into e-ZCMR, 40 mL(STP)/min; reaction time, 30 min.

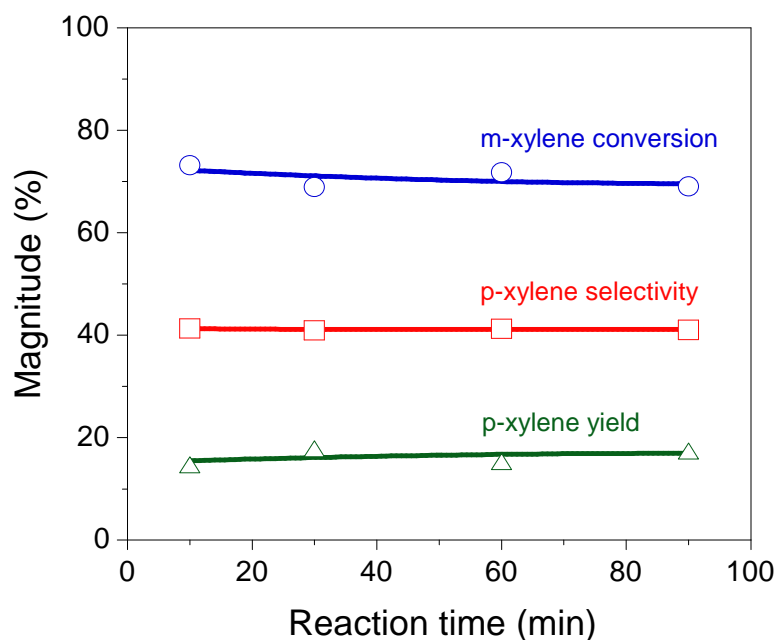


Figure 6.12: m-Xylene isomerization over Pt-HZSM-5 in an e-ZCMR at 673 K and 2.84-kPa m-Xylene feed partial pressure as a function of the reaction time. Experimental conditions: sweep gas flow rate into e-ZCMR, 40 mL(STP)/min.

Table 6.3: Productivities in FBR, e-ZCMR-IN and e-ZCMR-OUT configurations at permeate-only mode (top values) and combined mode (bottom values). Experimental conditions: temperature, 573 K; m-Xylene feed partial pressure, 2.84 kPa; feed flow rate, 10 mL(STP)/min; sweep gas flow rate, 40 mL(STP)/min

Product	Productivity (nmol.s <sup>-1</sup> .g <sub>cat</sub> <sup>-1</sup> )		
	FBR	e-ZCMR-IN	e-ZCMR-OUT
p-Xylene	-	2.0	1.4
	10.7	12.1	11.2
o-Xylene	-	0.1	0.8
	14.9	15.4	15.4

The results plotted in Fig. 6.7 show that, packing the catalyst in the membrane lumen, an increase of about 18% in the p-Xylene yield (from 18 to 28%) at 523 K can be reached in an e-ZCMR over a conventional FBR due to selective p-Xylene removal by the membrane (the p-Xylene selectivity in permeate-only mode approaches 100% < 573 K). The difference matches the p-Xylene yield measured for permeate-only mode (~5%). The higher p-Xylene yield at lower temperatures (i.e. 523 K) can be attributed to a higher concentration between the membrane and catalyst activities, providing a higher efficiency of the membrane reactor and consequently a higher differential in terms of p-Xylene yield compared to a FBR. Note

---

that the maximum p-Xylene permeance and membrane selectivity to p-Xylene is obtained at about 473 K. Moreover, lower temperatures are also beneficial due to the reduction of formation of by-products (i.e. toluene, trimethylbenzene and ethylbenzene).

Regarding the effect of GHSV on the isomerization in e-ZCMR, Fig. 6.11 shows that residence time does not exert a remarkable influence on either the p-Xylene yield or the selectivity. This observation, also reported by Zhang *et al.* [190], can be attributed to a reduced influence of p-Xylene production through an intermolecular transalkylation mechanism responsible for toluene and trimethylbenzene formation, the diphenylmethane intermediates of this reaction acting as promoters of coke formation on strong acid sites [261].

### 6.3.3 Catalyst and membrane stability

As depicted in Fig.6.12, the p-Xylene yield, p-Xylene selectivity and m-Xylene conversion remain practically unchanged by increasing the reaction time from 10 to 90 min, this reflecting that a 'true' steady state was attained during the period. It is good to note that the experiment was conducted continuously for about 8 hours to collect the data for the data points reported in Fig. 6.12. Therefore, the time indicated in Fig. 6.12 is the reaction time before sampling to obtain data for each data point. The observation suggests that, although coke might be formed on the catalyst surface during the reaction, as evidenced from the mismatch in mass balances (see Fig. 6.7 to Fig. 6.9); this does not promote catalyst deactivation throughout the experimental period. As a matter of fact, the maximum computed coke loading on the catalyst after 90 minutes continuous operation is lower than 0.1 wt.% for both FBR and e-ZCMR configurations (see Daramola *et al.* [262]).

As explained in Daramola *et al.* [262], the coke formation rate is inhibited at lower temperatures (i.e. 523 K) in configuration e-ZCMR-IN compared to the FBR. This result is accompanied by a reduction of the m-Xylene conversion and an increase of the p-Xylene yield, as shown in Fig. 6.7 and Fig. 6.9. As reported and explained in [262], a reduction of coke formation occurred at lower temperatures in e-ZCMR-IN configuration. The reduction of coke formation in e-ZCMR-IN configuration at lower temperatures suggests a higher role of m-Xylene isomerization through an intramolecular catalytic mechanism based on benzenium-ion intermediates instead of an intermolecular transalkylation mechanism promoting coke generation by disproportionation. Therefore, the reduction of coke formation in e-ZCMR-IN configuration should necessarily involve a reduction of diphenylmethane intermediates due to the selective p-Xylene extraction by the membrane, promoting isomerization through an intramolecular mechanism. This effect is expected to be more intense in the case of HZSM-5 catalysts than for HFAU zeolites due to the reduced pore size of the ZSM-5 channels, providing higher steric hindrance and inhibiting therefore the formation of bulky diphenylmethane intermediates.

---

### 6.3.4 Effect of reactor configuration

Regarding the effect of reactor configuration, Fig. 6.7 shows that, for the three configurations considered (i.e. e-ZCMR-IN, e-ZCMR-OUT and FBR), the p-Xylene yield decreases with temperature in the range 523-673 K (combined mode). However, while the p-Xylene yield evolves practically linearly with temperature in configuration e-ZCMR-IN while reducing the temperature, the trend becomes inhibited at lower temperatures for the other two configurations, showing almost a plateau. Furthermore, Fig. 6.10 depicts the molar compositions of p-Xylene, m-Xylene and o-Xylene in the permeate stream. As can be seen in Fig. 6.10, in e-ZCMR-IN, molar composition of p-Xylene approached 1.0 at about 600 K, but decreased as temperatures increased. But the molar composition of o-Xylene at this temperature was <0.1. At 600 K, the molar compositions of p-Xylene and o-Xylene in e-ZCMR-OUT were <0.2. These observations should be ascribed to the positive role of the membrane in p-Xylene extraction in the former case. In the case of configuration e-ZCMR-OUT, the trend of the p-Xylene yield with the temperature suggests a reduced effect of the membrane on the catalytic performance. The lack of membrane efficiency might be explained on the basis of diffusion limitations in the membrane support, as permeation proceeds from the outer surface to the inner top layer. Similar conclusions have been addressed recently by Zhang *et al.* [190].

### 6.3.5 Results compared with literature

Table 6.4 shows the results of this study compared with comparable results listed in Table 2.6 and reported in the literature on m-Xylene isomerization in e-ZCMRs using Pt-HZSM-5 and Pt/alumina-silica catalysts. Despite the different reaction conditions considered by these authors (e.g., GHSV, feed composition, membrane geometry), the results presented are comparable in terms of p-Xylene yield and selectivity enhancement. This could be attributed to the higher quality of the nanocomposite membranes prepared and used in this study, with permeances up to  $9.5 \text{ nmol.m}^{-2}.\text{s}^{-1}.\text{Pa}^{-1}$  and p/o and p/m-Xylene separation factors >50. Another interesting outcome of the selectivity of these membranes is the high purity of p-Xylene in the permeate, achieving molar fractions of about 95% at 573 K. Note that, for comparison, Zhang *et al.* [190] achieved p/m separation factors of only 16. The results presented in this study also improve significantly on the p-Xylene yields previously reported by van Dyk *et al.* [186].

Table 6.4: Comparison of the results obtained in this study with the literature

Membrane type/support	T (K)	P-Xylene yield (%)		P-Xylene sel. (%)		Refs.
		e-ZCMR	FBR	e-ZCMR	FBR	
Film-like Inert Ba-ZSM-5/SS e-CMR <sup>b</sup>	643	25	21	69	52	[198]
Inert silicalite/ $\alpha$ -alumina disk <sup>a</sup>	603	21.3	18.5	44.6	35	[190]
Catalytic H-ZSM-5/SS disk e-CMR <sup>a</sup>	673	6.9	5.87	66.7	55.6	[182]
Nanocomposite inert silicalite-1/ tubular $\alpha$ -alumina e-ZCMR <sup>a</sup>	577	11.2	10.2	65	58	[186]
Nanocomposite MFI-alumina e-ZCMR <sup>a</sup>	523	27	23	49	42	This study

<sup>a</sup>m-Xylene as feed; <sup>b</sup>ternary mixture of xylene isomer as feed

#### 6.4 Ultra-pure p-Xylene production via m-Xylene isomerization in e-ZCMR

In the previous section, an attempt was made to investigate the performance of e-ZCMR during m-Xylene isomerization over Pt-HZSM-5 catalyst and to compare the performance of e-ZCMR with a FBR for the transformation of m-Xylene to p-Xylene via isomerization reaction over a Pt-HZSM-5 catalyst. Furthermore, the influence of operating variables on the performance of the system was studied. Overall, the results have shown that e-ZCMR perform better than the FBR. The study has shown also that the p-Xylene purity in the permeate could reach 95%. However, for industrial application of p-Xylene, p-Xylene purity >95% is required. To achieve this purity level based on membrane technology, defect-free MFI membranes are necessary.

In Chapter 4 of this dissertation, separation performance of a tubular nanocomposite MFI-alumina membrane is reported. The separation performance indicated that the membrane has little or no inter-crystalline defects. Hence, the membrane is “defect-free”. The membrane was used in an e-ZCMR to explore the possibility of obtaining ultra-pure (~100% purity) p-Xylene from m-Xylene isomerization over Pt-HZSM-5 catalyst. The experimental procedure in this test followed the procedure described in sub-section 6.2.2. Moreover, for better understanding of the behaviour at lower reaction temperature, the reaction was conducted from 473 K to 573 K. To provide concrete evidence for the influence of sweep gas

---

flow rate on the performance of e-ZCMR during m-Xylene isomerization, the experiment was conducted at sweep gas flow rate of 5 mL(STP)/min.

#### 6.4.1 Results and discussion

Figure 6.13 showed that the p-Xylene yield increases with decrease in temperature. This is consistent with the observation reported in sub-section 6.3.2. The p-Xylene yield increased from 2.2% at 573 K approaching a maximum of about 2.7 % at 473 K (see Fig 6.13) with p-Xylene purity in the permeate approaching molar fractions of about 100% (see Figure 6.14 and Table 6.5) in the permeate-only mode. Figure 6.14 also plots the results for a representative m-Xylene isomerization experiment performed on the e-ZCMR at 473 K. At 473 K, purity of p-Xylene and para-selectivity of the membrane were both 100% in permeate-only mode (see Fig. 6.14). In the combined mode operation, a maximum p-Xylene yield of 19.0 % was obtained at 473 K (see Figure 6.14). The relative increase in p-Xylene selectivity and p-Xylene purity, obtained with this membrane tube in the permeate-only mode compared to the previous studies (see section 6.3 and [262]), could be attributed to its higher separation factors (p/o and p/m) and p-Xylene permeance. In fact, throughout the temperature range investigated, the membrane displayed 100% selectivity to p-Xylene in permeate-only mode, but the selectivity reduced to about 48% at combined mode (Fig. 6.15).

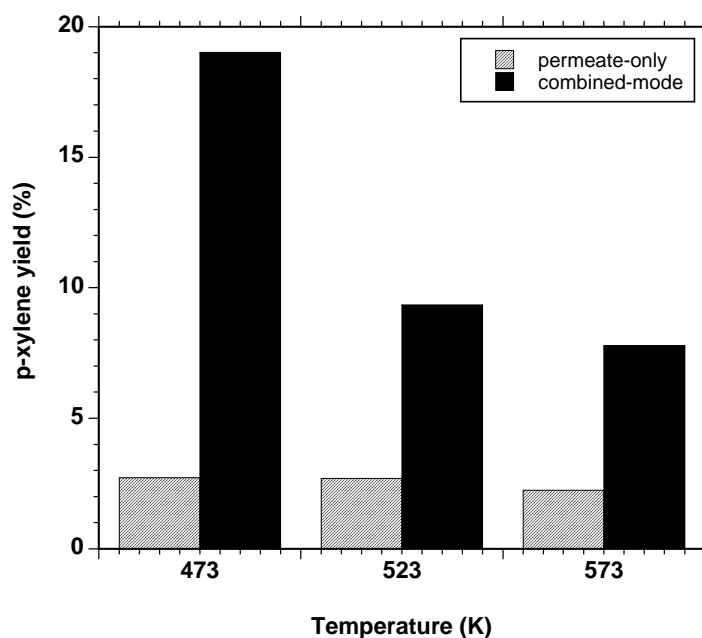


Figure 6.13: p-Xylene yield as a function of temperature Experimental conditions: feed composition, 2.30 kPa m-Xylene in 10 mL(STP)/min N<sub>2</sub>; sweep gas flow rate into e-ZCMR, 5 mL(STP)/min; reaction time, 30 min.

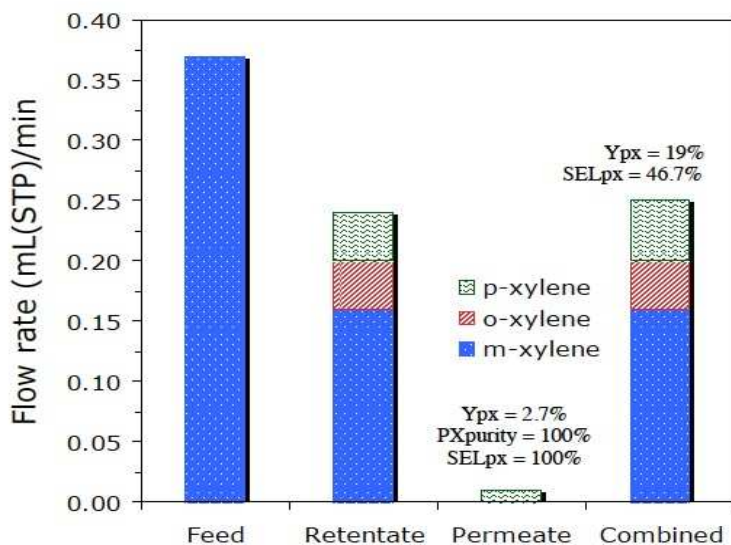


Figure 6.14: Xylene distribution in the feed and the product streams (permeate and retentate) at combined mode in e-ZCMR. Experimental conditions: Feed composition: 0.37 mL/min-MX. Sweep gas flow rate: 5mL (STP)/min. Reaction temperature: 473 K.

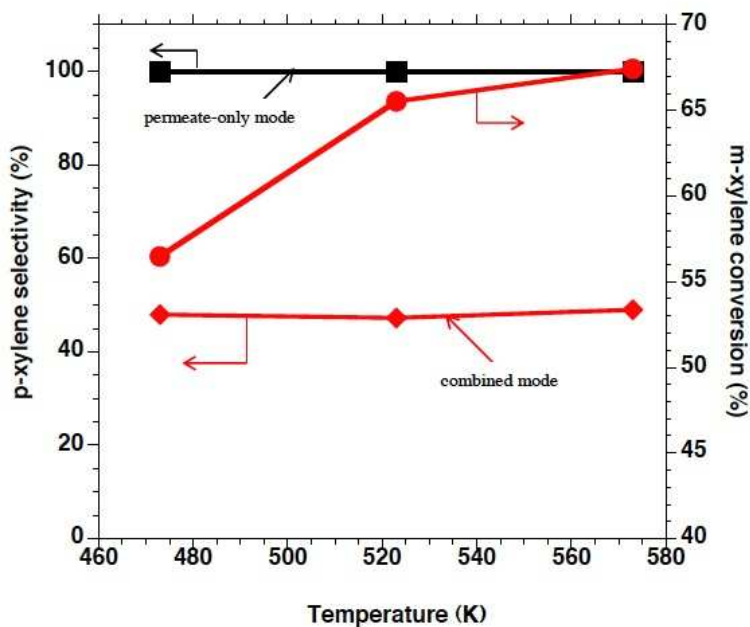


Figure 6.15: p-Xylene selectivity and m-Xylene conversion as a function of temperature in e-ZCMR. Experimental conditions: feed composition, 2.30 kPa m-Xylene in 10 mL(STP)/min  $N_2$ ; sweep gas flow rate into e-ZCMR, 5 mL(STP)/min; reaction time, 30 min.

Table 6.5: Representative performance of e-ZCMR at 473 K

e-ZCMR		
	Permeate-only mode	Combined mode
PX yield (%)	2.7	19.0
PX selectivity (%)	100.0	46.7
MX conversion (%)	-	56

Comparing the p-Xylene yield in the permeate-only mode with the results reported in a previous study [262], a disparity of about 1.4% was observed (although at a lower temperature, 473 K; see Fig. 6.14 and Table 6.5). This disparity could be attributed to the lower quality of the membrane used in the previous study compared to this study ( $p/o > 400$  vs  $p/o = 50$ ) and partly to the sweep gas flow rate used (5 mL(STP)/min in this study versus 40 mL(STP) in ref. [262]). It is expected that at a higher sweep gas flow rate, the p-Xylene flux through the membrane is enhanced due to the decrease in xylene coverage on the permeate side [242]. Furthermore, Table 6.6 shows the productivity of p-Xylene and o-Xylene in e-ZCMR in permeate-only mode (top values) and combined mode (bottom values) at 473 K. As can be seen in Fig. 6.6, the p-Xylene productivity is  $1.8 \text{ nmol.s}^{-1}.\text{g}_{\text{cat}}^{-1}$  in permeate-only mode with no o-Xylene. But in combined mode, p-Xylene and o-Xylene productivities are  $17.8 \text{ nmol.s}^{-1}.\text{g}_{\text{cat}}^{-1}$  and  $22.5 \text{ nmol.s}^{-1}.\text{g}_{\text{cat}}^{-1}$ , respectively.

Nevertheless, the results presented in this study are consistent with the behaviour observed in the previous studies and have shown that it is possible to produce ultra-pure p-Xylene with e-ZCMR. The results have shown also the possibility of obtaining an increase in p-Xylene yield in e-ZCMR compared to a FBR at operating temperature lower than the operating temperature currently applied in the industry (about 673 K), but with a trade-off between p-Xylene yield and p-Xylene selectivity at this temperature i.e., as far as combined-mode operation is concerned. Regarding the p-Xylene purity, at 473 K an improvement of 4.5% is obtained compared to the previous studies. Results presented in this section also affirm the possibility of p-Xylene purity enhancement in e-ZCMR even at a lower temperature. At the same time, the results of the study further substantiate the relative advantages of the nanocomposite architecture over the “film-like” in MFI-type zeolite membranes.

---

Table 6.6 Productivity in e-ZCMR in permeate only mode (top values) and combined mode (bottom values) in (nmol.s<sup>-1</sup>.gcat<sup>-1</sup>) at 473 K.

Product	e-ZCMR
PX	1.8
	17.8
OX	0.0
	22.5

## 6.5 Concluding remark

The results presented in this study further substantiate and confirm the potential of e-ZCMRs compared to the conventional FBRs for m-Xylene selective isomerization to p-Xylene. The membrane reactor has displayed a maximum p-Xylene yield of 5.1% at 523 K when computed at permeate-only mode, decreasing with temperature. At combined mode, the p-Xylene yield was about 28%, showing an increase of about 18% over an equivalent fixed-bed reactor. The selectivity of the membrane approached 100% towards p-Xylene at permeate-only mode, displaying a maximum value of about 42% at 523 K during combined mode. Higher performance was obtained when the catalyst packing was close to the inner top layer of the membrane support. Furthermore, the study revealed that gas-hourly-space-velocity (GHSV) does not have significant influence on the performance of e-ZCMR.

On the basis of the high p/o and p/m- xylene separation factors offered by the membrane, xylene compositions of about 95% can be achieved in the permeate stream for both membrane reactor configurations. Additionally, using a defect-free MFI-alumina membrane tube with p/o separation factor >400, it is shown that ultra-pure p-Xylene with xylene composition approaching 100% in the permeate side can be obtained even at a lower temperature of 473 K. However, more research efforts are needed in terms of membrane development to increase p-Xylene flux through the membrane while keeping the p-Xylene selectivity at present values. It is noteworthy to mention that during the experiments described in this chapter, about 16-20% of xylene was lost to formation of by-products such as trimethylbenzenes (TMBs) or Toluene (T) or ethylbenzene (EB) via disproportionation of m-Xylene in the retentate side (as vividly shown by the discrepancies in the mass balance in Fig. 6.6 and Fig. 6.14). Interestingly, none of these by-products permeated through the membrane into the permeate side (no related peaks observed in the GC analysis of the permeate stream). Inability of these products to permeate through the membrane could be attributed to the good quality of the membranes used in this study, which could be attributed to the nanocomposite architecture of the membranes. Additionally, the utmost goal of the experimental studies was

---

to evaluate the performance of the membranes (in terms of paraselectivity, p-Xylene yield and p-Xylene purity) rather than the performance of the catalyst during the m-Xylene isomerization, therefore, the contribution of the by-products toward the mass balance in the retentate side was neglected. This explains the discrepancy observed in the mass balance between the compositions in feed and in the combined mode operation as depicted in Fig. 6.6 and Fig. 6.14., respectively. This observation is a pointer to the fact that development of e-ZCMR-adaptable high selective catalysts is essential for xylene isomerization in e-ZCMR because the catalyst used in this study was originally designed for fixed-bed reactors. Also, it is noteworthy to mention that the membranes were inert during the separation test because no isomerization product was detected in both the retentate and permeate streams.

The results presented in this chapter also have shown that it is possible to obtain 100% purity for p-Xylene in the permeate-only mode operation with p-Xylene selectivity approaching 100% in an e-ZCMR. With these results, the possibility of cutting down operational cost via a reduction in energy consumption could be feasible with the application of e-CMR because no additional units are needed to get ultra-pure p-Xylene. However, “defect-free” MFI-type zeolite membranes with appreciable p-Xylene flux are necessary to make this technology attractive and competitive with existing technologies. Furthermore, compared to conventional “film-like” membranes, MFI-type membranes with nanocomposite architecture could be a promising option to obtain defect-free MFI membranes for application in e-ZCMR to produce high purity p-Xylene.

To improve on p-Xylene flux through the membrane, membranes with smaller effective membrane wall thickness are essential. As demonstrated in Chapter 5 of this dissertation and also reported by Daramola *et al.* [248], the application of nanocomposite MFI-ceramic hollow fibre membranes for xylene isomer separation could increase p-Xylene flux by about 30% over conventional membrane tubes due to their much lower MFI effective thickness (<1  $\mu\text{m}$  vs. >3  $\mu\text{m}$ ). Another advantage of hollow fibres is their higher surface-to-volume ratios. These fibres could be optimized into fibre modules. The modules, when used in e-CMR, could increase p-Xylene productivity while reducing module layouts. Alternatively, the retentate streams can be recycled, leading into increased production of ultra-pure p-Xylene in the permeate side. The novel contributions described in this chapter have resulted into two scientific manuscripts publishable in international scientific journals. One has been accepted for publication in *Catalysis Today* and the second one is under review in *Applied Catalysis A: General*.

---

## Chapter 7: Modelling of e-ZCMR during m-Xylene isomerization

Modelling and sensitivity analysis of m-Xylene isomerization over Pt-HZSM-5 catalyst in an e-ZCMR equipped with a nanocomposite MFI-alumina membrane tube as separation unit, are reported in this chapter. Model output was compared with experimental results while sensitivity analysis was also carried out to evaluate the sensitivity of the model to changes in certain process/design parameters. It must be stressed that this modelling study was of a preliminary nature and not the main focus of the work. Nevertheless, it provided useful assistance in understanding the fundamental behaviour of e-ZCMR during m-Xylene isomerization and offered a platform upon which further modelling studies on m-Xylene isomerization in e-ZCMR could be built.

### 7.1 Introduction

Mathematical modelling of chemical and biochemical processes plays an increasing role in today's competitive industries. Such models are typically needed for various tasks including process design, process analysis and optimization of process conditions, as well as for model-based control [263]. Application of mathematical models to the design of membrane processes is considered to be a useful tool in understanding these processes [264-267].

In the area of catalytic membrane reactors for xylene isomerization, modelling studies are still limited. For the application of e-ZCMR for xylene isomerization to p-Xylene, the first and perhaps the only work in open literature was reported by Deshayes *et al.* [201]. These authors reported a modelling study of the xylene isomerization reaction in an industrial FBR, focusing on the effect of incorporating multi-tubes containing Na-ZSM-5/SS membranes on the catalytic performance of the reactor. They predicted a 12% increase in p-Xylene yield over an equivalent FBR. However, to gain more insight into the behaviour of extractor-type catalytic membrane reactors for xylene isomerization, an extensive modelling study is essential. In view of the aforementioned comments, this chapter presents mathematical modelling and simulation of a laboratory-scale e-ZCMR having a nanocomposite MFI-alumina membrane tube as separation unit. The overall goal was to understand the fundamental behaviour of the system and to compare the simulation results with experimental results for model validation. Compared to the study of Deshayes *et al.* [201] and a recent study by Yeong *et al.* [268], where an acid functionalized catalytic membrane reactor prepared on disk shape configuration was modelled, in this study a nanocomposite MFI-alumina membrane prepared on  $\alpha$ -alumina support via pore-plugging technique was used. Advantages of nanocomposite architecture over "film-like" have been highlighted and motivated in the previous chapters.

---

## 7.2 Model development and formulation

The e-ZCMR modelled in this study consists of a catalyst packed-bed membrane reactor. The lumen of the membrane tube is packed with catalyst, while the permeate side of the membrane is kept under counter-current sweep gas flow. In solving reaction engineering problems, mass balance, rate law and transport law are important. These are dealt with in the subsequent sections.

### 7.2.1 Reaction model

Two reaction schemes, 1,3-methyl shift and 1,2-methyl shift, have been proposed and used in literature to model xylene isomerization reactions [42,255,269-271]. In the 1,3-methyl shift, o-Xylene could be converted directly into p-Xylene and vice versa (o-Xylene to p-Xylene). This phenomenon is explained by the fast movement of the para isomer inside the porous catalyst which might cause an apparent 1,3 shift of the methyl group in the benzene ring [47]. The second scheme on the other hand, assumes that the reaction proceeds via 1,2-methyl shift only (o-Xylene to m-Xylene to p-Xylene) where one of the methyl groups in m-Xylene might shift to the adjacent positions through a series of consecutive, reversible 1,2-methyl shift mechanism and become o-Xylene or p-Xylene [272-278].

In the study of the kinetics of xylene isomerization over zeolitic catalysts, several modeling techniques have been applied to obtain numerous kinetic parameters of this complex reaction system. Techniques that have been used include analytical methods such as the Wei-Prater method [271,273,274], Laplace transform [278] and finite integral transform [255,256], Curve fitting method [42] and least-squares method [256,279]. Numerous kinetic parameters have been reported by these authors, adopting 1,3-methyl shift pathway (see Fig .7.1) or 1,2-methyl shift pathway (see Fig.7.2) for xylene transformation over zeolitic catalysts.

In the scientific community, there has been a controversy on which pathway is the most suitable. In this regard, a recent work by Al-Khattaf *et al.* [280] provides ample evidence to suggest that direct inter-conversion between o- and p-Xylene isomers (a 1,3-methyl shift) occurs with the same rate as the conversion of m- to o-Xylene (a 1,2-methyl shift) over ZSM-5 zeolite catalyst. The authors also argued that the 1,3-methyl shift reaction path is a better representation of the xylene isomerization mechanism in ZSM-5 zeolite than the 1,2-methyl shift. Therefore, going by the outcome of the work of Al-Khattaf *et al.* [280], the reaction modelling in this section adopts 1,3-Methyl shift for the transformation of m-Xylene over Pt-HZSM-5 catalyst as reported in the experimental study described in Chapter 6 of this dissertation.

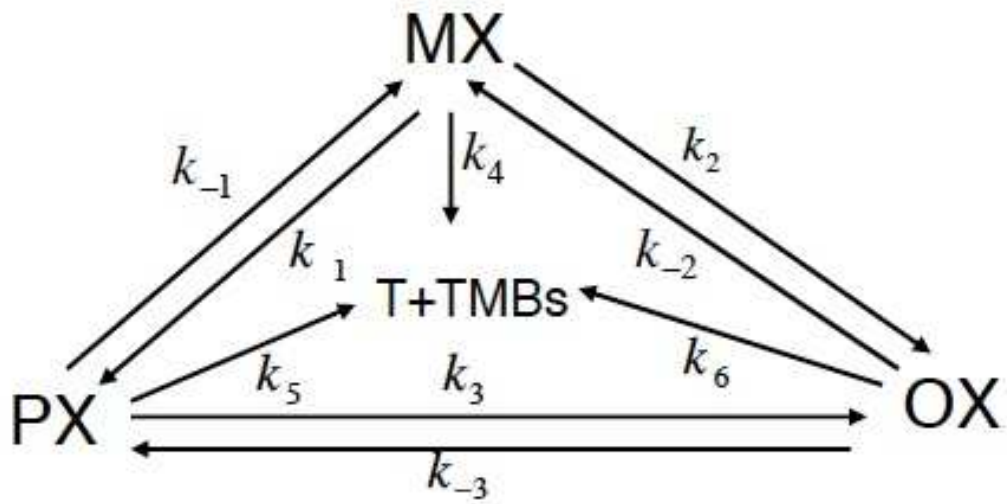


Figure 7.1: Xylene isomerization pathways of 1,3-methyl shift pathway (adapted from [280]).

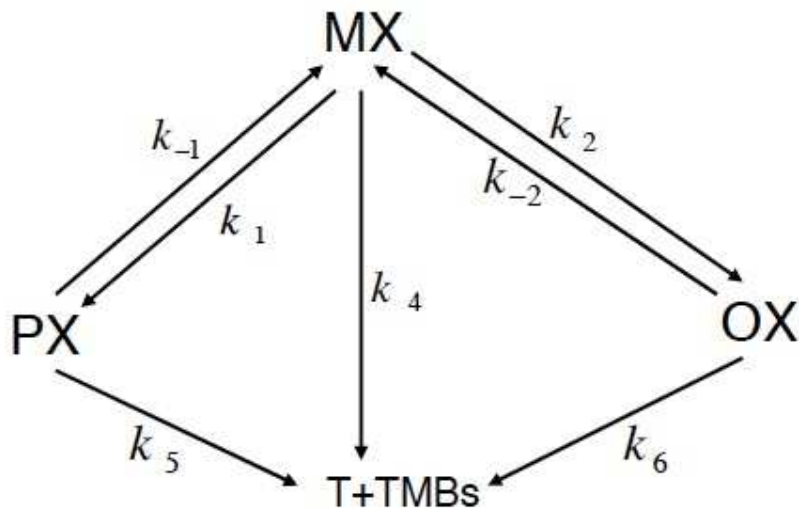


Figure 7.2: Xylene isomerization pathways of 1,2-methyl shift pathway(adapted from [280]).

---

Based on the 1,3-methyl shift and for model simplification, it was assumed that no toluene (T), ethylbenzene (EB) or trimethylbenzene (TMBs) is present in the product streams because in the experimental studies, the aim was to evaluate the separation performance of the inert MFI-aumina membrane during e-ZCMR operation rather than investigating the catalyst performance. It is good to emphasize here that by-products such as T, EB and TMBs are usually produced at the equilibrium point of m-Xylene isomerization reaction due to disproportionation of m-Xylenes [67,280]. Thus, in this model,  $k_4 = k_5 = k_6 = 0$ . The kinetic model based on the 1,3-methyl shift, as presented in this chapter, assumes first order kinetics. The overall kinetic model is presented below:

Rate of formation of p-Xylene:

$$r_{PX} = k_1 C_{MX} + k_{-3} C_{OX} - (k_{-1} + k_3) C_{PX} \quad (7.1)$$

Rate of consumption of m-Xylene:

$$r_{MX} = -(k_1 + k_2) C_{MX} + k_{-1} C_{PX} + k_2 C_{OX} \quad (7.2)$$

Rate of formation of o-Xylene:

$$r_{OX} = k_2 C_{MX} + k_3 C_{PX} - (k_{-2} + k_{-3}) C_{OX} \quad (7.3)$$

If the xylene vapours are assumed to behave as ideal gases, then:

$$C_{PX} = \frac{P_{PX}}{RT} \quad (7.4)$$

$$C_{MX} = \frac{P_{MX}}{RT} \quad (7.5)$$

$$C_{OX} = \frac{P_{OX}}{RT} \quad (7.6)$$

$C_{PX}$ ,  $C_{MX}$ ,  $C_{OX}$  are the molar concentration in  $\text{mol.m}^{-3}$  of  $PX$ ,  $MX$  and  $OX$ , respectively.  $k_1$ ,  $k_{-1}$ ,  $k_2$ ,  $k_{-2}$ ,  $k_3$ ,  $k_{-3}$  are the reaction rate constants in  $s^{-1}$  and  $r_{PX}$ ,  $r_{OX}$ ,  $r_{MX}$  are the rate of reaction in  $\text{mol.m}^{-3} \cdot s^{-1}$ . Moreover, if  $i = PX, MX, OX$ , the partial pressures in the tube side and the shell side are given as :

$$P_i^t = \frac{Q_i^t}{\sum_{i=1}^3 Q_i^t} \cdot P_O \quad (7.7)$$

$$P_i^s = \frac{Q_i^s}{\sum_{i=1}^3 Q_i^s} \cdot P_O \quad (7.8)$$

Incorporating Eq. 7.4 to Eq. 7.7 into Eq. 7.1 to Eq. 7.3, gives:

$$r_{PX} = \frac{P_O}{RT} \left[ k_1 \cdot \frac{Q_{MX}^t}{\sum_{i=1}^3 Q_i^t} + k_{-3} \cdot \frac{Q_{OX}^t}{\sum_{i=1}^3 Q_i^t} - (k_{-1} + k_3) \cdot \frac{Q_{PX}^t}{\sum_{i=1}^3 Q_i^t} \right] \quad (7.9)$$

$$r_{MX} = -\frac{P_O}{RT} \left[ (k_1 + k_2) \cdot \frac{Q_{MX}^t}{\sum_{i=1}^3 Q_i^t} - k_{-1} \cdot \frac{Q_{PX}^t}{\sum_{i=1}^3 Q_i^t} - k_2 \cdot \frac{Q_{OX}^t}{\sum_{i=1}^3 Q_i^t} \right] \quad (7.10)$$

$$r_{OX} = \frac{P_O}{RT} \left[ k_2 \cdot \frac{Q_{MX}^t}{\sum_{i=1}^3 Q_i^t} + k_3 \cdot \frac{Q_{PX}^t}{\sum_{i=1}^3 Q_i^t} - (k_{-2} + k_{-3}) \cdot \frac{Q_{OX}^t}{\sum_{i=1}^3 Q_i^t} \right] \quad (7.11)$$

$P_{PX}$ ,  $P_{MX}$  and  $P_{OX}$  are the partial pressures of  $PX$ ,  $MX$  and  $OX$ , respectively, in  $N.m^{-2}$ .  $Q_i^t$  is the molar flow rate of component  $i$  ( $i = PX$ ,  $MX$  or  $OX$ ) in  $mol.s^{-1}$  in the tube side and  $P_O$  is the operating pressure in  $N.m^{-2}$ .

### 7.2.2 Reactor model

The model presented here is based on the modification of the model presented by Kumar *et al.* [281]. The steady-state mass balance for component  $i$  was made for the tube side and the shell side using the schema presented in Fig. 7.3.

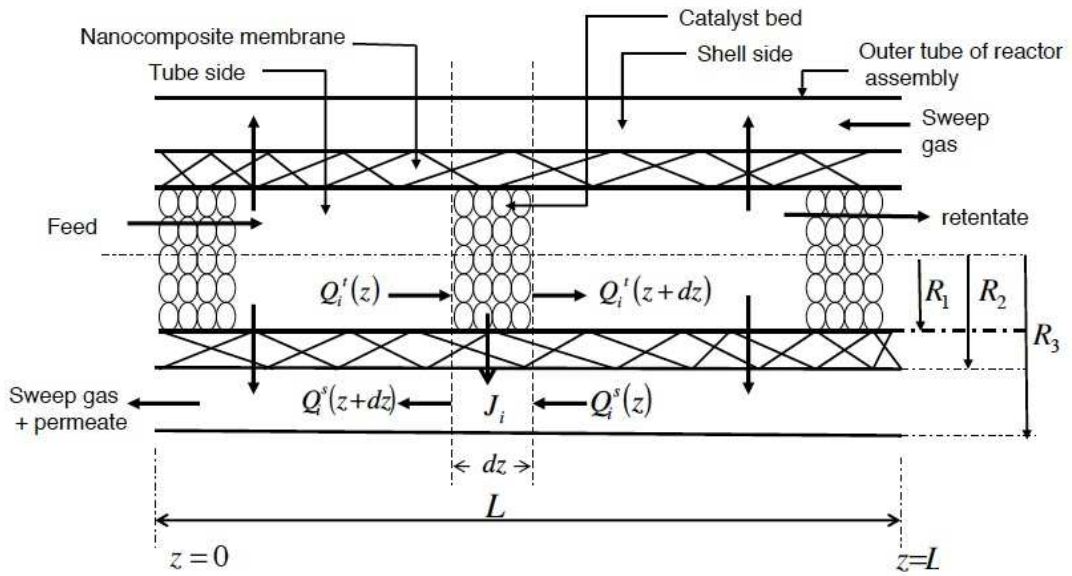


Figure 7.3: Schematic of the e-ZCMR packed with catalyst.

$R_1$ ,  $R_2$  and  $R_3$  are internal radius of the membrane tube, external radius of the membrane tube and internal radius of the shell, respectively.

### 7.2.2.1 Flux model

Figure 7.4 depicts the schema of the transport (flux) across a typical membrane (in this study, a nanocomposite MFI-alumina membrane incorporated in e-ZCMR).

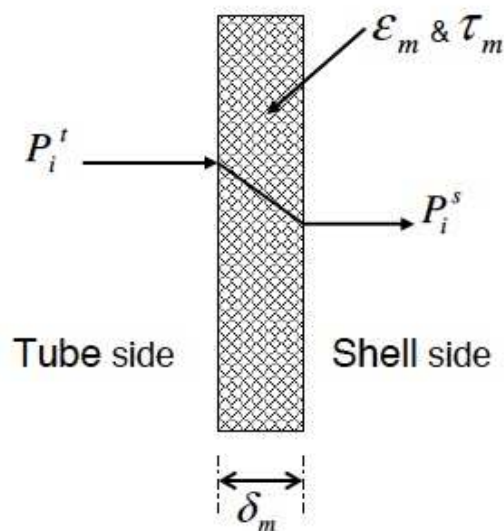


Figure 7.4: Schematic showing the transport (flux) across a membrane in e-ZCMR.

where  $\varepsilon_m$  is the porosity of the membrane;  $\tau_m$ , the membrane tortuosity [-];  $\delta_m$ , the membrane effective wall thickness [m];  $J_i$ , the cross-membrane flux ( $\text{mol}\cdot\text{s}^{-1}\cdot\text{m}^{-2}$ ).  $P_i^t$  and  $P_i^s$  is the partial pressures [Pa] of component  $i$  in the tube side and permeate side, respectively.

The flux through the membrane is based on Fickian diffusion model. In this case, the flux of component  $i$  across the membrane is defined as:

$$J_i = \frac{\varepsilon_m D_i}{\delta_m \tau_m RT} (P_i^t - P_i^s) \quad (7.12)$$

Incorporating Eq. 7.7 and Eq. 7.8 in Eq. 7.12, gives:

$$J_i = \frac{\varepsilon_m D_i P_O}{\delta_m \tau_m RT} \left( \frac{Q_i^t}{\sum_{i=1}^3 Q_i^t} - \frac{Q_i^s}{\sum_{i=1}^3 Q_i^s} \right) \quad [\text{mol}\cdot\text{m}^{-2}\cdot\text{s}^{-1}] \quad (7.13)$$

$D_i$ , the diffusivity (diffusion coefficient) of component  $i$  in  $\text{m}^2\cdot\text{s}^{-1}$  was obtained according to Eq.4.3.  $D_{ref,i}$  and  $E_{D,i}$  used in the computation of  $D_i$  were obtained from [242]. Computed  $D_i$  are presented in Appendix C.

### 7.2.2.2 Mass balance

The mass balance equations presented in this study include the transport through the tube space, transport through the shell space, transport inside the catalyst particles and transport through the membrane. The mass balance equations presented were based also on the following assumptions:

- Retentate and permeate sides of the reactor are operated under steady-state condition ( $\frac{dQ^s}{dt} = \frac{dQ^t}{dt} = \frac{dT}{dt} = 0$ )
- Isothermal condition ( $dT = 0$ )
- The behaviour of bulk gas is assumed to be ideal in both sides.
- Plug flow concept of reactor design is assumed. Axial diffusion of mass and heat and radial concentration gradients on both sides are considered to be negligible.

- Catalyst pellet equations are not considered because according to Gobina *et al.* [282], concentration gradients in catalyst pellets are negligible due to small pellet size.
- Sweep gas is non reactive. Therefore, no reaction occurs in the shell side.
- Stagnant gas films on both sides of membrane are considered, while radial temperature gradients across the membrane are neglected.
- Effectiveness factors with reaction rates are taken to be equal to unity (i.e.  $\eta_i = 1$ ) because the size of the catalyst pellet was  $< 0.8$  mm. Although no information about the catalyst crystal was provided by the supplier, it is expected that the crystal size should be so small to the extent that external and internal diffusion limitations will not be a problem.
- Pressure drop across the reactor length is neglected.

### **Tube side:**

$$\frac{dQ_i^t}{dz} - \pi R_1^2 \rho_{cat} \{ \eta_i (\pm v_i r_i) \} + 2\pi R_1 J_i = 0 \quad (7.14)$$

where  $R_1$  is the internal radius of the membrane tube [m];  $\rho_{cat}$ , the density of the catalyst [ $\text{kg.m}^{-3}$ ] and  $r_i$  is the rate of reaction in  $\text{mol.kg}^{-1}\text{s}^{-1}$ . For dimensional homogeneity,  $r_i$  in Eq. 7.14 is related to  $r_i$  in Eq. 7.1 to Eq. 7.3 as shown below:

$$r_i [\text{mol.kg}^{-1}\text{s}^{-1}] = r_i [\text{mol.m}^{-3}\text{s}^{-1}] \cdot \frac{V_{reactor}}{W_{cat}} [\text{m}^3.\text{kg}^{-1}] \quad (7.15)$$

Substituting Eq. 7.13 in Eq. 7.14 gives:

$$\frac{dQ_i^t}{dz} = \pi R_1^2 \rho_{cat} r_i - 2\pi R_1 \frac{\varepsilon_m D_i P_O}{\delta_m \tau_m RT} \left[ \frac{Q_i^t}{\sum_{i=1}^3 Q_i^t} - \frac{Q_i^s}{\sum_{i=1}^3 Q_i^s} \right] [\text{mol.m}^{-1}\text{s}^{-1}] \quad (7.16)$$

For instance, for isomerization of m-Xylene to PX and OX in e-ZCMR, the profile in the tube side is given by the following equations:

$$\begin{aligned} \frac{dQ_{PX}^t}{dz} &= \frac{\pi R_1^2 \rho_{cat} P_O}{RT} \left[ k_1 \cdot \frac{Q_{MX}^t}{\sum_{i=1}^3 Q_i^t} + k_{-3} \cdot \frac{Q_{OX}^t}{\sum_{i=1}^3 Q_i^t} - (k_{-1} + k_3) \cdot \frac{Q_{PX}^t}{\sum_{i=1}^3 Q_i^t} \right] \\ &- 2\pi R_1 \frac{\varepsilon_m D_{PX} P_O}{\delta_m \tau_m RT} \left[ \frac{Q_{PX}^t}{\sum_{i=1}^3 Q_i^t} - \frac{Q_{PX}^s}{\sum_{i=1}^3 Q_i^s} \right] \end{aligned} \quad (7.17)$$

$$\begin{aligned} \frac{dQ_{MX}^t}{dz} &= -\frac{\pi R_1^2 \rho_{cat} P_O}{RT} \left[ (k_1 + k_2) \cdot \frac{Q_{MX}^t}{\sum_{i=1}^3 Q_i^t} - k_{-1} \cdot \frac{Q_{PX}^t}{\sum_{i=1}^3 Q_i^t} - k_2 \cdot \frac{Q_{OX}^t}{\sum_{i=1}^3 Q_i^t} \right] \\ &- 2\pi R_1 \frac{\varepsilon_m D_{MX} P_O}{\delta_m \tau_m RT} \left[ \frac{Q_{MX}^t}{\sum_{i=1}^3 Q_i^t} - \frac{Q_{MX}^s}{\sum_{i=1}^3 Q_i^s} \right] \end{aligned} \quad (7.18)$$

$$\begin{aligned} \frac{dQ_{OX}^t}{dz} &= \frac{\pi R_1^2 \rho_{cat} P_O}{RT} \left[ k_2 \cdot \frac{Q_{MX}^t}{\sum_{i=1}^3 Q_i^t} + k_3 \cdot \frac{Q_{PX}^t}{\sum_{i=1}^3 Q_i^t} - (k_{-2} + k_{-3}) \cdot \frac{Q_{OX}^t}{\sum_{i=1}^3 Q_i^t} \right] \\ &- 2\pi R_1 \frac{\varepsilon_m D_{OX} P_O}{\delta_m \tau_m RT} \left[ \frac{Q_{OX}^t}{\sum_{i=1}^3 Q_i^t} - \frac{Q_{OX}^s}{\sum_{i=1}^3 Q_i^s} \right] \end{aligned} \quad (7.19)$$

### **Shell side**

For inert sweep gas on the shell side, the component mass balance at the shell side is given as:

$$\beta_s \frac{dQ_i^s}{dz} - \beta_f \cdot 2\pi R_2 J_i = 0 \quad (7.20)$$

where  $R_2$  is the external radius of the membrane [m];  $\beta_s$  dictates the direction of flow of the sweep gas. If the sweep flows co-currently,  $\beta_s = -1$ . However, for counter-current flow,  $\beta_s = +1$ .  $\beta_f$  is a factor that dictates the direction of flux. If the permeation is from the tube to the shell side,  $\beta_2 = +1$ , but if the opposite is considered,  $\beta_2 = -1$ . For this model, counter-current sweep flow is considered. Thus,  $\beta_s = +1$ . Therefore, for permeation of PX, MX and OX through the membrane to the shell side, the following equations apply:

$$\frac{dQ_{PX}^s}{dz} = 2\pi R_2 \frac{\varepsilon_m D_{PX} P_O}{\delta_m \tau_m RT} \left[ \frac{Q_{PX}^t}{\sum_{i=1}^3 Q_i^t} - \frac{Q_{PX}^s}{\sum_{i=1}^3 Q_i^s} \right] \quad [\text{mol.m}^{-1}.\text{s}^{-1}] \quad (7.21)$$

$$\frac{dQ_{MX}^s}{dz} = 2\pi R_2 \frac{\varepsilon_m D_{MX} P_O}{\delta_m \tau_m RT} \left[ \frac{Q_{MX}^t}{\sum_{i=1}^3 Q_i^t} - \frac{Q_{MX}^s}{\sum_{i=1}^3 Q_i^s} \right] \quad (7.22)$$

$$\frac{dQ_{OX}^s}{dz} = 2\pi R_2 \frac{\varepsilon_m D_{OX} P_O}{\delta_m \tau_m RT} \left[ \frac{Q_{OX}^t}{\sum_{i=1}^3 Q_i^t} - \frac{Q_{OX}^s}{\sum_{i=1}^3 Q_i^s} \right] \quad (7.23)$$

### Boundary conditions

The boundary conditions in the tube side and shell side are defined as:

$$\text{At } z = 0, Q_i^t(0) = Q_{i,0}^t \text{ and } Q_i^s(0) = Q_{i,0}^s$$

$$\text{At } z = L, Q_i^t(L) = Q_{i,f}^t \text{ and } Q_i^s(L) = Q_{i,f}^s$$

### **7.2.3 Model implementation and validation**

The rate of reaction constants for the reactions was adjusted values obtained from Al-Kattaf *et al.* [280]. Influence of temperature on the reaction rate parameters of the reaction was accounted for using Arrhenius equation of the form:

$$k_i(T) = k_i(T_{ref}) \exp \left[ \frac{E_i}{R} \left( \frac{1}{T_{ref}} - \frac{1}{T} \right) \right] \quad (7.24)$$

The adjusted rate of reaction constants are given in Table 7.1 and in also Appendix C. Table 7.2 gives the values of the constant parameters used for the simulation. To implement the model described above, the set of model equations was solved using the fourth-order Runge-Kutta method implemented in *matlab* within the *ODE45* environment. The model was validated with the experimental results (m-Xylene isomerization in e-ZCMR at 673 K) presented in Chapter 6. Experimental results obtained at 673 K were selected because m-Xylene isomerization to p-Xylene occurs at about 673 K in the industry. The experimental results used for model validation are presented in Appendix C:

Table 7.1: Rate of reaction constants used for reaction modelling at 673 K [280].

Rate of reaction constant $k_i$ ( $\times 10^4$ ), ( $\text{m}^3 \cdot (\text{kg of catalyst})^{-1} \cdot \text{s}^{-1}$ )					
$k_1$	$k_{-1}$	$k_2$	$k_{-2}$	$k_3$	$k_{-3}$
2.39	5.48	1.91	3.68	1.71	1.76

Table 7.2: Constant parameters used for reactor modeling.

Universal gas constant ( $\text{J} \cdot \text{mol}^{-1} \cdot \text{K}^{-1}$ )	8.314
Density of the MFI ( $\text{k} \cdot \text{gm}^{-3}$ )	1700
Porosity of the membrane (-)	0.13
Membrane tortuosity (-)	1.2
Membrane effectiveness thickness (m)	$3 \times 10^{-6}$
Reference atmospheric pressure (Pa)	101325
Membrane permeation length (m)	$130 \times 10^{-3}$
Internal radius of the membrane (m)	$3.5 \times 10^{-3}$
External radius of the membrane (m)	$3.505 \times 10^{-3}$
Internal radius of the stainless module (m)	$5 \times 10^{-3}$
Density of the catalyst ( $\text{k} \cdot \text{gm}^{-3}$ )	530

### 7.3 Results and discussion

Figure 7.5 presents the predicted profile of molar flow rate of xylene in the tube side during m-Xylene isomerization over Pt-HZSM-5 catalyst in e-ZCMR and Fig. 7.6 depicts the profile of molar flow rate of xylene in the shell side. P-Xylene yield, p-Xylene selectivity and m-Xylene conversion as computed from the simulation results are presented in Table 7.3. The

simulation results were compared with the results obtained from m-Xylene isomerization experiment conducted at 673 K.

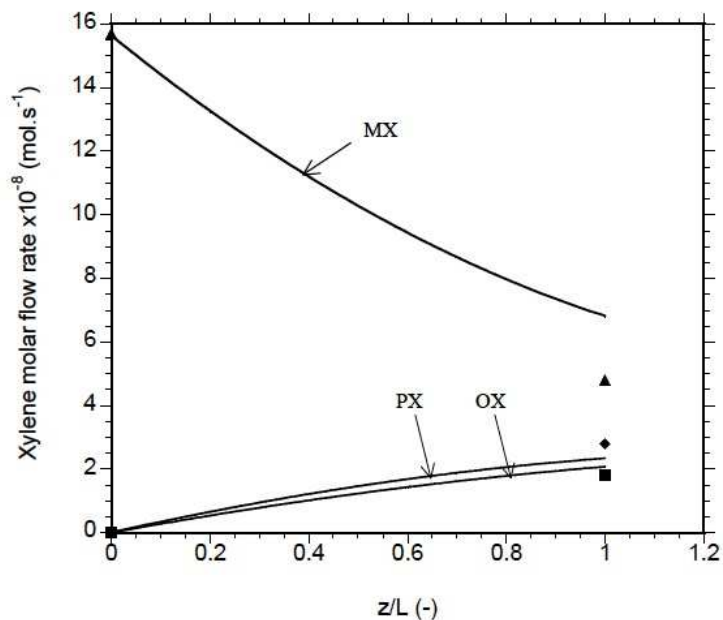


Figure 7.5: Molar flow rate profile of xylene in e-ZCMR at the tube side during isomerization at 673 K (Line=simulation; points=experimental).

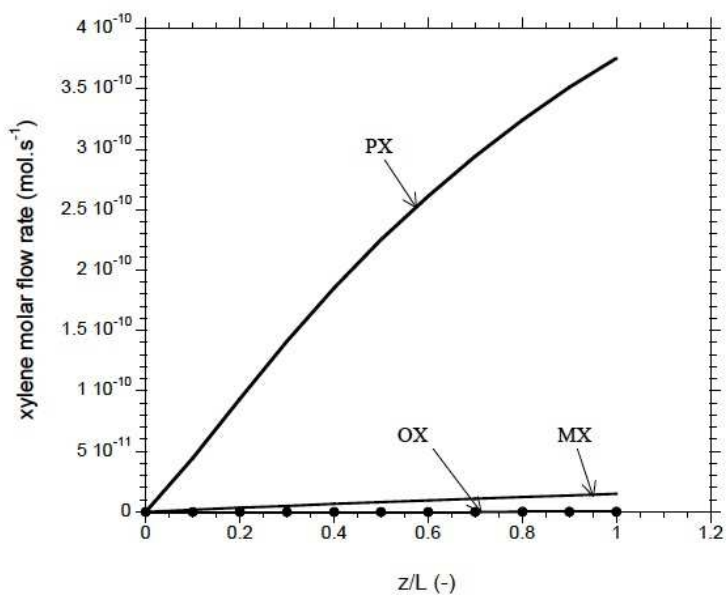


Figure 7.6: Molar flow rate profile of xylene in e-ZCMR at the shell side during isomerization at 673 K. (Lines=simulation; points=experimental).

Table 7.3: Comparison of experimental results with simulation results.

Performance indicator	Simulation	Experimental	% Error
* $Y_{PX}$ (%)	20.50	17.50	17.1
* $SEL_{PX}$ (%)	53.05	41.00	29
** $SEL_{PX}$ (%)	99.95	100.00	0.05
Conversion (%)	56.8	69.7	19.5

\*Combined mode operation; \*\*Permeate-only mode operation;  $Y_{PX}$ : PX yield ;  $SEL_{PX}$ : PX selectivity

The results as presented in the Table 7.3 show that the simulation results are in fair agreement with the experimental results with percentage errors (absolute) of 17%, 29%, 0.05% and 19.5% for p-Xylene yield in combined mode, p-Xylene selectivity in combined mode, p-Xylene selectivity in permeate-only mode and m-Xylene conversion, respectively.

As depicted in Fig. 7.5, the molar flow rate profile of m-Xylene in the tube side shows a decrease across the length of the reactor while the molar flow rate profile of p-Xylene and o-Xylene shows an increase across the reactor length. This is expected because m-Xylene is consumed and converted to p-Xylene and o-Xylene, respectively, during the isomerization. The observation in Fig. 7.5 is consistent with the results reported by Deshayes *et al.* [201]. Through modelling study, Deshayes *et al.* [201] investigated the influence of incorporating Na-ZSM-5/SS membranes on the performance of an industrial fixed-bed reactor during m-Xylene isomerization over Pt/silica catalyst. But in this study, a laboratory-scale e-ZCMR equipped with a nanocomposite MFI-alumina tube as the separation unit was modelled to understand its behaviour during m-Xylene isomerization over Pt/HZSM-5 catalyst. Despite the big difference in the size of reactors modelled, the two reactors showed similar trend in xylene molar flow rate profile in the tube side. Moreover, in Fig. 7.6, the predicted molar flow rate profiles in the shell side increase drastically for p-Xylene, m-Xylene and o-Xylene across the reactor length. The p-Xylene molar flow rate profile is much higher compared to those of m-Xylene and o-Xylene. This behaviour could be attributed to the excellent separation performance of the nanocomposite MFI-alumina membrane tube incorporated in the reactor. At  $z = L$ , the simulation results agree perfectly with the experimental results with percentage error (absolute) of 0.05% in the permeate-only mode operation.

The discrepancy observed between the model output and the experimental results can be attributed to the assumptions made in the model development and formulation and also to the quality of data (i.e. kinetics data, diffusion data) used in the simulation. This suggests that the model is sensitive to quality of data and assumptions. Nevertheless, it can be concluded that the model presented in this chapter can explain the fundamental behaviour of an e-ZCMR during m-Xylene isomerization over Pt-HZSM-5 catalyst. In addition, it is noteworthy to mention again that this is a first and somewhat preliminary attempt to model e-ZCMR

---

behaviour (when equipped with nanocomposite MFI-alumina membrane tubes) during m-Xylene isomerization. Hence the model is not void of discrepancies due to various assumptions made and the quality of kinetic data employed during model formulation and implementation. It nevertheless provides useful insight and a protocol towards further development of related concepts.

Furthermore, sensitivity analysis was conducted on the model to understand how the model respond to changes in some specific design parameters such as membrane thickness, membrane porosity, membrane tortuosity and internal diameter of the reactor tube (i.e. 2R1). This is described in the following section.

#### **7.4 Effect of design variables on e-ZCMR performance**

In e-ZCMR, enhancement of p-Xylene yield is expected due to the *in situ* extraction of p-Xylene from the reaction zone by the membrane. This in turn enhances more consumption of m-Xylene leading to enhancement of p-Xylene yield. However, the reactor performance depends on some parameters such as membrane parameters (membrane thickness, membrane porosity, membrane tortuosity); reactor design parameters (reactor size (tube and shell diameter), length etc.) and operating variables (feed flow rate, sweep gas flow rate, mass of catalyst, catalyst packing, reaction temperature and operating pressure). Membrane thickness is controllable during membrane preparation. Membrane porosity and tortuosity are intrinsic properties of membrane supports and can be controlled during the production of these supports.

Reactor design involves selecting the reactor configuration/geometry, sizing the reactor, selecting and optimizing reactor operating conditions, optimizing the reactor performance, selecting suitable material of construction, costing and scaling-up [283]. Often the reactor design is based on some reactor design equations that provide relationships relating the reactor operation with aforementioned reactor properties [284]. Reactor sizing basically involves specifying the reactor geometry such as vessel size and type, which depends on reactor diameter and length (for tubular) or reactor diameter and height (for Continuous Stirred Tank Reactors (CSTR) or batch reactors). During reactor sizing, a designer has control over these reactor dimensions. Although, specifying the dimensions depends largely on the reactor operating parameters such as the rate equation, feed flow rates, amount of catalyst, catalyst packing and sweep gas flow rates (in case of e-ZCMR) [284]. Furthermore, during the operation of an e-ZCMR, operating variables such as reaction temperature, operating pressure, feed flow rate, sweep gas flow rate can be manipulated to optimize the reactor performance. Manipulation of operational variables toward enhanced e-ZCMR performance was dealt with and described in Chapter 6 of this dissertation.

---

Furthermore, membrane thickness, membrane porosity and membrane tortuosity depend on the membrane preparation techniques/protocols and the quality of membrane supports, as the case is in the preparation of MFI-type alumina membranes-“film-like” or nanocomposite architecture-types. Regarding the reactor operating variables, at constant reaction temperature and operating pressure, as the case is in this study, other controllable operating variables are the feed flow rate and sweep gas flow rate. In Chapter 6, the effect of these variables on e-ZCMR performance has been demonstrated experimentally.

In this chapter, sensitivity of e-ZCMR performance to changes in properties describing the membrane morphology and the reactor geometry is presented. In the performance evaluation, response of p-Xylene yield in both combined mode and permeate-only mode operations and response of m-Xylene conversion to small perturbations in effective membrane thickness, membrane porosity, membrane tortuosity and reactor size (in terms of internal radius of the e-ZCMR tube) were studied. The advantage of this sensitivity analysis is not limited to better understanding of the fundamental behaviour of the e-ZCMR during m-Xylene isomerization, but provides further information on the optimization approach for the reactor design and perhaps the operational condition.

Sensitivity analysis is a general concept that aims at quantifying the variations of an output parameter of a system with respect to changes imposed to some input parameters [285,286]. Sensitivity analysis is therefore an excellent technique to help in understanding and preparing for “what to do” and “how to do” regarding the optimization of e-ZCMR process.

For instance, if  $\phi$  is the output function (such as p-Xylene yield, p-Xylene selectivity, m-Xylene conversion) such that  $\phi$  depends on  $n$  input parameters  $\delta_i$  (such as membrane thickness, membrane porosity, membrane tortuosity, reactor diameter;  $i=1, 2, \dots, n$ ):

$$\phi = \phi (\delta_1, \delta_2, \dots, \delta_n) \quad (7.25)$$

The differential form of Eq. 7.25 using the chain rule of differentiation yields:

$$d\phi = \frac{\partial \phi}{\partial \delta_1} d\delta_1 + \frac{\partial \phi}{\partial \delta_2} d\delta_2 + \dots + \frac{\partial \phi}{\partial \delta_n} d\delta_n \quad (7.26)$$

The gradient for the parameter  $\delta_1$  then follows as:

$$\frac{d\phi}{d\delta_1} = \frac{\partial\phi}{\partial\delta_1} + \frac{\partial\phi}{\partial\delta_2} * \frac{d\delta_2}{d\delta_1} + \dots + \frac{\partial\phi}{\partial\delta_n} * \frac{d\delta_n}{d\delta_1} \quad (7.27)$$

If it is assumed that the parameters  $\delta_i$  are mutually independent of one another then:

$$\frac{d\delta_2}{d\delta_1} = \frac{d\delta_3}{d\delta_1} = \dots = \frac{d\delta_n}{d\delta_1} = 0 \quad (7.28)$$

Therefore, the derivative of  $\phi$  with respect to  $\delta_1$  can be approximated as:

$$\frac{d\phi}{d\delta_1} = \frac{\partial\phi}{\partial\delta_1} \approx \frac{\Delta\phi}{\Delta\delta_1} \quad (7.29)$$

Therefore, the partial derivative,  $\frac{\partial\phi}{\partial\delta_1}$ , is the sensitivity coefficient of the function  $\phi$  for the

input parameter  $\delta_1$ . If the function  $\phi$  is not linear with respect to parameter  $\delta_1$ ,  $\frac{\partial\phi}{\partial\delta_1}$  will

vary from point to point [287]. To obtain the sensitivity coefficients of the aforementioned parameters with respect to the input variables as considered in this study, Eq. 7.29 was used. Variables considered in this study are contained in Table 7.4. The sensitivity analysis was based on  $\pm 20\%$  changes in the variables considered in Table 7.4. The variables are sub-divided into categories: (1) Variables influencing the membrane morphology and, (2) Variables influencing the reactor design. Model output at 673 K presented in the previous sections of this chapter was used as a reference (see Table 7.5).

Table 7.4: Design variables considered for sensitivity analysis.

Membrane property	Reactor property	Model Response
Membrane effective thickness	Internal radius of the reactor tube	P-Xylene yield at permeate-only mode
Membrane mean porosity	-	P-Xylene yield at combine mode
Membrane tortuosity	-	Conversion

Table 7.5: Model output at 673 K and at the reference values of the design variables.

Variables	Reference variables	* $Y_{PX}$ at permeate-only mode (%)	* $Y_{PX}$ at combined mode (%)
Membrane effective thickness ( $\mu\text{m}$ )	3.0	13.0	20.5
Membrane mean porosity (-)	0.13	13.0	20.5
Membrane tortuosity (-)	1.2	13.0	20.5
Internal radius of the tube (mm)	3.5	13.0	20.5

\* model output at 673 K and at the reference values of the design variables

#### 7.4.1 Effect of membrane effective thickness

As shown in Table 7.6, changing the membrane effective thickness by  $\pm 20\%$  has no effect on the p-Xylene yield in combined mode operation and in the m-Xylene conversion but it has a significant effect on the p-Xylene yield in the permeate-only mode operation. The effect of change in membrane effective thickness on the p-Xylene yield in permeate-only mode is depicted in Fig. 7.7.

Table 7.6: Effect of membrane effective thickness.

Thickness ( $\mu\text{m}$ )	** $Y_{PX}$ (%)	* $Y_{PX}$ (%)	Conv. (%)	SC wrt ** $Y_{PX}$
3.6	12.9	20.5	56.8	-
3.0	13	20.5	56.8	-0.17
2.4	15.9	20.5	56.8	-4.83

\*Combined mode operation; \*\*Permeate-only mode operation;  $Y_{PX}$ : PX yield; Conv.: conversion; SC: sensitivity coefficient; wrt: with-respect-to.

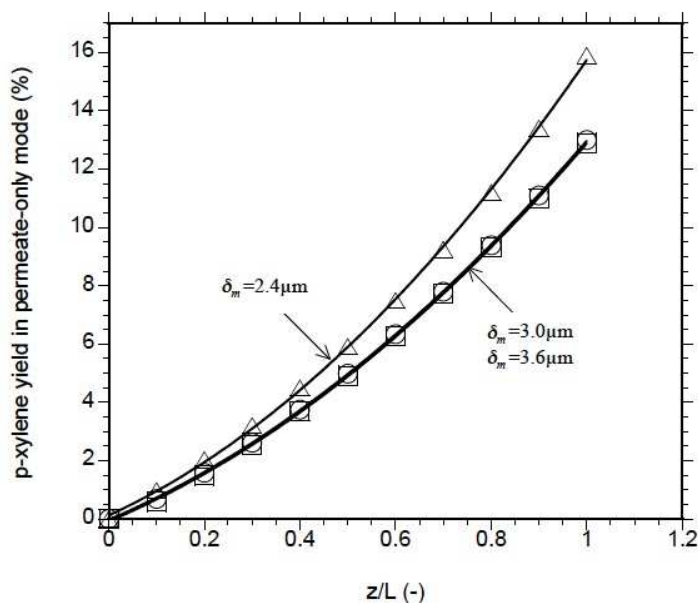


Figure 7.7: Effect of membrane effective thickness on p-Xylene yield in permeate-only mode.

Figure 7.7 shows that increasing the membrane effective thickness from 3  $\mu\text{m}$  to 3.6  $\mu\text{m}$  decreased the p-Xylene yield in the permeate-only mode by 0.1%. However, when the membrane effective thickness was reduced from 3  $\mu\text{m}$  to 2.4  $\mu\text{m}$  the p-Xylene yield in the permeate-only mode increased by 2.9% (see Fig. 7.7). Moreover, from the sensitivity coefficients (Table 7.6), the p-Xylene yield in the permeate-only mode is significantly affected by a reduction in membrane effective thickness rather than an increase in membrane effective thickness. The increase in p-Xylene yield in the permeate-only mode could be attributed to the increase in p-Xylene flux through the membrane. Considering Eq. 7.12, it is expected that the flux will be enhanced when the membrane effective thickness is reduced, holding other parameters constant. Therefore, the observation in this study is supported by Eq.7.12. Furthermore, the observation supports the observation described in Chapter 5 where a nanocomposite MFI-alumina hollow fibre membrane with membrane effective thickness of less than 1  $\mu\text{m}$  enhanced p-Xylene flux by 30% over a membrane tube with effective membrane thickness of 3  $\mu\text{m}$ . In this study, m-Xylene isomerization in an e-ZCMR, having a nanocomposite MFI-alumina hollow fibre membrane as separation unit is not presented. The present configuration of the hollow fibre membrane makes the application in e-ZCMR impractical and research is going on to optimize the configuration and also the preparation protocol. However, it is expected that p-Xylene yield will be enhanced in permeate-only mode if nanocomposite MFI-alumina hollow fibre membrane is used.

## 7.4.2 Effect of membrane porosity and tortuosity

As depicted in Table 7.7 changing the membrane mean porosity by  $\pm 20\%$  only shows a significant effect on the p-Xylene yield in permeate-only mode operation with no effect on the p-Xylene yield in the combined mode operation and on the m-Xylene conversion. The effect of change in membrane mean porosity on the p-Xylene yield in permeate-only mode is further explained with Fig. 7.8. Table 7.8 and Figure 7.9 depict the effect of changes in membrane tortuosity on e-ZCMR performance.

Table 7.7: Effect of membrane porosity on e-ZCMR performance

Porosity (-)	** $Y_{PX}$ (%)	* $Y_{PX}$ (%)	Conv. (%)	SC wrt $Y_{PX}$
0.156	13.3	20.5	56.8	-
0.130	13.0	20.5	56.8	11.54
0.104	12.9	20.5	56.8	3.85

\*Combined mode operation; \*\*Permeate-only mode operation;  $Y_{PX}$ : PX yield; Conv.: conversion; SC: sensitivity coefficient; wrt: with-respect-to

Table 7.8: Effect of membrane tortuosity on e-ZCMR performance

Tortuosity (-)	** $Y_{PX}$ (%)	* $Y_{PX}$ (%)	Conv. (%)	SC wrt $Y_{PX}$
1.44	12.9	20.5	56.8	-
1.20	13.0	20.5	56.8	-0.42
0.96	15.9	20.5	56.8	-12.08

\*Combined mode operation; \*\*Permeate-only mode operation;  $Y_{PX}$ : PX yield; SC: sensitivity coefficient; wrt: with-respect-to; Conv.: conversion.

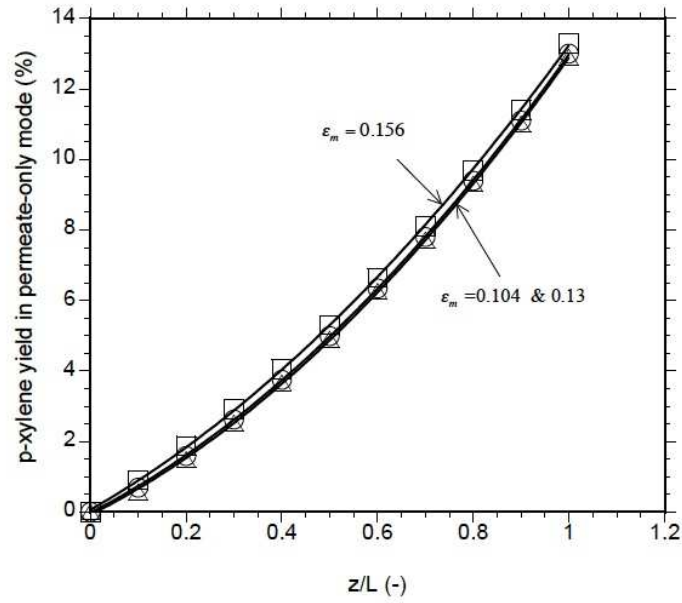


Figure 7.8: Effect of membrane porosity on p-Xylene yield in permeate-only mode.

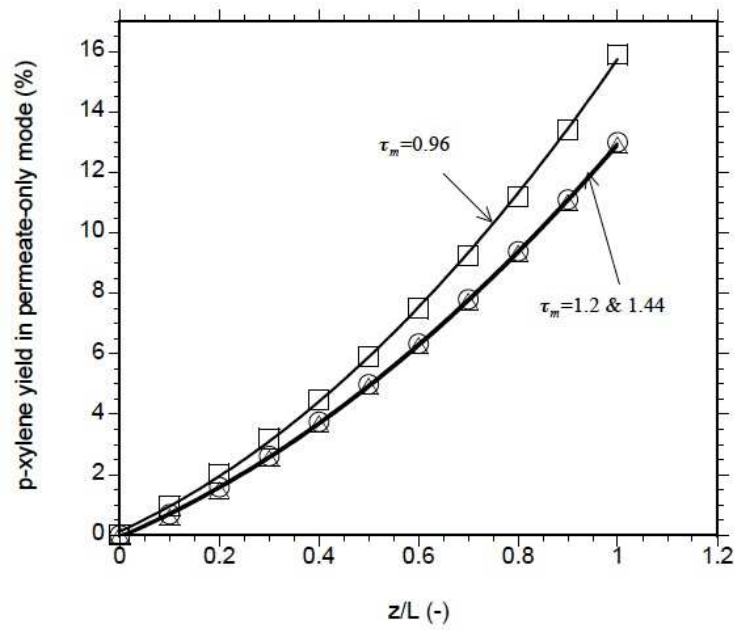


Figure 7.9: Effect of membrane tortuosity on p-Xylene yield in permeate-only mode.

---

As can be seen in Fig. 7.8 and Table 7.7, p-Xylene yield in the permeate-only mode is more sensitive to positive (+20%) changes in membrane mean porosity, displaying sensitivity coefficient of 11.5 compared to negative (-20%) changes in membrane mean porosity with sensitivity coefficient of 3.9. Furthermore, as depicted in Table 7.8 and Fig. 7.9, membrane tortuosity has a positive significance on the p-Xylene yield in permeate-only mode operation of e-ZCMR. However, p-Xylene yield in permeate-only mode is more sensitive to negative 20% (-20%) changes in tortuosity than positive 20% (+20%) changes in membrane tortuosity. At tortuosity of 0.96, an increase in p-Xylene yield of 2.9% was obtained over the tortuosity of 1.2. However, at tortuosity of 1.44, an increase of 0.1% was obtained. This observation is expected because membrane porosity and membrane tortuosity are intrinsic properties of the membrane. In the case of e-ZCMR, the membrane is associated with the performance enhancement in the permeate-only mode, although the effect is culminated in the performance of the reactor in combined mode, because the membrane selectively extract p-Xylene from the reaction zone into the permeate side. Furthermore, the extraction efficiency of the membrane depends on the membrane morphology, which determines the membrane selectivity towards the target product (p-Xylene) and perhaps the p-Xylene flux through the membrane. Membrane morphology is a factor, among others, of the membrane porosity and membrane tortuosity.

Comparison between the effect of change in membrane mean porosity and effect of change in membrane tortuosity on the p-Xylene yield in permeate-only mode shows “almost” an inverse relationship. Highest p-Xylene yield of 13.3% is obtained at positive 20% (+20%) changes in the membrane while the highest p-Xylene yield of 15.9% is obtained at negative 20% (-20%) changes in the membrane tortuosity (Table 7.7 and Table 7.8). Interestingly, changing the membrane mean porosity or membrane tortuosity has no effect on the p-Xylene yield in combined mode. Moreover, the relationship displayed here has been established by Matyka *et al.* [288]. The authors studied numerically the tortuosity-porosity relation in a porous medium at microscopic level. According to the authors, the relation between tortuosity and porosity can be represented as:

$$\tau - 1 \propto \ln(\varepsilon) \quad (7.30)$$

As observed in this study, interplay between membrane porosity and membrane tortuosity dictates to some extent the p-Xylene yield in permeate-only mode. Therefore, careful manipulation of these membrane properties is very essential to increasing p-Xylene yield in e-ZCMR.

---

### 7.4.3 Effect of reactor size

Table 7.9, Fig. 7.10 and Fig. 7.11 show the effect of change in the reactor size ( by changing the internal diameter of the reactor tube) on an e-ZCMR performance. In Table 7.9, Fig. 7.10 and Fig. 7.11,  $\pm 20\%$  change in reactor diameter shows significant influence on the p-Xylene yield in permeate-only mode, p-Xylene yield in combined mode and in the m-Xylene conversion. At reactor internal radius of 4.2 mm, the e-ZCMR displays an increase of 2.7%, 6.6% and 12.8% for p-Xylene yield in permeate-only mode, p-Xylene yield in combined mode and m-Xylene conversion in combined mode , respectively, over the performance at 3.5 mm. Furthermore, at 2.8 mm internal radius, e-ZCMR displays a decrease of 0.8%, 6.5% and 15% for p-Xylene yield in permeate-only mode, p-Xylene yield in combined mode and m-Xylene conversion, respectively, compared to these values at 3.5 mm. For p-Xylene yield in both permeate-only mode and combined mode, e-ZCMR is more sensitive to an increase in internal diameter of the reactor tube than a decrease in the internal diameter of the reactor tube (Fig. 7.10 and Fig. 7.11). However, the m-Xylene conversion in combined mode is more sensitive to a decrease in the internal diameter of the reactor tube (Table 7.9) than an increase in the internal diameter of the reactor tube.

In a reactor operation, in which feed flow rate and amount of catalyst are fixed, enhancement of conversion is expected when the volume of reactor is increased due to an increase in the reactor diameter. Furthermore, when operating at fixed feed flow rate and fixed amount of catalyst but at increased reactor volume, it is expected that the superficial velocity of the feed into the reactor will reduce. Reduction in the superficial velocity suggests longer residence time. At a longer residence time, contact time is enhanced, resulting into an increase in conversion. Hence, increase in productivity and yield. However, if the contact time is prolonged more than necessary, side reactions might be promoted.

It is noteworthy to emphasize that both feed flow rate and the amount of catalyst are fixed during the sensitivity analysis. therefore going by the aforementioned thought, the model suggests that, at positive 20% (+20%) change in the internal diameter of e-ZCMR, the contact time between m-Xylene and the Pt-HZSM-5 catalyst is enhanced, thereby resulting into an increase in m-Xylene conversion (increase in p-Xylene productivity) and p-Xylene yield on the tube side. The reverse of this behaviour is expected at negative 20% (-20%) change in the reactor internal diameter. However, disproportionation of m-Xylene to toluene and trimethylbenzene might be promoted if the contact time is prolonged more than necessary. As a result of increased m-Xylene conversion (increase in p-Xylene productivity) on the tube side, p-Xylene flux through the membrane increases due to an increase in p-Xylene concentration on the tube side. As a result of increased p-Xylene flux through the membrane, an increase in p-Xylene yield is expected in permeate-only mode operation. The

reverse of this behaviour is expected also at reduced reactor volume. Large reactor diameter also indicates large reactor volume. Eventually, this translates into large space occupation and an increase in capital cost for construction and maintenance. Therefore, a balance point between reactor size and costs (capital and operational cost) is needed to make the technology attractive and competitive with existing ones.

Table 7.9: Effect of reactor size on e-ZCMR performance.

$R_{int}$ (mm)	** $Y_{PX}$ (%)	* $Y_{PX}$ (%)	Conv. (%)	SC wrt Cov.	SC wrt ** $Y_{PX}$	SC wrt * $Y_{PX}$
4.2	15.7	27.1	69.6	-	-	-
3.5	13.0	20.5	56.8	18.29	3.86	9.43
2.8	11.2	14.0	41.8	21.43	2.57	9.29

\*Combined mode operation; \*\*Permeate-only mode operation;  $Y_{PX}$ : PX yield ;  $R_{int}$ : Internal radius of the reactor tube; SC: sensitivity coefficient; Conv.: conversion (%); wrt: with-respect-to.

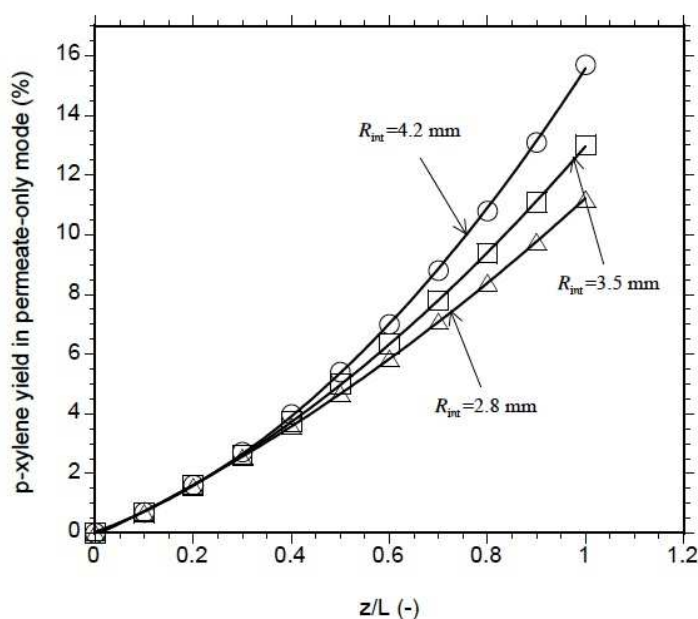


Figure 7.10: Effect of reactor size on p-Xylene yield in permeate-only mode.

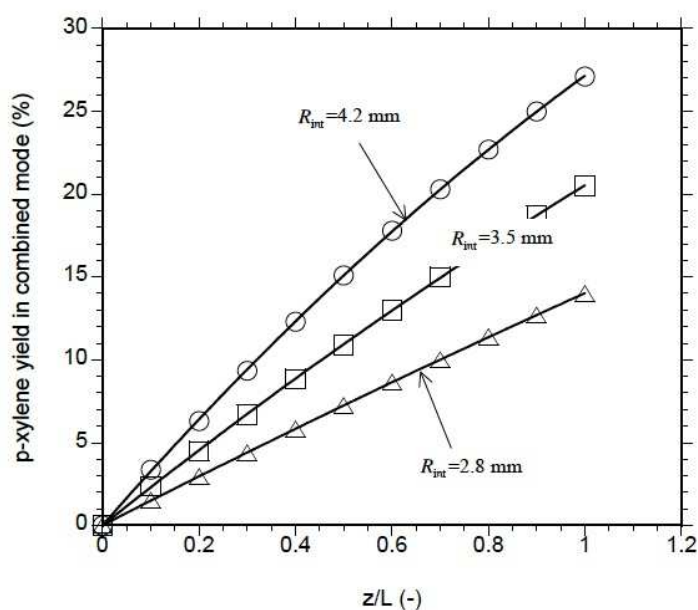


Figure 7.11: Effect reactor size on p-Xylene yield in combined mode.

Based on the sensitivity analysis described above, *tornado* plots depicted in Fig. 7.12 and 7.13 were made. In Fig. 7.12, at positive 20% (+20%) changes in the internal diameter of the reactor tube; in the membrane effective thickness; in the membrane mean porosity and in the membrane tortuosity, the p-Xylene yield in the permeate-only mode is significantly influenced positively by the membrane mean porosity followed by internal diameter of reactor tube. As can be seen in Fig. 7.13, at negative 20% (-20%) changes in these design parameters, the p-Xylene yield in the permeate-only mode is significantly influenced positively by the membrane tortuosity followed by the membrane effective thickness. The p-Xylene yield in combined mode is significantly influenced positively by positive 20% (+20%) changes in the internal diameter of the reactor tube while m-Xylene conversion in the reactor is significantly influenced negatively by negative 20% (-20%) changes in the internal diameter of the reactor tube.

In conclusion, from the sensitivity analysis it is obvious that enhancement of performance of e-ZCMR depends on the presence of membranes with optimized membrane properties. Such membrane properties are membrane mean porosity, membrane tortuosity and membrane effective wall thickness. At the same time, design parameters of the reactor such as the reactor volume/size also should be optimized.

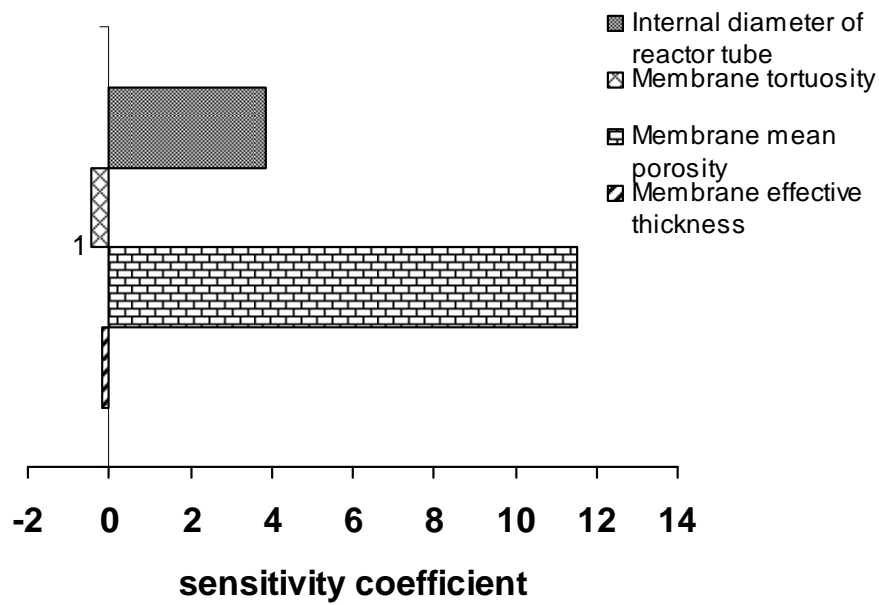


Figure 7.12: A *tornado* diagram showing sensitivity of p-Xylene yield in permeate-only mode to positive 20% (+20%) changes in design variables.

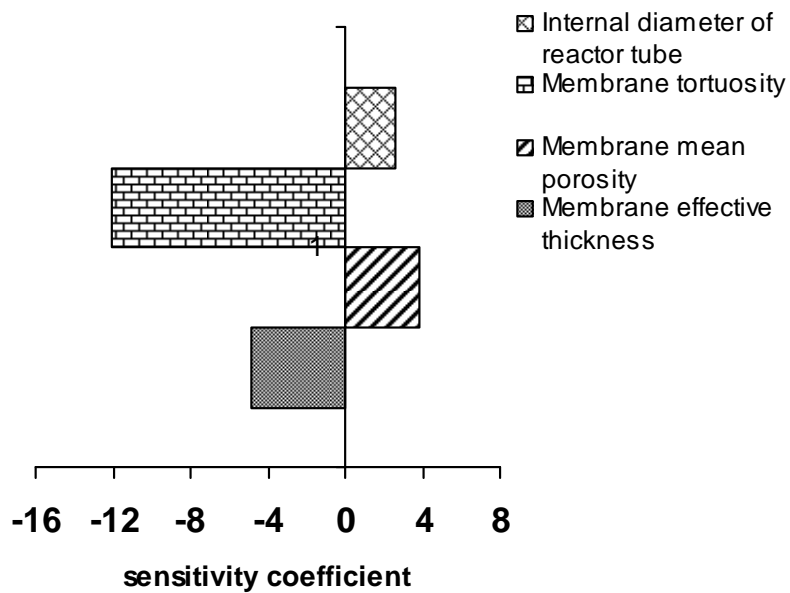


Figure 7.13: A *tornado* diagram showing sensitivity of p-Xylene yield in permeate-only mode to negative 20% (-20%) changes in design variables.

---

## 7.5 Concluding remark

An attempt has been made to model and simulate e-ZCMR for m-Xylene isomerization over Pt-HZSM-5. This is a preliminary study and it is expected that various assumptions made during model formulation and implementation might have significant influence on the model output. However, the model results are in fair agreement with experimental results with percentage errors (absolute) of 17%, 29%, 0.05% and 19.5% for p-Xylene yield in combined mode, p-Xylene selectivity in combined mode, p-Xylene selectivity in permeate-only mode and m-Xylene conversion, respectively. Thus, the model presented in this chapter is able to explain the behaviour of e-ZCMR during m-Xylene isomerization over Pt-HZSM-5 catalyst. In addition, the model is adaptable to e-ZCMR of different configuration such as a hollow fibre MFI-alumina membrane based e-ZCMR. Furthermore, the modeling study has provided the reader with modeling procedure that can be used as basis for further improved modelling studies.

As expected, the sensitivity analysis conducted on the model revealed that membrane mean porosity, membrane tortuosity, membrane effective wall thickness and reactor size play important role in optimizing the performance of an e-ZCMR equipped with a nanocomposite MFI-alumina membrane tube as separation unit, during m-Xylene isomerization over Pt-HZSM-5 catalyst. Furthermore, it is noteworthy to mention that membrane mean porosity, membrane tortuosity are intrinsic properties of the membrane. Membrane mean porosity and membrane tortuosity depend on the pore size distribution of membrane support while the membrane effective wall thickness depends on the membrane synthesis technique. However, it is expected that optimizing the aforementioned parameters will be instrumental in enhancing the performance of e-ZCMR during p-Xylene production.

This is the first open report, although somewhat of a preliminary nature, on the modelling and sensitivity analysis of an e-ZCMR equipped with a nanocomposite MFI-alumina membrane tube as separation unit for m-Xylene isomerization over Pt-HZSM-5 catalyst. Although the model presented in this study is sensitive to quality of data employed, it offers a fair description of the behaviour of e-ZCMR equipped with a nanocomposite MFI-alumina tube during m-Xylene isomerization over Pt-HZSM-5 catalyst. It is recommended that, in subsequent studies, a series of experiments should be conducted to generate accurate kinetics and diffusion data for model implementation and also to validate and improve various assumptions employed in the model formulation.

---

## Chapter 8: Conclusions, recommendations and future outlook

### 8.1. Conclusions

Based on the goals highlighted in Chapter 1 of the dissertation, the following studies have been carried out and reported:

- Influence of operating variables (temperature, sweep gas flow rate and xylene loading/partial pressures) on the separation performance of nanocomposite MFI-alumina membranes during xylene isomer separation.
- Evaluation of the separation performance of nanocomposite MFI-alumina hollow fibre membranes during xylene isomers separation.
- Influence of operating variables and reactor configuration on the performance of an extractor-type zeolite catalytic membrane reactor, having nanocomposite MFI-alumina membrane as separation unit, during m-Xylene isomerization over Pt-HZSM-5 catalyst to p-Xylene.
- Modelling, simulation and sensitivity analysis of an extractor-type zeolite catalytic membrane reactor, having nanocomposite MFI-alumina membrane as separation unit, during m-Xylene isomerization over Pt-HZSM-5 catalyst to p-Xylene.

The results obtained from the aforementioned studies have yielded the following novel contributions toward further research efforts on the development of membrane-based reactive separation system for the production of p-Xylene from mixed xylene:

- Excellent xylene isomer separation performance of nanocomposite MFI-alumina membranes at higher xylene loadings (or higher xylene compositions) over their “film-like” counterparts has been demonstrated. The membrane displayed continuous increase in selectivity at increased xylene loadings/partial pressures. This observation is contrary to the behaviour of their “film-like” counterparts at higher xylene loadings/vapour pressures. This is the first time this outstanding behaviour of MFI-type membranes based on nanocomposite architectures will be reported in the open literature. Thus, the outstanding behaviour of nanocomposite MFI-alumina membranes over their “film-like” counterparts will make them better candidates for application in the future development of energy-efficient process for xylene isomer separation based on membrane technology.
- The use of hollow fibre geometry has long been a solution for improving the performance of membrane-based separation processes but industrial application of this type of configuration is limited to water treatment where polymer hollow fibres are commonly used. Polymer hollow fibres are unsuitable for xylene isomers

---

separation because they are not chemically and thermally stable compared to inorganic/ceramic membranes. The results from the evaluation of separation performance of nanocomposite MFI-alumina hollow fibre membranes during xylene isomer separation showed that the membrane is highly selective to p-Xylene at higher temperature and also displayed about 30% increase in p-Xylene flux over an equivalent membrane tube prepared via this same technique as the fibres and operated at the same operating conditions. The enhancement of p-Xylene flux could be attributed to smaller membrane effective wall thickness ( $<1 \mu\text{m}$ ) compared to membrane effective thickness of  $3 \mu\text{m}$  for the membrane tube. This is the first time that a report on the evaluation of separation performance of nanocomposite MFI-alumina hollow fibre membrane will appear in open literature. Hollow fibres also offer the added advantage of membrane surface-to-volume ratios as high as  $3000 \text{ m}^2/\text{m}^3$  compared to more conventional membrane tubes. For example, a 5-fibre bundle occupying the volume meant for a single alumina tube could double the p-Xylene productivity operating at the temperature where the maximum flux is obtained, taking into account the higher separation surface of the bundle ( $5 \times 9.94 \sim 50 \text{ cm}^2$  vs.  $26 \text{ cm}^2$  for alumina tubes). Therefore, the results presented in this study open up a research line to scale-up the fibre preparation process aimed at obtaining fibre bundles for xylene isomer separation. Using this type of system might be instrumental in enhancing p-Xylene flux in e-ZCMR and in reducing both the size and cost of permeating modules for future xylene separation processes.

- None of previous studies reported p-Xylene purity during m-Xylene isomerization in e-ZCMR. Perhaps due to the low quality of the membranes used by these researchers, no appreciable p-Xylene purity could be obtained in the permeate stream. To obtain high-purity p-Xylene, a demanded form of p-Xylene for industrial applications, via conventional processes such as distillation is a difficult and laborious task. Furthermore, the current processes used to do this are energy consuming because of the similarity in the physical properties of these isomers [289]. Therefore, the results of this study has demonstrated, for the first time, the possibility of obtaining ultrapure p-Xylene ( $\sim 100\%$ ) in e-ZCMR, having a nanocomposite MFI-alumina membrane tube as separation unit, during m-Xylene isomerization over Pt-HZSM-5 catalyst. Moreover, these results showed significant improvement on the p-Xylene yields previously reported by van Dyk *et al.* [186]. Furthermore, the results presented in this study are encouraging and can provide a platform for developing scaled-up energy-efficient industrial processes for producing ultra-pure p-Xylene through catalytic isomerization of m-Xylene over Pt-HZSM-5 catalyst.

- 
- Application of mathematical models to the design of membrane processes is essential to understanding the process design, the process analysis, the optimization of process conditions, and, even, for model-based control. However, in the area of packed-bed catalytic membrane reactors for xylene isomerization, modelling study is still limited. For the application of e-ZCMR for xylene isomerisation to p-Xylene, the first and perhaps the only modelling and simulation without sensitivity analysis study in literature was by Deshayes *et al.* [201]. In view of this, this dissertation reports on the preliminary modelling and sensitivity analysis of an e-ZCMR equipped with a nanocomposite MFI-alumina membrane tube as separation unit during m-Xylene isomerization over Pt-HZSM-5. The simulation results are in fair agreement with experimental results with percentage errors (absolute) of 17%, 29%, 0.05% and 19.5% for p-Xylene yield in combined mode, p-Xylene selectivity in combined mode, p-Xylene selectivity in permeate-only mode and m-Xylene conversion, respectively. Therefore, the model could explain the fundamental behaviour of e-ZCMR during m-Xylene isomerization over Pt-HZSM-5 catalyst. However, the model presented in this study is sensitive to the quality of data employed for model implementation and the assumptions employed during model development. In light of this, it is recommended that, in subsequent studies, a series of experiments should be conducted to generate accurate kinetics and diffusion data for simulation and to validate or improve assumptions employed in the model development and formulation. As expected, the sensitivity analysis performed on the model also revealed that intrinsic membrane property (porosity, tortuosity), membrane effective thickness and reactor size play a vital role in the performance of e-ZCMR during p-Xylene production from the mixed xylenes.

Additionally, the results of this work provide a platform to develop feasible and energy-efficient process for producing high purity p-Xylene from mixed xylene based on the application of MFI-type zeolite membranes with nanocomposite architecture. Furthermore, in other applications of MFI membranes for gas separation, the use of nanocomposite architecture rather than “film-like” configuration could increase the life in service of the membranes.

In summary, the aforementioned novel contributions have been communicated to fellow researchers in the area of membrane-based reactive process as articles in international scientific journals (three published, two in press and one accepted) and in conference proceedings (four conference proceedings). Samples of the published articles can be found in Appendix E.

---

## 8.2. Recommendations and future outlook

To obtain total conversion during the xylene isomerization process, a chemical-equilibrium restricted reaction in conventional catalytic reactors is impossible. Thus, the existing industrial technology could only produce equilibrium or near equilibrium xylene mixtures. Recycling the xylene streams back into the process lines might ensure higher p-Xylene yield, but only at the expense of higher operation costs due to higher energy consumption. As documented in this dissertation, the use of e-ZCMRs could ensure production of high-purity p-Xylene above the equilibrium yield with a drastic reduction of operation costs due to a reduction of energy consumption. The enormous potential of large-scale applications of xylene isomerization in oil and petrochemical industries promises major advances and developments of such systems in the near future.

Due to the higher energy-efficiency of membrane-based reactive separation process compared to other commercial techniques, development of an industrial process based on the application of membrane-based reactive separation for the production of p-Xylene is foreseen. Furthermore, the use of MFI-alumina membranes with nanocomposite architectures could be an impetus to accelerating this development. However, further research efforts are essential in the development of defect-free MFI zeolite membranes for xylene isomer separation, and, in the process optimization.

In the area of process optimization, this dissertation has proposed the application of nanocomposite MFI-alumina hollow fibres in a membrane-based reactive separation process for the production of high-purity p-Xylene from mixed xylene because of (i) the high surface-to-volume ratios of the hollow fibres (as high as  $3000 \text{ m}^2/\text{m}^3$ ) compared to randomly ordered MFI membrane tubes; (ii) their higher p-Xylene flux through the membrane from their lower effective membrane thickness compared to randomly ordered MFI membrane tubes [248]. Optimization of the fibre preparation protocol and development of such materials towards obtaining fibres bundle and fibre module appears to be a promising option for the development of energy-efficient process for p-Xylene production in the near future. With the development of fibre modules, development of compact and cost-effective units for production of p-Xylene from mixed xylenes based on membrane-based reactive separation technology might be fast-tracked. As documented in this dissertation, nanocomposite MFI-alumina membranes could be a promising candidate for PV application to separate xylene isomers. Thus, evaluation of the separation performance of nanocomposite MFI-alumina membranes (tubes and fibres) in pervaporation application might be interesting.

Furthermore, catalytically active MFI membranes may be a good option. In general terms, catalytically active membranes are thought to be about 10 times more active than when the catalyst pellets are used in the fixed-bed reactors provided that the membrane thickness

---

and porous texture, as well as the quantity and location of the catalyst in the membrane are adapted to the reaction kinetics [290,291]. However, research effort in the application of catalytically active membranes for p-Xylene production is still limited.

In parallel, research and development of new efficient materials duly put in membrane form may help to address new research lines for xylene separation and/or isomerization. For instance, metal-organic frameworks (MOFs), which seem to be attracting increasing attention from the scientific community and industry, could be used as alternatives to classical MFI-type zeolites for gas separation, and alternatives to other zeolites (e.g. faujasites) for molecular sieving. As far as it has been ascertained, no application of MOF materials to xylene isomer separation and/or isomerization has been reported in either open or patent literature. Therefore, research effort in this area will be quite interesting and productive.

Finally, virtually all the research efforts involving the use of membranes for separation and production of p-Xylene from mixed xylenes are still limited to laboratory scale studies. In view of this, scale-up studies and techno-economic studies of the technology are necessary to evaluate the competitiveness of the technology with existing processes.

---

## References

1. International Energy outlook 2009 report, Energy Information Administration, Office of integrated Analysis and Forecasting, U.S. Department of Energy, Washington, DC 20585, *DOE/EIA-0484*, 2009; pp284.
2. J.J. McKetta.1999. Encyclopedia of Chemical Processing and Design, Vol 67, Marcel Dekker Inc., New York, 1999; p. 147.
3. B. Smitha, D. Suhanya, S. Sridhar, M. Ramakrishna, Separation of organic mixtures by pervaporation—a review, *J. Membr. Sci.* 241 (2004) 1-21.
4. G. Tweedle, The impact of Asian PX/PTA developments on Europe, 6<sup>th</sup> European Aromatics & Derivatives Conference, Antwerp, Belgium, 2007, personal communication (accessed 19<sup>th</sup> February 2009)
5. CMAI's World Xylenes and Terephthalates Analysis, 2007 ([www.cmaiglobal.com/marketing/News/WXTAO7.pdf](http://www.cmaiglobal.com/marketing/News/WXTAO7.pdf))
6. H-G. Franck, J.W. Stadelhofer, Industrial Aromatic Chemistry. Raw Materials, Process, Products, Springer-Verlag, Berlin, 1988.
7. Xylenes, Nexant Chem Systems. May, 2002.(<http://nexant.ecnext.com/coms2/>)
8. J. Fabri, H. Graeser, T.A. Simo. Xylenes, In: Ullmann's Encyclopedia of Industrial Chemistry, seventh ed., John Wiley & Sons, Inc. Germany, 2009.
9. D. Bessarabov, Membrane gas-separation technology in the petrochemical industry, *Membr. Technol.*, 107 (1999) 9–13.
10. R. Spillman, Economics of gas separation membrane processes, in: R.D. Noble and S.A. Stern (Eds.), *Membrane Separation Technology: Principles and Applications*, Elsevier, The Netherlands, 1995.
11. T. Matsuura, *Synthetic Membrane and Membrane Separation Processes*, CRC Press, New York, 1993.
12. S.S. Dhingra, Mixed gas transport study through polymeric membranes: a novel technique, PhD dissertation, Virginia Polytechnic Institute, USA, 1997.
13. L. D. van Dyk, Evaluation and improvement of dehydrogenation conversion and isomerization selectivity in an extractor catalytic membrane reactor, PhD dissertation, Department of Process Engineering, University of Stellenbosch, South Africa, 2005.
14. W.J. Cannella, in: *Kirk-Othmer Encyclopedia of Chemical Technology*, vol. 16, New Jersey, 2001, p. 841.

- 
15. J. Cejka, B. Wichterlova, Acid-catalyzed synthesis of mono- and dialkyl benzenes over zeolites: active sites, zeolite topology, and reaction mechanisms, *Catal. Rev.* 44 (2002) 375-421.
  16. S.A. Laurich, US Patent 3,467,724, Chevron Research Corporation, 1969.
  17. G. M. Minceva, A. E. Rodriguez, Understanding and revamping of industrial scale SMB units for p-Xylene separation, *AIChE J.* 53(1) (2007)138-149.
  18. C.M. Roesler, S. Kulprathipanja, J.E. Rekoske, US Patent 200220103408, 2002.
  19. G.H. Vickers, US Patent 20040010170, BP American Inc., 2004.
  20. P. Leflaive, K. Barthelet, US Patent 200704443253, 2007.
  21. J. Blehaut, R-M. Nicoud, Recent aspects in simulated moving bed, *Analisis magazine* 26 (7) (1998) M60-M70.
  22. R.A. Meyers, Handbook of petrochemicals production processes, McGraw-Hill Professional, New York, 2004.
  23. J.F. Le Page, Applied heterogeneous catalysis: Design, manufacture, use of solid catalysts, Technip, Paris. 1987.
  24. C.A. Henriques, J.L.F. Monteiro, P. Magnoux, M. Guisnet, Characterization of the coke formed during o-Xylene isomerization over mordenites at various temperatures, *J. Catal.* 172 (1997) 436-445.
  25. H. Gonzalez, A. Rodriguez, L. Cedeno, J. Ramirez, Isomerization of C8 aromatics over a Pt/Mordenite catalyst. A statistical model, *Ind. Eng. Chem. Res.* 35 (1996) 3964-3972.
  26. E. Benazzi, J-F. Joly, J.M. da Silva, G., Ribeiro, M.F.G. Ribeiro, Catalyst with a base of modified MFI zeolite, and its use in the isomerization of a C<sub>8</sub> aromatic cut, US Patent 6, 245,704, Institut Francais du Pétrole, France, 2001.
  27. Y-G. Li, H. Jun, Kinetics study of isomerization of xylene on ZSM-5 zeolites: the effect of modification with MgO and CaO, *Applied Catal. A: General* 142 (1996) 123-137.
  28. S. Al-Khattaf, Enhancing p-Xylene selectivity during m-Xylene transformation using mildly pre-coked ZSM-5 catalyst, *Chem. Eng. Process: Process Intensif.* 2007; 46 (2007) 964-974.
  29. R.D. Wilson, D.G. Barton, C.D. Baertsch, E. Iglesia, Reaction and deactivation pathways in xylene isomerization on Zirconia modified by Tungsten Oxide, *J. Catal.* 194 (2000) 175-187.
  30. D.A. Young, J.W. Koepke, Chemical reaction promoted by catalytically active amorphous silica, US Patent 4,501,925, Union Oil Company of California, Los Angeles, 1985.

- 
31. A. Corma, E. Sastre, Evidence for the presence of a bimolecular pathway in the isomerization of xylene on some large-pore zeolites, *J. Catal.* 129 (1991) 177- 185.
  32. T.S. Gendy, K.C. Pratt, Catalyst activity decay functions in liquid and vapour phase xylenes isomerization over H-Y zeolite, *Chem. Eng. Sci.*37(1) (1982)37-43.
  33. S. Morin, N.S. Gnep, M. Guisnet, Simple method for determining the relative significance of the unimolecular and bimolecular pathways of xylene isomerization over HY zeolite, *J. Catal.* 159 (1996) 296-304.
  34. F.J. Llopis, G. Sastre, A. Corma., Isomerization and disproportionation of m-Xylene in a zeolite with 9-and 10-membered ring pores: Molecular dynamics and catalytic studies, *J. Catal.* 242 (2006) 195-206.
  35. D-Y. Jan, G.J. Lewis, J.G. Moscoso, M.A. Miller, Q. Chen, Xylene isomerization process using UZM- and UZM-6 zeolites, US Patent 6,388,159 UOPLLC, Des Plaines, 2002.
  36. A.A Belhekar, R.K. Ahedi, S. Kuriyavar, S.S. Shevade, B.S. Rao, R. Anand, Z. Tvaruzkova, Effect of acid sites of Al- and Fe-Ferrierite on m-Xylene isomerization, *Catal. Commun.* 4(6) (2003) 295-302.
  37. F. Bauer, W-H. Chen, H. Ernst, S-J. Huang, A. Freyer, S-B. Liu, Selectivity improvement in xylene isomerization, *Micropor. Mesopor. Mater.* 72(1-3) (2004) 81-89.
  38. B. Sulikowski, M-Xylene isomerization/disproportionation selectivity over dealuminated Y zeolite, *React. Kin. Catal. Lett.* 31 (1986) 215-219.
  39. A. Iliyas, S. Al-Khattaf, Xylene transportation over USY zeolite: an experimental and Kinetic study, *Applied catalysis A: General* 269 (2004) 225-236.
  40. S. Laforge, D. Martin, M. Guisnet, m-Xylene transformation over H-MCM-22 zeolite .2. Method for determining the catalytic role of the three different pore systems, *Micropor. Mesopor. Mater.* 67(2-3) (2004) 235-244.
  41. O. Akpolat, G. Gunduz, Isomerization of m-Xylene, *J. Applied Sci.* 5(2) (2005) 236-248.
  42. Y.S. Hsu, T.Y.Lee, H.C. Hu, Isomerization of Ethylbenzene and m-Xylene on zeolites, *Ind. Eng. Chem. Res.*27(6) (1988) 942-947.
  43. S. Zheng, H.R. Heydenrych, A. Jentys, J.A. Lercher, Influence of surface modification on the acid site distribution of HZSM-5, *J. Phys. Chem. B.*106 (2002) 9552-9558.
  44. T-C. Tsai, I. Wang, C-K. Huang, S-D. Liu, Study on ethylbenzene and xylene conversion over modified ZSM-5, *Applied Catal. A: General* 321(2) (2007) 125-134.

- 
45. B. Sulikowski, J. Haber, A. Kubacka, K. Pamin, Z. Olejniczak, J. Ptasynski, Novel "ship-in-the-bottle" type catalyst: evidence for encapsulation of 12-tungstophosphoric acid in the supercage of synthetic faujasite, *Catal. Lett.*, 39 (1996) 27-31.
  46. T. Yashima, Y. Sakaguchi, S. Namba. Selective formation of p-Xylene by alkylation of toluene with methanol on ZSM-5 type zeolites, *Stud. Surf. Sci. Catal.* 7 (1981) 739-751.
  47. L.B. Young, S.B. Butter, W.W. Kaeding, Shape selective reactions with zeolite catalysts III. Selectivity in xylene isomerization, toluene-methanol alkylation, and toluene disproportionation over ZSM-5 zeolite catalysts, *J. Catal.* 76(2) (1982) 418-432.
  48. W.W. Kaeding, C. Chu, L.B. Young, B. Weinstein, S.B. Butter., Selective alkylation of toluene with methanol to produce para-xylene, *J. Catal.* 67(1) (1981) 159-174.
  49. R.W. Baker, *Membrane Technology and Applications*, second (Eds.), John Wiley, New Jersey, 2004.
  50. M. Porter, *Handbook of Industrial Membrane Technology*, Noyes Publications, New Jersey, 1990.
  51. A. Kargari, T. Kaghazchi, M. Soleimani, Extraction of gold (III) ions from aqueous solutions using polyamine type surfactant liquid membrane, *Canad. J. Chem. Eng.* 82 (2004) 1301–1306.
  52. A. Kargari, T. Kaghazchi, M. Soleimani, Mass transfer investigation of liquid membrane transport of gold(III) by methyl iso-butyl ketone mobile carrier, *J. Chem. Eng. Tech.* 27(9) (2004) 1014–1018.
  53. V.S. Cunha, M.L.L. Paredes, C.P. Borges, A.C. Habert, R. Nobrega, Removal of aromatics from multicomponent organic mixtures by pervaporation using polyurethane membranes: experimental and modelling, *J. Membr. Sci.* 206(1-2) (2002) 277-290.
  54. H.L. Chen, L.G. Wu, J. Tan, C.L. Zhu, PVA membrane filled  $\beta$ -cyclodextrin for separation of isomeric xylenes by pervaporation, *Chem. Eng. J.* 78 (2000) 159-164.
  55. J. Hao, K. Tanaka, H. Kita, K. Okamoto, The pervaporation properties of sulfonyl-containing polyimide membranes to aromatic/aliphatic hydrocarbon mixtures, *J. Membr. Sci.* 132(1) (1997) 97-108.
  56. J. Fang, K. Tanaka, H. Kita, K. Okamoto, Pervaporation properties of ethanol-containing copolyimide membranes to aromatic/non-aromatic hydrocarbon mixtures, *Polymer* 40(11) (1999) 3051-3059.
  57. T. Miyata, T. Iwamoto, T. Uragami, Characteristics of permeation and separation of xylene isomers through poly (vinylalcohol) membranes containing cyclodextrin, *Macromol. Chem. Phys.* 197 (1996) 2909-2921.

- 
58. I. Cabasso, Organic liquid mixtures separation by permselective polymer membranes. 1. Selection and characteristics of dense isotropic membranes employed in the pervaporation process, *Ind. Eng. Chem. Prod. Res. Dev.* 22 (1983) 313-319.
  59. J. Sikonia, F. McCandless, Separation of isomeric xylenes by permeation through modified plastic films, *J. Membr. Sci.* 4 (1978) 229-241.
  60. C. Lee, Synthetic membranes containing schardinger cyclodextrin additives, *J. Appl. Polym. Sci.* 26 (1981) 489-497.
  61. M.H.V. Mulder, F. Krutz, C. A. Smolers, Separation of isomeric xylenes by pervaporation through cellulose ester membranes, *J. Membr. Sci.* 11(3) (1982) 349-363.
  62. K. Ishihara, K. Matsui, H. Fujii, H. Nishide, I. Shinohara, Separation of xylene isomers by pervaporation through a highly permselective polymer membrane having dinitrophenyl group, *Chem. Lett.* 11 (1985) 1663-1666.
  63. M. Wessling, U. Werner, Pervaporation of aromatic C<sub>8</sub>-isomers, *J. Membr. Sci.* 57 (1991) 257-270.
  64. J. Caro, M. Noack, Zeolite membranes-Recent developments and progress, *Micropor. Mesopor. Mater.* 115(3) (2008) 215-233.
  65. A. Julbe, Zeolite membranes-synthesis, characterization and application, in: J. Cejka, H. van Bekkum, A. Corma and F. Schuth (Eds.), *Introduction to zeolite Science and Practice*, Stud. Surf. Sci. Catal. Elsevier B.V., Amsterdam, 2007, pp.181-219.
  66. T.C. Bowen, R.D. Noble, J.L. Falconer, Fundamentals and applications of pervaporation through zeolite membranes, *J. Membr. Sci.* 245 (2004) 1-33.
  67. Y.Y. Fong, A.Z. Abdullah, A.L. Ahmad, S. Bhatia, Development of functionalized zeolite membrane and its potential role as reactor combined separator for para-xylene production from xylene isomers, *Chem. Eng. J.* 139(1) (2008) 172-193.
  68. Y. Morigami, M. Kondo, J. Abe, H. Kita, K. Okamoto, The first large-scale pervaporation plant using tubular-type module with zeolite NaA membrane, *Sep. Purif. Technol.* 25 (2001) 251-260.
  69. S. Tennison, Current hurdles in the commercial development of inorganic membrane reactors, *Membr. Technol.* 128 (2000) 4-9.
  70. S.P. Nunes, K-V. Peinemann, *Membrane Technology in the Chemical Industry*, Wiley-VCH, Weinheim, 2001.
  71. K. Scott, *Handbook of Industrial Membranes*, first ed. Elsevier Science Publishers Ltd, Oxford, 1995.
  72. X. Feng, R. Y.M. Huang, Liquid separation by membrane pervaporation: A review, *Ind. Eng. Chem. Res.* 36 (1997) 1048-1066.

- 
73. J.G. Wijmans, R.W. Baker, Solution-diffusion model: a review, *J. Membr. Sci.* 107(1-2) (1995) 1-21.
  74. R.J. Argauer, M. Kensington, G.R. Landolt, US Patent 3,702,886, 1972.
  75. G.T. Kokotailo, S.L. Lawton, D.H. Olson, W.M. Meier, Structure of synthetic zeolite ZSM-5, *Nature* 272 (1978) 437-438.
  76. G. Vezzalini, S. Quartieri, E. Galli, A. Alberti, G. Cruciani, A. Kvick, Crystal structure of the zeolite mutinaite, the natural analog of ZSM-5, *Zeolites* 19 (1997) 323-325.
  77. R.W. Grose, E.M. Flanigen, Crystalline silica, *US Patent* 4,061,724, Union Carbide Corporation, New York, 1977.
  78. E.M. Flanigen, J.M. Bennett, R.W. Grose, J.P. Cohen, R.L. Patton, R.M. Kirchner, Silicalite, a new hydrophobic crystalline silica molecular sieve, *Nature* 271 (1978) 512-516.
  79. D.W. Breck, *Zeolite molecular sieves: Structure, chemistry and use*, John Wiley & Sons, New York, 1974.
  80. C. Baerlocher, W.M. Meier, D.H. Olson, *Atlas of Zeolite Framework Types*, Fifth ed., Elsevier, Amsterdam, 2001.
  81. D.H. Olson, G.T. Kokotailo, S.L. Lawton, W.M. Meier, Crystal structure and structure-related properties of ZSM-5, *The Journal of Physical Chemistry* 85 (1981) 2238-2243.
  82. G. Artioli, A. Pavese, G.L. Marra, C. Lamberti, Structure study of hydroxyl groups in silicalite, ISIS Experimental Report, ISIS98, The RAL ISIS Facility annual report, 1998; RB8702, p.1.
  83. C-K. Lee, A.S.T. Chiang, Adsorption of aromatic compounds in large MFI zeolite crystals, *J. Chem. Soc., Faraday Trans.* 92 (1996) 3445-3451.
  84. H. van Koningsveld, J.C. Jansen, H. van Bekkum, The monokini framework structure of zeolite H-ZSM-5. Comparison with the orthorhombic framework of as-synthesized ZSM-5, *Zeolites* 10(4) (1990) 235-242.
  85. L.J. Song, Z.L. Sun, H.Y. Ban, M. Dai, L.V.C. Rees, Benzene adsorption in microporous materials, *Adsorption* 11(3-4) (2005) 325-339.
  86. D.M. Ruthven, B.K. Kaul, Adsorption of aromatic hydrocarbon in NaX zeolite 1. Equilibrium, *Ind. Eng. Chem. Res.* 32 (1993) 2047-2052.
  87. J-P. Bellat, M-H. Simonot-Grange, S. Julian, Adsorption of gaseous p-Xylene and m-Xylene on NaY, KY, and BaY zeolites: Part 1. Adsorption equilibria of pure xylenes, *Zeolites* 15(2) (1995) 124-130.

- 
88. V. Cottier, J-P. Bellat, M-H. Simonot-Grange, A. Méthivier, Adsorption of p-Xylene/m-Xylene gas mixtures on BaY and NaY zeolites. Coadsorption equilibria and selectivities, *J. Phys. Chem. B* 101 (1997) 4798-4802.
  89. V. Lachet, A. Boutin, B. Tavitian, A.H. Fuchs, Molecular simulation of p-Xylene and m-Xylene adsorption in Y zeolite. Single components and binary mixtures study, *Langmuir* 15 (1999) 8678-8685.
  90. M.M. Laboy, I. Santiago, G.E. Lopez, Computing adsorption isotherms for benzene, toluene, and p-Xylene in heulandite zeolite, *Ind. Eng. Chem. Res.* 38 (1999) 4938-4945.
  91. M. Minceva, A.E. Rodrigues, Adsorption of xylenes on faujasite-type zeolite. Equilibrium and kinetics in batch adsorber, *Chem. Eng. Res. Design* 82(5) (2004) 667-681.
  92. M.A. Hernandez, L. Corona, A.I. Gonzalez, F. Rojas, V.H. Lara, F. Silva, Quantitative study of the adsorption of aromatic hydrocarbons (benzene, toluene, and p-Xylene) on dealuminated clinoptilolites, *Ind. Eng. Chem. Res.* 44(9) (2005) 2908-2916.
  93. S. Mardonio, P. Lucena, R.Q. Snurr, C.L. Cavalcante (Jr), Studies on adsorption equilibrium of xylenes in AEL framework using biased GCMC and energy minimization, *Micropor. Mesopor. Mater.* 111(1-3) (2008) 89-96.
  94. K. Yamahara, K. Okazai, K. Kawamura, Molecular dynamics studies on thermal behaviour of an MFI-type zeolite, *Catal. Today* 23 (1995) 397-402.
  95. O. Talu, C.J. Guo, D.T. Hayhurst, Heterogeneous adsorption equilibria with comparable molecule and pore sizes, *J. Phys. Chem.* 93 (1989) 7294-7298.
  96. P. Gelin, J.F. Dutel, B.F. Mentzen, p-Xylene adsorption on silicalite measured by a quasi-equilibrium gravimetric technique, *Micropor. Mater.* 4(4) (1995) 283-290.
  97. C.A. Fyfe, J.S.J. Lee, L.M.D. Cranswick, I. Swainson, Powder neutron diffraction determination of the structure of the o-Xylene/zeolite ZSM-5 complex, *Micropor. Mesopor. Mater.* 112(1-3) (2008) 299-307
  98. C.A. Fyfe, G.J. Kennedy, C.T. DeSchutter, G.T. Kokotailo, Sorbate-induced structural changes in ZSM-5(silicalite), *J. Chem. Soc., Chem. Commun.* 8 (1984) 541-542.
  99. C.A. Fyfe, H. Strobl, G.T. Kokotailo, G.J. Kennedy, G.E. Barlow, Ultra-high-resolution  $^{29}\text{Si}$  solid-state MAS NMR investigation of sorbate and temperature-induced changes in the lattice structure of zeolite ZSM-5, *J. Am. Chem. Soc.* 110 (1988) 3373-3380.

- 
100. C.A. Fyfe, Y. Feng, H. Grondey, G.T. Kokotailo, Characterization of a high-loaded intercalate of p-Xylene with a highly siliceous form of ZSM-5 by high resolution  $^{29}\text{Si}$  solid-state NMR spectroscopy, *J. Chem. Soc., Chem. Commun.* 18 (1990) 1224-1226.
101. P.T. Reischman, K.D. Schmitt, D.H. Olson, A theoretical and NMR study of p-Xylene sorption into ZSM-5, *J. Phys. Chem.* 92 (1988) 5165-5169.
102. H. van Koningsveld, F. Tuinstra, H. van Bekkum, J.C. Jansen, The location of p-Xylene in a single kristal of zeolite H-ZSM-5 with a new, sorbate-induced, orthorhombic framework symmetry, *Acta Cryst.* B45 (1989) 423-431.
103. B.F. Mentzen, F. Bosselet, Characterization of guest molecules adsorbed on zeolites of known structure. Part III-Localization of the p-XYLI and p-XYLII species sorbed in a high coverage B.ZSM-5/p-Xylene complex, *Mater. Res. Bull.* 23 (1998) 227-235.
104. B.F. Mentzen, P. Gelin, The silicalite/p-Xylene system: Part I – Flexibility of the MFI framework and sorption mechanism observed during p-Xylene pore-filling by X-ray power diffraction at room temperature, *Mater. Res. Bull.* 30 (1995) 373-380.
105. R. Goyal, A.N. Fitch, H. Jovic, Powder neutron and X-ray diffraction studies of benzene adsorbed in zeolite ZSM-5, *J. Phys. Chem. B* 104 (2000) 2878-2884.
106. G. Xomeritakis, S. Nair, M. Tsapatsis, Transport properties of alumina-supported MFI membranes made by secondary (seeded) growth, *Micropor. Mesopor. Mater.* 38 (2000) 61-73.
107. T. Takaishi, K. Tsutsumi, K. Chubachi, A. Matsumoto, Adsorption induced phase transition of ZSM-5 by p-Xylene, *J. Chem. Soc., Faraday Trans.* 94 (1998) 601-608.
108. R.E. Richards, L.V.C. Rees, The sorption of p-Xylene in ZSM-5, *Zeolites* 8(1) (1988) 35-39.
109. A. Jentys, H. Tanaka, J.A. Lercher, Surface processes during sorption of aromatic molecules on medium pore zeolites, *J. Phys. Chem. B* 109 (2005) 2254-2261.
110. E.A. Havenga, Y. Huang, A study of binary adsorption of aromatics in completely siliceous zeolite ZSM-5 by FT-Raman Spectroscopy, *J. Phys. Chem. B* 109 (2005) 18031-18036.
111. G. Muller, E. Bodis, J. Kornatowski, J.A. Lercher, IR microspectroscopic investigation of the acid sites in metal substituted  $\text{AlPO}_4\text{-5}$  molecular sieves Part 1. Sorption of benzene and strong bases, *Phys. Chem. Chem. Phys.* 1 (1999) 571-578.
112. Y-C. Long, H-W. Jiang, H. Zeng, Sorbate/framework and sorbate/sorbate interaction of organics on siliceous MFI type zeolite, *Langmuir* 13 (1997) 4094-4101.
113. S.H. Mohanty, A.V. McCormick, Prospects for principles for size and shape selective separations using zeolites, *Chem. Eng. J.* 74(1-2) (1999) 1-14.

- 
114. S.H. Mohanty, H.T. Davis, A.V. McCormick, Sorbate/Sorbent phase transition during adsorption of p-Xylene in silicalite, *AIChE J.* 46(8) (2000) 1662-1675.
115. S.H. Mohanty, H.T. Davis, A.V. McCormick, Shape selective adsorption in atomistic nanopores: study of xylene isomers in silicalite, *Chem. Eng. Sci.* 55 (2000) 2779-2792.
116. S. Chempath, R.Q. Snurr, J.J. Low, Molecular modelling of binary liquid-phase adsorption of aromatics in silicalite, *AIChE J.* 50(2) (2004) 463-469.
117. R.Q. Snurr, A.T. Bell, D.N. Theodorou, Prediction of adsorption of aromatic hydrocarbons in silicalite from grand canonical Monte Carlo simulation with biased insertions, *J. Phys. Chem.* 97 (1993) 13472-13752.
118. C-J. Guo, O. Talu, D.T. Hayhurst. Phase transition and structural heterogeneity; benzene adsorption on silicalite, *AIChE J.* 35(4) (1989) 573-578
119. M.S. Sun, O. Talu, D.B. Shah, Adsorption equilibria of C<sub>5</sub>-C<sub>10</sub> normal alkanes in silicalite crystals, *J. Phys. Chem.* 100 (1996) 17276-17280.
120. T.J.H. Vlugt, W. Zhu, F. Kapteijn, J.A. Moulijn, B. Smit, R. Krishna, Adsorption of linear and branched alkanes in the zeolite silicalite-1, *J. Am. Chem. Soc.* 120 (1998) 5599-5600.
121. T.J.H. Vlugt, R. Krishna, B. Smit, Molecular simulations of adsorption isotherms for linear and branched alkanes and their mixtures in silicalite, *J. Phys. Chem. B* 103 (1999) 1102-1118.
122. J. Li, O. Talu, Adsorption equilibrium of benzene-p-Xylene vapour mixture on silicalite, *Chem. Eng. Sci.* 49(2) (1994) 189-197.
123. J. Narkiewicz-Michalek, P. Szabelski, W. Rudzinski, A.S.T. Chiang, Heterogeneous three-site lattice model for adsorption of aromatics in ZSM-5 zeolites: temperature dependence of adsorption isotherms, *Langmuir* 15 (1999) 6091-6102.
124. P. Szabelski, J. Narkiewicz-Michalek, Three-site lattice gas model for adsorption of binary aromatic mixtures in silicalite, *Langmuir* 17 (2001) 61-68.
125. M. Yu, J.T. Hunter, J.L. Falconer, R.D. Noble, Adsorption of benzene mixtures on silicalite-1 and NaX zeolites, *Micropor. Mesopor. Mater.* 96(1-3) (2006) 376-385.
126. W. Rudzinski, J. Narkiewicz-Michalek, P. Szabelski, A.S.T. Chiang., Adsorption of aromatics in zeolites ZSM-5: A thermodynamic-Calorimetric study based on the model of adsorption on heterogeneous adsorption sites, *Langmuir* 13 (1997) 1095-1103.
127. A.L. Myers, J.M. Prausnitz, Thermodynamics of mixed gas adsorption. *AIChE J.* 11 (1965) 121-127.

- 
128. J. Li, O. Talu, Structural effect on molecular simulations of tight-pore systems, *J. Chem. Soc. Faraday Trans.* 89 (1993) 1683-1687.
129. M. Grahn, A. Holmgren, J. Hedlund, Adsorption of n-hexane in thin silicalite-1 films studied by FTIR/ATR spectroscopy, *J. Phys. Chem. C* 112 (2008) 7717-7724.
130. H. Jobic, J. Karger, M. Bee, Simultaneous measurement of self- and transport diffusivities in zeolites, *Phys. Rev. Lett.* 82(21) (1999) 4260-4263.
131. S. Brandani, M. Jama, D. Ruthven, Diffusion, self-diffusion and counter-diffusion of benzene and p-Xylene in silicalite, *Micropor. Mesopor. Mater.* 35-36 (2000) 283-300.
132. A. Zikanova, M. Bülow, H. Schlotter, Intracrystalline diffusion of benzene in ZSM-5 and silicalite, *Zeolites* 7(2) (1987) 115-118.
133. D.B. Shah, D.T. Hayhurst, G. Evarina, C.J. Guo, Sorption and diffusion of benzene in HZSM-5 and silicalite crystals, *AIChE J.* 34(10) (1988) 1713-1717.
134. M. Eic, D.M. Ruthven, *Zeolites, Facts, Figures, Future*, Elsevier, Amsterdam, 1989, pp. 897.
135. W. Niessen, H.G. Karge, Diffusion of p-Xylene in single and binary systems in zeolites investigated by FTIR spectroscopy, *Micropor. Mater.* 1 (1993) 1-8.
136. H.G. Karge, W. Nießen, A new method for the study of diffusion and counter-diffusion in zeolites, *Catal. Today* 8 (1991) 451-465.
137. C. Förste, J. Kärger, H. Pfeifer, L. Riekert, M. Bülow, A. Zikanova, Comparison of nuclear magnetic resonance tracer exchange and molecular uptake of benzene on pentasil, *J. Chem. Soc., Faraday Trans.* 86 (1990) 881-885.
138. D. Shen, L.V.C. Rees, Diffusivities of benzene in HZSM-5, silicalite-1, and NaX determined by frequency-response techniques, *Zeolites* 11(7) (1991) 666-671.
139. L. Song, Z-L. Sun, L.V.C. Rees, Experimental and molecular simulation studies of adsorption and diffusion of cyclic hydrocarbons in silicalite-1, *Micropor. Mesopor. Mater.* 55 (2002) 31-49.
140. L. Song, L.V.C. Rees, Adsorption and diffusion of cyclic hydrocarbon in MFI-type zeolites studied by gravimetric and frequency-response techniques, *Micropor. Mesopor. Mater.* 35-36 (2000) 301-314.
141. H. Jobic, M. Bee, S. Pouget, Diffusion of benzene in ZSM-5 measured by the neutron spin-echo technique, *J. Phys. Chem. B* 104 (2000) 7130-7133.
142. J. Kärger, J. Caro, Interpretation and correlation of zeolitic diffusivities obtained from nuclear magnetic resonance and sorption experiments, *J. Chem. Soc. Faraday Trans.* 73 (1977) 1363-1376.

- 
143. H. Karsh, A. Culfaz, H. Yücel. Sorption properties of silicalite-1 of pure silica form: The influence of sorption history on sorption kinetics of critically sized molecules, *Zeolites* 12(6) (1992) 728-732.
144. V.R.Choudhary, V.S. Nayak, T.V. Choudhary, Single-component sorption/diffusion of cyclic compounds from their bulk liquid phase in H-ZSM-5 zeolite, *Ind. Eng. Chem. Res.* 36 (1997) 1812-1818.
145. R. Krishna, Problems and pitfalls in the use of the Fick formulation for intraparticle diffusion, *Chem. Eng. Sci.* 48(5) (1993) 845-861.
146. A.I. Skoulidas, D.S. Sholl, Transport diffusivities of CH<sub>4</sub>, CF<sub>4</sub>, He, Ne, Ar, Xe, and SF<sub>6</sub> in silicalite from atomistic simulations, *J. Phys. Chem. B* 106 (2002) 5058-5067.
147. D.M Ruthven, Diffusion of aromatic hydrocarbons in silicalite/HZSM-5, *Adsorption* 13 (2007) 225-230.
148. G. Muller, T. Narbeshuber, G. Mirth, J.A. Lercher, Infrared microscopic study of sorption and diffusion of toluene in ZSM-5, *J. Phys. Chem.* 98 (1994) 7436-7439.
149. L. Song, Z.L. Sun, H.Y. Ban, M. Dai, L.V.C. Rees, Studies of unusual adsorption and diffusion behaviour of benzene in silicalite-1, *Phys. Chem. Chem. Phys.* 6, (2004) 4722-4731.
150. R. Krishna, Multicomponent surface diffusion of adsorbed species: A description based on the generalized Maxwell-Stefan equations, *Chem. Eng. Sci.* 45(7) (1990) 1779-1791.
151. W.R. Qureshi, J. Wei, One-and two component diffusion in zeolite ZSM-5 II. Experimental, *J. Catal.* 126 (1990) 147-172.
152. D.M. Ruthven, M. Eic, E. Richard, Diffusion of C<sub>8</sub> aromatic hydrocarbons in silicalite, *Zeolites* 11 (1991) 647-653.
153. H. Ban, J. Gui, L. Duan, X. Zhang, L. Song, Z. Sun, Sorption of hydrocarbons in silicalite-1 studied by intelligent gravimetry, *Fluid Phase Equil.* 232(1-2) (2005) 149-158.
154. Y. Fujikata, T. Masuda, H. Ikeda, K. Hashimoto, Measurement of the diffusivities within MFI-and Y-type zeolite catalysts in adsorption and desorption processes, *Micropor. Mesopor. Mater.* 21(4-6) (1998) 679-686.
155. T. Masuda, Y. Fujikata, T. Nishida, K. Hashimoto, The influence of acid sites on intracrystalline diffusivities within MFI-type zeolites, *Micropor. Mesopor. Mater.* 23 (1998) 157-167.
156. P. Wu, A. Debebe, Y.H. Ma, Adsorption and diffusion of C<sub>6</sub> and C<sub>8</sub> hydrocarbons in silicalite, *Zeolites* 3(2) (1983) 118-122.

- 
157. R. Krishna, J.A. Wesselingh, The Maxwell-Stefan approach to mass transfer, *Chem. Eng. Sci.* 52(6) (1997) 861-911.
158. D. Paschek, R. Krishna, Monte Carlo simulations of sorption and diffusion of isobutane in silicalite, *Chem. Phys. Lett.* 342 (2001) 148-154.
159. D.A. Reed, G. Ehrlich, Surface diffusion, atomic jump rates and thermodynamics, *Surf. Sci.* 102 (1981) 588-609.
160. A.B. Shelekhin, A.G. Dixon, Y.H. Ma, Theory of gas diffusion and permeation in inorganic molecular-sieve membranes, *AIChE J.* 41(1) (1995) 58-67.
161. R. Krishna, T.J.H. Vlught, B. Smit, Influence of isotherm inflection on diffusion in silicalite, *Chem. Eng. Sci.* 54(12) (1999) 1751-1959.
162. J.L.P. van den Broeke, R. Krishna, Experimental verification of the Maxwell-Stefan theorie for micropore diffusion, *Chem. Eng. Sci.* 50(16) (1995) 2507-2522.
163. B. Millot, A. Methivier, H. Jobic, H. Moueddeb, J.A. Dalmon, Permeation of linear and branched alkanes in ZSM-5 supported membranes, *Micropor. Mesopor. Mater.* 38(1) (2000) 85-95.
164. N. Nishiyama, K. Ueyama, M. Matsukata, Synthesis of defect-free zeolite-alumina composite membranes by a vapour-phase transport method, *Micropor. Mater.* 7 (1996) 299-308.
165. N. Nishiyama, T. Matsufuji, K. Ueyama, M. Matsukata, FER membrane synthesized by a vapour-phase transport method: its structure and separation characteristics, *Micropor. Mater.* 12 (1997) 293-303.
166. T. Matsufuji, S. Nakagawa, N. Nishiyama, M. Matsukata, K. Ueyama., Synthesis and permeation studies of ferrierite/alumina composite membranes, *Micropor. Mesopor. Mater.* 38 (2000) 43-50.
167. K. Wegner, J. Dong, Y.S. Lin, Polycrystalline MFI zeolite membranes: xylene pervaporation and its implication on membrane microstructure, *J. Membr. Sci.* 158(1-2) (1999) 17-27.
168. W. Yuan, Y.S. Lin, W. Yang, Molecular sieving MFI-type zeolite membranes for pervaporation separation of xylene isomers, *J. Am. Chem. Soc.* 126 (2004) 4776-4777.
169. S. Xiang, Y.H. Ma, in: *Proceedings of the third International Conference on Inorganic Membranes, Formation and Characterization of Zeolite Membranes from Sols.*, Worcester, MA, 1994.

- 
170. J. O'Brien-Abraham, M. Kanezashi, Y.S. Lin, Effects of adsorption-induced microstructural changes on separation of xylene isomers through MFI-type zeolite membranes, *J. Membr. Sci.* 320 (2008) 505-513.
171. T. Matsufuji, N. Nishiyama, M. Matsukata, K. Ueyama, Separation of butane and xylene isomers with MFI-type zeolitic membrane synthesized by a vapour-phase transport method, *J. Membr. Sci.* 178 (2000) 25-34.
172. Z. Lai, G. Bonilla, I. Diaz, J.G. Nery, K. Sujaoti, M.A. Amat, E. Kokkoli, O. Terasaki, R.W. Thompson, M. Tsapatsis, D.G. Vlachos, Microstructural optimization of a zeolite membrane for organic vapour separation, *Science* 300, (2003) 456-460.
173. G. Xomeritakis, M. Tsapatsis, Permeation of aromatic isomer vapours through oriented MFI-type membranes made by secondary growth, *Chem. Mater.* 11(4) (1999) 875-878.
174. Y.F. Yeong, A.Z. Abdullah, A.L. Ahmad, S. Bhatia, Process optimization studies of p-Xylene separation from binary xylene mixture over silicalite-1 membrane using response surface methodology, *J. Membr. Sci.* 341(1-2) (2009) 96-108.
175. C.J. Gump, V.A. Tuan, R.D. Noble, J.L. Falconer, Aromatic permeation through crystalline molecular sieve membranes, *Ind. Eng. Chem. Res.* 40 (2001) 565-577.
176. A.M. Tarditi, E.A. Lombardo, Influence of exchanged cations ( $\text{Na}^+$ ,  $\text{Cs}^+$ ,  $\text{Sr}^{2+}$  and  $\text{Ba}^{2+}$ ) on xylene permeation through ZSM-5/SS tubular membranes, *Sep. Purif. Technol.* 61 (2008) 136-147.
177. K. Keizer, A.J. Burggraaf, Z.A.E.P. Vroon, H. Verweij, Two-component permeation through thin zeolite MFI membranes, *J. Membr. Sci.* 147 (1998) 159-172.
178. H. Sakai, T. Tomita, T. Takahashi, P-Xylene separation with MFI-type zeolite membrane, *Sep. Purif. Technol.* 25 (2001) 297-306.
179. G. Xomeritakis, Z. Lai, M. Tsapatsis, Separation of xylene isomer vapours with oriented MFI membranes made by seeded growth, *Ind. Eng. Chem. Res.* 40 (2001) 544-552.
180. J. Hedlund, J. Sterte, M. Anthonis, A.J. Bons, B. Carstensen, N. Corcoran, D. Cox, H. Deckman, W. De Gijnsr, P.-P. de Moor, F. Lai, J. McHenry, W. Mortier, J. Reinoso, J. Peters, High-flux MFI membranes, *Micropor. Mesopor. Mater.* 52 (2002) 179-189.
181. C.D. Baetsch, H.H. Funke, J.L. Falconer, R.D. Noble, Permeation of aromatic hydrocarbon vapours through silicalite-zeolite membranes, *J. Phys. Chem.* 100 (1996) 7676-7679.

- 
182. S. Haag, S.M. Hanebuth, G.T.P. Mabande, A. Avhale, W. Schwieger, R. Dittmeyer, On the use of a catalytic H-ZSM-5 membrane for xylene isomerization, *Micropor. Mesopor. Mater.* 96 (2006) 168-176.
183. X.Gu, J. Dong, T.M. Nenoff, D.E. Ozokwelu, Separation of p-Xylene from multicomponent vapour mixture using tubular MFI zeolite membranes, *J. Membr. Sci.* 280 (2006) 624-633.
184. A.M. Tarditi, G.I. Horowitz, E.A. Lombardo, A durable ZSM-5/SS composite tubular membrane for the selective separation of p-Xylene from its isomers, *J. Membr. Sci.* 281 (2006) 692-699.
185. A.M. Tarditi, S. Irusta, E.A. Lombardo, Xylene isomerization in a membrane reactor Part I: The synthesis of MFI membranes for the p-Xylene separation, *Chem. Eng. J.* 122(3) (2006) 167-174.
186. L. Van Dyk, L. Lorenzen, S. Miachon, J-A. Dalmon, Xylene isomerization in an extractor type catalytic membrane reactor, *Catal. Today* 104 (2005) 274-280.
187. Z. Lai, M. Tsapatsis, Gas and organic vapour permeation through b-oriented MFI membranes, *Ind. Eng. Chem. Res.* 43 (2004) 3000-3007.
188. G.T.P. Mabande, M. Noack, A. Avhale, P. Kolsch, G. Georgi, W. Schwieger, J. Caro, Permeation properties of bi-layered Al-ZSM-5/Silicalite-1 membranes, *Micropor. Mesopor. Mater.* 98(1-3) (2007) 55-61.
189. A.M. Tarditi, E.A. Lombardo, A.M. Avila, Xylene permeation transport through composite Ba-ZSM-5/SS tubular membranes: Modelling the steady-state permeation, *Ind. Eng. Chem. Res.* 47 (2008) 2377-2385.
190. C. Zhang, Z. Hong, X. Gu, Z. Zhong, W. Jin, N. Xu, Silicalite-1 zeolite membrane reactor packed with HZSM-5 catalyst for meta-xylene isomerization, *Ind. Eng. Chem. Res.* 48 (2009) 4293-4299.
191. A. Giroir-Fendler, J. Peureux, H. Mozzanega, J-A. Dalmon, Characterization of a zeolite membrane for catalytic membrane reactor application, *Stud. Surf. Sci. Catal.* 101 (1996) 127-136.
192. T.Q. Gardner, J.G. Martinek, J.L. Falconer, R.D. Noble, Enhanced flux through double-sided zeolite membranes, *J. Membr. Sci.* 304(1-2) (2007) 112-117.
193. W.J. Koros, Y.H. Ma, T. Shimidzu, Terminology for membranes and membrane processes, *Pure Appl Chem.* 68(7) (1996) 479-1489.
194. S. Miachon, J-A. Dalmon, Catalysis in membrane reactors: what about the catalyst? *Topics in Catalysis* 29(1-2) (2004) 59-65.

- 
195. H.P. Hsieh, *Inorganic Membranes for separation and reaction*, Elsevier, Amsterdam, 1996.
196. M. Reif, R. Dittmeyer, Porous, catalytically active ceramic membranes for gas-liquid reactions: a comparison between catalytic diffuser and forced through flow concept, *Catal. Today* 82 (2003) 3-14.
197. J.N. Armor, Applications of catalytic inorganic membrane reactors to refinery products, *J. Membr. Sci.* 147(2) (1998) 217-233.
198. A.M. Tarditi, G.I. Horowitz, E.A. Lombardo, Xylene isomerization in a ZSM-5/SS membrane reactor, *Catal Lett.* 123 (2008) 7-15.
199. R.D. Chirico, W.V. Steele, Thermodynamic equilibrium in xylene isomerization. 5. Xylene isomerization equilibria from thermodynamic studies and reconciliation of calculated and experimental product distributions, *J. Chem. Eng. Data* 42(4) (1997) 784-790.
200. J.M. Ferraro, R.M. Osman, D-Y. Ou, Process for production of para-Xylene, US Patent 6376733 B1, ExxonMobil Chemicals, Houston, Texas, 2002.
201. A.L. Deshayes, E.E. Miro, G.I. Horowitz, Xylene isomerization in a membrane reactor: Part II. Simulation of an industrial reactor, *Chem. Eng. J.* 122 (2006) 149-157.
202. M. Matsukata, N. Nishiyama, K. Ueyama, Zeolitic membrane synthesized on a porous alumina support, *Chem. Commun.* 3 (1994) 339-340
203. M. Matsukata, N. Nishiyama, K. Ueyama, Synthesis of zeolites under vapour atmosphere. Effect of synthetic conditions on zeolite structure, *Micropor. Mater.* 1(3) (1993) 219-222.
204. B.H. Davis, K.S.W. Singh, in: F. Schüth, K.S.W. Singh, J. Weitkamp (Eds.), *Handbook of porous solids*, Vol .1 , Wiley-VCH, Weinheim, 2002.
205. J.L.H. Chau, C. Tellez, K.L. Yeung, K. Ho, The role of surface chemistry in zeolite membrane formation, *J. Membr. Sci.* 164(1-2) (2000) 257-275.
206. L.C. Boudreau, J.A. Kuck, M. Tsapatsis, Deposition of oriented zeolite A films: In situ and secondary growth, *J. Membr. Sci.* 152 (1999) 41-59.
207. S. Miachon, E. Landrison, M. Aouine, Y. Sun, I. Kumakiri, Y. Li, O. Pachtova Prokopova, N. Guilhaume, A. Giroir-Fendler, H. Mozzanega, J.-A. Dalmon, Nanocomposite MFI-alumina membranes via pore-plugging synthesis: preparation and morphological characterization, *J. Membr. Sci.* 281 (2006) 228-238.

- 
208. S. Miachon, P. Ciavarella, L. van Dyk, I. Kumakiri, K. Fiaty, Y. Schuurman, J.-A. Dalmon, Nanocomposite MFI-alumina membranes via pore-plugging synthesis: Specific transport and separation properties, *J. Membr. Sci.* 298 (2007) 71-79.
209. Y. Li, M. Pera-Titus, G. Xiong, W. Yang, E. Landrison, S. Miachon, J.-A. Dalmon, Nanocomposite MFI zeolite – alumina membranes via pore-plugging synthesis: genesis of the material, *J. Membr. Sci.* 325 (2008) 973-981.
210. A. Alshebani, M. Pera-Titus, E. Landrison, T. Schiestel, S. Miachon, J.-A. Dalmon, Nanocomposite MFI-ceramic hollow fibres: Prospects for CO<sub>2</sub> separation, *Micropor. Mesopor. Mater.* 115 (2008) 197-205.
211. F. Kapteijn, J.M. van de Graaf, J.A. Moulijn, One-component permeation maximum: Diagnostic tool for silicalite-1 membranes? *AIChE J.* 46 (2000) 1096-1100.
212. W.J.W. Bakker, L.J.P. van den Broeke, F. Kapteijn, J.A. Moulijn, Temperature dependence of one-component permeation through a silicalite-1 membrane, *AIChE J.* 43 (1997) 2203-2214.
213. ASTM Standard F316-03, Standard test methods for pore size characteristics of membrane filters by bubble point and mean flow pore test, ASTM International, West Conshohocken, PA, 2003 ([www.astm.org](http://www.astm.org)).
214. O. Levenspiel, *Chemical reaction engineering*, third ed., Wiley, New York, 1999.
215. A. Alshebani, Développement de membranes céramiques pour la séparation des gaz. Fibres creuses et composites mésoporeux de nouvelle génération, PhD dissertation, Institut de recherches sur la catalyse et l'environnement de Lyon (IRCELYON), France, 2008.
216. M.A. Snyder, Z. Lai, M. Tsapatsis, D.G. Vlachos, Combining simultaneous reflectance and fluorescence imaging with SEM for conclusive identification of polycrystalline features of MFI membranes, *Micropor. Mesopor. Mater.* 76 (2004) 29-33.
217. G. Bonilla, M. Tsapatsis, D.G. Vlachos, G. Xomeritakis, Fluorescence confocal optical microscopy imaging of the grain boundary structure of zeolite MFI membranes made by secondary (seeded) growth, *J. Membr. Sci.* 182 (2001) 103-109.
218. F. Jareman, J. Hedlund, J. Sterte, Effects of aluminum content on the separation properties of MFI membranes, *Sep. Purif. Technol.* 32 (2003) 159-163.
219. T. Tsuru, T. Hino, T. Yoshioka, M. Asaeda, Permporometry characterization of microporous ceramic membranes, *J. Membr. Sci.* 186 (2001) 257-265.

- 
220. T. Tsuru, Y. Takata, H. Kondo, F. Hirano, T. Yoshioka, M. Asaeda, Characterization of sol-gel derived membranes and zeolite membranes by nanoporometry. *Sep. Purif. Technol.* 32 (2004) 23-27.
221. O. Pachtova, I. Kumakiri, M. Kocirik, S. Miachon, J.-A., Dalmon. 2003. Dynamic desorption of adsorbing species under cross membrane pressure difference: a new defect characterization approach in zeolite membranes, *J. Membr. Sci.* 226 (2003) 101-110.
222. S.I. Nakao, Determination of pore size distribution.3. Filtration membranes, *J. Membr. Sci.* 96 (1-2) (1994) 131-165.
223. E. Jacobs, W.J. Koros, Ceramic membrane characterization via the bubble point technique, *J. Membr. Sci.* (1997) 149-159.
224. K. Venkataraman, W.T. Choate, Ee.R. Torre, R.D. Husung, Characterization studies of ceramic membranes. A novel technique using a coulter<sup>®</sup> porometer, *J. Membr. Sci.* 39 (1998) 259-271.
225. S. Brunner, P.H. Emmett, E. Teller, Adsorption of gases in multimolecular layers, *J. Am. Chem. Soc.* 60 (1938) 309-319
226. H. Yasuda, S.T. Tsai, Pore size of microporous polymer membranes, *J. Appl. Polym. Sci.* 18 (1974) 805-819.
227. S.H. Stern, S.K. Sen, A.H., Rao, The permeation of gases through symmetric and asymmetric (Leob-type) cellulose acetate membranes, *J. Macromol. Sci. Phys.* 10 (1974) 507-528.
228. H. Ohya, Y. Imura, T. Moriyama, M. Kitaoka, A study on pore size distribution of modified ultrathin membranes, *J. Appl. Polym. Sci.* 18(6) (1974) 1855-1867.
229. S.J. Gregg, K.S.W. Sing, Adsorption, surface area and porosity, second ed., Academic Press, London, 1982.
230. F. Vigo, A. Bottino, S. Munari, G. Capannelli, Preparation of asymmetric PTFE membranes and their application in water purification by hyperfiltration, *J. Appl. Polym. Sci.* 21(12) (1977) 3269-3290.
231. F. Erbe, The determination of pore distribution according to size in filters and ultra-filters, *Kolloid-Z.* 63 (1933) 277-285.
232. D. Farrusseng, A. Julbe, C. Guizard, Evaluation of porous ceramic membranes as O<sub>2</sub> distributors for the partial oxidation of alkanes in inert membrane reactors, *Sep. Purif. Tech.* 25(1-2) (2001) 137-149.

- 
233. J. Sanchez, C.L. Gîjiu, V. Hynek, O. Muntean, A. Julbe, The application of transient-lag method for the diffusion coefficient estimation on zeolite composite membranes. *Sep. Purif. Tech.* 25 (2001) 467-474.
234. M. Hanebuth, R. Dittmeyer, G.T.P. Mabande, W. Schwieger, On the combination of different transport mechanisms for the simulation of steady-state mass transfer through composite systems using H<sub>2</sub>/SF<sub>6</sub> permeation through stainless steel supported silicalite-1 membranes as a model system, *Catal. Today* 104 (2005) 352-359.
235. A. Alshebani, M. Pera-Titus, K.L. Yeung, S. Miachon, J.-A. Dalmon, Influence of desorption conditions before gas separation studies in nanocomposite MFI-alumina membranes, *J. Memb. Sci.* 314 (2008) 143-151.
236. H.H. Funke, K.R. Frender, K.M. Green, J.L. Wilwerding, B.A. Sweitzer, J.L. Falconer, R.D. Noble, Influence of adsorbed species on the permeation properties of silicalite membranes, *J. Membr. Sci.* 129 (1997) 77-82.
237. S.K. Moore, Sorting out the prospects for novel separations, *Chemical Week* 161(44) (1991) 53.
238. Energy and Environmental Profile of the U.S. Chemical Industry May 2000. U.S. Department of Energy Office of Industrial Technologies. Energetic Inc., Columbia Maryland, (<http://www1.eere.energy.gov/industry/chemicals/pdfs>), 2000.
239. C. Buchaly, P. Kreis, A. Gorak, Hybrid separation processes: combination of reactive distillations with membrane separation, *Chem. Eng. Process.* 46 (2007) 790-799.
240. W. Stephan, R.D. Noble, C.A. Koval, Design methodology for a membrane/distillation column hybrid process, *J. Membr. Sci.* 99 (1995) 259-272.
241. J. Hedlund, F. Jareman, A.J. Bons, M. Anthonis, A masking technique for high quality MFI membranes, *J. Membr. Sci.* 222 (2003) 163-179.
242. M.O. Daramola, A.J. Burger, M. Pera-Titus, A. Giroir-Fendler, L. Lorenzen, J.-A. Dalmon, *Sep. Sci. Technol.* 45(1) (2010) 21-27.
243. J. Hedlund, M. Noack, P. Kolsch, D. Creaser, J. Caro, J. Sterte, ZSM-5 membranes synthesized without organic templates using a seeding technique, *J. Membr. Sci.* 159 (1999) 263-273.
244. F. Kapteijn, W.J.W. Bakker, J. van de Graaf, G. Zheng, J. Poppe, J.A. Moulijn, Permeation and separation behaviour of a silicalite-1 membrane, *Catal. Today* 25 (1995) 213-218.
245. C. Bai, M.D. Jia, J.L. Falconer, R.D. Noble, Preparation and separation properties of silicalite composite membranes, *J. Membr. Sci.* 105 (1995) 79-87.

- 
246. J. Coronas, J.L. Falconer, R.D. Noble, Characterization and permeation properties of ZSM-5 tubular membranes, *AIChE J.* 43 (1997) 1797-1812.
247. L.M. Gualtieri, A.F. Gualtieri, J. Hedlund, F. Jareman, J. Sterte, M. Dapiaggi, Accurate measurement of the thermal expansion of MFI zeolite membranes by in situ HTXRPD, *Stud. Surf. Sci. Catal.* 154A (2004) 703-709.
248. M.O. Daramola, A.J. Burger, M. Pera-Titus, A. Giroir-Fendler, L. Lorenzen, S. Miachon, J-A. Dalmon, Nanocomposite MFI hollow-fibre membranes via pore-plugging synthesis: prospects for xylene isomer separation, *J. Membr. Sci.* 337 (2009) 106-112.
249. W.J.W. Bakker, F. Kapteijn, J. Poppe, J.A. Moulijn, Permeation characteristics of a metal-supported silicalite-1 zeolite membrane, *J. Membr. Sci.* 117 (1996) 57-78.
250. F. Kapteijn, J.M. van de Graaf, J.A. Moulijn, One-component permeation maximum: Diagnostic tool for silicalite-1 membranes? *AIChE J.* 46(5) (2000) 1096-1100.
251. M.P. Bernal, J. Coronas, J. Santamaria, Characterization of zeolite membranes by temperature-programmed permeation and step desorption, *J. Membr. Sci.* 195 (2002) 125-138.
252. A. Goldbach, T. Mauer, N. Stroh, Ceramic hollow fiber and capillary membranes (Keramische Hohlfaser- und Kapillarmembranen), *Keram. Z.* 53(11), (2001) 1012-1016.
253. Z. Deng, C-H. Nicholas, M.O. Daramola, J. Sublet, Th. Schiestel, A.J. Burger, Y. Guo, A. Giroir-Fendler, M. Pera-Titus, Nanocomposite MFI-alumina hollow fibre membranes prepared via pore-plugging synthesis: influence of the pore structure of the hollow fibres on the gas/vapour separation performance, *J. Membr. Sci.* (2010) in press.
254. V.R. Choubhary, D.B. Akolekar, Influence of intercrystalline mass transfer on catalytic properties of Pt.HZSM-5. $\text{Al}_2\text{O}_3$  catalyst, *J. Catal.* 116(1) (1989) 130-143.
255. Y. Li, X. Chang, Z. Zeng, Kinetics study of the isomerization of xylene on HZSM5 zeolite. 1. Kinetics model and reaction mechanism, *Ind. Eng. Chem. Res.* 31(1) (1992) 187-192.
256. Y.H. Ma, L.A. Savage, Xylene isomerization using zeolites in a gradientless reactor system, *AIChE J.* 33 (1987) 1233-1240.
257. M.-G. Yang, I. Nakamura, K. Fujimoto, M-Xylene transformation over  $\text{NiS}/\text{Al}_2\text{O}_3$ -USY hybrid catalysts: effects of hydrogen spillover, *Appl. Catal. A: General* 144(1-2) (1996) 221-235.

- 
258. R.C. Reid, J.M. Prausnitz, T.K. Sherwood, The properties of gases and liquids, third ed., McGraw-Hill, New York, 1977.
259. D.R. Stull, E.F. Westrum, G.C. Sinke, The chemical thermodynamics of organic compounds; Wiley, New York, 1969.
260. M. Guisnet., N.S. Gnep, in: F.R. Ribeiro, M. Nijhoff (Eds.), Zeolites: Science and Technology;; Wiley , Hague, 1984, p571.
261. M. Guisnet, N.S. Gnep, S. Morin, Mechanisms of xylene isomerization over acidic solid catalysts, Micropor. Mesopor. Mater. 35-36 (2000) 47-59.
262. M.O. Daramola, Z. Deng, M. Pera-Titus, A. Giroir-Fendler, A.J. Burger, L. Lorenzen & Y. Guo, Nanocomposite MFI-alumina membranes prepared via pore-plugging synthesis: application as packed-bed membrane reactors for m-Xylene isomerization over a Pt-HZSM-5 catalyst, Catal. Today (2010) in press.
263. M. Brendel, D. Bonvin, W. Marquardt, Incremental identification of kinetic models for homogeneous reaction systems, Chem. Eng. Sci. 61 (2006) 5404-5420.
264. M.M. El-Halwagi, Synthesis of reverse osmosis networks for waste reduction, AIChE J. 38(8) (1992) 1185-1198.
265. R. Qi, M.A. Henson, Optimal design of spiral-wound membrane networks for gas separations, J. Membr. Sci. 148 (1998) 71-89.
266. J.I. Marriott, E. Sorenzen, I.D.L. Bogle.2001. Detailed mathematical modeling of membrane modules, Comp. and Chem. Eng.25 (2001) 693-700.
267. J.I. Marriott, E. Sorenzen, I.D.L. Bogle, in: FOAPD proceedings, Rigorous optimal design of a pervaporation plant, Breckenridge, Colorado, 1999.
268. Y.F. Yeong, A.Z. Abdullah, A. L. Ahmad, S. Bhatia. Xylene isomerization kinetic over acid-functionalized silicalite-1 catalytic membranes: Experimental and modelling studies, Chem. Eng. J. 157 (2010) 579-589.
269. A.J. Silvestri, C.D. Prater, Kinetic studies of the selectivity of xylene isomerization over silica-alumina catalyst, J. Phys. Chem. 68 (11) (1964) 3268-3281.
270. K.H. Robschlager, E.G. Christoffel, Kinetic investigation of the isomerization of C<sub>8</sub>-aromatics, Can. J. Chem. Eng. 58 (1980) 517-520.
271. D. J. Collins, R.J. Medina, B.H. Davis, Xylene isomerization by ZSM-5 zeolite catalyst, Can. J. Chem. Eng. 61 (1983) 29-35.
272. M.A. Lanewola, A.P. Bolton, The isomerization of the xylenes using zeolite catalysts, J. Org. Chem. 34 (1969) 3107-3112.

- 
273. P. Chutoransky, F.G. Dwyer, in: *Advances in Chemistry Series*, Chp. 49, vol. 121, Effect of zeolite crystallite size on the selectivity kinetics of the heterogeneous catalyzed isomerization of xylenes., 1973, pp.540-552.
274. D.J. Collins, K.J. Mulrooney, R.J. Medina, Xylene isomerization and disproportionation over Lanthanum Y catalyst, *J. Catal.* 75 (1982) 291-301.
275. A. Cortes, A. Corma, The mechanism of catalytic isomerization of xylenes: Kinetic and isotopic studies, *J. Catal.* 51 (1978) 338-344.
276. A. Cortes, A. Corma, I. Nebot, F. Tomas, On the mechanism of catalytic isomerization of xylenes. Molecular orbital studies, *J. Catal.* 57 (1979) 444-449.
277. A. Corma, A. Cortes, Kinetics of the gas-phase catalytic isomerization of xylenes, *Ind. Eng. Chem. Process Des. Dev.* 19(2) (1980) 263-267.
278. Do, D, Enhanced paraxylene selectivity in a fixed-bed reactor, *AIChE J.* 31(4) (1985) 574-580.
279. O. Cappellazzo, G. Cao, G. Messina, M. Morbidelli, Kinetics of shape-selective xylene isomerization over a ZSM-5 catalyst, *Ind. Eng. Chem. Res.* 30(10) (1991) 2280-2287.
280. S. Al-Khattaf, N.M. Tukur, A. Al-Amer, Modelling xylene reactions over ZSM-5 zeolite in a riser simulator: 1,3- versus 1,2-Methyl shift, *Ind. Eng. Chem. Res.* 44 (2005) 7957-7968.
281. S. Kumar, S. Shankar, P. R. Shah, S. Kumar, A comprehensive model for catalytic membrane reactor, *IJCRE Article A5* (4) (2006) 1-26.
282. E. Gobina, K. Hou, R. Hughes, Mathematical analysis of ethylbenzene dehydrogenation: Comparison microporous and dense membrane systems, *J. Membr. Sci.* 105 (1995) 163-176.
283. R.H. Perry, D.W. Green, *Perry's Chemical Engineer's handbook*, seventh ed., McGraw-Hill, New York, 1997.
284. H. S. Fogler, *Elements of Chemical Reaction Engineering*, fourth ed., Prentice Hall, Englewood Cliffs, New Jersey, 2005.
285. H. E. Marshall, in: *Engineering handbook, Sensitivity analysis*, CRC Press Inc., Boca Raton, 1996.
286. A. Saltelli, K. Chan, E.M. Scott, *Sensitivity analysis*, Wiley, Chicester, 2000.
287. D. Njomo, M. Daguene, Sensitivity analysis of thermal performances of flat plate solar air heaters, *Heat Mass Transfer* 42 (2006) 1065-1081.
288. M. Matyka, A. Khalili, Z. Koza, Tortuosity-porosity relation in the porous media flow, *Phys. Rev. E.* 78, 026306 (2008) 1-8.

- 
289. M.O. Daramola, A.J. Burger, M. Pera-Titus, A.Giroir-Fendler, S. Miachon, J.-A. Dalmon, L. Lorenzen, Separation and isomerization of xylene using zeolite membranes: a short overview, *Asia-Pacific Journal of Chemical Engineering* (2009) in press.
290. M. P. Harold, C. Lee, A.J. Burggraaf, K. Keizer, V.T. Zaspalis, R.S.A. De Lange, Catalysts with inorganic membranes, *MRS Bull.* 19(4) (1994) 34-39.
291. V.T. Zaspalis, W. Van Praag, K. Keizer, J.G. Van Ommen, J.R.H. Ross, A.J. Burggraaf, Reaction of methanol over catalytically active alumina membranes, *Appl. Catal.*74(2) (1991) 205-222.

---

## Symbols

$T$	Absolute temperature [K]
$K_A$	Adsorption coefficient in site A [ $\text{Pa}^{-1}$ ]
$K_B$	Adsorption coefficient in site B [ $\text{Pa}^{-1}$ ]
$P_i^o(T, \Phi)$	Adsorptive saturation pressure of $i^{\text{th}}$ species in the gas phase at the solution temperature and surface potential
$K(T_{ref})$	Adsorption constant of p-Xylene on MFI at $T_{ref}$ [ $\text{Pa}^{-1}$ ]
$E_i$	Activation energy component $i$ [ $\text{J.mol}^{-1}$ ]
-1	Conversion of PX to MX
1	Conversion of MX to PX
2	Conversion of MX to OX
-2	Conversion of OX to MX
3	Conversion of PX to OX
-3	Conversion of OX to PX
CMR	Catalytic membrane reactors
$\mu_i$	Chemical potential of $i^{\text{th}}$ species
$\mu$	Chemical potential
$\theta$	Contact angle [degree]
$\rho_{MFI}$	Density of the MFI [ $\text{kg.m}^{-3}$ ]
$\rho_{cat}$	Density of the catalyst [ $\text{kg.m}^{-3}$ ]
$E_D$	Diffusion activation energy [ $\text{Jmol}^{-1}$ ]
$\rho$	Density
$D_i$	Diffusion coefficient of species $i$ [ $\text{m}^2.\text{s}^{-1}$ ]
$\eta_i$	Effectiveness factor for the catalyst [-]
$\Delta H_{vap}$	Enthalpy of vapourization [ $\text{J.mol}^{-1}$ ]
e-CMR	Extractor-type catalytic membrane reactors
e-ZCMR	Extractor-type zeolite catalytic membrane reactors
e-ZCMR-IN	Extractor-type CMR with catalyst packed inside the membrane
e-ZCMR-OUT	Extractor-type CMR with catalyst packed outside the membrane
$R_2$	External radius of the membrane [m]

---

FID	Flame Ionization Detector
<i>feed</i>	Feed stream
<i>f</i>	Final
$D_T$	Fick or transport diffusivity [ $\text{m}^2.\text{s}^{-1}$ ]
FBR	Fixed-bed reactor
GC	Gas chromatograph
$H_A$	Henry coefficient [ $\text{mol}.\text{g}^{-1}.\text{Pa}^{-1}$ ]
<i>o</i>	Initial
$R_1$	Internal radius of the membrane [m]
$R_3$	Internal radius of the stainless module [m]
$K$	Kernel
$c_{sat}$	Loading at saturation [ $\text{mol}.\text{kg}^{-1}$ ]
$\tau_m$	Membrane tortuosity [-]
$\delta_m$	Membrane effectiveness thickness [m]
$L$	Membrane permeation length [m]
$M_w$	Molecular weight [ $\text{gmol}^{-1}$ ]
$q_i^o$	Molar loadings of pure species <i>i</i> [mol]
$q_i$	Molar loading of $i^{th}$ species for a given mixture [mol]
$J_i$	Molar flux of species / component <i>i</i> [ $\text{mol}.\text{m}^{-2}.\text{s}^{-1}$ ]
$C_i$	Molar concentration of component <i>i</i> in the reaction [ $\text{mol}.\text{m}^{-3}$ ]
$\ell$	MFI effective thickness [m]
$D_O(T_{ref})$	MS surface diffusivity at zero coverage at $T_{ref}$ [ $\text{m}^2.\text{s}^{-1}$ ]
$X_{MX}$	m-Xylene conversion [-]
<i>x</i>	Mole fraction [-]
$Q_i$	Molar flow rate of component <i>i</i> [ $\text{mol}.\text{s}^{-1}$ ]
MX	Meta-xylene (m-Xylene)
$f(d)$	Number pore size distribution
OX	Ortho-Xylene (o-Xylene)
$\varepsilon_m$	Porosity of the membrane [-]
$P_i$	Partial pressure of component <i>i</i> [Pa]
$\Pi_i$	Permeance of species/ component <i>i</i> [ $\text{mol}.\text{m}^{-2}.\text{s}^{-1}.\text{Pa}^{-1}$ ]

---

$P_p$	Permeate pressure [Pa]
$Y_{PX}$	p-Xylene yield [%]
$S_{PX}$	p-Xylene selectivity [%]
$d$	Pore size [m]
PX	Para-xylene (p-Xylene)
$\pi$	$pi$ (3.142)
PV	Pervaporation
$Perm$	Permeate stream
$r_i$	Rate of reaction of component $i$ [mol.kg <sup>-1</sup> .s <sup>-1</sup> ]
$V_{reactor}$	Reactor volume [m <sup>3</sup> ]
$k_i$	Rate of reaction constant for component $i$ [m <sup>3</sup> .(kg of catalyst) <sup>-1</sup> .s <sup>-1</sup> ]
$P_o$	Reference atmospheric pressure [Pa]
$ret$	Retentate stream
$P_R$	Retentate pressure [Pa]
$\nu_i$	Stoichiometric coefficient component $i$ in the reaction [-]
$\Delta H^o_{ads}$	Standard adsorption enthalpy [J.mol <sup>-1</sup> ]
$\gamma$	Surface tension of ethanol [N/m]
$z$	Spatial coordinate [m]
SF	Separation factor
$\Phi$	Surface potential
$\gamma$	Surface tension
$D^*$	Self diffusivity [m <sup>2</sup> .s <sup>-1</sup> ]
$N_i^s$	Surface flux of $i^{th}$ species [mol.m <sup>-2</sup> .s <sup>-1</sup> ]
$\Delta P$	Transfibre differential pressure [Pa]
$t$	Tube side
$R$	Universal gas constant (8.314) [J.mol <sup>-1</sup> .K <sup>-1</sup> ]
VP	Vapour permeation
$W_{cat}$	Weight of catalyst [kg]
ZSM-5	Zeolite Socony Mobil-Five

---

## Appendix

### Appendix A: Evaluation of saturation system

To evaluate saturation efficiency of the saturation system, equimolar mixture of xylene was saturated in N<sub>2</sub> (carrier gas) with carrier gas flow rates varied between 2 mL(STP)/min and 16 mL(STP)/min using the two bubblers combined in series. The liquid volume in each saturator was about 100ml. Time to fill up the gas space in the unit and in the line connecting it to the GC was calculated by dividing the gaseous volume by the carrier gas flow rate.

Then time to attain saturation was obtained by multiplying the time to fill up the gaseous space by 3. The values obtained were overestimated to accommodate some uncertainties. A steady state of about 2 hours was allowed at a desired temperature before the vapour was sent to the GC for analysis. The peak areas obtained at these carrier gas flow rates were plotted against the carrier gas flow rates. A plateau region in the plot signifies the saturation region. And the N<sub>2</sub> flow rates at this region were taken as saturation flow rates for the saturation unit. Samples of the results obtained for the evaluation of the saturation unit are depicted in Fig. A1 and Fig. A2. The variation of the carrier gas flow rate was between 4 mL(STP)/min and 17 mL(STP)/min. The result, as presented in the Figure A1 below, shows a plateau between 4 mL(STP)/min and 11mL(STP)/min. The plateau region is the region of saturation. The plateau region widened as saturation temperature increased. Similar results were obtained for saturation of ternary liquid mixture of xylene.

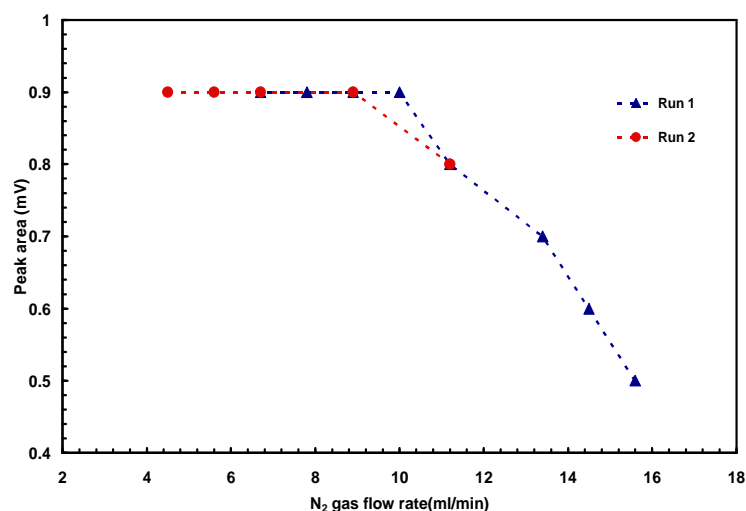


Figure A1: Evaluation of saturation unit at 315 K. Run 1: Decrease N<sub>2</sub> gas flow rate from 17mL(STP)/min to 4 mL(STP)/min. Run 2: Increase N<sub>2</sub> gas flow rate from 4 mL(STP)/min to 17 mL(STP)/min.

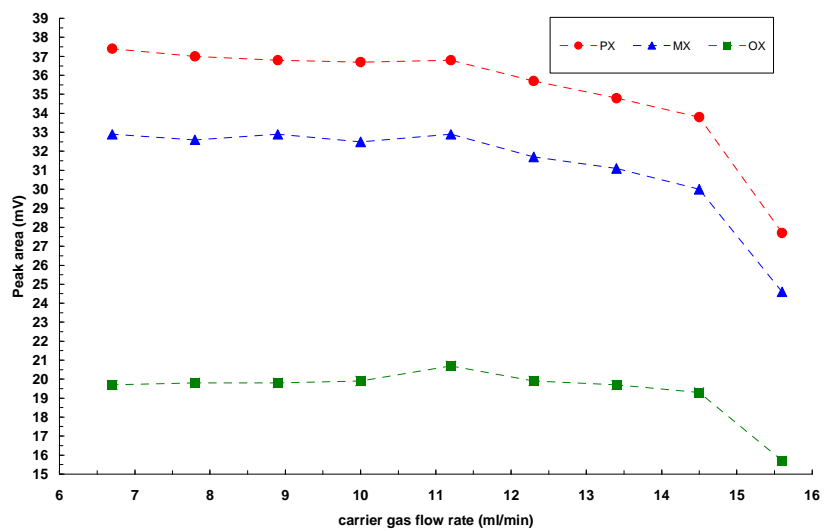


Figure A2: Evaluation of saturation unit at 335 K with ternary mixture of xylene isomers.

---

## Appendix B: Calibration of mass flow controller and flow meters and GC

### Calibration of the mass flow controller and flow meter

The calibration of the mass flow controller and flow meters was done at ambient temperature and pressure. These conditions were referred to as Normal Temperature and Pressure (NTP). The values at Standard Temperature and Pressure (STP) were obtained with Eq. B1. During the calibration, the valve opening of the mass flow controller was controlled between 0% and 100% and the flow rate of the gas through the valve was measured with ADM1000. To ensure accuracy, the measurements were repeated 3 times and the values averaged. Plots of the average flow rate/ were made against the valve openings:

$$F_{gSTP} = \frac{(T_{STP} * F_{gNTP})}{T_{NTP}} \quad (B1)$$

where  $T_{STP}$  is the temperature at STP,  $T_{NTP}$  is the temperature at NTP,  $F_{gSTP}$  and  $F_{gNTP}$  are the gas flow rate in mL/min at STP and NTP, respectively. The sample calibration equations are presented in Table B1.

Table B1: Sample of GC calibration equations

Component	Calibration Equation	R <sup>2</sup>
Saturator N <sub>2</sub>	0.2231 * (MFC%):	0.9998
Feed N <sub>2</sub>	0.9706 * (MFC%):	0.9999
Feed H <sub>2</sub>	1.0579 * (MFC%)-11.062	0.9999
Sweep N <sub>2</sub>	1.4092 * (MFC%):	0.9994

### Calibration of the GC

Each component of xylene isomers was calibrated. The Calibration of the GC was done at a carrier gas flow rate chosen within the saturation region. At the constant feed flow rate, the saturation temperature was varied in such a way that the saturation region was not exceeded. The GCs were calibrated using multiple point external standard method.

In this method, xylene liquid (single component) was saturated in N<sub>2</sub> at a desired temperature and at N<sub>2</sub> flow rate obtained in Appendix A. The saturated partial pressure of the xylene vapour (single component) was obtained from Antoine equation at that temperature. After attaining a steady-state at this temperature, xylene vapour was sent to GC for analysis to

---

obtain its peak area. This procedure was repeated for at least twice for different temperatures within the range 293 K-363 K.

The saturated partial pressures of xylene vapour (each component) at the desired temperatures as obtained from Antoine equation were plotted against the peak areas obtained from the GC at those temperatures to obtain calibration curves/equations. Samples of the calibration equations are presented in the Table B2. Throughout the calibration, all lines to the GC were heated with heating tapes and maintained at 393 K to prevent condensation of xylene vapour and to ensure accurate xylene vapour pressures. Detailed step-by-step procedure and assumptions during GC calibration is presented below:

The saturation vapour pressure of each component at the temperature point was obtained from the Antoine equation:

$$\ln P_i^{sat} = A - \frac{B}{T + C} \quad (B2)$$

A, B and C are the Antoine constants.

In vapour liquid equilibrium (VLE), for every component  $i$  in the mixture, the condition of thermodynamic equilibrium will be given by (Poling *et al.*, 2001):

$$y_i * P = x_i * \gamma_i * P_{vpi} * \phi_i \quad (B3)$$

where  $\gamma_i$  is the activity coefficient of component  $i$ ,  $y_i$  and  $x_i$  are the vapour mole fraction and the liquid mole fraction, respectively.  $P$  is the system total pressure and  $P_{vpi}$  is the vapour pressure of component  $i$ .  $\phi_i$  is the correction factor. Thus the partial pressure of component  $i$  in the vapour-liquid equilibrium depends on the temperature, pressure, activity coefficient, its composition in the mixture. However, if a pure liquid mixture is assumed (which was the case in this study),  $\gamma_i = 1$ . Also if the pressure is assumed to be sufficiently low,  $\phi_i = 1$ . Therefore, Eq. B3 becomes the popular Raoult's law. With Raoult's law assumed, composition corresponding to the temperature and saturation vapour pressure was obtained:

---


$$Py_i = P_i^{sat}(T, \Phi)x_i \quad (\text{for a component, } x_i=1) \quad (\text{B4})$$

$$Py_i = P_i^{sat}(T, \Phi) \quad (\text{B5})$$

$$y_i = \frac{P_i^{sat}(T, \Phi)}{P} \quad (\text{B6})$$

where  $P$  is the operating pressure (in this case, atmospheric pressure) and  $P_i^{sat}(T, \Phi)$ , the saturation vapour pressure.

For each component, the compositions obtained at different temperatures were plotted against the peak areas obtained from the GC analysis. With the calibration equations, partial pressures (compositions) of p-Xylene, m-Xylene and o-Xylene in the feed, the permeate and the retentate were obtained.

Table B2: Sample of GC calibration equations

Component	Calibration Equation	R <sup>2</sup>
PX	$P_{PX} = 0.0002.A^2 + 0.0176A$	0.9918
MX	$P_{MX} = 0.00002.A^2 + 0.0191A$	0.9920
OX	$P_{OX} = 0.0014.A^2 + 0.0015A$	0.9817

$P_{PX}$ ,  $P_{MX}$  and  $P_{OX}$  are saturation partial pressures [Pa] of PX, MX and OX, respectively, at specific temperature.  $A$  is the peak area obtained from the GC at that particular saturation temperature.

## Appendix C: Diffusivity and rate of reaction constants for reactor modelling

Table C1: Diffusivities of component  $i$  at 673 K for reactor modelling

Component	$D_{ref}^a$ ( $m^2 \cdot s^{-1}$ )	$T_{ref}$ (K)	$E_D$ ( $KJ \cdot mol^{-1}$ )	$R$ ( $J \cdot mol^{-1} \cdot K^{-1}$ )	$D_i$ ( $m^2 \cdot s^{-1}$ )
PX	$3.10 \times 10^{-11}$	400	60 <sup>a</sup>	8.314	$2.268 \times 10^{-10}$
MX	$8.00 \times 10^{-15}$	400	60*	8.314	$5.855 \times 10^{-14}$
OX	$1.10 \times 10^{-15}$	400	60*	8.314	$8.050 \times 10^{-15}$

$D_{ref}$  for the isomers were obtained from Daramola *et al.*[241]. \*assumed for MX and OX.

<sup>a</sup>Obtained from Daramola *et al.*[241].

Table C2: Rate of reaction constant of component  $i$  at 673 K for reactor modelling

$k_i$ ( $m^3 \cdot (kg$ of catalyst) <sup>-1</sup> · $s^{-1}$ )	$k_i(T_{ref}) \times 10^4$ ( $m^3 \cdot (kg$ of catalyst) <sup>-1</sup> · $s^{-1}$ )	$T_{ref}$ (K)	$E_i$ ( $KJ \cdot mol^{-1}$ )	$R \times 10^3$ ( $J \cdot mol^{-1} \cdot K^{-1}$ )	$k_i(T = 673K) \times 10^4$ ( $m^3 \cdot (kg$ of catalyst) <sup>-1</sup> · $s^{-1}$ )
$k_1$	2.00	623	12.37	8.31	2.38829
$k_{-1}$	4.84	623	8.75	8.31	5.48722
$k_2$	1.47	623	18.14	8.31	1.90685
$k_{-2}$	2.71	623	21.23	8.31	3.67467
$k_3$	1.33	623	17.31	8.31	1.70483
$k_{-3}$	1.33	623	19.47	8.31	1.75848

$k_i(T_{ref})$  was obtained from ref. [278] and  $k_i$  computed using Eq. 8.23.

Table C3: Isomerization performance of e-ZCMR at 673 K at combined mode operation

Reactor	Feed (kPa MX)	Mass of catalyst (g)	PX yield (%)	PX selectivity (%)	Yield increase (%)	MX conversion (%)
e-ZCMR	2.4	2.18	17.5	40.5	1.8	69.7

---

## Appendix D: CMR testing rigs and operational procedures

The experimental rigs used for this study were modified to comply with current operational and safety standards at the IRCE, Lyon and the Department of Process Engineering, Stellenbosch University. These rigs were test-run thoroughly by performing series of preliminary experiments to ensure the efficiency and accuracy of the rigs for the studies. Photographs and operational procedures of the modified rigs are presented below.

### Operational procedure for CMR rig at IRCE, Lyon, France

Below are the photographs of the CMR rig at IRCE. Figure D1 is the front view showing the control panel and Fig. D2 shows the front view of the hot-box (oven) in which the pipes are heated and maintained at a constant temperature. Figure D3 depicts valve positions with direction.



Figure D1: The photograph of the CMR rig at IRCE, Lyon with the front view showing the control panel.



Figure D2: The photograph of the CMR rig at IRCE, Lyon, showing the front view of the hot-box.

Below are the valves with flow direction:

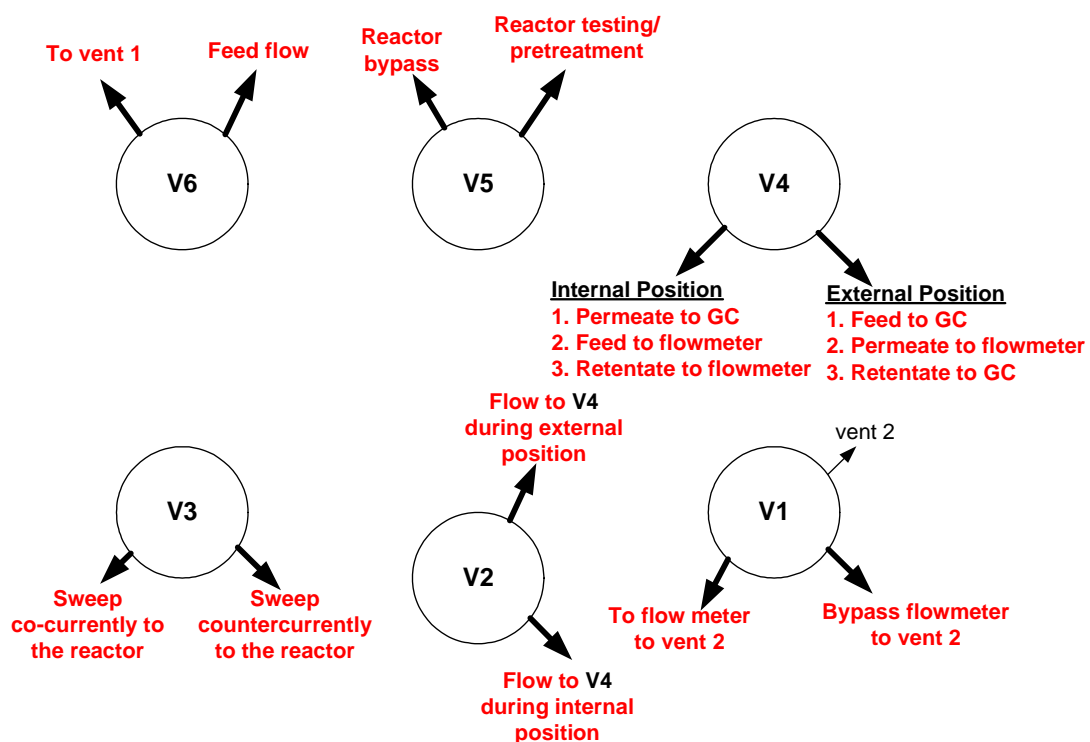


Figure D3: Valves showing positions and flow direction.

---

### Valves and operation procedure

#### A. During GC calibration, saturator evaluation and feed analysis

1. Put V6 in Feed flow position
2. Put V5 in Reactor bypass position
3. Put V4 in External position (feed straight to GC) and V2 in Flow to V4 during external position
4. To measure the flow rate, put V4 in Internal position, V2 in Flow to V4 during internal position and V1 in Flow meter to vent position

#### B. Reactor testing and Pre-treatment

1. Put V6 in Feed flow position
2. Put V5 in Reactor testing position
3. Put V3 in Sweep countercurrently to reactor position

Feed analysis as described in A.

### Operational procedure for CMR rig at the Department of Process Engineering, Stellenbosch University, Stellenbosch, South Africa.

The side view of the CMR rig at the Department of Process Engineering, Stellenbosch University is presented in Fig. D4, while Fig. D5 shows the front view of the rig with control valves/ knobs.



Figure D4: The photograph of the CMR rig at the Department of Process Engineering, Stellenbosch University, South Africa showing the side view.



Figure D5: The photograph of the CMR rig at the Department of Process Engineering, Stellenbosch University, South Africa; showing the front view of the control panel.

### Operational procedure

#### A. Membrane pre-treatment

- Put V1 in **Pre-treatment** position
- Close VB
- Close VA
- Open VC
- Open VD with the arrow end pointing **Backward**
- Put V3 in **Retentate/Permeate analysis** position
- Put V4 in **External- GC-Vent** position
- Put V5 in **Counter-current** position
- Use V7 & V8 to regulate TMP
- Open the feed gas and put at the set point
- Open the sweep gas and put at the set point
- Set oven temperature having fixed the module to the oven and set the temperature according to the HTP programme

#### B. Membrane/separation testing

- Put V1 in Membrane testing position
- Close VC
- Open VA
- Open VB
- Open feed/carrier gas and put at the set point using MFC

- 
- Open VD with arrow end pointing **Forward** to analyse feed and later inverse to do separation testing, and wait to attain a steady state. After attaining a steady state, analysis the feed stream.
  - To analyse feed, put V3 in **Feed analysis** position , wait for about 10min and inject to the GC
  - To do separation, Put V3 in **Retentate/Permeate analysis** position , open sweep gas and put at the set point, V4 in **External-GC-Vent** position , V5 in **Counter-current** position , set the module temperature and wait to attain the set-point, regulate TMP by using V7 & V8 , and wait for a pre-determined time before sampling.
  - To analyse the permeate stream, put V3 in **Retentate/Permeate analysis** position, put V4 in **External-GC-Vent** position (retentate stream flows to the soap bubble flow meter to measure flow rate), V5 remains in **Counter-current** position. Inject the sample into the GC and analysis. Measure retentate flow rate.
  - To analyse the retentate stream, put V3 in **Retentate/Permeate analysis** position, put V4 in **Internal-GC-Vent** position (permeate stream flows to the soap bubble flow meter to measure flow rate), V5 remains in **Counter-current** position. Inject the sample into the GC and analysis. Measure permeate flow rate.

---

## Appendix E: List of published and submitted papers related to this work

### Articles published in peer-reviewed journals

1. **M.O. Daramola**, A.J. Burger, M. Pera-Titus, A.Giroir-Fendler, S. Miachon, L. Lorenzen, J.A.Dalmon. 2009. Nanocomposite MFI-ceramic hollow fibre membranes via pore-plugging synthesis: Prospects for separation of xylene isomers, *J. Membr. Sci.* 337, 2009, 106-112.
2. **M.O. Daramola**, A.J. Burger, M. Pera-Titus, A.Giroir-Fendler, L. Lorenzen, J.-A. Dalmon. Xylene vapour mixture separator in nanocomposite MFI-alumina tubular membranes: influence of operating variables, *Sep. Sci. Technol.* 45(1),2010,21-27.
3. **M.O. Daramola**, A.J. Burger, M. Pera-Titus, A.Giroir-Fendler, S. Miachon, J.-A. Dalmon, L. Lorenzen. Separation and isomerization of xylene using zeolite membranes: a short overview, *Asia-Pacific Journal of Chemical Engineering*, 2009, DOI:10.1002/apj.414.
4. **M.O. Daramola**, Z. Deng, M. Pera-Titus, A.Giroir-Fendler, A.J. Burger, L. Lorenzen, & Y. Guo. Nanocomposite MFI-alumina membrane prepared via pore-plugging syntheses: application as packed-bed membrane reactors for m-Xylene isomerisation over a Pt-HZSM-5 catalyst, *Catalysis Today*, 2010, in press.
5. Z. Deng, C-H. Nicolas, **M.O. Daramola**, J. Sublet, Th. Schiestel, A.J. Burger, Y. Guo, A. Giroir-Fendler, M. Pera-Titus .Nanocomposite MFI-alumina hollow fibre membranes prepared via pore-plugging synthesis: Influence of the porous structure of hollow fibres on the gas/vapour separation performance, *J. Membr. Sci.*, 2010, (in press).
6. **M.O. Daramola**, A.J. Burger, S. Miachon, A.Giroir-Fendler, L. Lorenzen. Extractor-type catalytic membrane reactors having nanocomposite MFI-alumina membrane tube as separation unit: prospect for ultra-pure p-Xylene production from m-Xylene isomerization over Pt-HZSM-5 catalyst, *Appl.Catal.A:General* (accepted).

### Articles published in conference proceedings

7. **M.O. Daramola**, A.J. Burger, A. Giroir-Fendler, S. Miachon. 2009. Nanocomposite MFI-alumina membranes: influence of operating parameters on xylene vapour mixture separation. In: Proceedings of the 3<sup>rd</sup> International conference on Nanoscience and Nanotechnology (NanoAfrica 2009), Feb 1-4, Pretoria, South Africa, pp. 1-9.

- 
8. **M.O. Daramola**, A.J. Burger, A.Giroir-Fendler, S. Miachon. 2009. Energy efficient process for xylene isomers separation: The use of nanocomposite MFI-ceramic hollow fibers. In: Proceedings of the 2<sup>nd</sup> International Conference on Engineering Management and Environmental Planning (CEMEPE2009 & SECOTOX), June 21 -26, Greece, pp. 1847-1855.
  9. **M.O. Daramola**, Z. Deng, M. Pera-Titus, A. Giroir-Fendler, A.J. Burger & Y. Guo. 2009. Nanocomposite MFI-ceramic hollow fibres: preparation and application to xylene isomer separation. In: Proceedings of the 9<sup>th</sup> International Conference on Catalysis in Membrane Reactors, June 28 – July 2, Lyon, France, pp. 133-134.
  10. **M.O. Daramola**, A.J. Burger, A.Giroir-Fendler, S. Miachon.2009. Nanocomposite MFI/alumina based catalytic membrane reactors: Application for meta-xylene isomerization over Pt-HZSM-5 zeolite catalyst. In: Proceedings of the South African Chemical Engineer's conference (SACEC2009), September 21 -23, South Africa.